The modelling and measurement of nuclear reaction cross-sections & the production of a technetium fission yield tracer

Ross A.M. Allen



UNIVERSITY OF BIRMINGHAM

A thesis submitted to
the University of Birmingham
for the degree of
Doctor of Philosophy (Ph.D.)

Nuclear Physics Group
School of Physics and Astronomy
College of Engineering and Physical Sciences
University of Birmingham

UNIVERSITY OF
BIRMINGHAM

University of Birmingham Research Archive

e-theses repository

This unpublished thesis/dissertation is copyright of the author and/or third parties. The intellectual property rights of the author or third parties in respect of this work are as defined by The Copyright Designs and Patents Act 1988 or as modified by any successor legislation.

Any use made of information contained in this thesis/dissertation must be in accordance with that legislation and must be properly acknowledged. Further distribution or reproduction in any format is prohibited without the permission of the copyright holder.

Abstract

The 20^{th} century saw the dawn of the nuclear age, in which humanity harnessed the strong nuclear force through the nuclear processes of fission and fusion. Nuclear science expanded our understanding of matter beyond chemical elements, to include over 7,000 predicted nuclei, each with discrete characteristics born out of their nuclear structure. An understanding of nuclear reactions and decay of nuclei enabled energy production with densities orders of magnitude greater than traditional means, and the diagnosis and treatment of a range of diseases. These advancements also came with baggage in the form of security and environmental challenges. The characterisation and detection of radionuclides is of huge importance in nuclear science, whether that be optimising the operation of nuclear reactors based on the distribution of fuel products, the detection of clandestine nuclear activity by rogue states through the detection of products produced in nuclear weapons testing, and the mitigation of environmental damage by accurately being able to quantify the transport of radionuclides through matter and the biosphere. All isotopes of a given element act chemically identically due to their identical electron configuration, however, they each possess unique physical fingerprints in the form of decay channels, reaction probabilities, and reaction mechanisms. The combination of these factors opens up a realm of possibilities, whereby the chemical transport of different isotopes of the same element is identical, while the presence of different isotopes can be determined by their unique nuclear characteristics, two facts which are leveraged with radiotracers. The field of radiotracers is ubiquitous in medicine, energy, and nuclear security, with the production of high-purity radioactive isotopes with specific physical and chemical characteristics for a range of applications in an evolving field.

The development of such a tracer involves several stages, centering around the optimisation of nuclear reactions to enable the production of exotic elements and isotopes often not present in nature, which through optimised particle accelerator production combined with a series of refined chemical separation steps can produce high isotopic purities. This thesis focuses on developing a radio-tracer of ^{97}Tc for the analysis of long-lived fission product ^{99}Tc. The workflow can act as an effective template for future tracer development, with clear steps from concept to a standardised tracer suitable for

commercial deployment. With ^{99}Tc being a high-yield fission product produced 6.1% of the time in thermal neutron-induced fission of ^{235}U [1], a commercially viable mass tracer for technetium-99 is highly sought after in the nuclear industry, with applications in nuclear security, decommissioning, environmental monitoring and optimising reactor power cycles.

As a mass spectrometry tracer of ^{99}Tc, ^{97}Tc was determined as the only suitable candidate isotope, produced indirectly through the decay of a ^{97}Ru generator. Six reactions were then compared using natural abundance targets: ^{nat}Mo(^{3}He,xn)^{97}Ru, ^{nat}Mo(α,xn)^{97}Ru, ^{nat}Ru(p, X)^{97}Ru, ^{nat}Ru(d, X)^{97}Ru, ^{nat}Ru(^{3}He,X)^{97}Ru, and ^{nat}Ru(α,X)^{97}Ru. A computational tool for the running of nuclear reaction modelling and isotope inventory calculations called "The University of Birmingham Tool for Isotope Production (UoB-TIP)" was developed during this project. This software enabled a range of nuclear reactions to be modelled using TALYS and TASMAN nuclear reaction codes and FISPACT-II transmutation code. This enabled the rapid comparison of accelerator-driven production routes, while also executing the parsing and visualisation of data, enabling determination of the optimum target-beam combination, particle energy, and the time to chemically separate to maximise quantity and purity.

Quantitative results from this software package, along with coordination with the National Physical Laboratory on the potential chemical purification, ^{nat}Mo(α, xn)^{97}Ru was determined to be the most promising reaction. This is due to the large cross-section of ^{97}Ru production, high threshold energy of contaminant isotope ^{99}Mo, and a novel separation scheme developed during this project which utilised the recently developed TK202 extraction chromatography resin.

A high-precision nuclear reaction cross-section method was developed for charged particle spectroscopy at the University of Birmingham MC40 cyclotron, including experimental set-up and semi-automated analysis software. This method was used to improve accuracy in nuclear reaction cross-sections for Mo-α, with the method and experimental results in this thesis.

Following this, a novel chemical separation method was developed at the National Physical Labo-

ratory using TK202 resin. The optimum operating conditions were found to be 5M NaOH for a high retention of Tc. This enables easy separation of the Tc produced in the reaction from the ^{97}Ru generator with a successive step extracting the ^{97}Tc, produced through the decay of the tracer with a half-life of 2.83(32) d, from any stable Ru and Mo in the remaining target.

Acknowledgements

Getting to the stage of completing this PhD would not have been achieved without the help and support of so many people, with the people I mention on this page being far from exhaustive.

It would be wrong to begin these acknowledgements by thanking anybody but Hannah, who throughout this PhD has been an absolute rock by my side. Not only for her tremendous support, and ability to listen to my ponders and grumbles, but most importantly a reality check, of reminding me how incredibly boring I can be drivelling on about nuclear physics...

Thank you to my family for their support, persistent love, and patience. Mum, no, I'm not the useful kind of doctor. Grandma, I hope you were looking for a thesis-shaped door wedge.

To all of my incredible friends; the swans must get a special shoutout as they have supported me, tolerated me and been some of my greatest inspirations over the years. To my Monument Road housemates, for being there through this chapter and hopefully far beyond.

When I started this PhD, little was I to know I'd finish writing it in a small town in Northern Ireland (whose name I can't even pronounce), surrounded by people at the start that I had no idea existed. The Davison family have been an incredible support throughout my PhD, somehow tolerating me throughout the entirety of lockdown, several Christmas' and holidays.

I undoubtedly thank my supervisor Professor Tzany Kokalova-Wheldon, for the opportunity to study this PhD, your continued support and guidance throughout this project, and your ability to bring me back to earth. My wider supervisory entourage of Carl Wheldon, Ben Russell, and Peter Ivanov, thank you for all you have taught me, and for trusting (enduring) Tzany's decision to accept me. The Nuclear Metrology group have been pivotal throughout this project and I appreciate all of their assistance, guidance and effort. Thank you additionally to the teachers who believed in me before any other,

David Godwin, Catherine Sinnott, Sarah Burton, your contributions could never be understated.

To the many PhD students of the nuclear physics group and the many friendships within, for their company and distraction, with an additional nod to our adopted collegaues from lesser research groups. Additionally to my colleagues who lost sleep and patience during my long experimental runs: Trinder, Mark, Pedro and Dawid. It would be unfair to not give a special thank you to Angus for his persistent guidance in my computational exploits.

I would additionally like to thank all UK taxpayers for unknowingly funding the last four years of my life, preventing me from contributing to the tax system or the wider economy. Thank you to the Nuclear Decommissioning Authority for funding this project, and to Robert Mills of the National Nuclear Laboratory for his industrial supervision.

Dedication

To my Mum, my greatest supporter and inspiration

Contents

Abstract I

Acknowledgements IV

Dedication VI

Contents VII

List of Figures XIV

List of Tables XXVI

1 Introduction 1

1.1 Nuclear Fission . . . 1

1.1.1 Nuclear Power . . . 3

1.1.2 Fission Products . . . 4

1.1.2.1 Spent Nuclear Fuel . . . 6

1.1.3 Environmental Radioactivity Monitoring . . . 7

1.2 The Need for Radiotracers . . . 8

1.3 Technetium-99 . . . 9

1.4 Technetium-99 Analysis . . . 12

1.5 ICP-MS Analysis . . . 13

1.6 Technetium yield tracers . . . 17

1.7 Nuclear Reactions . . . 19

1.7.1 Nuclear Structure 20
1.7.1.1 Liquid Drop Model 21
1.7.1.2 Spherical Shell Model 22
1.7.1.3 Coulomb Repulsion 25
1.7.2 Compound Reactions 27
1.7.3 Direct Reactions 28
1.7.4 Pre-equilibrium reactions 28
1.8 Cross-Section 28
1.9 Isotope production 31
1.9.1 Particle Beam 32
1.9.2 Targetry 32
1.9.3 Cyclotron Accelerators 34
1.9.4 Chemical Separation 36

2 Theoretical Cross-Section & Transmutation Modelling 39
2.1 Nuclear Data 40
2.1.1 Nuclear Reaction Data 41
2.1.2 Evaluated Nuclear Data Libraries 41
2.1.3 EXFOR 42
2.1.4 Unevaluated Nuclear Data Library (XUNDL) 42
2.1.5 Parameter Library 42
2.2 Nuclear Reaction Modelling 43
2.3 T6 Software Suite 44
2.4 TALYS 45
2.4.1 Optical Model Potential 46
2.4.2 TALYS outputs 49
2.5 TASMAN 50
2.6 University of Birmingham - Tool for Isotope Production 53
2.6.1 TALYS Automation 54

2.6.2 Output Parsing . . . 58
2.6.3 Plotting Tool . . . 61
2.7 FISPACT-II . . . 61
2.7.1 FISPACT-II Energy Loss Program . . . 61

3 Reaction Optimisation 65

3.1 Ru-97 generator . . . 67
3.2 Products of Concern . . . 69
3.3 Tc-97 Isomeric State Decay . . . 70
3.4 Reaction Modelling . . . 72
3.5 Ruthenium Targets . . . 73
3.5.1 Proton irradiation of ^{nat}Ru . . . 74
3.5.2 Deuteron irradiation of ^{nat}Ru . . . 75
3.5.3 Helium-3 irradiation of ^{nat}Ru . . . 76
3.5.4 Helium-4 irradiation of ^{nat}Ru . . . 78
3.6 Molybdenum targets . . . 79
3.6.1 Helium-3 irradiation of ^{nat}Mo . . . 80
3.6.2 Helium-4 irradiation of ^{nat}Mo . . . 81
3.7 Reaction Comparison . . . 82
3.7.1 Stopping Power Comparison . . . 82
3.7.2 Ruthenium Target Reaction Comparison . . . 84
3.7.3 Molybdenum Target Reaction Comparison . . . 87
3.7.4 Cross-Section Summary . . . 89
3.8 FISPACT-II Calculations . . . 89
3.8.1 Mo-α transmutation calculations . . . 90
3.8.2 Ru-p transmutation calculations . . . 92
3.9 Reaction Optimisation Conclusion . . . 93

4 Experimental Mo-α Cross-Section Measurement **95**

4.1 Introduction . . . 95

4.2 Foil Thickness Measurement . . . 99

4.2.1 Experimental set-up . . . 99

4.2.2 Foil Thickness Experiment . . . 102

4.2.3 Results . . . 105

4.3 Beam Energy Measurements . . . 107

4.3.1 Kinematic Reconstruction . . . 107

4.3.2 Experimental set-up . . . 109

4.3.3 Calibration . . . 111

4.3.4 Results . . . 114

4.4 Calculation of Beam Energy Through Each Foil . . . 116

4.4.1 Stopping power and alpha particles ranges . . . 116

4.4.2 Calculations of alpha particle energies at the centre of each foil . . . 118

4.5 Current Measurement . . . 120

4.5.1 Experimental set-up . . . 120

4.5.2 Data Analysis . . . 122

4.5.3 Results . . . 125

4.6 High-Resolution gamma-ray Spectroscopy . . . 126

4.6.1 Experimental Set-Up . . . 126

4.6.2 HPGe Detector . . . 128

4.6.3 Energy Resolution . . . 129

4.6.4 Detector Efficiency . . . 133

4.6.4.1 Solid Angle Calculation . . . 136

4.6.4.2 Efficiency Fitting . . . 136

4.6.4.3 Efficiency Measurement Results . . . 137

4.6.5 Data Analysis . . . 139

4.6.5.1 Data Cleaning . . . 140

4.6.5.2 Online Data Visualisation . . . 141
4.6.5.3 Peak Fitting . . . 142
4.6.5.4 Calculating Decay Curves . . . 143
4.6.5.5 Cross-Section Calculation . . . 145
4.6.6 Data Correction . . . 146
4.6.6.1 Counts corrections . . . 146
4.6.6.2 Efficiency Corrections . . . 146
4.6.7 Sequential decays . . . 150
4.6.8 Predicted isotopes and γ emissions produced in the Mo-α reaction . . . 152
4.7 Cross-Section Results . . . 157
4.7.1 Ruthenium-103 . . . 157
4.7.2 Ruthenium-97 . . . 158
4.7.3 Ruthenium-95 . . . 160
4.7.4 Ruthenium-94 . . . 162
4.7.5 Technetium-99m . . . 164
4.7.6 Technetium-96 . . . 165
4.7.7 Technetium-95g . . . 167
4.7.8 Technetium-94g . . . 169
4.7.9 Technetium-93m . . . 170
4.7.10 Technetium-93 . . . 171
4.7.11 Molybdenum-99 . . . 173
4.7.12 Molybdenum-93m . . . 174
4.7.13 Niobium-90 . . . 176
4.7.14 Conclusion . . . 177

5 Tc-97 Chemical Purification 179
5.1 Introduction . . . 179
5.2 Technetium separation . . . 180
5.2.1 Medical Isotopes . . . 180

5.2.2 Environmental Monitoring and Nuclear Decommissioning 181
5.3 Triskem Technetium Resins 182
5.3.1 TEVA 182
5.3.2 TK-TcScint 182
5.3.3 TK200 183
5.3.4 TK201 183
5.3.5 TK202 183
5.4 Method Development 185
5.4.1 Reverse Generator 186
5.4.2 Sample Preparation 187
5.4.3 Optimising Separation Conditions 188
5.5 Chemical Separation Scheme 194
5.6 Surrogate Target Experiment 195
5.6.1 Mass Spectrometry Measurement 196
5.6.2 Mass Spectrometry Results 196
5.7 Active Sample Validation 196
5.7.1 Irradiation 196
5.7.2 Chemical Separation 200
5.7.3 Gamma-ray Spectrometry Measurement 201
5.7.3.1 Gamma-Ray Spectrometry Results 202
5.7.3.2 Presence of ^{99}Mo 205
5.7.3.3 Molybdenum Saturation 205
5.8 Conclusion 205

6 Conclusions **207**

6.1 Nuclear Data Software Development 208
6.2 Technetium Radiotracer Development 209
6.2.1 Future Method Improvements 209
6.3 Cross-Section Method Development 210

6.3.1 Future Method Improvements 211
6.4 Technetium Chemical Separation 212
6.4.1 Future Work 212
6.5 Additional Benefits of Mo-α Nuclear Data 212
6.5.1 Nuclear Medicine 212
6.5.2 Fusion Energy 213
6.6 Future Tracer Development 213

A Conference Presentations **215**

B Variable Cross-Section Reaction Rate Derivation **217**

C Nuclear Reaction Modelling Results **219**

D Non-relativistic two-body kinematic scattering **223**

E Spectrum Decay Count Correction **227**

F Statistics **229**
F.1 Error Propagation 229
F.2 Weighted average of value with errors 230

List of Figures

1.1 Visuaisation of the Karlsruhe chart of nuclides, showing the neutron number, N, on the horizontal axis and the proton number, Z, on the vertical axis.[2]. 2

1.2 Visualisation of the fission process, with a large nucleus breaking up into two discrete fission products and neutrons following the pinch process of fission. 3

1.3 Cumulative fission yield of thermal neutron-induced fission of ^{235}U. Data are extracted from the JEFF 3.3 database [1]. 5

1.4 The fission product mass over time for spent fuel per kg of uranium, plotted on a log-log scale, for a standard PWR irradiation. [12]. 7

1.5 Decay scheme of ^{99}Mo to the stable isotope ^{99}Ru, through the successive decay of ^{99m}Tc and ^{99}Tc [24]. 10

1.6 The calculated release of technetium-99 from Sellafield into the Irish sea between the years of 1952 and 2016 [28]. 11

1.7 Schematic highlighting the peak tailing between neighbouring analysis peaks in mass spectrometry from m/Z=98 and m/Z=99. 15

1.8 Schematic of a mass spectrometer reaction cell and quadrupole magnets, illustrating the mechanisms to remove common interferences for the detection of ^{99}Tc [43]. . . 17

1.9 The change in the binding energy of introducing a final neutron, against increasing parent nucleus mass [69]. 23

1.10 Nuclear energy level structure predicted by the spherical shell model, with the shell and overall occupancy annotated along with the presence of magic numbers [72]. . 25

1.11 The force between two interacting nuclei as a function of radius, r, for a nucleus with the long-range repulsive Coulomb potential dominating outside of the nuclear radius. The red line shows the contribution from Coulombic repulsion, the blue line is the attractive strong nuclear force, and the black line is the overall force. 26

1.12 Schematic of a compound reaction, showing the production of a compound nucleus of ^{97}Tc*, through a range of reaction mechanisms. 27

1.13 A plot showing the cross-section of various emission channels for proton irradiation of ^{92}Mo, calculated using TALYS. The bands around the data lines show the uncertainty calculated using TASMAN. The horizontal axis is the projectile energy in MeV. 29

1.14 Cross-section plot showing different ejectile combinations which result in the same residual nucleus. The cross-section is measured in millibarns and the horizontal axis is the projectile energy in MeV. The calculations were performed using TALYS nuclear reaction code for the production of the ^{97}Mo-α reaction producing technetium-97. 30

1.15 Stopping power against energy for a range of target-beam combinations calculated using the SRIM stopping power code [76]. 33

1.16 Schematic of cyclotron particle accelerators, one with two dees and two dummy dees, one with an azimuthally varying field that causes focusing and defocusing to account for relativistic effects. 35

1.17 Plot of the fundamental and first harmonic of the MC40 cyclotron particle accelerator with the angular extent of a quarter dee (90°) highlighted in purple. 36

2.1 Visualisation of the nuclear data pipeline from measurement to application [78]. . . 40

2.2 T6 software workflow [98]. 44

2.3 TALYS calculation workflow, from input, nucleus and reaction modelling to outputs [84]. 46

2.4 Visualisation of how the optical model is used to calculate different nuclear reaction mechanisms, being spread through the pre-equilibrium and compound systems [102]. 47

2.5 Plot of the random permutation (multiplication factor) of several optical model parameters in TASMAN for; lvadjust, awadjusta, avadjusta, lvsoadjust overlaid to show the truncated Gaussian spread of data. 52
2.6 The multiplication factor on the awadjusta OMP parameter for NTALYS=50, 100, 500 & 1000. 53
2.7 UoB-TIP example code to run the cross-section calculations for ^{100}Mo-p and ^{nat}Mo-α 55
2.8 An example of a simple TALYS input file produced by UoB-TIP for the ^{100}Mo-p reaction using an external 'energies' file, the 'best' keyword and 'maxlevelsres'. . . . 56
2.9 Example directory tree for multiple runs for the production of ^{99m}Tc. 57
2.10 UoB-TIP JSON output structure for the ^{98}Mo-α reaction. The file structure is broken down by each product isotope. 60
2.11 Visualisation of the CCFE-162, CCFE-709 and CCFE-1102 group structures. . . . 62
2.12 Plot of particle range through a target visualising the correlation between a drop in energy, dE, and a change in distance, dx. 63
2.13 Irradiation target split into slices of thickness, dx, relating to a drop in energy, dE. . 63

3.1 Chart of nuclides focusing on Nb, Mo, Tc and Ru elements near stability [2]. . . . 66
3.2 Decay chain showing ^{97}Tc and all of the beta decay chain including ^{97}Ru, ^{97}Rh, and ^{97}Pd. 68
3.3 Level scheme for the decay of ^{97}Ru, showing the branching of the isomeric state of ^{97}Tc into the ground state with a probability of 0.9606, with the remaining 0.0394 decaying via electron capture to ^{97}Mo. [56] 70
3.4 Isotope fraction of ^{97}Tc and decay products of mass A=97 over a period of five years. 71
3.5 Isomeric ratio of ^{97}Tc over total ^{97}Mo and ^{97}Tc over a period of five years. 72
3.6 Isotopes of ruthenium near stability, showing A=95 to A=103, with the decay path for radioctive isotopes shown. [2]. 73
3.7 Production cross-sections for the Ru-p reaction. 74
3.8 Production cross-sections for the Ru-d reaction. 75

3.9 Production cross-sections for the Ru-^{3}He reaction, where h in the reaction denotes ^{3}He induced reactions. 76

3.10 Contributions to the production of ^{97}Pd from ^{nat}Ru(^{3}He,X) reactions. The natural reaction is nearly entirely dominated by the ^{96}Ru reaction, causing both the mean cross-section and the error margins to overlap over the entire energy range, diverting slightly above 35 MeV. 77

3.11 Plot of the residual production cross-sections for the Ru-α reaction, showing the production of ^{97}Ru and ^{99}Mo. 79

3.12 Isotopes of molybdenum with stable isotopes in black [2]. 79

3.13 Plot of the residual production cross-sections for the Mo-^{3}He reaction. 80

3.14 Plot of the residual production cross-sections for the production of ^{97}Ru and ^{99}Mo through the Mo-α reaction. 81

3.15 Projected particle range of protons, deuterons, helium-3 and helium-4, through Ru and Mo targets. 83

3.16 Comparison of ^{97}Ru production for Ru target reactions. 85

3.17 Comparison of ^{99}Mo production for Ru target reactions 86

3.18 Comparison of ^{97}Ru production for molybdenum target reactions. 87

3.19 Comparison of ^{99}Mo production for molybdenum target reactions. 88

3.20 Activity throughout the irradiation and during subsequent decay of Mo-α. 91

3.21 Number of production atoms throughout the irradiation and during subsequent decay of Mo-α. 91

3.22 Activity throughout the irradiation and during subsequent decay of Ru-p. 92

3.23 Number of atoms throughout the irradiation and during subsequent decay of Ru-p. 93

4.1 A schematic aerial view of the University of Birmingham MC40 cyclotron, with beam-lines 4 and 4a used in this experiment highlighted. 97

4.2 A render of a DSSD detector highlighting the front vertical strips and rear horizontal strips of the detector. The 32 individual wires are seen, connecting to a 32-pin connector (including 2 ground pins) which can be connected to a pre-amplifier for signal processing [114]. 99

4.3 A render of the 3D printed collimator. 100

4.4 Electronic set-up for the foil thickness measurement, showing a single DSSD detector connected to two pre-amplifiers, one for each of the front and rear channels, connected in series to an amplifier, ADC, VME and a computer with MIDAS software installed. The front detector channels were connected to the ADC additionally via an LED, FIFO, gate and delay, and trigger SAC all acting as a coincidence unit. 101

4.5 A cross-sectional side view of the experimental set-up for alpha stopping power thickness measurements, showing the DSSD, collimator, foil and source set-up. 101

4.6 Triple-α spectra recorded on the DSSD charged particle detector, with recorded spectra overlaid both with and without a Mo foil present. 104

4.7 A plot showing particle energy against projected range in mm for an α particle travelling through a Mo foil, calculated using SRIM. Three annotations have been made to the plot, highlighting the change in energy caused by passing through a 1 μm Mo foil. 105

4.8 Schematic of two-body kinematic scattering of a projectile from a stationary target, where θ is the scattering angle of the target nucleus nucleus from the beam axis and ϕ is the scattering angle of the projectile particle from the beam axis. 107

4.9 Schematic of a beam passing through the Au foil, scattering at $\frac{x}{2}$, halfway through the foil. 109

4.10 Birmingham cyclotron's beam-line 4 vacuum chamber, with two DSSD detectors set up at 210 mm from the Au foil. The two detectors were set up at different angles of $\theta = 51.5°$ and $\phi = -24.5°$. Collimators are present prior to the scattering point to maintain a clean beam profile for scattering and detection. 110

4.11 Electronic set-up of the DSSD detectors. 111

4.12 Detector 1 with an attenuating R-mask overlaid, to enable the orientation of the channels to be determined. 112

4.13 Plot of counts against energy with triple-α peaks highlighted with each of the channels overlaid for all 64 channels in both detectors. The three energies of the triple-α are annotated along with the low-energy noise. 113

4.14 Both DSSD detectors, measuring a triple alpha-source, showing both uncalibrated and calibrated. 114

4.15 Schematic of the foil stack with alternating Mo and Al. 116

4.16 Stopping power and projected range for an α particle passing through Mo, calculated using SRIM. 117

4.17 Stopping power and projected range for an α particle passing through Al, calculated using SRIM. 117

4.18 This plot shows the energy at which each foil was irradiated. The data point for each foil is the mean energy halfway through the thickness of the target, while the errors are taken from propagating the maximum beam energy ($E + dE$) and the minimum thicknesses ($x - \sigma x$) for the upper bound, and taking the minimum beam energy ($E - dE$) and the maximum thicknesses ($x + \sigma x$) for the lower bound. 119

4.19 A CAD output of the water-cooled target used for cross-section measurements at the University of Birmingham cyclotron. This is mounted externally to beamline 3. . . 120

4.20 A CAD render of beam-line $4a$ at the University of Birmingham cyclotron. The beamline was commissioned for high-precision cross-section measurements. 121

4.21 A schematic side-profile cross-section of beamline 4a at the University of Birmingham MC40 cyclotron, with the beamline, collimators, target holder and insulating section highlighted with all relevant dimensions. A mock beam profile is shown in purple. . 122

4.22 The output of the cyclotron current logger for the day 1 irradiation of foils 1-4. The electrical current is measured nA, and the time is seconds from the start of the measurement. 123

4.23 The output of the current logger for the day 1 irradiation at the MC40 cyclotron, showing current in nA against time since the start of the measurement in seconds. The two panels show outputs from the current algorithm, which converts a current spectrum to a series of step functions. Different parameters were used for each to highlight the flexibility of the algorithm. 124

4.24 The calculated final activity of a 1800s half-life isotope irradiated using the day 1 current profile at the MC40 cyclotron, where the irradiation is broken into n discrete constant-current irradiations. Along the horizontal axis is the step-size, measured in seconds, used in the algorithm, showing a clear improvement in accuracy with decreasing step size and large oscillations around this value at high values of step size. 125

4.25 The electronic setup of the Hyper-Pure Germanium detector, showing the detector with the high voltage (HV) power supply, and the signal sequence consisting of an inbuilt pre-amplifier, amplifier, analogue-to-digital convertor (ADC) and MCA, connected in series to a PC with Maestro acquisition software. 127

4.26 A render of the 3D printed target holder, containing a circular hole for the HPGe detector to slide into. There are then several slits at various distances throughout the device to enable perspex plates holding the irradiated foils to be placed. 128

4.27 Schematic of both HPGe detectors used in the experiment with dimensions overlaid [110]. 128

4.28 The detector response of a γ ray, broken down into its constituent contributions, including a normal Gaussian, skewed Gaussian and Compton edge labelled as 'Step' in the above image [117]. 130

4.29 Resolution against gamma-ray energy for the G11 HPGe detector, shown on a log-log plot, with the two fit lines shown, for the respective energy regions in red and blue and the dominating resolution shown in green. The cross-over between the two lines is at 148 keV, the energy at which the number of signal carriers is sufficient not to be resolution limiting. 132

4.30 Resolution against gamma-energy for the B15 HPGe detector, shown on a log-log plot, with a linear fit line shown in green, with a gradient of -0.99. 133

4.31 The relative probability of any particular detection mechanism occurring for photon energy, E and detector atomic number, Z [118]. 134

4.32 Efficiency plot for the G11 HPGe detector, taken for a ^{152}Eu calibration source at 15 cm for 12 hours. 138

4.33 Efficiency plot for the B15 HPGe detector, taken for a ^{152}Eu calibration source at 15 cm for 12 hours. 139

4.34 A flowchart of the gamma-ray spectrometry analytical framework developed through this project, offering options for both online automated and offline data fitting. . . 140

4.35 Online gamma-ray spectra visualisation, showing a 2D and 3D representation of channel and counts for each successive spectrum. 142

4.36 A decay curve for ^{97}Ru measured using the $215.70(3)$ keV γ-emission for foil 1. . . 145

4.37 Plot of the decay of ^{97}Ru measures on foil 1, with the data points taken at different distances given in different colours to highlight the dislocation in the count rate. . . 147

4.38 A plot of the intrinsic efficiency calculations performed using a ^{152}Eu calibration source for each source position used in the experiment. 148

4.39 Plot of the decay of ^{97}Ru measures on foil 1, with the data points taken at different distances given in different colours, with the new efficiency correction applied. . . . 149

4.40 Plot of the decay of the 140.511 keV γ-emission, showing a non-linear trend due to the contributions from ^{99m}Tc produced directly in the reaction, exhibiting the intrinsic half-life of $6.0067(5)$ h, dominated at longer decay times by the ^{99}Mo half-life of $65.976(24)$ h due to the equilibrium between the ^{99}Mo and ^{99m}Tc. 150

4.41 Plot of the decay of the 140.511 keV γ-emission, showing a non-linear trend due to the contributions from ^{99m}Tc produced directly in the reaction, with a half-life of $6.0067(5)$ h, dominated at longer decay times by the ^{99}Mo half-life of $65.976(24)$ h due to the equilibrium between the ^{99}Mo and ^{99m}Tc.The data have been fit as the sum of two exponential decays, one for the short-lived ^{99m}Tc and one for the longer lived ^{99}Mo. 151

4.42 Spectra with peaks highlighted for energy < 350 keV for foils 1 and 8 on days 1 and 7. The highlighted peaks can be found in table 4.9 and 4.10. 153

4.43 Spectra with peaks highlighted for energy 350-700 keV for foils 1 and 8 on days 1 and 7. The highlighted peaks can be found in table 4.9 and 4.10. 153

4.44 Spectra with peaks highlighted for energy 700-1050 keV for foils 1 and 8 on days 1 and 7. The highlighted peaks can be found in table 4.9 and 4.10. 154

4.45 Spectra with peaks highlighted for energy > 1050 keV for foils 1 and 8 on days 1 and 7. The highlighted peaks can be found in table 4.9 and 4.10. 154

4.46 Plot of the eight experimental cross-section results, with associated errors, overlaid with cross-section calculations for ^{nat}Mo(α, xn)^{103}Ru calculated using TALYS and TASMAN up to 40 MeV. 158

4.47 Plot of the eight cross-section data points, with errors, overlaid with cross-section calculations for ^{nat}Mo(α, xn)^{97}Ru calculated using TALYS and TASMAN up to 40 MeV. 160

4.48 Plot of the mean production cross-section for ^{nat}Mo(α, xn)^{95}Ru calculated for the eight energies using data acquired through gamma-ray spectrometry analysis. The data are overlaid with cross-section models, calculated using TALYS and TASMAN up to 40 MeV. 162

4.49 A plot of the mean production cross-sections for ruthenium-94 using data acquired through gamma-ray spectrometry analysis. The data are overlaid with cross-section models, calculated using TALYS and TASMAN up to 40 MeV. 163

4.50 A plot of the mean production cross-section of ^{99m}Tc, calculated for foils 1-6, with associated error. The data are overlaid with cross-section models for ^{nat}Mo(α, pxn)^{99m}Tc, calculated using TALYS and TASMAN up to 40 MeV. 165

4.51 Plot of the mean production cross-section of ^{96}Tc, calculated for foils 1-6, with error. The data are overlaid with cross-section models for ^{nat}Mo(α, pxn)^{96}Tc, calculated using TALYS and TASMAN up to 40 MeV. 166

4.52 Plot of the mean ^{95g}Tc production cross-section, calculated for the eight energies with their associated error. The data are overlaid with cross-section models calculated using TALYS and TASMAN up to 40 MeV. The corrected value uses the calculated value of cross-section, subtracting the calculated production of ^{95}Ru, multiplied by the probability of decay into ^{95g}Tc (97.4%). 168

4.53 Plot of the mean cross-section calculated for foils 1-6, with error. The data are overlaid with cross-section models for ^{nat}Mo(α, pxn)^{94}Tc, calculated using TALYS and TASMAN up to 40 MeV. 170

4.54 Plot of the production cross-section of ^{93m}Tc and short lived ^{93}Ru, calculated for foils 1 and 2, with error. The data are overlaid with cross-section models for ^{nat}Mo(α, pxn)^{93}Tc, ^{nat}Mo(α, xn)^{93}Ru, and the sum of these calculated using TALYS and TASMAN up to 40 MeV. 171

4.55 Plot of the mean cross-section calculated for the two energies, with their associated error. The data are overlaid with cross-section models for ^{nat}Mo(α, pxn)^{94}Ru, calculated using TALYS and TASMAN up to 40 MeV. 172

4.56 Plot of the mean cross-section calculated for foils 1-6, with error. The data are overlaid with cross-section models for ^{nat}Mo(α, αxn)^{99}Mo, calculated using TALYS and TASMAN up to 40 MeV. 174

4.57 Plot of the mean cross-section calculated for foils 1-5, with error. The data are overlaid with cross-section models for ^{nat}Mo(α, αxn)^{93m}Mo, calculated using TALYS and TASMAN up to 40 MeV. 175

4.58 Plot of the mean cross-sections calculated for foils 1 and 2, with error. The data are overlaid with cross-section models for ^{nat}Mo(α, αxn)^{90}Nb, calculated using TALYS and TASMAN up to 40 MeV. 177

4.59 Plot of the cross-sections of all analysed isotopes. 178

5.1 Affinity of Tc, Re and Mo to TK202 over a range of NaOH alkaline conditions from 1 M-10 M as published by Triskem [123]. 184

5.2 Distribution coefficients for Tc in 5M NaOH on TK202 resin versus molybdenum mass [135]. 185

5.3 A schematic of the reverse generator approach for the isolation of ^{97}Tc. 186

5.4 Percentage recovery in the load collected of Mo, Ru and Re in varying NaOH molar concentrations through TK202. 189

5.5 Percentage recovery in the wash of Mo, Ru and Re in varying NaOH molar concentrations through TK202. 190

5.6 Percentage recovery in the elution of Mo, Ru and Re in varying NaOH molar concentrations through TK202. 190

5.7 Percentage recovery in the load collected of Mo, Ru and Re in varying KOH molar concentrations through TK202. 191

5.8 Percentage recovery in the wash of Mo, Ru and Re in varying KOH molar concentrations through TK202. 192

5.9 Percentage recovery in the elution of Mo, Ru and Re in varying KOH molar concentrations through TK202. 192

5.10 The recovery of Ru, Mo and Re under the optimum conditions of 5M NaOH . . . 194

5.11 Chemical separation scheme for isolating ^{97}Tc from a Mo irradiated target through a ^{97}Ru generator isotope. 195

5.12 The activity of various products of interest from the end of the irradiation to 1 year of decay time, for a fully-depleted 15.5 MeV α beam in a 250μm Mo target. 197

5.13 The number of atoms of various products of interest from the end of the irradiation to 1 year, for a fully-depleted α beam in a 250 μm Mo target. 198

5.14 A plot showing the number of atoms of ^{97}Tc and ^{97}Ru following a Mo-α irradiation, with the in-growth of the ^{97}Tc from the decay of ^{97}Ru evident. 200

5.15 Gamma-ray spectra acquired on LANCELOT HPGe detector at the National Physical Laboratory for six measurements of 2 mL ISO ampoules of 1 g sample fractions, taken from a separated, irradiated Mo-α foil at different times and stages. 202

5.16 Decay corrected counts per second per gram for the six measurements taken on the "LANCELOT" HPGe gamma-ray detector at the National Physical Laboratory for the separated sample. 203

5.17 Ratio of counts of four key isotopes ^{95}Tc, ^{95m}Tc, ^{99}Mo and ^{103}Ru over ^{97}Ru for the Mo-α irradiated target separated at NPL, analysed under the "LANCELOT" gamma-ray spectrometer. 204

6.1 Flowchart for developing a novel radio-isotope tracer for difficult-to-measure (DTM) nuclides, taking input from industry, followed by an iterative research and development project and final standardisation and commercialisation. 214

D.1 Schematic of two-body kinematic scattering of a projectile on a stationary target. . . 224

List of Tables

1.1 Summary table highlighting recent analysis of technetium-99 using ICP-MS [28], showing the sample type, separation resin and limits of detection (LoD) in both mass and activity. 12

1.2 Summary table of recent liquid scintillation counting measurements [28], showing the sample type, separation resin, counting time and limits of detection (LoD) in both mass and activity. 12

1.3 Half-life of Tc tracer candidate isotopes, showing the ground state (GS), first isometric state (1*st* IS) and data reference. 18

3.1 Possible reaction channels to directly produce ^{97}Tc. 66

3.2 Possible reaction channels to produce ^{97}Ru generator. 67

3.3 Possible reaction channels to produce ^{97}Rh generator. 68

3.4 Possible reaction channels to produce ^{97}Pd generator. 68

3.5 Atomic percentage of ^{97}Tc over the total atomic percentage of isotopes with mass A=97. 72

3.6 Table showing the natural abundance of ruthenium isotopes, along with the error, extracted from NIST [104]. 73

3.7 Natural abundance values of molybdenum isotopes, with errors, extracted from NIST [104]. 80

3.8 Projected particle range for different projectiles in Ru and Mo, in units of g.cm^{-2}. . 83

3.9 Projectile range for p, d, ^{3}He and α in Ru and Mo at their maximum energy in a K=40 cyclotron, in units of g.cm^{-2}. 84

3.10 Threshold energies for the various ruthenium target reactions. 85

3.11 Threshold for ^{99}Mo reactions with Ru targets. 86

3.12 ^{97}Ru scaled production reaction rate for each of the ruthenium reactions from 0 MeV to 3 MeV below the ^{99}Mo threshold energy. The production rate was calculated using the proportionality in equation 3.1. 87

3.13 Production quantities for Mo-α initially following irradiation and after all ^{95}Ru has decayed 92

3.14 Production quantities for Ru-p initially following irradiation and after all ^{95}Ru has decayed 93

4.1 Alpha energies of the triple-alpha calibration source, along with the degraded energy due to a thin gold flashing, labelled as calibration energy. 102

4.2 Calculation of the thickness of the molybdenum foils, taken as a weighted average of the values calculated from each triple-α result, along with the mean thickness, $\bar{x}$. Energy values are all given in units of MeV and thicknesses in units of μm. The error on the thicknesses are given for both positive and negative values as $\delta(x)_{upp}$ and $\delta(x)_{low}$ respectively. 106

4.3 Calculation for the thickness of the aluminium foils, taken as a weighted average of the values calculated from each triple-α result. Energy values are given in units of MeV and distances in units of μm. 106

4.4 Beam energy calculation using kinematic reconstruction for the 40 MeV α beam. . 114

4.5 Beam energy calculation using kinematic reconstruction for the 29 MeV α beam. . 115

4.6 Table of the foil energies for the 1st irradiation performed with foils 1-4 at $39.03(15)$ MeV. The mean energy is the average energy at $x/2$ distance through the target, while the upper and lower energies are the limits at the edge of the target, using the error bounds of the energy and thicknesses. 118

4.7 Table of the foil energies for the 2nd irradiation performed with foils 5-8 at $26.84(15)$ MeV. The mean energy is the average energy at $x/2$ distance through the target, while the upper and lower energies are the limits at the edge of the target, using the error bounds of the energy and thicknesses. 118

4.8 The current results for the two Mo foil irradiations, showing the data, start and end time of the irradiation, the number of 1 second non-zero steps and the integrated current in μAh with error. 125

4.9 Table of predicted gamma-ray energies 0-35 from the ^{nat}Mo-α reaction, extracted from ENSFD [25]. 155

4.10 Table of predicted gamma-ray energies 36-70 analysed from the ^{nat}Mo-α reaction. . 156

4.11 Molybdenum-α cross-section results for ruthenium-103, for the $497.085(10)$ keV emission, for foils 1-4. All cross-section values are in units of millibarns (mb). . . . 157

4.12 Molybdenum-α cross-section results for ruthenium-103, for the $497.085(10)$ keV emission, for foils 5-8. All cross-section values are in units of millibarns (mb). . . . 157

4.13 Molybdenum-α cross-section results for ruthenium-97, for the $215.70(3)$ keV and $324.48(3)$ keV emissions, along with the weighted mean, for foils 1-4. All cross-section values are in units of millibarns (mb). 159

4.14 Molybdenum-α cross-section results for ruthenium-97, for the $215.70(3)$ keV and $324.48(3)$ keV emissions, along with the intensity-weighted mean, for foils 5-8. All cross-section values are in units of millibarns (mb). 159

4.15 Molybdenum-α cross-section results for ruthenium-95, for the $336.40(10)$ keV and $626.83(10)$ keV emissions, along with the intensity-weighted mean, for foils 1-4. All cross-section values are in units of millibarns (mb). 161

4.16 Molybdenum-α cross-section result for ruthenium-95, for the $336.40(10)$ keV and $626.83(10)$ keV emissions, along with the intensity-weighted mean, for foils 5-8. The mean cross-section for foils 3-6 was taken only from the $336.40(10)$ keV peak due to much higher statistics. All cross-section values are in units of millibarns (mb). . . . 161

4.17 Molybdenum-α cross-section results for ruthenium-94, for the $367.2(5)$ keV emission, for foils 1-4. All cross-section values are in units of millibarns (mb). 163

4.18 Molybdenum-α cross-section results for ruthenium-94, for the $367.2(5)$ keV emissions for foils 5-7. All cross-section values are in units of millibarns (mb). 163

4.19 Molybdenum-α cross-section results for technetium-99m, for the $140.511(1)$ keV emission, for foils 1 and 6. All cross-section values are in units of millibarns (mb). . 164

4.20 Table of results for the total technetium-96 production cross-section. The results are for the $778.22(4)$ keV gamma-ray emission for foils 1-6. All cross-section values are in units of millibarns (mb). 166

4.21 Molybdenum-α cross-section results for technetium-95g, for the $765.789(9)$ keV and $1073.71(2)$ keV emissions, along with the intensity-weighted mean, for foils 1-4. All cross-section values are in units of millibarns (mb). 167

4.22 Molybdenum-α cross-section results for technetium-95g, for the $765.789(9)$ keV and $1073.71(2)$ keV emissions, along with the intensity-weighted mean, for foils 5-8. All cross-section values are in units of millibarns (mb). 168

4.23 Molybdenum-α cross-section results for technetium-94, for the $702.67(7)$ keV and $817.05(7)$ keV emissions, along with the intensity-weighted mean, for foils 1 and 6. All cross-section values are in units of millibarns (mb). 169

4.24 Molybdenum-α cross-section results for technetium-93m, for the $391.83(8)$ keV emissions, along with the intensity-weighted mean, for foils 1 and 2. All cross-section values are in units of millibarns (mb). 171

4.25 Molybdenum-α cross-section results for technetium-93, for the $1362.94(7)$ keV emissions, for foils 1 and 2. All cross-section values are in units of millibarns (mb). . . . 172

4.26 Molybdenum-α cross-section results for ^{99}Mo, for the 140.511 keV from the successive ^{99m}Tc decay and $739.500(17)$ keV emissions, along with the intensity-weighted mean, for foils 1-6. All cross-section values are in units of millibarns (mb). 173

4.27 Molybdenum-α cross-section results for ^{93m}Mo, for the $263.049(13)$ keV and $684.693(21)$ keV emissions, along with the intensity-weighted mean, for foils 1-5. All cross-section values are in units of millibarns (mb). 175

4.28 Molybdenum-α cross-section results for ^{90}Nb, for the $1129.224(15)$ keV emission for foils 1 and 2. All cross-section values are in units of millibarns (mb). 177

5.1 Percentage recovery of Mo, Ru and Re in the elution using de-ionised H_2O, following running the samples through the TK202 extraction chromatography resin with varying molar concentrations of NaOH. 191

5.2 Percentage recovery of Mo, Ru and Re at varying molar concentrations of KOH through TK202 extraction chromatography resin. 193

5.3 Table containing the 2 mL ISO ampoules containing 1 g fractions of the aqueous samples of the dissolved target. 201

5.4 Table of the measurements performed on the "LANCELOT" HPGe gamma-ray spectrometer at the National Physical Laboratory. 201

5.5 Decay corrected gamma-spectrum counts per second per gram using the "LANCELOT" detector for the six measurements of a separated Mo-α target at varying separation stages. 202

5.6 Decay corrected counts per second per gram for each of the six measurements for each isotope of interest as a ratio over the decay corrected counts per second per gram of ^{97}Ru. 203

C.1 TASMAN reaction results for Ru-p, showing the residual production cross-section and exclusive cross-section along with key values: Q-value, energy threshold, maximum cross-section and the energy of the maximum. The values of Q, E_thres, and E(XS_{max}) are in units of MeV, and σ_{max} and error(σ_{max}) are in units of mb. 219

C.2 TASMAN reaction results for Ru-d, showing the residual production cross-section and exclusive cross-section along with key values: Q-value, energy threshold, maximum cross-section and the energy of the maximum. The values of Q, E$_t hres$, and E(XS$_{max}$) are in units of MeV, and σ_{max} and error(σ_{max}) are in units of mb. 220

C.3 TASMAN reaction results for Ru-^{3}He, showing the residual production cross-section and exclusive cross-section along with key values: Q-value, energy threshold, maximum cross-section and the energy of the maximum. The values of Q, E$_t hres$, and E(XS$_{max}$) are in units of MeV, and σ_{max} and error(σ_{max}) are in units of mb. 220

C.4 TASMAN reaction results for Ru-α, showing the residual production cross-section and exclusive cross-section along with key values: Q-value, energy threshold, maximum cross-section and the energy of the maximum. The values of Q, E$_t hres$, and E(XS$_{max}$) are in units of MeV, and σ_{max} and error(σ_{max}) are in units of mb. 221

C.5 TASMAN reaction results for Mo-^{3}He, showing the residual production cross-section and exclusive cross-section along with key values: Q-value, energy threshold, maximum cross-section and the energy of the maximum. The values of Q, E$_t hres$, and E(XS$_{max}$) are in units of MeV, and σ_{max} and error(σ_{max}) are in units of mb. 221

C.6 TASMAN reaction results for Mo-α, showing the residual production cross-section and exclusive cross-section along with key values: Q-value, energy threshold, maximum cross-section and the energy of the maximum.The values of Q, E$_t hres$, and E(XS$_{max}$) are in units of MeV, and σ_{max} and error(σ_{max}) are in units of mb. 222

1

Introduction

The field of nuclear physics involves the study of the atomic nucleus, nuclear structure and the reactions between nuclei and nucleons. A precise understanding of these has applications in nuclear energy, including fission and fusion, nuclear security and environmental analysis. This thesis details the development of fundamental nuclear physics to assist in the analysis of difficult-to-measure nuclides, through cross-section measurements and the development of a high-purity tracer with a broad range of applications, along with general method development enabling an effective workflow for future work.

1.1 Nuclear Fission

Nuclear fission is a natural process in which large neutron-rich nuclei split into two smaller fragments called fission products. The fission process may occur spontaneously as a decay channel or through reactions with an external particle, most commonly neutrons. Fission occurs in high-mass nuclei, which can be seen on the chart of nuclides in figure 1.1 in the top right corner, highlighted in green.

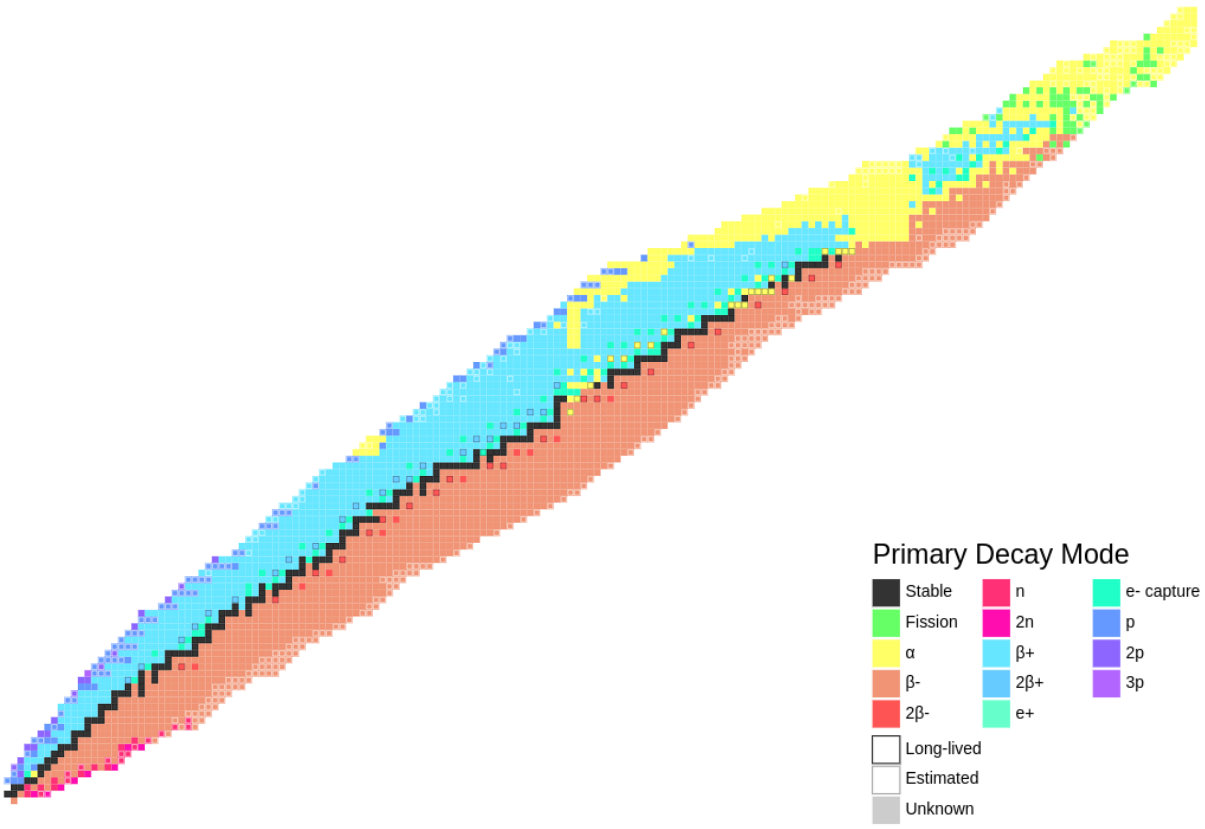


Figure 1.1: *Visuaisation of the Karlsruhe chart of nuclides, showing the neutron number, N, on the horizontal axis and the proton number, Z, on the vertical axis.[2].*

It was neutron-induced fission which led to the discovery of the fission process. On the back of the discovery of the neutron in 1932 by James Chadwick [3], and the successful creation of radioactive isotopes by Irene Curie and Frédéric Joliot by bombarding elements with alpha particles [4], Enrico Fermi brought these two concepts together, benefiting from the neutral charge of the neutron, as probing the nucleus with neutrons does not require a particle accelerator as there is no Coulomb barrier to overcome. In 1934 Enrico Fermi bombarded uranium atoms with neutrons produced using a polonium-beryllium neutron generator, expecting small changes in mass and the production of elements heavier than uranium due to the absorption of the projectile [5]. It was German chemist Otto Hahn who first noticed the production of much lower mass barium as products of the reaction, and pondered the prospect of the nucleus splitting in two [5]. It took physicist Lise Meitner to determine the physics of the process. As a neutron-rich nucleus is impacted by a neutron, the nucleus deforms and elongates. This results in a pinch process in the middle of the nucleus, with the two nearly discrete

nuclei, which are then repelled due to Coulomb forces [6]; the fission process is visualised in figure 1.2. During the process, huge amounts of energy are released, producing two fission products and free neutrons. It is these free neutrons that may then interact with further fissionable nuclei. With fissile material present, which are nuclei with the ability to fission through the absorption of a thermal (low energy) neutron, a chain reaction may occur. The combination of the release of a huge amount

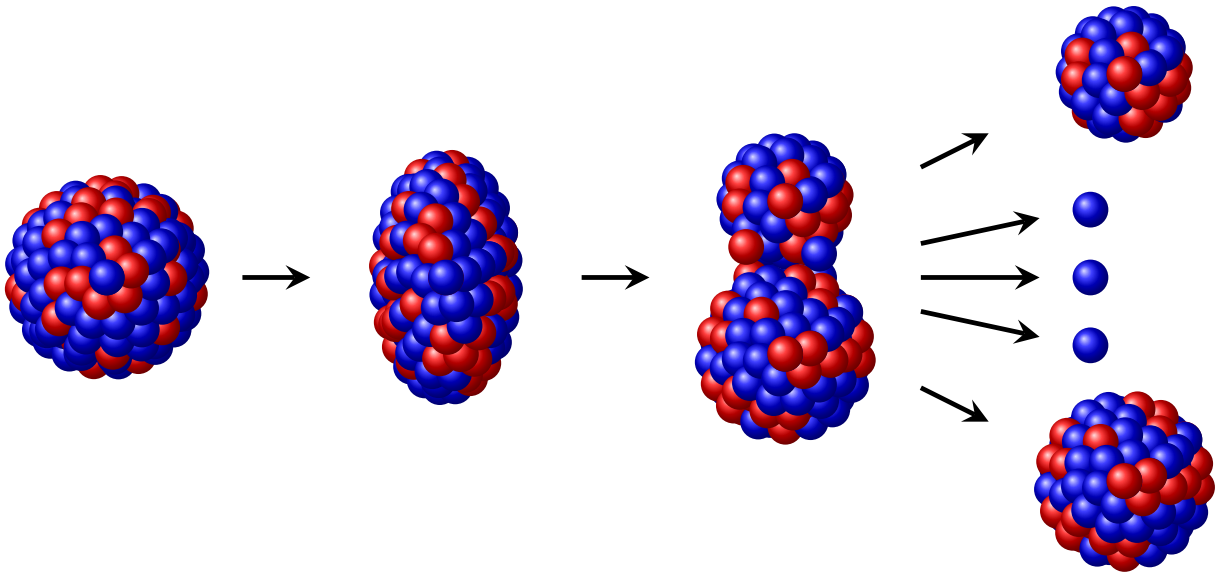


Figure 1.2: *Visualisation of the fission process, with a large nucleus breaking up into two discrete fission products and neutrons following the pinch process of fission.*

of energy and the ability to form a self-sustaining chain reaction is what brought nuclear fission into prominence. Initially, through the possibility of producing the atomic bomb, and nuclear power.

1.1.1 Nuclear Power

Nuclear reactors were first built upon the pursuit to produce weapons-grade plutonium, followed by the gradual transition to focus on energy production for the grid. Over the years, the world has amassed a huge nuclear fleet containing both naval and civil reactors. As of 2022, 439 nuclear power reactors are producing a combined power of 393 GW [7]. There are 53 reactors currently under construction globally, with a total power output of 54GW. The total energy production from nuclear power accounts for roughly 20% of the global demand. Additionally to the current fleet, there are over 200 commercial and prototype reactors and over 500 research reactors which have been decommissioned to date.

For the huge number of nuclear sites around the globe, there is a requirement for high amounts of fuel, despite fission's high energy density. The fuel of choice in commercial reactors is enriched uranium. Natural uranium is comprised of three isotopes ^{234}U, ^{235}U and ^{238}U with atomic abundances of 0.0054%, 0.7204% and 99.274% respectively. However, most fission reactors enrich ^{235}U to between 2-5%. ^{235}U is fissile, being able to fission from the interaction with a thermal neutron (0.0025 eV), whereas ^{238}U is fertile and will only fission through the interaction with a fast neutron with a threshold energy of 1 MeV, of through neutron capture with a neutron of any energy with successive beta decays to ^{239}Pu, which is fissile. The inverse velocity ($1/\nu$) dependence with cross-section enables the fissile ^{235}U and overtime the produced ^{239}Pu to reach a much high reaction rate [8].

The fission of a single ^{235}U nucleus produces roughly 200 MeV. For a 1 GWe facility, this can be about 1 kg of uranium per day. Multiplying this with the global nuclear power output leaves around 393 kg of fission products produced annually. While other radioactive waste streams are produced through the fission process, only the fission products are addressed in this thesis.

1.1.2 Fission Products

During the fission process, a large nucleus breaks into two smaller fragments. This is often an asymmetrical breakup process producing one larger and one smaller nucleus. This results from several factors, including shell effects, the Coulomb potential, and the quadrupole moment (the measure of the nuclei's deformation from spherical) [9], however a full theoretical model for the process has not yet been developed.

A fissioning nucleus does not break up into pre-defined products but has a probability of producing a range of products, with varying proton and neutron numbers. The distribution of these depends on the fissioning nucleus, whether the fission is spontaneous or which projectile has induced the fission, and in the latter case, the energy imparted by the projectile. This distribution is known as the fission yield and is the proportion of fissions which result in the production of a given isotope. There are two types of fission yield, independent and cumulative. Independent is the percentage of products

produced directly in fission, including those following prompt neutron emission but not radioactive decay. Cumulative fission yield is the proportion of fission which leads to the production of a given isotope, either produced directly or through nuclear decay of produced isotopes.

Experimental analysis of fission yields for ^{235}U clearly shows the spread of isotopes produced and the asymmetric mass nature of the products in figure 1.3.

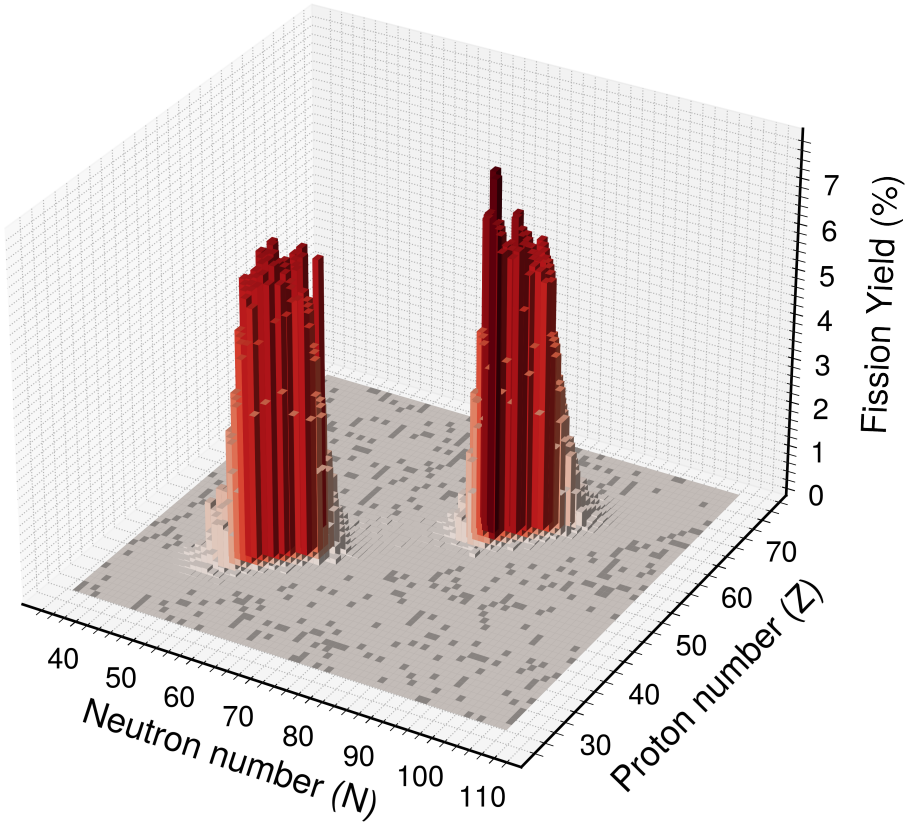


Figure 1.3: *Cumulative fission yield of thermal neutron-induced fission of ^{235}U. Data are extracted from the JEFF 3.3 database [1].*

The products directly produced in fission are often neutron-rich and, therefore, unstable. With short half-lives, these isotopes decay towards the stability line through a series of decays; initially, these are prompt and delayed neutron emissions followed by beta minus decays.

1.1.2.1 Spent Nuclear Fuel

A nuclear reactor is loaded with fuel composed of any fissionable nucleus, often U or Pu isotopes. The majority of reactors today are thermal-spectrum, and the majority of energy produced is from the thermal-neutron-induced fission of fissile isotopes such as ^{235}U. Ceramic uranium oxide (UO_2) is the most common fuel type, with ^{235}U enriched from 0.07% to $\sim 3\%$. As the fuel is burnt up in the reactor, the proportion of ^{235}U drops dramatically until the power output from the reactor cannot be sustained and the fuel needs to be replaced. At this point, the fuel is termed as spent.

Spent fuel contains high quantities of ^{238}U, fission products and minor actinides including plutonium, neptunium, and thorium isotopes produced through neutron capture reactions and subsequent decays, particularly with ^{238}U. Spent fuel initially has a high heat output due to the decay of short-lived products and requires cooling, often left in cooling ponds for several months or years, while the heat output diminishes. The fuel being in cooling ponds provides effective radioactive shielding. At reactor shutdown, the heat output is $\sim 6.5\%$ of the reactor's power during operation; however, this power decreases exponentially over several days, reaching 1.5% after 1 hour and 0.4% after a week[10].

Over time the proportion of isotopes making up the activity evolves as high-specific activity short-lived isotopes decay, leaving an array of longer-lived isotopes. The mass of products against time is given in figure 1.4. For the thermal spectrum reactor burn-up of a UO_2 fuel pellet, a typical irradiation is given as 33 GWd/t or 44 GWd/t at 38.5 MW/t in 3 or 4 cycles of 12 months with 40 days shutdowns between cycles [11].

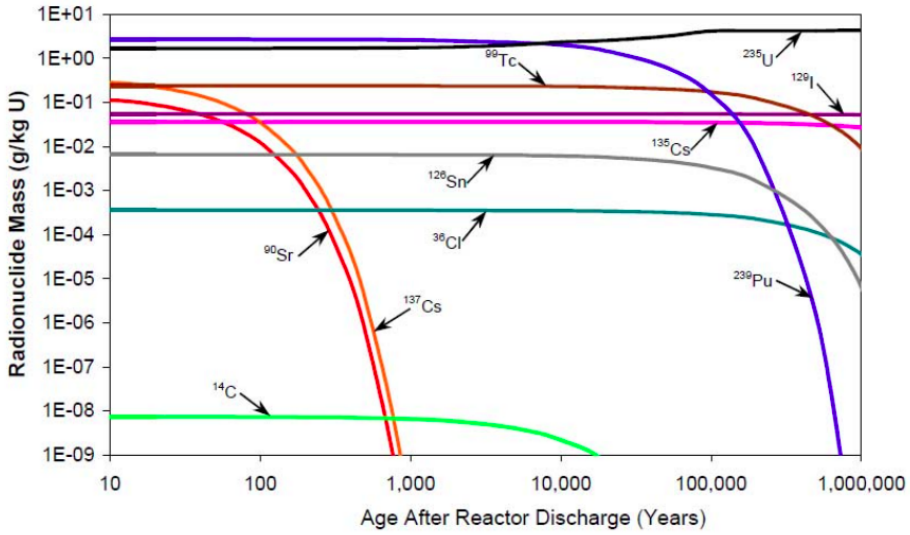


Figure 1.4: *The fission product mass over time for spent fuel per kg of uranium, plotted on a log-log scale, for a standard PWR irradiation. [12].*

The quantity and ratio of isotopes are highly dependent on the fuel type, reactor type, the neutron energy spectrum and the level of fuel burn-up.

1.1.3 Environmental Radioactivity Monitoring

Isotopes of the spent fuel can often spread from containment due to damaged fuel or post irradiation mechanical processes and fuel reprocessing, particularly gaseous and soluble isotope products. On-going analysis is required to determine the migration of fission products through ponds and into the biosphere. During and after the fuel's operational life, fission products can leach out into surrounding reactor materials, including the fuel cladding, reactor containment vessel, primary coolant pipes and anything else coming into direct contact with the primary coolant loop.

Analysis and characterisation of spent fuel and contaminated components are essential in the processing of spent nuclear fuel and the handling, processing and storage of nuclear waste. Environmental monitoring is performed on various samples surrounding reactor sites, including air, water, soil and rock samples, to investigate the transport and potential health risk of radioactive isotopes through the biosphere, which animals and humans can ingest. The cost of nuclear waste management and decommissioning in the EU is expected to exceed €150Bn - with a large portion being characterisation

and analysis [13]. Accurate and precise analysis can reduce the timescales and costs of clean-up.

1.2 The Need for Radiotracers

Analysing radioactive samples is a challenging task due to the large array of isotopes and matrix present within a sample. Chemical separation is usually performed before analysis, preventing tailing and overlap of analysis peaks. This is true for both radiometric techniques, such as gamma-ray and alpha particle spectrometry and liquid scintillation counting, as well as mass techniques using mass spectrometry.

Chemical separation enables the purification of an element in a sample; its limitation is that not 100% of the sample will be recovered at the end of the process. The proportion of an element that makes it through the chemical separation process is known as the chemical yield. It is affected by several factors, including the chemical conditions and the quantity of the elements being separated. Radiotracers offer the ability to quantify this problem. If a known quantity of a tracer is introduced before the chemical separation process, the chemical yield can be determined from the quantity of the tracer passed through the process [14, 15]. There are several criteria for a radiotracer:

- Behave chemically identically to the analyte, ideally being an isotope of the same element.
- Be at chemical equilibrium with the sample. The tracer should therefore be introduced to the sample as early as possible.
- Possess a unique analytical signal and not interfere with that of the analyte.
- Should not already be present within the sample as this will affect the quantities being analysed.
- Ideally the tracer can be analysed by the same analytical method as the analyte.

This set of requirements greatly affects the list of candidate isotopes available as a tracer and the production and separation methods. Meeting these requirements greatly improves the robustness of the

radioanalytical procedure.

There are currently several well-established radiotracers used for a range of isotopes, including ^{232}U as a tracer for ^{235}U and ^{238}U [16], ^{223}Ra as a tracer for ^{226}Ra [17] and ^{242}Pu as a tracer for ^{239}Pu [18]. There are several isotopes and analytical methods without ideal tracers, including Ba as a tracer for ^{226}Ra [19]. As analytical techniques improve and diversify, there is an ongoing need to make sure these techniques are supported by suitable radiotracers.

1.3 Technetium-99

Technetium is the 43rd element and gets its name from the Greek technetos (τεχντος), meaning artificial or synthetic. Technetium is the lowest mass element with no stable isotopes, with only small quantities present in nature from spontaneous fission [20], at natural nuclear reactors such as Oklo in Gabon [21] and cosmic-ray induced transmutation [22]. The lack of stable isotopes led to the late discovery of Tc in 1937 by Emilio Segrė, through synthesis by exposing a Mo plate to high energy deuteron beams [23].

Technetium is naturally found only in small quantities, in uranium ore, due to the spontaneous fission of uranium. The nuclear age has led to significant concentrations of Tc in spent fuel and discharges from nuclear activities, including nuclear weasons testing, meaning the quantity of Tc in the environment has increased. Technetium is a long-lived fission product of several actinides, most importantly fissile ^{235}U, with its analysis being essential for spent fuel, contaminated nuclear reactor components and environmentally, as seen in figure 1.4.

Technetium-99 has a cumulative fission yield of $6.132(92)$ % [1] from the thermal neutron-induced fission of ^{235}U. The isotope is predominantly produced through the decay of molybdenum-99, which is a direct product of fission. As can be seen from the decay scheme in figure 1.5, ^{99}Mo decays with a half-life of $2.83(23)$ d [24] to an excited state ^{99m}Tc before decaying with a half-life of $6.0067(5)$ h to the ground state [24]. ^{99}Tc is a pure beta-emitter with an end-point energy of $297.5(10)$ keV [25]. It is

this ground state of ^{99}Tc, with a half-life of $2.11 \times 10^5(12)$ y [24], which requires analysis due to its long half-life.

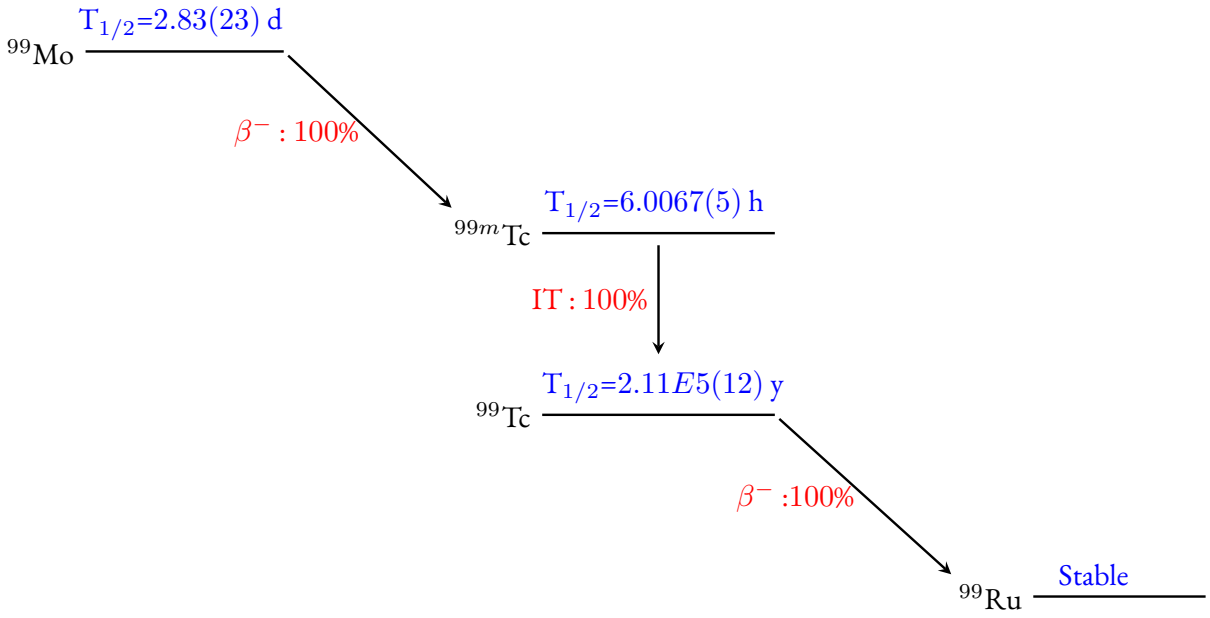


Figure 1.5: *Decay scheme of ^{99}Mo to the stable isotope ^{99}Ru, through the successive decay of ^{99m}Tc and ^{99}Tc [24].*

The excited state, ^{99m}Tc is a medically relevant isotope, emitting a gamma-ray at $140.511(1)$ keV. This isotope accounts for 80% of medical isotopes used worldwide. Technetium-99 is produced through the neutron-induced fission of ^{235}U using specially made targets, commonly irradiated at research reactors. There is a push to move production away from uranium, using several accelerator reactions ^{100}Mo(n,2n)^{99}Mo, ^{98}Mo(p,γ)^{99}Tc and ^{100}Mo(γ,n)^{99}Mo. The medical production of ^{99}Mo only adds to the technetium required for analysis.

The most significant quantities of ^{99}Tc in the biosphere come from permitted release from nuclear fuel reprocessing plants; La Hague in France has released 154 TBq between 1966-2016, and Sellafield (UK) has discharged 1720 TBq from 1952-2005 [26, 27]. The release from Sellafield over time between 1952-2016 is shown in figure 1.6.

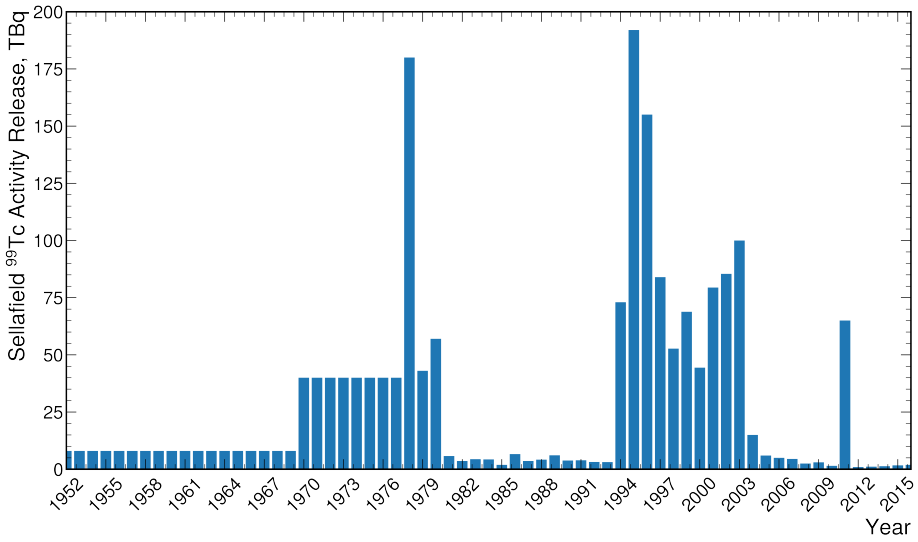


Figure 1.6: *The calculated release of technetium-99 from Sellafield into the Irish sea between the years of* 1952 *and* 2016 *[28].*

There is a significant push to lower the release from these values. For example, in the UK, there is a target to lower ^{99}Tc releases to 1 TBq in 2020s and 0.1 TBq in the 2030s [27]. Other sizable releases of ^{99}Tc are fallout from atmospheric weapons testing, which has contributed a further 140 TBq and the Chernobyl nuclear disaster causing the release of 0.97 TBq [29]. Analysis of the Fukushima nuclear disaster has estimated the ^{99}Tc release at 220 TBq based on Tc/Cs seawater ratios [30]. Above-ground atomic weapons testing between the 1940s and 1970s is estimated to have caused the release of 140 TBq, predominantly localised to the Northern hemisphere where testing occurred [31].

In the environment, Tc primarily exists in two oxidation states; as Tc^{4+} under reducing conditions and Tc^{7+} as pertechnetate ion (TcO_4^-) in oxidising conditions. Tetravalent Tc^{4+} is the most stable oxidation state and hydrolyses in aqueous solutions and forms many stable complexes with inorganic and organic ligands. This only adds to the requirement to analyse technetium effectively, as the solubility will enable it to pass through the ecosystem readily [32].

1.4 Technetium-99 Analysis

Analysis of technetium is well understood with detailed methods developed for both mass spectrometry techniques, typically inductively coupled plasma-mass spectrometry (ICP-MS) and radiometric counting methods, typically liquid scintillation counting (LSC). Both analysis techniques require the separation of many interferences due to the complex matrices technetium samples are taken from [22]. Several analyses have been performed to analyse ^{99}Tc with ICP-MS shown in table 1.1. In all cases, separation was required prior to the measurement.

Table 1.1: *Summary table highlighting recent analysis of technetium-99 using ICP-MS [28], showing the sample type, separation resin and limits of detection (LoD) in both mass and activity.*

Reference	**Sample**	**Separation**	**LoD** mg.kg^{-1}	**LoD** Bq.kg^{-1}
Wu et al. (2014) [33]	LLW cement	TEVA	0.795	1.5
Zhang et al. (2017) [34]	Groundwater	TEVA	0.155	0.00015
Sahli et al. (2017) [35]	River sediment	TEVA	0.0028	0.03
Kołacińska et al. (2018) [36]	Reactor coolant water	TEVA	0.00056	0.006

The main advantage of mass spectrometry is the ability to rapidly measure a large number of samples, due to the short measurement time, in the order of several minutes. The published analysis using liquid scintillation counting is extensive, with several recent publications shown in table 1.2.

Table 1.2: *Summary table of recent liquid scintillation counting measurements [28], showing the sample type, separation resin, counting time and limits of detection (LoD) in both mass and activity.*

Reference	**Sample**	**Separation**	**Count time** **h**	**LoD** mg.kg^{-1}	**LoD** Bq.kg^{-1}
Kabai et al. (2013)[37]	Milk	TEVA	1	0.2	19
Chen et al. (2014) [38]	LLW	TEVA	2	-	-
Khan and Um (2015) [39]	Urine and water		2.5	0.23-0.25	22
Temba et al. (2016) [40]	Power plant filters	TEVA	3	3.15	294

LSC involves dissolving or suspending samples in a scintillation cocktail containing both a solvent and scintillation particles known as 'fluors'. The energy emitted through the beta decay of ^{99}Tc is transferred into the solvent and, subsequently, the fluor particles causing scintillation. It is the scintillation photons emitted by the fluor which are detected through interactions with a photocathode and subsequent multiplication using a photomultiplier tube.

Liquid scintillation counting is an advantageous method owing to its minimal self-absorption, high counting efficiency and homogenous distribution of the sample in the scintillation cocktail [41].

The limitation of liquid scintillation counting is counting times of several hours and interference from other beta-emitting isotopes. Below in section 1.5, the inductively coupled plasma mass-spectometry (ICP-MS) technique is described in more detail.

1.5 ICP-MS Analysis

Inductively Coupled Plasma-Mass Spectrometry (ICP-MS) is an increasingly common analysis method for long-lived radionuclides, owing to its high throughput, with sample processing taking in the order of several minutes and multi-element capacity. Mass spectrometry is only suitable for isotopes with a long half-life, with a higher atom count per unit of activity. Decay counting is not optimum for samples with a low specific activity such as ^{99}Tc, requiring high quantities of samples and incredibly long measurement times (typically in the order of hours or days) to gain the required statistics for precision analysis. The ICP-MS analysis performed during this thesis used an Agilent 8800 tandem ICP-MS [42].

Mass spectrometry offers very low limits of detection due to the nature of atom counting, providing detection limits in the parts per trillion (ppt) and lower. On the simplest level, a mass spectrometer strips the electrons from the sample (after it has been made into an aerosol), creating a charged ion beam. The sample is then passed through an inductively coupled plasma, consisting of an argon plasma and sustained by an oscillating magnetic field. The deflection of the ion by a magnetic field is related to the charge-to-mass ratio (A/Z), enabling the ion's mass to be deduced.

The sample is typically introduced into the mass spectrometer as an aqueous sample in a dilute acidic or alkaline solution. The sample passes through a nebuliser that mixes the sample with argon gas to create an aerosol. A spray chamber then filters the aerosol particles, only allowing the smaller particles

to pass through to the ICP (inductively coupled plasma), with larger particles exiting as waste. Atoms contained within a larger number of smaller vapour particles are more effectively ionised compared to coarse vapour particles, due to the increased surface area. The sample can then be effectively converted into plasma in a successive stage. The efficiency of the sample introduction system is often in the order of 5-10%; however, this is greatly affected by the chamber design and can be increased to enable lower limits of detection.

The creation of charged sample ions in the form of a plasma enables their eventual detection in the mass spectrometer. Argon gas is introduced into the aerosol used due to its high ionisation potential, compared to all elements except for He, F and Ne, its high abundance and chemical inertness. The high ionisation potential enables the preferential transfer of free electrons to the argon ions rather than the sample ions.

Following sample introduction and heating using induction coils to assist with the ionisation of the sample ions, the sample is passed through two successive cones, the sample cone and the skimmer cone. As the plasma is forced along the instrument, the pressure drops, resulting in the ion beam's expansion. The sample passes through the sample cone first, refining the beam of particles through collimation. The sample then continues to expand before interacting with the skimmer cone. The spatially refined ion beam is then suitable for passing through the mass analyser.

The mass analyser is then composed of tuned magnets, often one or more quadrupole elements. The particles are filtered out based on their mass-to-charge ratio. The strength of the magnets can be altered to enable different m/Z ratios to pass into the detector. A single m/Z value may be set or a sweep which runs over a range of m/Z values. Some ICP-MS instruments possess multiple detectors with the mass analyser separating the streams of ions, which are detected in parallel. This is optimum for low limits of detection and low sample volumes.

The detector then records the ions which pass through the cathode. A secondary electron multi-

plier uses a series of plates with increasing voltages applied across them to multiply the number of electrons, increasing the signal strength. The counts are then measured in counts per second (CPS). A standard of known concentration can be run through the machine to provide a conversion to concentration. This factor may shift over time and varies with mass.

This detection method does introduce potential interferences which must be understood and suppressed, known as isobaric, polyatomic and peak tailings. Isobaric interferences are caused by isotopes of different elements with the same atomic mass number (^{99}Tc=^{99}Ru). Polyatomic interferences are caused by the reaction between sample isotopes and gases in the plasma and/or reaction cell. These reactions can cause the production of multi-element species whose mass sums to the analyte (^{99}Tc=^{98}Mo^{1}H). Polyatomic and isobaric interferences can be suppressed and removed by sample preparation and the choice of gases introduced into the spectrometer. The third type of interference is peak-tailing due to the statistical variance in detected peaks resulting in the detection of a single mass resulting in a Gaussian response around a given m/Z ratio. This can cause overlap between peaks of neighbouring masses, resulting in inaccuracies in the count rate. Peak tailing is visualised in figure 1.7.

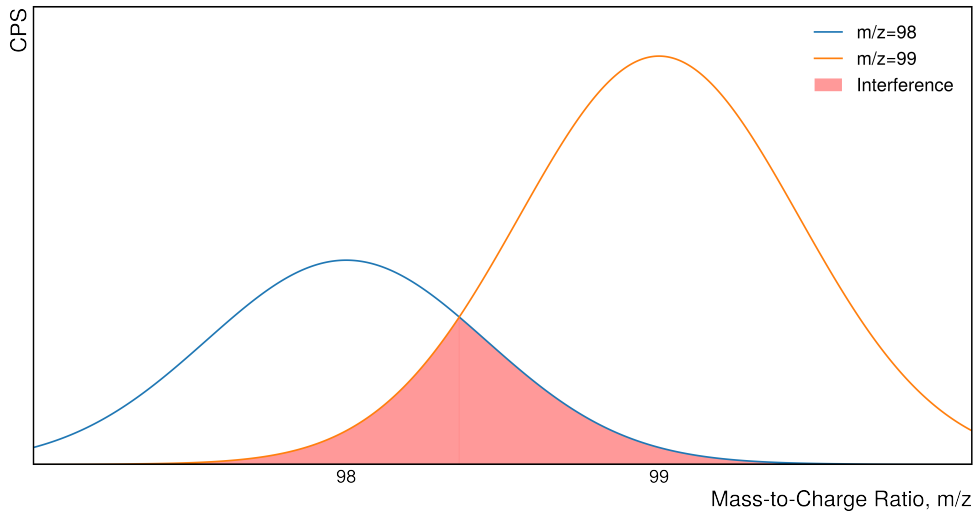


Figure 1.7: *Schematic highlighting the peak tailing between neighbouring analysis peaks in mass spectrometry from m/Z=98 and m/Z=99.*

Depending on the instrument design, mass spectrometry can require high levels of sample preparation.

However, sophisticated chemical separation schemes and the reaction cell can be used to overcome this. Mass techniques are essential when there are no distinct radiometric characteristics, the analyte's half-life is too long, or the concentration is too low.

There is a range of instrument designs which can support or replace offline chemical separation. One of these is tandem ICP-MS which is being used in this study. This introduces an additional quadrupole magnet with the two quadrupoles separated by a collision-reaction cell. A gas or mixture of gases is inserted into the collision-reaction cell, such as hydrogen, oxygen, ammonia and methane, with the gas chosen to react with interferences or the analyte to remove mass overlaps which would otherwise prevent accurate measurement. The reactions form multi-element species causing a mass-shift. The different mass-to-charge ratio causes the interference to be ejected in the second quadrupole magnet. Tandem ICP-MS devices have a quadrupole magnet before the reaction cell as well as after, limiting the interferences which successfully enter the reaction cell, further limiting the amount of interference detected and the additional mass filter improves tailing removal. Figure 1.8 shows a schematic of an ICP-MS in tandem mode showing how the tandem ICP-MS setup can support offline separation compared to alternative instrument designs in several ways:

1. The second quadrupole mass filter improves ^{98}Mo tailing removal

2. O_2 introduction in the reaction cell shifts Tc to TcO_2, whilst Ru remains on mass or forming with a single oxygen atom (RuO). This enables Tc and Ru to be analysed when there are isotopes of both elements with equal mass.

3. The introduction of O_2 results in MoH forming MoO and MoO_2, converting a polyatomic that does overlap with Tc to one that does not.

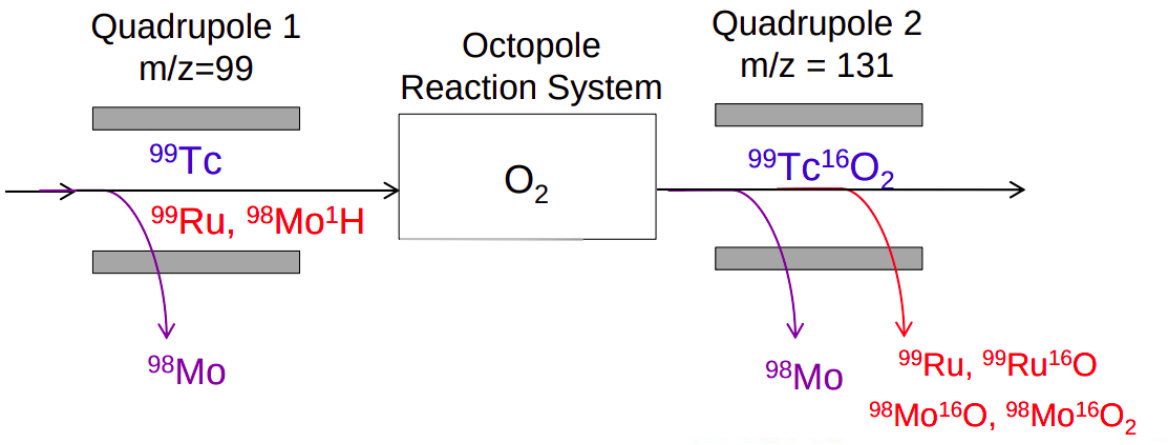


Figure 1.8: *Schematic of a mass spectrometer reaction cell and quadrupole magnets, illustrating the mechanisms to remove common interferences for the detection of ^{99}Tc [43].*

This set-up has been used extensively for the analysis of long-lived radionuclides, which traditionally have significant interferences, including ^{125}Cs, ^{129}I and ^{236}U [44].

1.6 Technetium yield tracers

The analysis of technetium-99 has utilised a number of tracer isotopes, including ^{95m}Tc [45, 46], ^{97}Tc [47], ^{97m}Tc [48], ^{99m}Tc [49, 50] and stable Re [51], composed of two isotopes ^{185}Re and ^{187}Re with abundances of 37.4% and 62.6% respectively.

There are several short-lived tracers of technetium used for radiometric analysis. Most commonly ^{99m}Tc is used, which de-excites to ^{99}Tc through the emission of a $140.511(1)$ keV γ-ray, with a half-life of $6.0067(5)$ h. This wouldn't be a suitable tracer for mass techniques as it is an isomer of the analyte decaying into the analyte, has equivalent mass (within the resolving power of the spectrometer) and has a very short half-life. Another short-lived technetium tracer often used for radiometric techniques is ^{95m}Tc, emitting γ-rays suitable for gamma-ray spectrometry. With a half-life of $61(2)$ d, the isotope ^{95m}Tc is less suitable for mass techniques, and samples have often been found to be contaminated with ^{99}Tc, increasing the blank level (sample containing only the tracer and no analyte) and lowering the limit of ^{99}Tc detection [52].

Due to the lack of stable isotopes of technetium and the difficult production of isotopes with suitable characteristics, isotopes of rhenium can be used [51]. While rhenium acts chemically very similarly to technetium, there are distinctions, particularly in certain chemical environments, limiting the accuracy of rhenium. The element Re has two stable isotopes with masses of 185 and 187, considerably higher than the mass of ^{99}Tc. Closer masses are favoured for mass spectrometry, as there is a relationship between mass and detector response function, making Ru isotopes (with similar masses to Tc) far more suitable. The masses are close together due to the elements being only one atomic number apart Z(Ru)=Z(Tc)+1.

Focusing on the characteristics of a mass spectrometry tracer, the tracer isotope should have a long half-life, be at least two mass numbers from the analyte to prevent potential interference with ^{99}Tc due to tailing and the production of hydrides with mass A=99.

When only isotopes of Tc are considered, the number of candidate isotopes is greatly reduced. The half-lives for Tc isotopes, not including mass 99 and adjacent isotopes, are shown in table 1.3.

Table 1.3: *Half-life of Tc tracer candidate isotopes, showing the ground state (GS), first isometric state (1st IS) and data reference.*

	^{94}**Tc**	^{95}**Tc**	^{96}**Tc**	^{97}**Tc**
1st IS	52.0(10) m	61(2) d	51.5(10) m	91.0(6) d
GS	293(1) m	20.0(1) h	4.28(7) d	4.21E6(16) y
Ref.	[53]	[54]	[55]	[56]

	^{98}**Tc**	^{100}**Tc**	^{101}**Tc**	^{102}**Tc**
1st IS	x	x	x	5.28(15) s
GS	4.2E6(3) y	15.46(19) s	14.02(1) m	4.35(7) m
Ref.	[57]	[58]	[59]	[60]

The only long-lived isotope of technetium, suitable as a tracer isotope, is ^{97}Tc. While ^{98}Tc has a long half-life, it is unsuitable due to the potential for tailing and ^{98}Tc^{1}H interferences. Technetium-97 has a ground state half-life of 4.21x10^{6}(16) y, over ten times the half-life of ^{99}Tc, an adequately long half-life for mass spectrometry. As ^{97}Tc is not found naturally, it is produced through nuclear reactions either using a particle accelerator or a neutron source. The production and preparation of ^{97}Tc as a

yield tracer has already been explored [61]; however, a commercially suitable route has not yet been discovered, preventing the tracer from being used within the nuclear industry. The development of a suitable production route will open the path to a commercial ^{97}Tc radiotracer.

1.7 Nuclear Reactions

Nuclear reactions are the underpinning mechanism behind isotope production and enable the transmutation of one isotope into another. A nuclear reaction is usually the collision of a projectile, r, with a target, T, producing a discrete product, P, and an ejectile, j

$$T + r \rightarrow P + j. \tag{1.1}$$

In nuclear physics, it's a convention to write such a nuclear reaction in bracket notation, where the projectile and ejectiles are shown within brackets and the target and product on either side, e.g.

$$T(r, j)P. \tag{1.2}$$

The benefit of this notation is the ability to refer to a reaction mechanism, such as a (p,d), known as a pick-up reaction, where a proton is incident on a nucleus, and a deuteron is ejected, reducing the mass of the target nucleus by 1. Several mechanisms may lead to the same product from the same target and beam combination due to the different compositions of the ejectiles. For example, (p,$2d$) would lead to the production of the same product as (p,α).

The lowest energy reactions are scattering reactions, also known as momentum transfer reactions, where a projectile scatters off a target nucleus. The target nucleus will then recoil while the projectile loses energy. At low energies, this is a purely elastic process, during which the product and ejectiles remain in their ground states. As the projectile energy increases above the minimum excitation energy of the target nucleus, some of the transferred energy may excite the target nucleus, decreasing the total kinetic energy of the system.

For more complicated reaction mechanisms to occur, a minimum threshold energy must be reached, with neutral particles such as neutrons and photons being the exception. Due to their lack of charge, these particles are not influenced by electromagnetic forces, meaning they do not have to overcome the Coulomb potential. For charged particle reactions, which will be the focus of this work, there are two possible barriers to a reaction occurring; Coulomb repulsion and change in nuclear binding energy between the reactant and products/ejectiles. Once these energetic obstacles are overcome, the possibility of both compound and direct reactions opens up.

1.7.1 Nuclear Structure

Since Ernest Rutherford discovered the atomic nucleus in 1911 [62, 63], increasingly more accurate attempts have been made to describe the structure of the nucleus mathematically. To date, no comprehensive theory of the nucleus describes nuclei predictively; however, several models offer accurate descriptions for particular regions of the nuclear chart. The assumption that every nucleus is a homogeneous spherical mix of protons and neutrons is long disproved. Experimentally, nuclei have been observed in prolate-deformed, oblate-deformed and, notably, pear-shaped. It is not only the shape of the nucleus that does not fit the historical models, as nuclei have been discovered with neutron-skins [64] and are composed of quasi-discrete nuclear clusters such as a series of alpha particles [65], making the development of a predictive model incredibly complicated. A general ab initio method proves to be elusive.

Taking note of the limitation of current nuclear models, they are still an essential tool in predicting the possibility and the probability of a nuclear reaction occurring based on the energetics.

For example, the mass of an atomic nucleus is lower than the sum of the individual nucleon masses due to the energetic gain of nucleons forming a given nucleus. As nucleons come together to form a stable nucleus, energy is released, which is associated with a change in mass according to Einstein's famous energy-mass equivalence

$$E = mc^2, \tag{1.3}$$

where m is the mass, and c is the speed of light [66]. The difference in mass between the sum of individual nucleons and the mass of a bound nucleus is due to the binding energy, where the change in binding energy between nuclei in a nuclear reaction is often referred to as the Q-value

$$Q = E_f - E_i, \tag{1.4}$$

where E_f and E_i are the binding energies of the final and initial nuclei respectively. A positive Q-value shows an energy release from the reaction, which results in the nuclear excitation or kinetic energy of an ejectile. A negative Q-value reaction absorbs energy to reach a less stable state. A nuclear reaction with a negative Q-value requires the projectile (in the centre-of-mass frame) to possess a minimum of the magnitude of the Q-value as kinetic energy for the reaction to be possible.

1.7.1.1 Liquid Drop Model

In 1929, George Gamow first proposed the liquid drop model (LDM)[67], with a semi-empirical method of describing the binding energy of a nucleus, known as the liquid-drop model formulated by Carl Friedrich von Weizsäcker in 1935 [68]. As the model's name alludes, the model works under the assumption that the strong nuclear force binding the nucleons within a nucleus is akin to the forces holding a drop of liquid together, such as surface tension. The liquid-drop model describes this binding energy as a function of the atomic number A and the atomic number Z

$$B(A,Z) = a_V A - a_S A^{2/3} - a_C Z(Z-1)A^{-1/3} - a_{asym}\frac{(A-2Z)^2}{A} + \delta(A,Z), \tag{1.5}$$

where each of the constants denoted by a with varying sub-scripts are values determined experimentally: a_V =15.75 MeV, a_S =17.8 MeV, a_C =0.711 MeV, a_{asym} =23.7 MeV. The delta function, $\delta(A,Z)$=$\frac{11.18MeV}{A^{1/2}}$ for even-even, equal magnitude but negative for odd-odd nuclei, otherwise zero. Each of the terms of this equation corresponds to a different force contribution to the nucleus.

The first term is the volume term and is the main contributor to the binding energy. Within the nucleus, nucleons interact with each other through the short-range nuclear force. The energetic advan-

tage of this is proportional to the number of nucleons, as the nuclear force has a short-range effect, only interacting significantly between a nucleon and its nearest neighbouring nucleons, causing a linear scaling with atomic mass, A. The second term is the surface term and acts as a correction factor to the volume term. Nucleons on the nucleus's surface interact with fewer nucleons due to having fewer nearest neighbours. This factor scales as the surface area. The third term is a negative contribution to the binding energy and is due to the Coulomb repulsion of the protons, therefore scaling with proton number Z, interacting with each other proton $(Z - 1)$.

The fourth term is the asymmetry term and counteracts the Coulomb term's desire for fewer protons. Quantum mechanically, this term accounts for the fact that protons and neutrons are both fermions, and two like fermions cannot exist in the same energy level, requiring successive like-nuclei to populate increasing energy levels within a nucleus. This principle is known as the Pauli Exclusion Principle (PEP). It is, therefore, favourable for a given mass to have a near-equal number of protons and neutrons.

The final term is a pairing term that shows a preference of the nucleus to have even numbers of like nucleons as opposite spin-state nucleon pairs. The most preferential state is even-even, whereby all protons and neutrons are paired.

1.7.1.2 Spherical Shell Model

Experimental observations have played a huge role in the development of nuclear theory, one such instance being the development of the shell model of the nucleus. Evidence for the shell model comes from several experimental outcomes, including isotopic abundances, nuclear size, binding energy and neutron absorption cross-sections. The change in the binding energy of the final neutron for a range of neutron numbers is shown in figure 1.9 (it should be noted that this effect is also seen with protons), where it is clear that there are great affinities to reach certain neutron values, with binding energy increasing with additional mass until a certain mass is reached, after which the binding energy of an additional neutron drops significantly and becomes negative. These mass numbers appear at n=2, 8,20, 28, 50, 82, 126... and are known as magic numbers. A nucleus is known as doubly magic

when it possesses magic numbers of both protons and neutrons, giving an extra boost to stability. This structure indicates the presence of shells, which have a preference for being filled, analogous to atomic electron shells. Magic number nuclei are comparable to noble gases, with their high chemical stability attributed to their full electron shells.

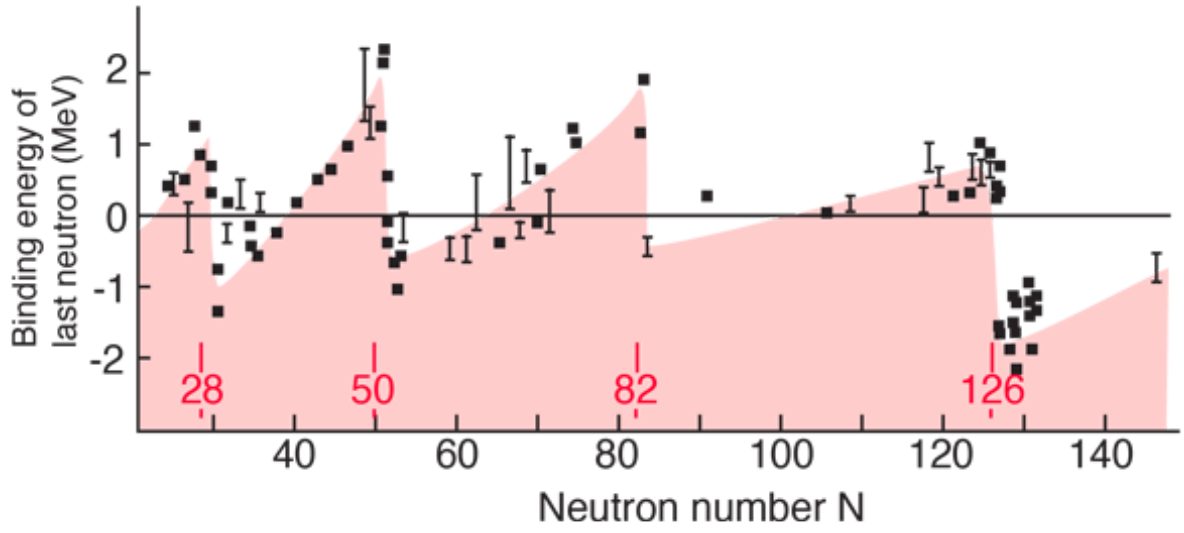


Figure 1.9: *The change in the binding energy of introducing a final neutron, against increasing parent nucleus mass [69].*

Shell-model calculations are performed by solving the Schrödinger equation with an appropriate potential well. The potential well is constructed by considering the interactions between neighbouring nucleons using the mean-field approach. Calculating the interaction between every individual nucleon would be more accurate; this becomes computationally for large nuclei due to the number of individual interactions with each other nucleus, and the effect of nucleons diminishes rapidly with distance. Several potentials could be used for the calculations, including the square well and harmonic oscillators, however, most commonly, the Woods-Saxon potential [70] is used

$$V(r) = \frac{V_0}{1 + \exp(\frac{r-R}{a})}, \tag{1.6}$$

where V_0 is the depth of the potential well, r is the radius, R is the mean radius of the nucleus, and a is the diffuseness constant. The Woods-Saxon potential has good agreement experimentally to observed nuclear densities. The potential drops to zero at roughly $r = R + 5$ fm, the range of the positively

attractive strong nuclear force.

The aforementioned fermionic nature of nucleons governs the population of energy levels within the potential well. According to Pauli's Exclusion Principle (PEP) [71], like-nucleons cannot exist in the same energy state, causing them to populate increasingly higher energy levels. Two like-fermions can reside in the same energy level, provided they possess opposing intrinsic spins $\vec{s} = +\frac{1}{2}$ or $\vec{s} = -\frac{1}{2}$. There is even an energetic benefit to nucleons being paired (seen experimentally through the stability of nuclei with an even number of like nucleons).

While the shell model treats nucleons as particles acting independently, filling their respective energy state, the relative velocity of nucleons has a significant effect on the degeneracy of the energy shells. As a nucleon with intrinsic spin orbits a nucleus, it will be more or less attracted to other nucleons based on their intrinsic spin. This force causes nucleons orbiting closer to the nucleus's surface to be less tightly bound and perturbs the energy levels. This effect is known as the spin-orbit potential.

The shell-model predicted level scheme is shown in figure 1.10 where the magic numbers are annotated, and the effect of the spin-orbit potential on their occurrence is clear.

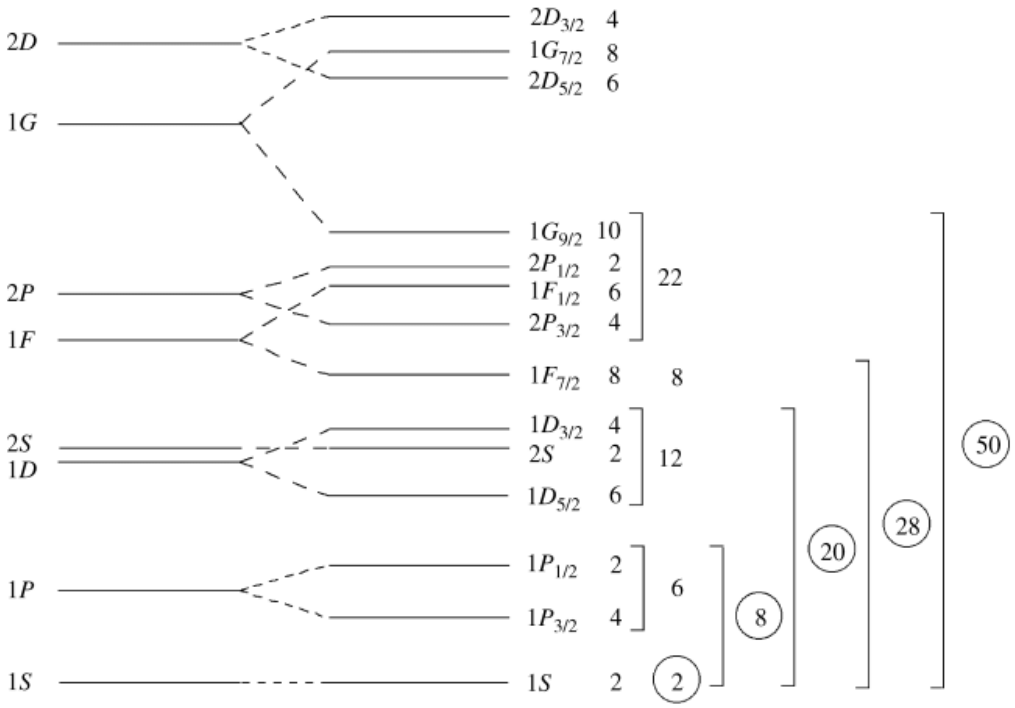


Figure 1.10: *Nuclear energy level structure predicted by the spherical shell model, with the shell and overall occupancy annotated along with the presence of magic numbers [72].*

The level notation gives several pieces of information, for example, $1p_{3/2}$; the notation can be broken into three components. The first number, in this case, 1, refers to the radial quantum number, p is the spectroscopic number, refers to the orbital angular momentum, where n=s, p, d, f... for ℓ=0, 1, 2, 3... and the subscript, in this case, $3/2$, is $j = \ell \pm s$, where the occupancy of the level can be calculated as $2j + 1$.

1.7.1.3 Coulomb Repulsion

When a charged particle interacts with a nucleus, the particle must overcome the long-range Coulomb potential between the positively charged target nucleus and the projectile before the energetic benefit from the short-range strong nuclear force comes into effect. The force between two interacting nuclei, F(r), can be visualised as a function of nuclear radius, as shown in figure 1.11.

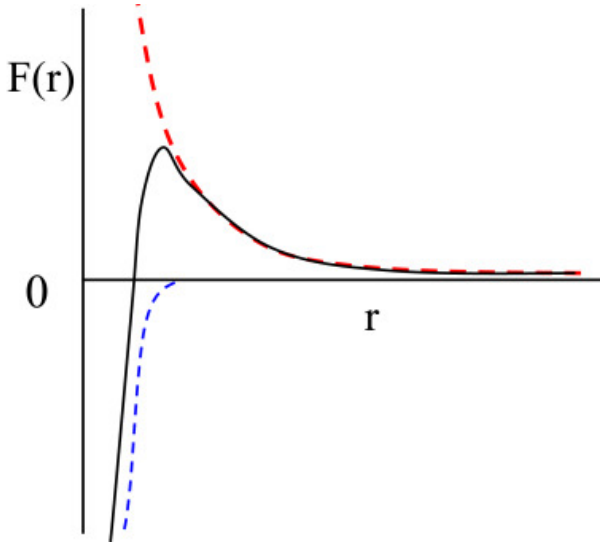


Figure 1.11: *The force between two interacting nuclei as a function of radius, r, for a nucleus with the long-range repulsive Coulomb potential dominating outside of the nuclear radius. The red line shows the contribution from Coulombic repulsion, the blue line is the attractive strong nuclear force, and the black line is the overall force.*

While it is difficult to calculate the energy required to overcome this repulsion, a reasonable approximation can be made using the nearest approach. A method which led to Ernest Rutherford's discovery of the nucleus in 1911 by analysing data of Geiger and Marsden on the scattering of α particles off of thin gold foils and calculating the distance of closest approach for the alpha particles and gold nuclei [62, 63].

The closest approach relies upon the principle that the Coulomb potential will increase inversely with the distance of separation. Assuming the radius of both the nucleus and the projectile is known, the Coulomb potential, V, at this distance can be calculated

$$V = \left[\frac{(Z_p Z_T)e}{4\pi\epsilon_0(r_T + r_p)}\right], \tag{1.7}$$

where T and p denote the target and projectile, respectively. Z is the proton number, and r is the respective radii.

The Coulomb repulsion that must be overcome is much greater in α and ^{3}He reactions than p and d, due to the extra proton in the projectile. Higher mass isotopes such as ^{99}Mo have greater Coulomb

repulsion than low masses such as ^{16}O as the charge term is more significant than the radius. For protons incident on ^{16}O and ^{99}Tc the potential at the nearest approach is 2.34MeV and 7.86MeV respectively. For α particles on ^{16}O and ^{99}Tc the threshold energy is 5.01MeV and 14.80MeV in the lab-frame respectively. These values are not absolute, as the radius of the nucleus cannot always be approximated as a perfect sphere (note the above barriers were calculated using $1.4 \times A^{1/3}$ fm for the nuclear radii [73]), and the effects of quantum mechanical tunnelling have not been considered.

1.7.2 Compound Reactions

Compound reactions occur when the target nucleus fully absorbs a projectile, and the particle's kinetic energy is distributed throughout the nucleus, reaching equilibrium. These reactions predominate above the Q-value and Coulomb potential but at lower energies than direct reactions. In compound reactions, the projectile and target fully merge, and there is no memory of the initial formation channel. The lifetime of a compound nucleus must be several times the time it takes a particle to transit the nucleus, often around 10^{-19} s.

The main consequence of forming a compound nucleus is that any ejectile emitted from the nucleus is independent of the target and projectile and only related to the mass, atomic number, excitation energy and angular momentum of the compound nucleus. This can be seen experimentally when a compound nucleus is formed from a range of reaction pathways; the outcome is independent of the reaction path.

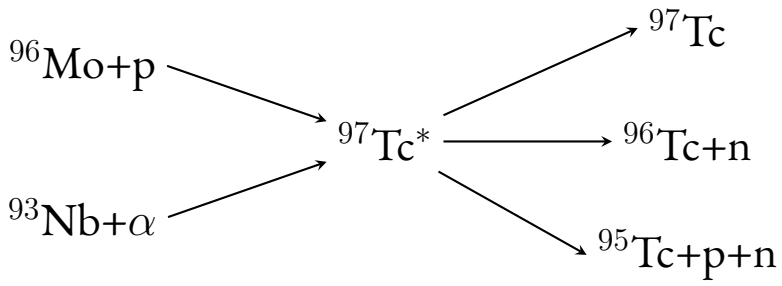


Figure 1.12: *Schematic of a compound reaction, showing the production of a compound nucleus of ^{97}Tc*, through a range of reaction mechanisms.*

1.7.3 Direct Reactions

Direct reactions predominate at higher energies than compound reactions, usually taking place above 5MeV/A$_p$ where A$_p$ is the mass of the projectile. These reactions occur over $\sim$ 1000th the timescale of compound reactions. The projectile has time to only interact with a single nucleon. There are several sub-classes of direct reaction, however, the defining factor is that the projectile can only interact with a single nucleon within the nucleus. These reactions can be pick-up reactions such as (p,d) where the proton picks up a neutron from the nucleus, stripping where a neutron is deposited in the nucleus, such as (d,p) and break-up where the projectile breaks up into individual nucleons (d,pn).

1.7.4 Pre-equilibrium reactions

While compound and direct reactions describe the two extremes of the energetics of a nuclear reaction, a large number of reactions at intermediate energies are in between the two. This is where the projectile is absorbed by the nucleus and interacts with several nucleons but does not reach equilibrium.

1.8 Cross-Section

Now that the different reaction mechanisms have been defined, it's essential to understand the probability of a reaction occurring. The probability is tied to a value known as the microscopic cross-section, σ, however, it is commonly referred to solely as the cross-section. The cross-section can be described as the number of reactions per unit time, R, divided by the number of incident beam particles per unit time per unit area, known as the beam flux, I,

$$\sigma = \frac{R}{I}. \tag{1.8}$$

The cross-section is the relative area of the nucleus with units of cm^2 and can be far larger than the physical area of the nucleus. Due to the fermiscopic scale of the nucleus (10^{-15} m), the unit of barns is conventionally used, where 1 barn = 10^{-28} m^2.

The reaction mechanisms previously mentioned are highly dependent on the energy of the reaction. As the projectile energy is increased, new reaction channels open, while channels that dominate at lower energies become less probable. For example, as energy increases, the $(p,2n)$ reaction will dominate the (p,n) reaction. This is shown in figure 1.13.

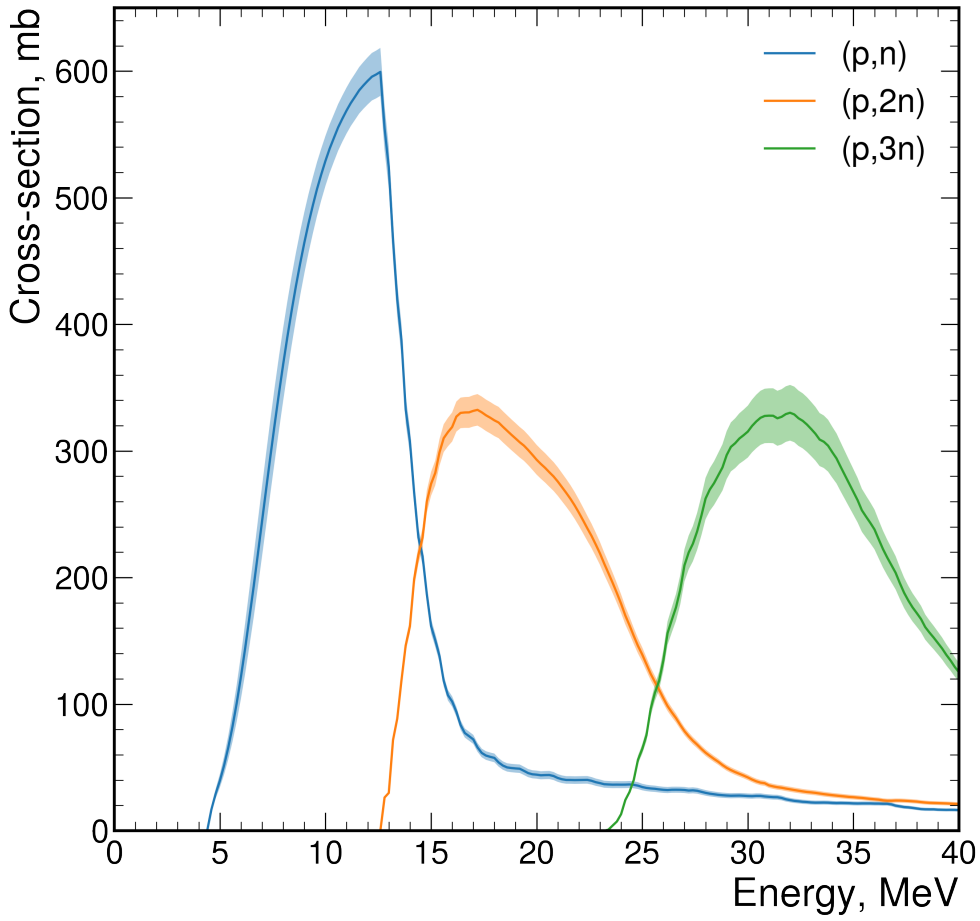


Figure 1.13: *A plot showing the cross-section of various emission channels for proton irradiation of ^{92}Mo, calculated using TALYS. The bands around the data lines show the uncertainty calculated using TAS-MAN. The horizontal axis is the projectile energy in MeV.*

From the irradiation of an isotope, the production of a given product may be fuelled through several reaction paths, due to the different combinations of ejectiles and recoiling product nuclei, which can add up to the same mass and charge.

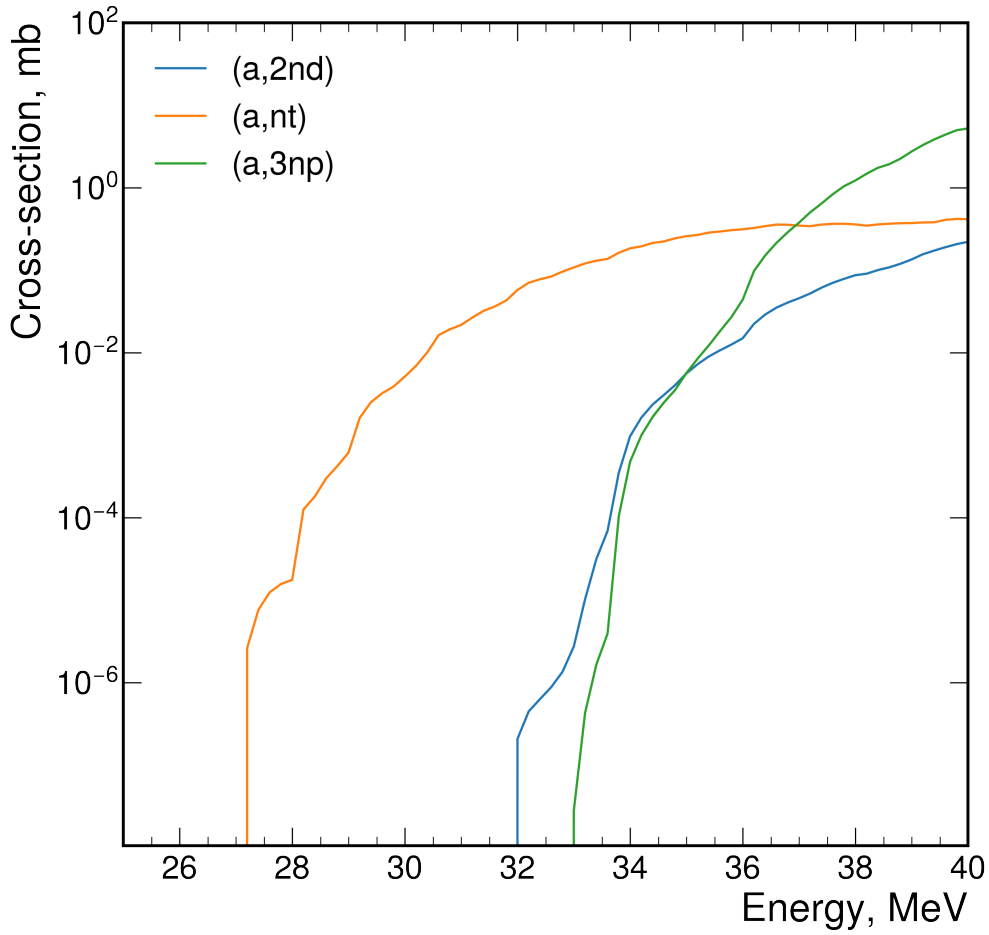


Figure 1.14: *Cross-section plot showing different ejectile combinations which result in the same residual nucleus. The cross-section is measured in millibarns and the horizontal axis is the projectile energy in MeV. The calculations were performed using TALYS nuclear reaction code for the production of the* ^{97}*Mo-*α *reaction producing technetium-*97*.*

It is often the product isotope that is of interest rather than the reaction channel itself. In this case, the sum of all reaction channels which produce the isotope of interest is calculated and it is known as the residual production cross-section, $\sigma_{rp} = \sum(\sigma_i)$.

The cross-sections mentioned so far are variants of microscopic cross-sections with units of area. There is another cross-section parameter that is commonly used, called the macroscopic cross-section, particularly when considering neutron and photon-induced reactions. The macroscopic cross-section

is related to the probability that a particle will undergo a reaction per unit path length travelled through a material, given by the symbol, Σ, and is the microscopic cross-section, σ, multiplied by the number density of the target, N, commonly given in units of cm^{-3},

$$\Sigma = \sigma N. \tag{1.9}$$

The reaction rate can be calculated for a single nucleus by multiplying the macroscopic cross-section by the flux of particles in $\mathrm{cm}^{-2}\mathrm{s}^{-1}$ [74]. This value must be multiplied by the active target volume (Ax) to calculate the reaction rate for a target being irradiated and is of interest in isotope production calculations

$$R_R = \sigma N \phi A x \tag{1.10}$$

$$= \Sigma \phi A x. \tag{1.11}$$

1.9 Isotope production

Isotope production is the process of irradiating a target with a flux of particles to produce isotopes which are not naturally occurring in the form produced. Targets are commonly, but not restricted to, being solid, stationary and composed of stable isotopes. Interactions employ particle beams accelerated to produce an isotope of interest, while at the same time minimising unwanted products.

The activity of an isotope, Y_i, with decay constant, λ_i, following an irradiation of time, τ, of a target with number density, N_T, and volume, $V = Ax$, by a mono-energetic flux of particles, ϕ, is given by

$$Y_{i0} = \sigma_i \phi N_T A x (1 - e^{-\lambda_i \tau}), \tag{1.12}$$

and the activity of the isotope at time, t, after irradiation can be described using the usual decay equation

$$A_i = A_i(0) e^{-\lambda t}. \tag{1.13}$$

1.9.1 Particle Beam

A charged particle beam is produced by accelerating a charged ion in an electric field. Neutral particles may be created in a secondary process. However, in this thesis, the focus of the work will be on charged particle reactions.

Once a particle beam has been accelerated, the beam may be shaped using quadrupole magnets, or electric quadrupoles, enabling a high-intensity beam to be focused on a small target surface.

1.9.2 Targetry

As a charged particle beam passes through a target, the beam's energy degrades as a function of depth due to a combination of electromagnetic and nuclear interactions. This effect is important to quantify, because as the projectile's energy degrades as a function of depth; the cross-section will also vary. This function is known as stopping-power and may be quantified as a particle's energy loss per unit length, $\frac{dE}{dx}$ using the Bethe-Bloch equation [75]

$$\frac{dE}{dx} = \left(\frac{e^2}{4\pi\epsilon_0}\right)^2 \frac{4\pi z^2 N_0 \rho Z_p}{mc^2\beta^2 A}\left[ln\left(\frac{2mc^2\beta^2}{I}\right) - ln(1-\beta^2) - \beta^2\right] \tag{1.14}$$

where $\beta = \frac{v}{c} = \frac{[(E/m_pc^2+1)^2-1]^{1/2}}{(E/m_pc^2+1)}$, ze is the electric charge of the projectile, Z, A, and ρ are the atomic number, atomic weight, and density of the stopping medium and, I, the mean excitation energy of the atomic electrons. The majority of the parameters in the equation are common physical constants, including N_0, Avogadro's constant, and m, the electron mass. Stopping power increases as energy drops, reaching a Bragg peak at low energies, where most energy is deposited over a very short range. This is due to the greater time for electron interactions at lower energies, causing a faster energy loss. The stopping power is shown for Ne (A=20.1797u, Z=10) and Sn (A=118.71u, Z=50) targets with proton (Z=1, A=1) and alpha (Z=2, A=4) beams in figure 1.15, showing the effect of target and beam atomic number and charge.

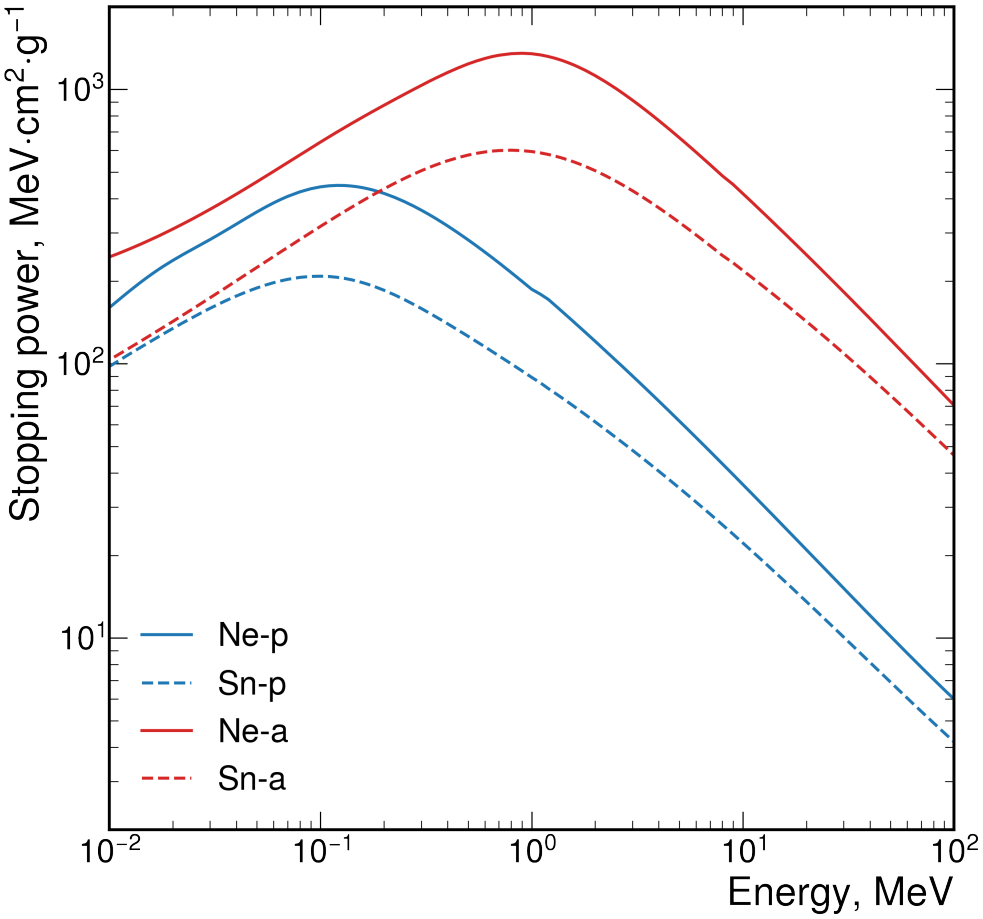


Figure 1.15: *Stopping power against energy for a range of target-beam combinations calculated using the SRIM stopping power code [76].*

The stopping power of a projectile through a target medium is higher for higher atomic number projectiles and targets. The unit of stopping power is MeV.cm^{2}g^{-1}, which makes the stopping power independent of density. Multiplying the stopping power by density gives stopping power in MeV.cm^{-1}.

The stopping power can also be used to calculate the range of a particle, where the particle range from one energy to another is the integral of the inverse stopping power between two energies

$$\text{Range} = \int_{E_f}^{E_i} \frac{1}{\frac{dE}{dx}} dE, \tag{1.15}$$

measured in units of g.cm^{-2}. The range of a particle between two energies is important in determining the target thickness to cover the desired energy range relating to cross-sections region of interest, whether maximising yield or avoiding the production of certain products.

For thick targets, the cross-section cannot be assumed to be constant, due to the loss in energy throughout the target. This greatly affects the target yield, which can no longer be calculated as a function of target thickness as in equation 1.12. Accounting for the variation in energy and cross-section gives

$$Y_{i0} = \phi N_T A(1 - e^{-\lambda_i \tau}) \int_{E_f}^{E_i} \sigma_i(E) \left(\frac{dE}{dx}\right)^{-1} dE, \tag{1.16}$$

where $\sigma_i(E)$ is the microscopic cross-section of the reaction, varying with particle energy, E, and measured in units of area, E_i and E_f is the energy at the front and rear of the target, respectively, ϕ is the particle flux, N_T is the target number density, and A is the surface area of the beam. The derivation of the reaction rate is given in the appendix, in section B.

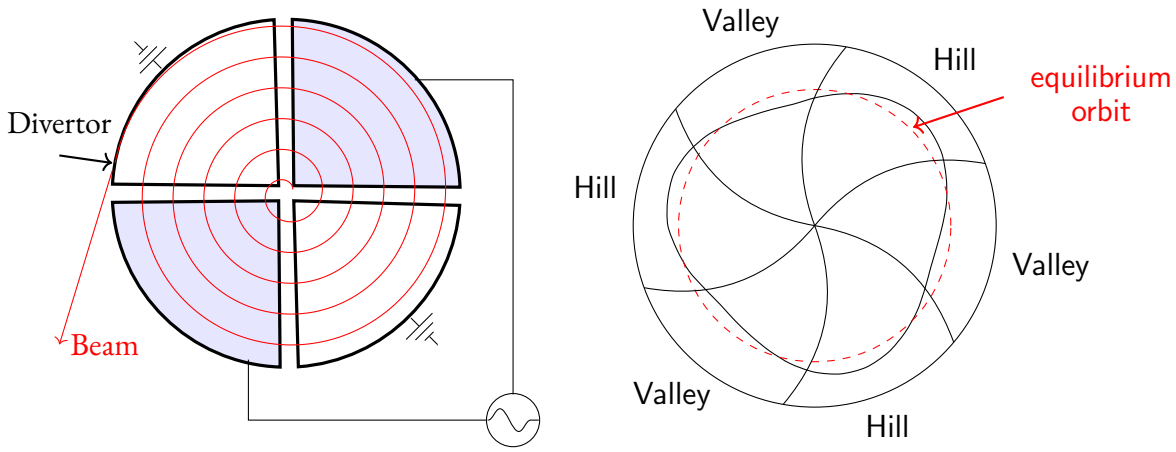
1.9.3 Cyclotron Accelerators

A cyclotron is a commonly used orbital particle accelerator, with a Scanditronix MC40 cyclotron at the University of Birmingham used throughout this work [77]. Ions produced in a central ion source are injected into the centre of the circular device inside a uniform magnetic field generated by electric current flowing in copper windings above and below the vacuum vessel. Four quarter-circular magnets (dees) are used for acceleration of the particles. Two are called 'dummy dees' and are on opposing sides (180°) and remain at earth potential, while the other two are connected to an oscillating radio-frequency (RF) electrical current. As ions are accelerated from the central ion source, the radius of the particle orbit increases to the perimeter of the cyclotron. The radius of the particle's orbit is proportional to the velocity as shown in equation 1.17.

$$r = \frac{mv}{qB}, \tag{1.17}$$

where m, v, and q are the mass, velocity and charge of the particle, respectively, and B is the magnetic field strength. As the particle crosses between the dees, the potential difference between the two dees

causes the particle to accelerate. This occurs uniformly over many orbits until the particle reaches its maximum energy at the outer radius of the cyclotron. The maximum energy of a particle is governed by the radius and the magnetic field strength, with the magnetic field being an adjustable parameter on the machine, up to a limit. The orbital frequency of the particles must be the same at all radii, and in most instances is the case, as r is proportional to v. At higher energies, however, relativistic effects become significant, affecting particles at larger radii more. Isochronous cyclotrons account for this by increasing the field with radius, which itself causes an issue called axial defocusing, with the effect resolved by introducing spiral-shaped sectors, which cause alternating focusing and defocusing. Cyclotrons with these spiral sectors, such as the MC40 are known as Azimuthally Varying Field (AVF) cyclotrons. A schematic of a cyclotron with four dees and isochronous focusing is seen in figure 4.1.



(a) *Schematic of a cyclotron with four dees, including two dummy dees which are connected to ground.*

(b) *Cyclotron with isochronous focusing and defocusing sectors.*

Figure 1.16: *Schematic of cyclotron particle accelerators, one with two dees and two dummy dees, one with an azimuthally varying field that causes focusing and defocusing to account for relativistic effects.*

The maximum energy of a cyclotron is given by its K-value. This describes the kinetic energy limit (in MeV) for protons, from the cyclotron bending strength in a non-relativistic approximation,

$$K = \frac{e^2}{2m_p}(B\rho_{max})^2 \tag{1.18}$$

where e and m_0 are the charge and the rest mass of the proton, B is the magnetic field strength and ρ_{max} is the maximum radius of the cyclotron. The K-value of the University of Birmingham Scanditronix

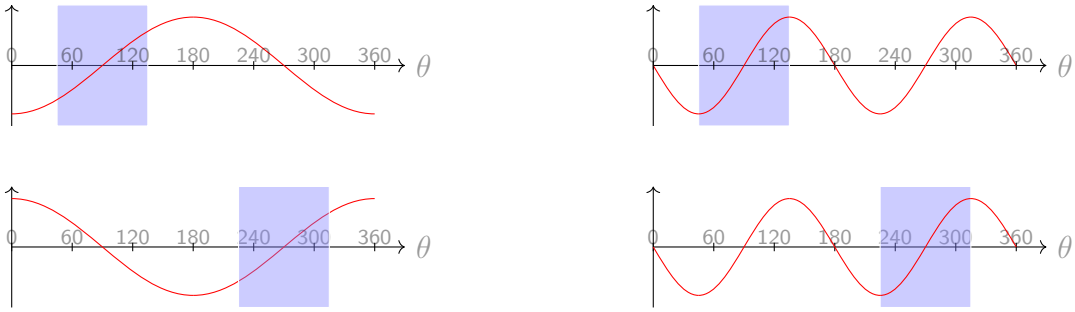
MC40 cyclotron is 40 [77]. This K-value is defined for protons but may easily be scaled for other particles

$$E_k = \frac{KQ^2}{A}, \tag{1.19}$$

where Q is the particle charge, and A is the atomic mass of the particle. This gives a maximum energy of ^{4}He to be 40 MeV, deuterons to be 20 MeV and ^{3}He to be 53 MeV. A limiting factor on cyclotron energies is often the possible RF frequencies for a given B field, which limits the minimum and maximum energy, however, the use of harmonic frequencies increases this range greatly. The frequency of a particle's orbit in a cyclotron can be related to the magnetic field, B, the electron charge, e, and the mass of the particle, m,

$$f = \frac{Be}{2\pi m}. \tag{1.20}$$

The first mode (fundamental) requires the RF to perform one cycle for every orbit, with the potentials on the two dees being in anti-phase. The 2nd mode (first harmonic) requires the RF to perform two cycles during every orbit, with the two potentials being in phase. This is illustrated in figure 1.17.



(a) *Fundamental mode (N=1)* ***(b)*** *First harmonic (N=2)*

Figure 1.17: *Plot of the fundamental and first harmonic of the MC40 cyclotron particle accelerator with the angular extent of a quarter dee (90°) highlighted in purple.*

1.9.4 Chemical Separation

Following the irradiation of a target, the sample usually has an array of isotopes spanning several elements. For example, the α bombardment of ruthenium will primarily produce palladium through a range of (α, Xn) reactions. Proton (α, pXn), deuteron (α, dXn), and triton (α, tXn) ejectile channels will produce rhodium, while there are a large number of possible reaction channels emitting

two protons which produce ruthenium isotopes; $(\alpha, 2pXn)$, $(\alpha, pdXn)$, $(\alpha, 2dXn)$, $(\alpha, ptXn)$, $(\alpha, dtXn)$, $(\alpha, 2tXn)$, $(\alpha, {}^{3}\mathrm{He}Xn)$ and $(\alpha, \alpha Xn)$. Higher and lower atomic number elements may be produced through more complicated reaction channels along with the subsequent decay of radioisotopes.

To separate undesired elements or the target element from the desired product element, chemical separation techniques are used. There are several chemical separation methods, while one commonly employed for analytical chemistry is extraction chromatography. Chemical separation methods will only separate one element from another; the contamination of different isotopes of the same element can only be solved by reaction optimisation or target enrichment unless more expensive and complex mass separation techniques are employed.

Extraction chromatography is a form of chromatography which enables the separation of different elements determined by their relative affinity to an extractant. The chromatography resin consists of beads which are composed of a stationary phase composed of the resin, which the atoms bind to, and an inert support, which is responsible for keeping the resin in place. The remaining volume is a fluidic stream, known as the mobile phase. The mobile phase is a solution, commonly acidic. Extraction chromatography works on the principle of elution, where an ion with a high affinity will pass through the extraction column much slower than one with a low affinity. A useful parameter when understanding a resin's ability to extract ions is the distribution coefficient, defined as

$$k_d = D_w \frac{V_s}{V_m}, \tag{1.21}$$

where V_s is the volume of the stationary phase, V_m is the volume of the mobile phase, and D_w is the distribution factor, which gives the ratio of molar concentrations in the stationary and mobile phases at equilibrium. The k_d shows the affinity ratio to the stationary phase over the mobile phase. A high k_d value means the ion has a high affinity to the stationary phase over the mobile phase and is likely to elute slowly through the column. For a low k_d, there is a relatively low affinity to the stationary phase,

with the ion will pass through more quickly, without strongly binding to the column.

The geometry of the column is of great importance to the efficiency of the separation process, where the length and width of the column and the resin particle size can be optimised. A useful metric of this is band spread, the distribution of an ion over the length of the column. For perfect retention, a resin with a narrow band, as close to the column inlet would be used. Chapter 5 describes the development of a chemical separation method for a technetium-97 radiotracer using novel extraction chromatography resins.

2

Theoretical Cross-Section & Transmutation Modelling

Theoretical cross-section calculations are not absolute, due to the lack of an accurate comprehensive predictive theory of the nucleus. Models rely on empirical data for parameterisation, while experimental data are incomplete and inexact. Cross-section calculations are in fact predictions, based on a spread of theoretical models, with phenomenologically optimised parameters. Precise and accurate cross-section calculations are essential in determining the products which will be produced in a reaction as well as their quantities. This chapter details the different classes of nuclear data available, some of the possible modelling techniques, and advances made through this project for the optimisation of isotope production calculations through established codes, executing simulations, and parsing, analysing and visualising those data.

2.1 Nuclear Data

There is a huge spread of available nuclear data, including published experimental cross-sections, decay data, and energy levels, evaluated databases, modelled data for lesser-known reactions, or the model parameter libraries. For all nuclear data, there is a pipeline which takes experimental measurements to application shown in figure 2.1.

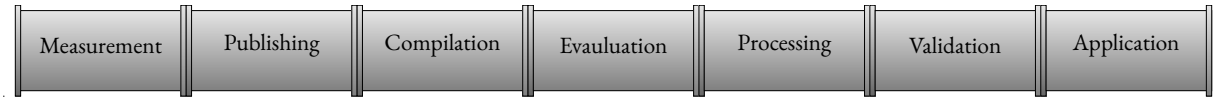


Figure 2.1: *Visualisation of the nuclear data pipeline from measurement to application [78].*

Data are measured experimentally at universities and research facilities to address gaps in data or improve less accurate data. These data are then published in recognised academic journals. The data from these journals are then compiled into libraries such as EXFOR [79] for reaction data and XUNDL [80] for nuclear decay and structure data.

It is the next step, evaluation, where the quality of nuclear data are verified, a process whereby a skilled nuclear physicist reviews the available data, often with discrepancies between different data sets. The experimental methodology and analysis are investigated to determine which data are most reliable with respect to the uncertainties given, often with the evaluated data coming from a weighting of several published values. These data are then stored in evaluated nuclear data libraries.

The suitable data determined by nuclear data evaluators are then processed using several computational tools, converting the evaluated nuclear data files (ENDF) into a format required by a given application. An example of this is the Monte-Carlo N-Particle (MCNP) [81] software that requires data in the ACE format [82], with the NJOY tool used for the conversion [83].

The validation process is the final step in the pipeline before dissemination, where the data are compared using quantitative models [84, 85, 86] using independently measured values from benchmark-quality experiments. The evaluated, processed data are input into the models, and an iterative process is

performed, with adjustments made to the evaluated data. These data are then published in evaluated nuclear data libraries for various applications. This completes a single run of the nuclear data pipeline, however, based on updated needs and requirements, new data may be required, and the pipeline is iterated [78].

2.1.1 Nuclear Reaction Data

The International Network of Nuclear Reaction Data Centres (NRDC) was established in 1966 to disseminate nuclear reaction data and associated documents [87]. The network runs under the auspice of the International Atomic Energy Agency. It holds Nuclear Data Centres around the globe as members, including the US National Nuclear Data Centre (NNDC), IAEA Nuclear Data Services (NDS) and Japanese Atomic Energy Authorities Nuclear Data Centre (JAEA/NDC). While each nuclear data centre publishes its own nuclear data evaluated library, there are international libraries that compile nuclear data from a range of these evaluated nuclear data libraries.

2.1.2 Evaluated Nuclear Data Libraries

There are several evaluated nuclear data libraries, each possessing different information, with some libraries being general-purpose and others being focused on particular applications. A list of general-purpose evaluated nuclear data libraries are:

- **ENDF/B-VIII.**0 USA, 2018,
- **JEFF**-3.3 Europe, 2017,
- **JENDL**-5 Japan, 2021,
- **CENDL**-3.2 China, 2020,
- **ROSFOND**-2010 Russia, 2010,
- **TENDL**-2021 Vienna, 2021.

Many special-purpose libraries contain data for specific applications, including dosimetry, activation and fusion. An example is the Fusion Evaluated Nuclear Data Library (FENDL-3.2b), with data specifically for fusion applications [88]. All evaluated nuclear data libraries are presented in files with the same format, developed by the Cross-Section Evaluation Working Group (CSEWG) known as the ENDF-6 format, which has existed since the 1960s [89]. The format aims to be easily both machine and human-readable, but it is often seen as outdated with initiatives such as the Generalised Nuclear Data (GND) format [90] aiming to move to a more modern database form.

2.1.3 EXFOR

Experimentally measured reaction data will contain discrete points for either the energy-dependent cross-section, angular cross-section or the energy-angle-dependent cross-section. Published nuclear reaction data are compiled into a database known as EXFOR prior to evaluation.

2.1.4 Unevaluated Nuclear Data Library (XUNDL)

The Unevaluated Nuclear Data Library (XUNDL) [80] is a database which compiles published data on nuclear decay and structure, enabling easy access before evaluation. For work published in Physical Review C and the European Physical Journal, data is compiled during the submission process, while data from many other journals are added retrospectively.

2.1.5 Parameter Library

Parameters for nuclear models are important for running accurate reaction calculations. These parameters include masses, discrete levels, level densities and optical model potentials. The most commonly used library is the Reference Input Parameter Library (RIPL-3) [91], which is used for many nuclear reaction codes, including TALYS. The library is periodically updated, most recently in September 2020.

2.2 Nuclear Reaction Modelling

Nuclear Reaction Modelling has grown significantly in its predictive power over the years, benefiting both from increased computational performance, advanced statistical methods and improved nuclear reaction theory. Several tools are available, with varying degrees of complexity, accuracy and usability. Codes can be segregated into two main categories, Monte Carlo and deterministic. Monte Carlo (MC) methods are employed when coupling interactions from a large number of components, and are often used for radiation transport simulations, which rely upon reaction cross-sections to determine the transport of a particle through a material and are often used for geometrically defined systems such as reactor modelling. A particle is randomly sampled, with statistical computations performed throughout the life of the particle and residual nucleus or secondary particle; when a large number of particles are simulated, the results converge on a deterministic result. Common Monte Carlo codes are Geant4 [92], MCNP [81], Fluka [93] and OpenMC [94]. For this project, Geant4 is utilised for the calculation of secondary neutrons produced in an experiment and the resulting activation.

Depletion codes, including FISPIN [95] and FISPACT-II [96], are deterministic codes which can be used to calculate the evolution of material over time, whether in a flux of particles, or subsequent decay. These codes are known as transmutation and deletion codes. FISPACT-II is utilised for both fuel burn-up and target irradiation calculations throughout this project.

Other more fundamental deterministic codes are EMPIRE [85] and TALYS [84], utilising nuclear structure theory and model parameters to calculate cross-sections. Each of these codes allows model and parameter variation and the computation of a large range of reaction combinations using a phenomenological approach of experimental data and nuclear structure and reaction theory. Throughout this work, the TALYS nuclear reaction code is used for performing nuclear reaction calculations, part of the T6 software suite. This is due to its mature nature, being the reaction code behind the TENDL [97] database, with established coupling to FISPACT-II [96].

2.3 T6 Software Suite

The T6 software suite has evolved from the single 'T', TALYS nuclear reaction code, with the other arms of the suite being developed to enable precision cross-section calculations of specific reaction types and regimes, accounting for resonances, fission, and parameter uncertainties. The T6 suite is used to create the TALYS Evaluated Nuclear Data Libraries (TENDL) [97] released biennially, with the last iteration released in 2021. T6 is a collection of six programs which enable the running of nuclear reactions, optimising cross-sections, parameters and models and the output of ENDF-6 files [89]. The workflow of the T6 software suite is shown in figure 2.2.

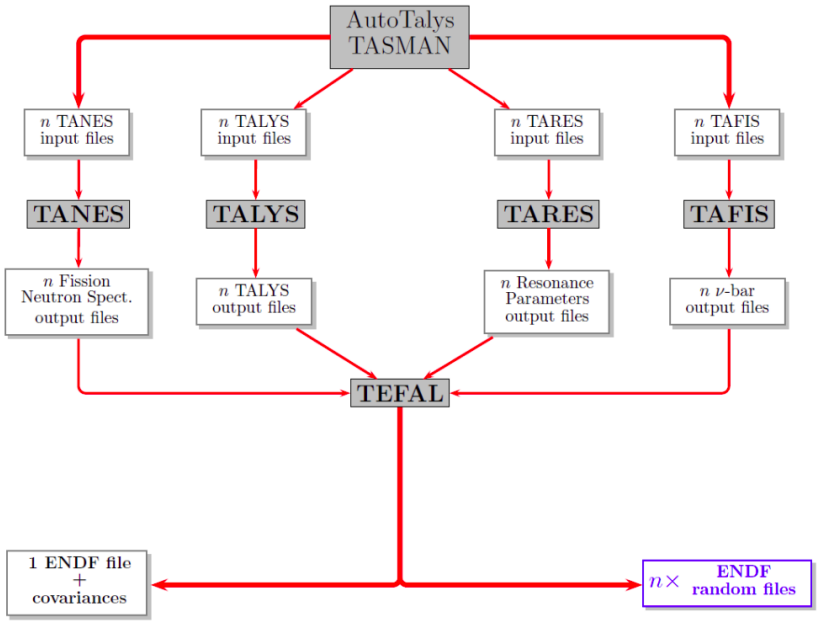


Figure 2.2: *T6 software workflow [98].*

AutoTalys is a package used to automatically create TALYS input files and is an addition and not itself one of the six programs making up T6. Two additional programs within T6 do not perform calculations but are utility tools, TASMAN and TEFAL. TASMAN is a statistical program used to vary nuclear reaction parameters, and TEFAL is used to format output into ENDF-6 format. The remaining four programs are part of the nuclear reaction calculation cycle. TALYS is the backbone of the code, running complete open-channel nuclear reaction calculations, TANES performs prompt fission spectra calculations, TARES performs neutron resonance calculations, and TAFIS calculates

the average number of fission neutrons, $\bar{\nu}$.

TALYS and TASMAN were the two modules of the T6 suite used within this project, with the University of Birmingham - Tool for Isotope Production (UoB-TIP), a python module developed throughout this project for the automation, parallelisation, parsing, and visualisation of TALYS and TASMAN reaction calculations. All calculations were performed on the University of Birmingham BlueBEAR high-performance computer [99].

2.4 TALYS

TALYS nuclear reaction code is actively developed by A.Koning [84], and is the backbone of the T6 software suite, outputting all calculated physical quantities. The only components of reactions that are not accounted for in TALYS are accounted for in separate codes, including resonances (TARES), fission neutron emission (TAFIS), and prompt fission spectra (TANES). Development of TALYS began in 1998 with iterations still ongoing; at the time of writing this thesis, version 1.96 was the most recent release, published in December 2021, and this version was used for all calculations shown in this project.

TALYS aims to accurately simulate nuclear reactions up to beam energies of 200 MeV for targets from mass $A = 12$ and above, for a range of projectiles (neutrons, photons, protons, deuterons, triton, ^{3}He and ^{4}He). TALYS may be used as a nuclear data tool in which the predictive power of TALYS and its underpinning models can be used to calculate nuclear reaction outcomes, or used as a nuclear physics tool, for the analysis of nuclear reaction experiments. The former was the focus of TALYS in this work.

TALYS requires the use of a large number of nuclear structure parameters, optical models and complicated nuclear reaction theory. Figure 2.3 shows the workflow adopted by TALYS to go from the input file to output data.

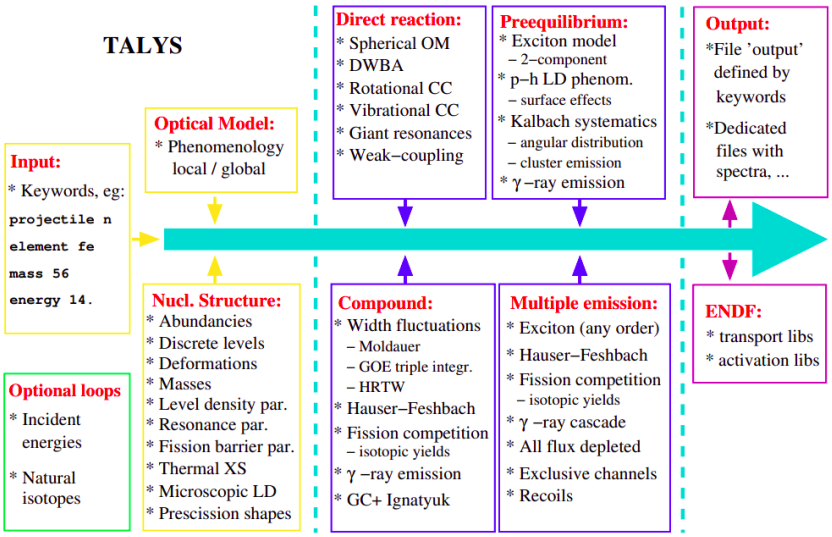


Figure 2.3: *TALYS calculation workflow, from input, nucleus and reaction modelling to outputs [84].*

TALYS utilises the optical model to simulate the nucleus, with what are understood to be the best parameterisations stored for many nuclei. Optical model potential (OMP) parameters are taken from Koning and Delaroche [100] for nuclei with sufficient experimental scattering data; these are known as local parameterisations. For nuclei without these data, global assumptions are made, where the parameters are a function of the atomic number, Z, and atomic mass, A, of the nucleus. Additionally to the OMP, there are vast numbers of models that can then be selected, to account for the complexity of the nucleus - providing different descriptions of the nucleus' structure, level densities and resonances. Certain models are more effective at accurately describing the nucleus in given mass regions.

2.4.1 Optical Model Potential

The Optical Model Potential [101] is a nuclear model which describes the direct component of the nuclear reaction. The pre-equilibrium and compound nucleus components of the cross-section are produced by spreading these models over various open, outgoing channels, as visualised in figure 2.4.

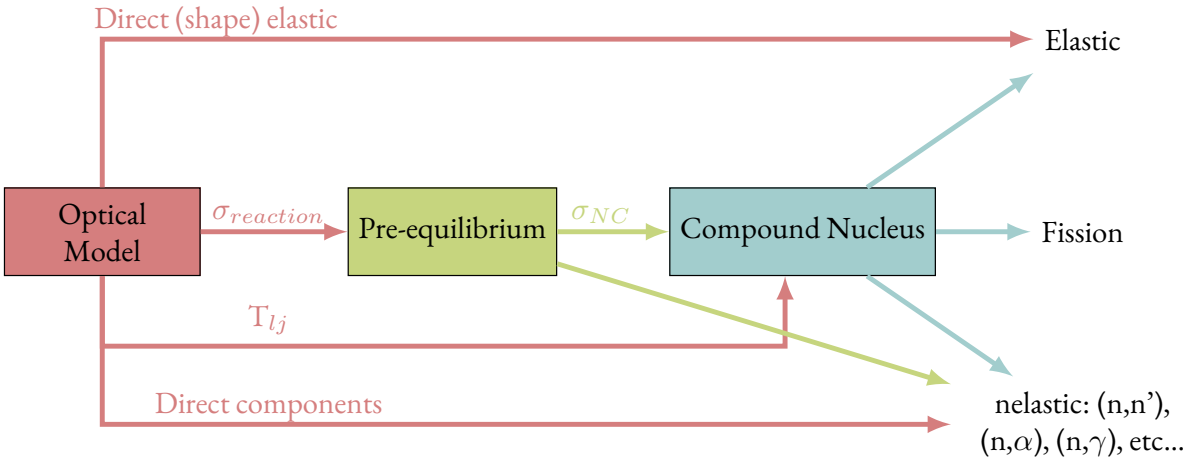


Figure 2.4: *Visualisation of how the optical model is used to calculate different nuclear reaction mechanisms, being spread through the pre-equilibrium and compound systems [102].*

The optical model gets its name from the interaction of light with a droplet of water, whereby the fractions of the light may be scattered, absorbed and transmitted. The optical model, therefore, describes the projectile and target reaction as the interaction of a wave function with a potential, according to the Schrödinger equation [103]

$$\left(-\frac{\hbar^2}{2m}\nabla^2 + U - E \right)\Psi = 0, \tag{2.1}$$

where $\hbar$ is the reduced Planck's constant $\frac{h}{2\pi}$, m is the particle mass, U is the potential energy, E is the kinetic energy, and Ψ is the quantum mechanical wave-function.

The wave function solution is calculated using the partial wave expansion method. The potential is complex, with the imaginary component accounting for a component of the projectile flux being lost from the elastic scattering channel, which is observed experimentally. The most common OMP is the phenomenological optical model potential, described by four components; Coulomb, volume, surface, and spin-orbit. The various parameters for this are determined by fitting the potential to experimental data. This greatly benefits the accuracy of the model to within 1%. A global parameterisation is used for nuclei which have not been experimentally validated, where the parameters are defined as a function of atomic number, Z and atomic mass A, greatly reducing the accuracy.

An example set of optical model potentials is shown for the spherical phenomenological optical model [84]

$$\begin{aligned} U(r,E) = &-v_V(r,E) - iw_V(e,E) - iw_D(r,E) \\ &+v_{SO}(r,E).I.\sigma + iw_{SO}(r,E).I.\sigma + v_C(r), \end{aligned} \tag{2.2}$$

where

$$\begin{aligned} v_V(r,E) =& V_V(E) f(r,R_V,a_V), \\ w_V(r,E) =& W_V(E) f(r,R_V,a_V), \\ w_D(r,E) =& -4a_D W_D(E) \frac{d}{dr} f(r,R_D,a_D), \\ v_{SO}(r,E) =& V_{SO}(E) \Big(\frac{\hbar}{m_\pi c}\Big)^2 \frac{1}{r}\frac{d}{dr} f(r,R_{SO},a_{SO}), \\ w_{SO}(r,E) =& w_{SO}(E) \Big(\frac{\hbar}{m_\pi c}\Big)^2 \frac{1}{r}\frac{d}{dr} f(r,R_{SO},a_{SO}). \end{aligned}$$

Both the real and imaginary parts of the volume-central (V), surface central (D) and spin-orbit (SO) are included in the potential, with energy given in the laboratory frame. The imaginary components account for particle absorption. Each of the factors has the Woods-Saxon form,

$$f(r,R_i,a_i) = \frac{1}{1+\exp(\frac{r-R_i}{a_i})}, \tag{2.3}$$

where, R_i, the nuclear radius may be approximated as

$$R_i = r_i A^{1/3}, \tag{2.4}$$

with r_i being a constant of proportionality and a_i being the diffuseness, and A being the atomic mass.

Specifically, parameterised potentials have been derived for proton and neutron projectiles, similar in form to the nuclear potential. For multi-nucleon projectiles, such as deuterons, tritons, and alphas, the potentials are constructed by combining proton and neutron potentials. For example for an α particle,

the potentials are sums of the neutron and proton contributions

$$V_V^{alphas}(E) = 2V_V^{neutron}(E/4) + 2V_V^{proton}(E/4), \tag{2.5}$$

$$V_D^{alphas}(E) = 2V_D^{neutron}(E/4) + 2V_D^{proton}(E/4), \tag{2.6}$$

$$W_V^{alphas}(E) = 2W_V^{neutron}(E/4) + 2W_V^{proton}(E/4), \tag{2.7}$$

$$W_D^{alphas}(E) = 2W_D^{neutron}(E/4) + 2W_D^{proton}(E/4), \tag{2.8}$$

$$V_{SO}^{alphas}(E) = W_{SO}^{alphas}(E) = 0, \tag{2.9}$$

$$r_V^{alphas} = (r_V^{neutron} + r_V^{proton})/2, \text{ and} \tag{2.10}$$

$$a_V^{alphas} = (a_V^{neutron} + a_V^{proton})/2. \tag{2.11}$$

2.4.2 TALYS outputs

TALYS outputs several nuclear reaction parameters, emissions and cross-sections. Cross-sections include the total particle production, exclusion reaction channel cross-section and residual production cross-sections.

The total particle production cross-sections are output for all possible projectiles; neutrons, protons, deuterons, tritium, ^{3}He and ^{4}He. Outputs are shown as cross-sections with units of millibarn (mb), and yield per source projectile. A value for production is given for each reaction mechanism. For example, the neutron production cross-section in a neutron-induced reaction can be written as a sum of all possible exit channels, with the cross-section of each channel weighted by the number of neutrons in the exit channel as

$$\sigma_{n,xn} = \sigma_{n,n'} + 2\sigma_{n,2n'} + \sigma_{n,np} + 2\sigma_{n,2np} + ..., \tag{2.12}$$

which can be written in the form of a sum

$$\sigma_{n,xn} = \sum_{i_n=0}^{\infty}\sum_{i_p=0}^{\infty}\sum_{i_d=0}^{\infty}\sum_{i_t=0}^{\infty}\sum_{i_h=0}^{\infty}\sum_{i_\alpha=0}^{\infty} i_n \sigma^{ex}(i_n, i_p, i_d, i_t, i_h, i_\alpha). \tag{2.13}$$

The production cross-section is an important parameter in understanding the production of secondary particles, which can initiate other nuclear reactions. However, the energy spectrum must be understood to gain an accurate picture of secondary particle effects.

The exclusive production cross-section defines the cross-section for a particular reaction channel, with a particular incoming particle and a particular combination of outgoing particles. For the production of a given isotope, there may be several exclusive cross-sections which contribute due to the sum of the ejectiles having the same proton and neutron number. The two exclusive cross-sections (n,pn) and (n,d) are separate cross-sections that result in the same product nucleus, known as a residual product.

The residual product cross-section is important for isotope production. It has been alluded to as the total production cross-section of an isomer, or the sum of all exclusive channels resulting in the production of the nucleus as:

$$\sigma_{prod}(Z,N) = \sum_{i_n=0}^{\infty}\sum_{i_p=0}^{\infty}\sum_{i_d=0}^{\infty}\sum_{i_t=0}^{\infty}\sum_{i_h=0}^{\infty}\sum_{i_\alpha=0}^{\infty}\sigma^{ex}(i_n,i_p,i_d,i_t,i_h,i_\alpha)\delta_N\delta_Z, \tag{2.14}$$

where δ_N and δ_Z are Kronecker delta functions defined as:

$$\delta_N = 1 \text{ if } i_n + i_d + 2i_t + i_h + 2i_\alpha = N_c - N, \text{ and} \tag{2.15}$$

$$\delta_Z = 1 \text{ if } i_n + i_d + i_t + 2i_h + 2i_\alpha = Z_c - Z. \tag{2.16}$$

where N_C and Z_C are the neutron and proton number of the compound nucleus, and N and Z are the total number of neutrons and protons respectively.

2.5 TASMAN

TALYS calculates nuclear reaction solutions for a given target-beam combination with a particular parameterisation. Based on the current theory and experimental parameterisations, these results are the solution for the most probable parameter combination, however, each parameter has a degree of error,

and there is a range of possible solutions, resulting in a spread of possible results. Due to the coupled effect of the many parameters, to determine error or sensitivity to changes in the parameters a large statistical pool of results can be sampled to determine the variance or sensitivity to parameter alterations.

TASMAN is a computational package which performs these statistical perturbations of nuclear models and parameters using the TALYS nuclear reaction code. Several optical model parameters and other structural models are altered randomly for each TALYS run, giving a distribution around a most probable solution, with errors given, with the default being a 2-σ distribution. The TASMAN output files are identical in structure to the standard TALYS output, however, they have ".ave" appended to the end of the filename and instead of a single cross-section value for each energy, three values are printed for the lower limit, average and upper limits of the cross-sections, written as low, ave and upp sections respectively.

The parameters are altered by applying a multiplication factor to them, the probability of each multiplication factor is a truncated Gaussian distribution around one, with the width of the peak determined by the error given in the parameter database. Figure 2.5 shows the distribution of parameter values for lvadjust, awadjusta, avadjusta, and lvsoadjust for OMP parameters in a Mo-α reaction calculation. The values awadjusta and avadjusta are multiplication factors of the a_w and a_v alpha particle OMP parameters respectively, and the values lvadjust and lvsoadjust are normalisation factors on the central potential and the spin-orbit potential respectively for JML (Jeukenne-Lejeune-Mahaux) OMP calculations.

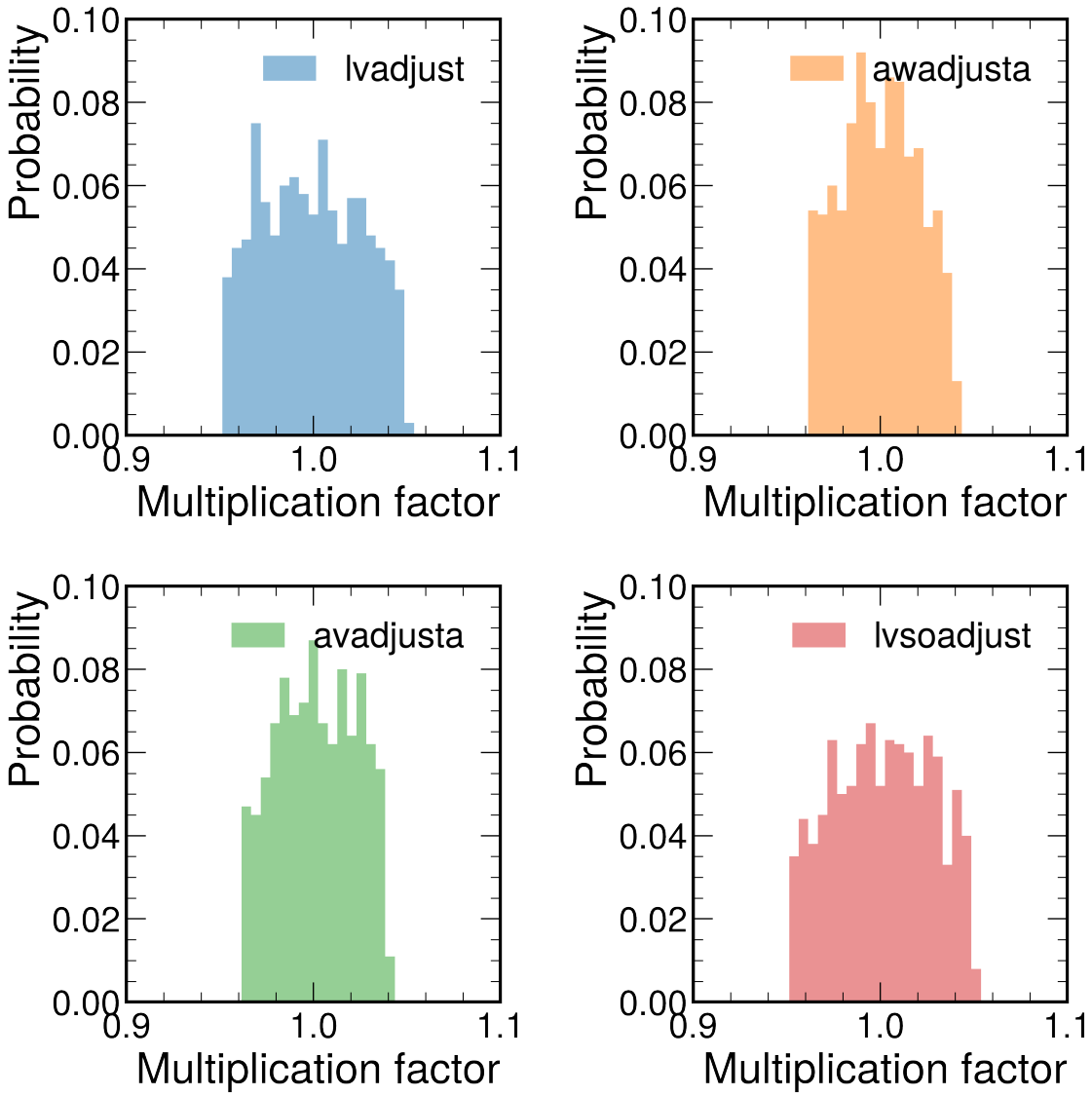


Figure 2.5: *Plot of the random permutation (multiplication factor) of several optical model parameters in TASMAN for; lvadjust, awadjusta, avadjusta, lvsoadjust overlaid to show the truncated Gaussian spread of data.*

By default, TASMAN runs 10 TALYS calculations, however, this can be altered up to a maximum of 6, 000 calculations. For all of the TASMAN calculations performed in this project 1, 000 TALYS runs were performed. The number of calculations being performed is a trade-off between increased accuracy and computational workload, with diminishing returns at higher numbers of calculations once a statistically significant distribution of calculations has been performed. Figure 2.6 illustrates the effect of different numbers of calculations on the parameter distribution for the awadjusta OMP

parameter. All calculations were run on the University of Birmingham BlueBEAR high-performance computer [99].

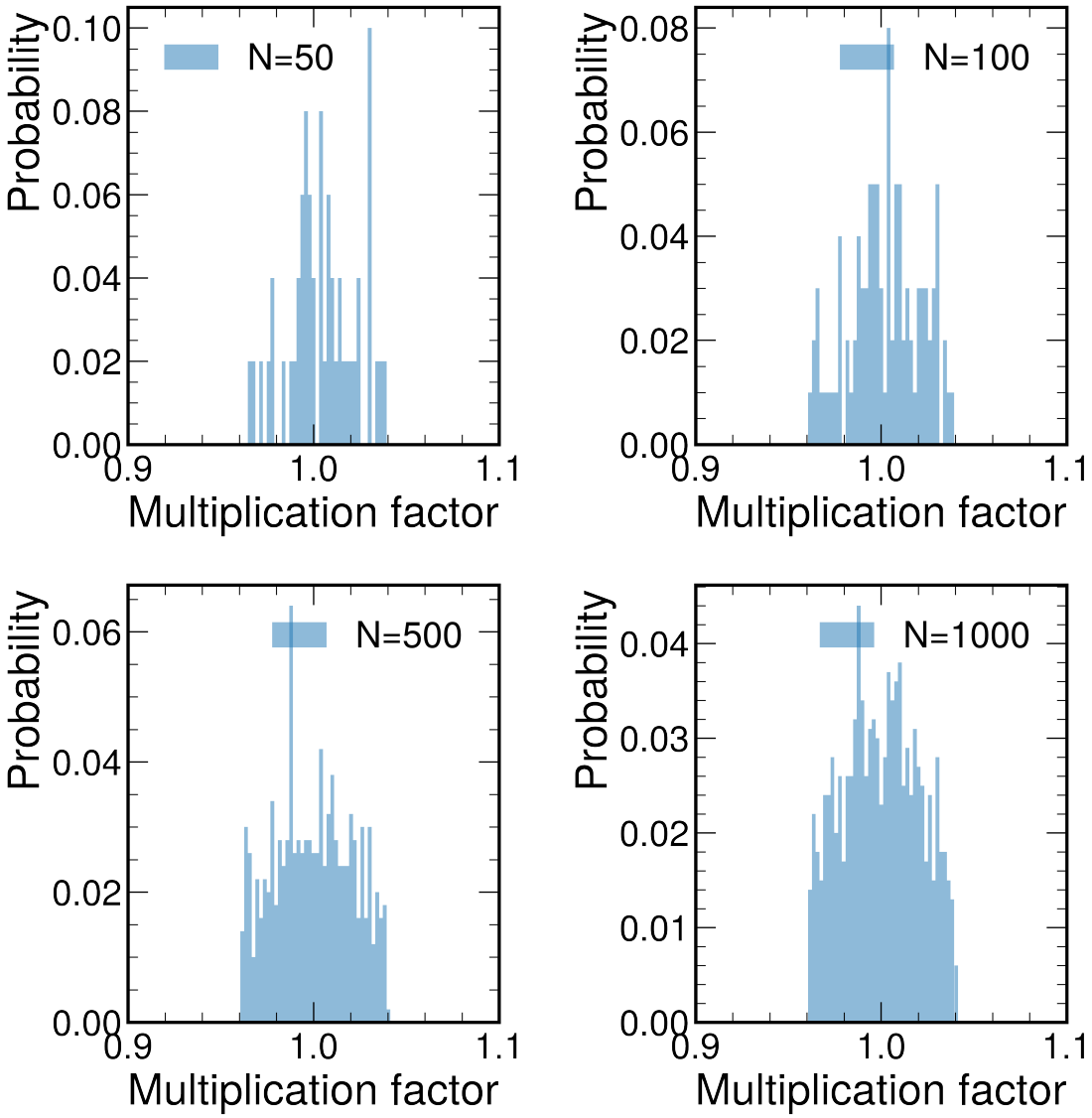


Figure 2.6: *The multiplication factor on the awadjusta OMP parameter for NTALYS*=50, 100, 500 & 1000.

2.6 University of Birmingham - Tool for Isotope Production

The University of Birmingham - Tool for Isotope Production (UoB-TIP) is a computational tool developed to improve the efficiency of executing, comparing and visualising nuclear reaction calculations,

with a particular focus on, but not limited to, isotope production. The tool performs calculations through a Python API, offering automation of the construction of TASMAN and TALYS input files, parsing output files into comma-separated variable format (.csv) and JavaScript Object Notation (JSON) format, and a data visualisation suite which takes in either format as an input.

2.6.1 TALYS Automation

The first component of UoB-TIP is the ability to automate the running of TALYS. Several functions, including `create_inputs()` python function `Run()` can be executed to produce TALYS input files and execute the files for a single reaction or list of reactions, an energy range and any number of parameters which are desired. An example of the `xs_full()` function with several parameters is shown in figure 2.7.

```
import uobtip as ubt

talys_parameters = ubt.TALYS_Parameters()

talys_parametrs.nuc_reaction = ['100Mo-p' 'Mo-n']
talys_parametrs.energy = ['1 40 1']
talys_parametrs.maxlevelsres = 20
talys_parametrs.best = y

tasman_parameters = ubt.TASMAN_Parameters()
tasman_paramaters.NTALYS = 1000
tasman_paramaters.residual = y
tasman_paramaters.rvadjust_a = 1.
tasman_paramaters.avadjust_a = 1.
tasman_paramaters.avsoadjust_a = 1
tasman_paramaters.awadjust_a = 1
tasman_paramaters.awsoadjust_a = 1
tasman_paramaters.d1adjust_a = 1
tasman_paramaters.d2adjust_a = 1
tasman_paramaters.d3adjust_a = 1
tasman_paramaters.lv1adjust = 1
tasman_paramaters.lvadjust = 1

tasman = ubt.TASMAN(talys_parameters, tasman_parameters)


root_path = '/path/to/runtalys'
project_name = 'technetium'

ubt.Run(tasman, root_path, project_name)
```

Figure 2.7: *UoB-TIP example code to run the cross-section calculations for* ^{100}*Mo-p and* ^{nat}*Mo-*α

This will produce reaction input files for each of the reactions requested. An example input file for the ^{100}Mo-p reaction is shown in figure 2.8, with optional parameters `maxlevelsres` and `best=y`. The `energies` keyword relates to another file produced which contains column data from $1 - 40$ with steps of 1. This relates to the energy steps in MeV.

```
energy energies
mass 100
element Mo
projectile p
maxlevelsres 20
best y
```

Figure 2.8: *An example of a simple TALYS input file produced by UoB-TIP for the ^{100}Mo-p reaction using an external 'energies' file, the 'best' keyword and 'maxlevelsres'.*

To run elements with natural abundance isotopes, the reaction ID can be written as either $0, 'nat'$ or not including a number with the element symbol. For natural abundances, the usual TALYS natural abundance run can be used, whereby a single TALYS calculation is run, however, not all data on isomers are output for individual isotope contributions. Using `TALYS_parametrs.natural = 'split'` runs a TALYS calculation for each isotope individually, with the outputs given separately along with a combined natural output with abundances extracted from NIST [104] applied as a weighted sum of each isotope.

The `Run()` function can be run an indefinite number of times, even with the same `project` keyword. For successive runs using the same project name, the data are stored in folders with increasing integer names. In the parent directory, a `reaction_index.txt` file is created detailing the reactions run, including information on the target, projectiles, energies, all optional parameters and the paths to either the JSON or .csv files. An additional benefit of this is the ability to run the function with the `run=False` parameter, which builds the input files for all of the reactions but does not run either TALYS or TASMAN. Instead, an executable bash script is created, which can run all of the reactions in the future. This is particularly useful if the files need staging onto a computer cluster before running.

The input files, along with the output data (if executed), are stored in a hierarchical format. The depth of the folder structure depends on whether the reaction being run is for a single isotope, multiple isotopic targets, natural-abundance-element or enriched-element target, or a compound or molecule composed of multiple isotopes. The folder for a given reaction contains the input file, TALYS or

TASMAN output files, and the UoB-TIP specific JSON or txt file. The directory structure is visualised in figure 2.9.

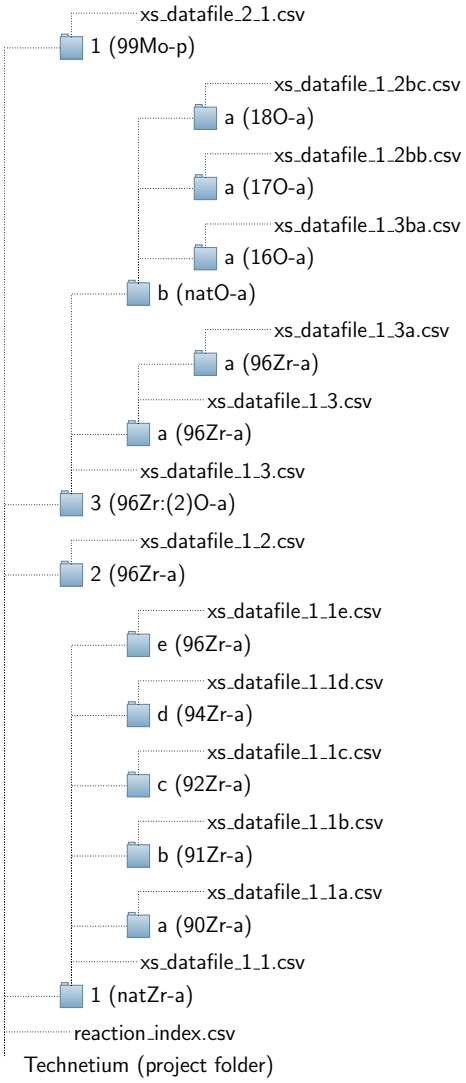


Figure 2.9: *Example directory tree for multiple runs for the production of* ^{99m}Tc.

The data can then be imported from these .csv files into excel, python or any other analysis stream. The xs_full() function returns a dictionary containing pandas data frames of the output residual cross-sections. This enables continued analysis with the output data stored in memory rather than having to reimport for further analysis.

An additional benefit of the program is pulling information from the output file directly to a python interface; particularly useful when utilising the python API through interactive python such as UoB-

TIP's default examples in Jupyter [105] notebooks. For example, a progress bar is an output showing the progress of the calculation as a ratio of the number of energy values in the calculation. The possible parameters for both TALYS and TASMAN can be called, with the default value, range of allowed values and a description of the value given — a far faster and more integrated way of learning the possible parameter variation than referencing the user manual. With information stored on all possible parameters and accepted values, UoB-TIP has a vast testing suite whereby the parameters and input files are tested before running, preventing errors occurring upon calculation execution.

2.6.2 Output Parsing

Both TALYS and TASMAN data are output in several cross-section output files, which can be categorised into several groups; exclusive (xs*), residual production (rp*) and particle production (*prod.tot) cross-sections. The data for each reaction channel produced isotope or secondary particle is output into its own file. Each reaction is given as a separate file and requires a layer of parsing before further analysis and plotting can be performed on outputs.

Data are parsed into JSON, produced using a set of python scripts. One of the additional benefits of the JSON data format is its ability to be imported as a python dictionary structure, without any additional transformations needing to be performed. There are four variants of the JSON output file depending if the reaction is a single isotope or contains several isotopes (e.g. natural abundance) and if it is a standard TALYS run or TASMAN containing .ave files.

For the output of a single isotope reaction, the top tier of the directory contains a tab for exclusive cross-sections, residual product nuclei, particle production and input file. Within the particle production tab are the 4 particle productions, with the energy and cross-section values written as a list. Under the input file tab is a dictionary format of the variables and the value of everything within the reaction input file. The majority of the information comes under the residual products tab. As UoB-TIP is an isotope production tool, the emphasis is placed on the products produced, rather than the exclusive cross-section. The next tier contains the products extracted from the residual

production cross-section, broken into a hierarchy of element, mass, and energy levels. Under each product produced, the Q-value, the reaction energy threshold (E-thres) and mass are given. The residual cross-section is then given as “rp” with “xs” and ”energy” being lists of the cross-section in mb and energy in MeV. An exclusive cross-section tab is given under the tab “exclusive”, containing each of the ejectiles which produce the given residual nucleus in the reaction as the next tab, followed by “xs” and “energy” as with the residual production cross-section. The JSON output is displayed in figure 2.10.

```
{"root":
    "inputfile":
        "element":Mo
        "mass":98
        "projectile":a
        "residual":20
    "production":
        "n": ...
            "xs": [XS(E0), XS(E1), XS(E2), ... XS(En)]
            "energy": [E0, E1, E2, ..., En]
        "p": ...
        "d": ...
        "t": ...
        "h": ...
        "a":...
    "products":
        "Nb": ...
        "Mo": ...
        "Tc": ...
            "95": ...
            "96": ...
            "97": ...
            "98": ...
            "99": ...
                "L00": ...
                "L02": ...
                    "Q-value":-14.9327
                    "mass":92.906809
                    "E-thres":24.6
                    "xs": [XS(E0), XS(E1), XS(E2), ... XS(En)]
                    "energy": [E0, E1, E2, ..., En]
                    "exclusive":
                        "pd":
                            "xs": [XS(E0), XS(E1), XS(E2), ... XS(En)]
                            "energy": [E0, E1, E2, ..., En]
                        "h": ...
                "tot": ...
            "100": ...
            "101": ...
            "102": ...
        "Ru": ...
}
```

Figure 2.10: *UoB-TIP JSON output structure for the ^{98}Mo-α reaction. The file structure is broken down by each product isotope.*

For reactions with natural abundances or with multiple isotopes, the format is identical; however, the top tier is broken into a natural tab and an additional tab for each of the individual isotopes. For the natural tab under each isomeric level (e.g.: L00, tot), there is an extra tier, "contribution". The contribution tab contains data including, Q-value, mass, E-thres, XS and energy for each of the contributing isotopes and a weighted sum of the cross-sections 'total', which account for the contributions to the full reaction.

2.6.3 Plotting Tool

The JSON format enables simple, intuitive and layered plotting of cross-section outputs. In isotope production, there is a focus on visualising the production of a particular product. This can be comparing the production cross-section of an isotope from different reaction routes (reaction comparison plot), plotting the target isotopic contributions to the production of a product (contribution plotting) and plotting the contribution of exclusive cross-sections to a residual production (exclusive plotting), which can be used in combination with the other plotting variations. These plots are used throughout this thesis, particularly in section 3 to compare possible tracer production routes.

2.7 FISPACT-II

FISPACT-II is a computational code developed by M. Gilbert et al. at UKAEA [106] primarily for materials irradiation applications in fusion energy [96]. A single or multiple irradiation scheme may be simulated over a given period and a period of cooling. This enables inventories of isotopes to be calculated against time. Therefore, this code has great flexibility for calculations in isotope production.

2.7.1 FISPACT-II Energy Loss Program

FISPACT-II offers a huge potential for isotope production calculations, especially neutron calculations, where the energy spectrum can be assumed to be uniform throughout the target. However, this is not the case for charged particles, as explained in section 1.9.2. As a charged particle passes through a target, the energy degrades as the projectile interacts with atoms and electrons within the target material,

which is modelled by the Bethe-Bloch stopping power equation. As the energy does not drop linearly with distance, it is impossible to spread the flux over the energy range between the front and the back of the target. This project developed a python tool to model the target as discrete slices with a thickness corresponding to a given drop in energy.

FISPACT-II's energy structure is broken down into different energy group structures, 162 energy bins for charged particles and 709 historically for neutrons, however in the recent releases CCFE-1102 has become the default due to the fine bin structure in the MeV range. The three energy group-structures, CCFE-162, CCFE-709 and CCFE-1102 are visualised in figure 2.11.

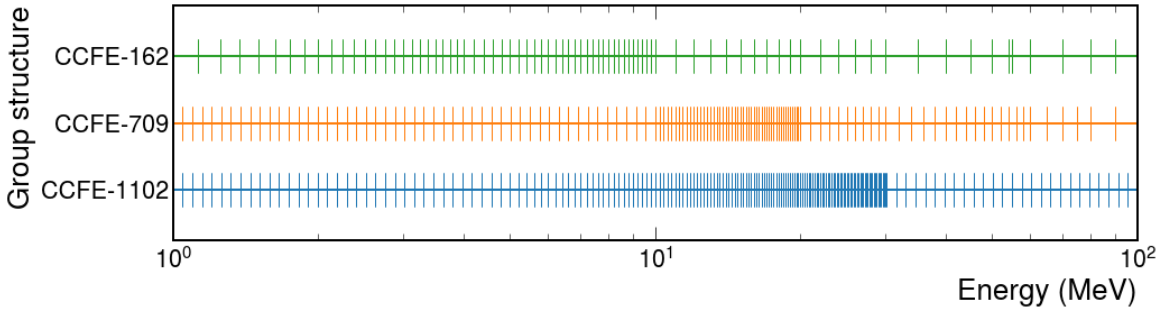


Figure 2.11: *Visualisation of the CCFE-*162*, CCFE-*709 *and CCFE-*1102 *group structures.*

Using the ion stopping power code SRIM, the thickness of material a projectile would pass through for a given drop in energy can be calculated as visualised in figure 2.12. The correlation between energy and energy bin allows a calculation to be performed for individual slices of the target, with each calculation only populating a single energy bin.

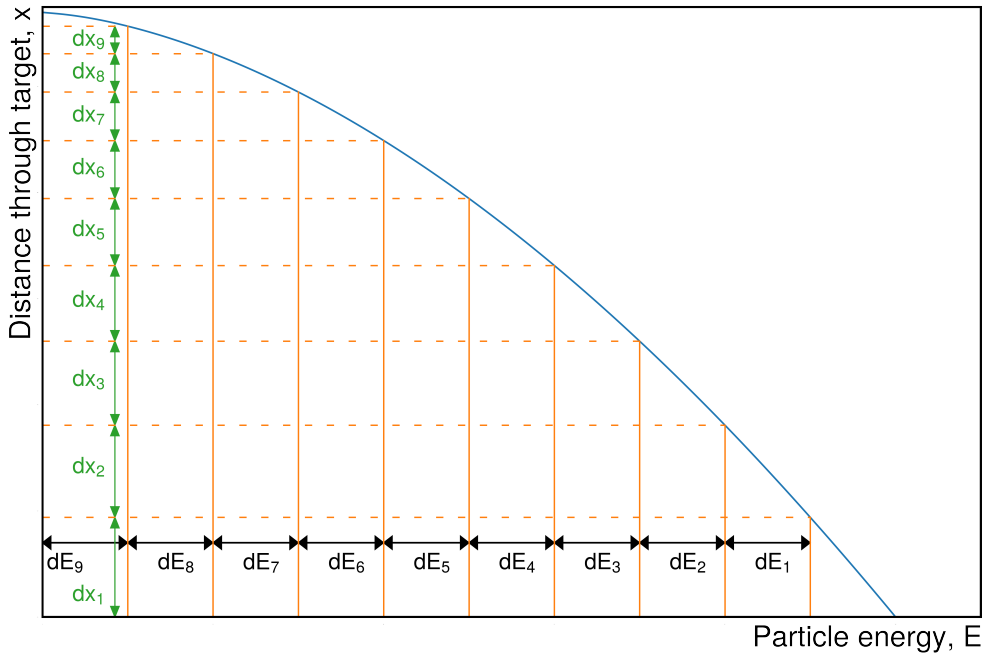


Figure 2.12: *Plot of particle range through a target visualising the correlation between a drop in energy, dE, and a change in distance, dx.*

The mass of the target which is required for the calculation, is calculated by multiplying the thickness, dx, by the cross-sectional area of the target, A, by the density, ρ. A target sliced into individual targets with thickness dx_i is shown in figure 2.13.

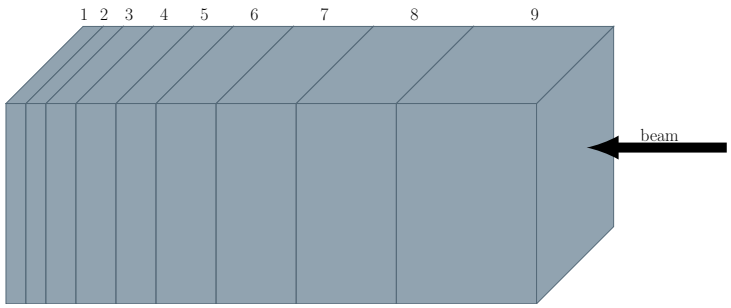


Figure 2.13: *Irradiation target split into slices of thickness, dx, relating to a drop in energy, dE.*

The python code developed in this project takes the target material, the projectile type and the projectile energy as inputs. Automation of SRIM [76] is then performed using functions calling the PySRIM module [107], enabling the mass of each slice to be calculated. Due to the higher fidelity of

the CCFE-1102 energy group structure compared to the standard CCFE-162 used for FISPACT-II charged particles, the data processing tool NJOY [83] was used to create ENDF-6 charge particle files in the CCFE-1102 format for higher accuracy calculations.

When executing, the code directory is created with a sub-file for each of the energy bins created. All bins below 1 MeV are treated as a single bin, which is well below the energy threshold of all charged particle reactions. Reactions will not occur below this energy, and the number of calculations is greatly reduced due to the logarithmic nature of the energy bins. However, the upper energy limit of the lowest energy bin is a parameter that the user can change. A set of input files is automatically created within the sub-directory, with a separate function to execute FISPACT-II for all sub-directories within the parent directory.

Once the run has been performed, the data can be parsed. Parsing the data is handled through a separate function, as the energy range of the target can be altered as parameters. This enables the effect of changing beam energy to be calculated without having to re-run FISPACT-II. The inventory data are output in .csv files for each output type: number of atoms, activity and dose rate. The files contain the product as row values and the time in hours from the end of the irradiation. All times during the irradiation are negative, going from $t = -t_{irrad}$ at the start to $t = 0$ at the end of the irradiation. These files are processed by parsing the 'inventory.log' files produced by FISPACT-II for each energy bin and performing a sum for common isotopes.

3

Reaction Optimisation

When determining the optimum reaction for the production of an isotope, an understanding of the available ion beams is essential. For this work, only charged particles were addressed due to the ability to optimise the energy more easily, and the relative ease of separating target and product isotopes from different elements. The University of Birmingham MC40 cyclotron can routinely accelerate ^{1}H, ^{2}H, ^{3}He and ^{4}He beams. While other exotic beams are possible, they were not considered for this work as they would greatly limit the available irradiation facilities for a commercial radiotracer. The possible target materials could then be assessed based on the assumption that the emission of two protons (in any combination) and four neutrons is the maximum nucleon evaporation in a reaction, limiting the possible target materials to produce ^{97}Tc. A section of the chart of nuclides is shown in figure 3.1 with the candidate target materials, Nb, Mo and Ru shown.

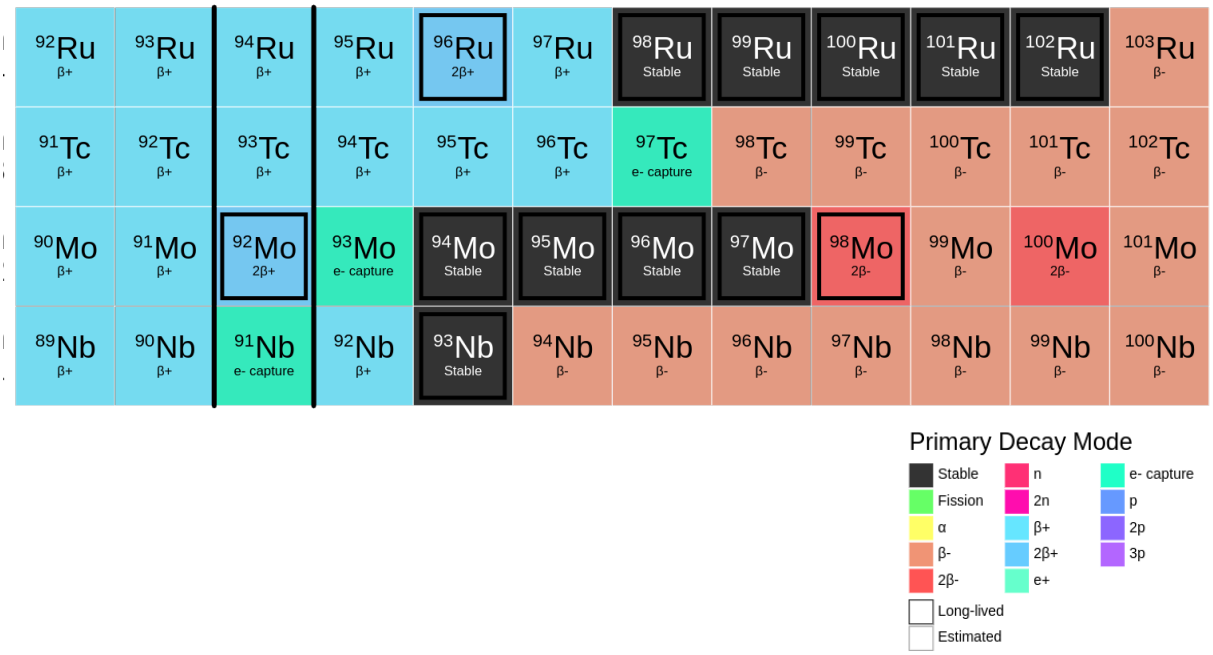


Figure 3.1: *Chart of nuclides focusing on Nb, Mo, Tc and Ru elements near stability [2].*

Technetium targets were not considered as there are no stable isotopes, and the tracer isotope ^{97}Tc would also be the same element as the target, preventing chemical separation. These restrictions provided a concise list of candidate reactions to be investigated for the potential production, which are given in table 3.1 with the target, beam and reaction.

Table 3.1: *Possible reaction channels to directly produce ^{97}Tc.*

Target	^{93}**Nb**	^{96}**Mo**	^{97}**Mo**	^{98}**Mo**	^{100}**Mo**	^{nat}**Mo**
Projecitle	α	p	p	p	p	p
Ejectile	γ	γ	n	$2n$	$3n$	xn
Target	^{95}**Mo**	^{96}**Mo**	^{97}**Mo**	^{98}**Mo**	^{100}**Mo**	^{nat}**Mo**
Projecitle	d	d	d	d	d	d
Ejectile	γ	n	$2n$	$3n$	$4n$	xn

One of the limitations of producing ^{97}Tc directly is the production of other technetium isotopes which cannot be chemically separated but will cause tailing and analytical overlap with both the tracer and the analyte.

3.1 Ru-97 generator

Only reactions directly producing ^{97}Tc have been considered so far. However, the production of a generator isotope is a feasible option and may offer significant benefits. A generator isotope is an isotope of an element that will eventually decay into the desired isotope of another element. The parent isotope should have the properties to chemically bind to a molecular surface, whereas the product isotope will not.

In the case of ^{97}Tc, a potential generator isotope is ^{97}Ru. Decaying into ^{97}Tc with a 100% branching ratio and a half-life of $2.83(23)$ d [56]. The reactions which may produce the ^{97}Ru generator are shown in table 3.2.

Table 3.2: *Possible reaction channels to produce ^{97}Ru generator.*

Target	^{94}**Mo**	^{95}**Mo**	^{96}**Mo**	^{97}**Mo**	^{nat}**Mo**	^{94}**Mo**	^{95}**Mo**	^{96}**Mo**
Projecitle	α	α	α	α	α	^{3}He	^{3}He	^{3}He
Ejectile	n	$2n$	$3n$	$4n$	xn	γ	n	$2n$

Target	^{97}**Mo**	^{98}**Mo**	^{nat}**Mo**	^{96}**Ru**	^{98}**Ru**	^{99}**Ru**	^{100}**Ru**	^{nat}**Ru**
Projectile	^{3}He	^{3}He	^{3}He	p	p	p	p	p
Ejectile	$3n$	$4n$	xn	γ	$2n$	$3n$	$4n$	xn

Target	^{96}**Ru**	^{98}**Ru**	^{99}**Ru**	^{nat}**Ru**	^{96}**Ru**	^{98}**Ru**	^{99}**Ru**	^{nat}**Ru**
Projectile	d	d	d	d	n	n	n	n
Ejectile	n	$3n$	$4n$	xn	γ	$3n$	$4n$	xn

The decay chain extends beyond ^{97}Ru, with very short-lived products ^{97}Rh and ^{97}Pd with half-lives of $30.7(6)$ m and $3.10(9)$ m, respectively [56]. The decay chain is shown in figure 3.2.

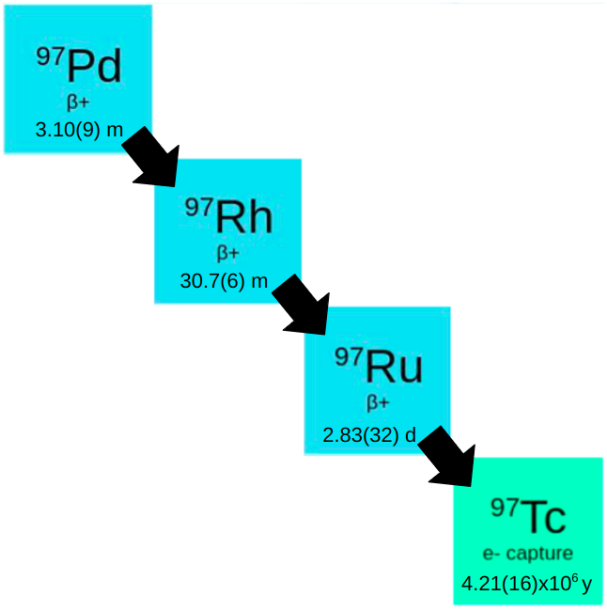


Figure 3.2: *Decay chain showing ^{97}Tc and all of the beta decay chain including ^{97}Ru, ^{97}Rh, and ^{97}Pd.*

The reactions for producing ^{97}Rh are given in table 3.3.

Table 3.3: *Possible reaction channels to produce ^{97}Rh generator.*

Target	^{96}**Ru**	^{98}**Ru**	^{99}**Ru**	^{100}**Ru**	^{nat}**Ru**	^{96}**Ru**	^{98}**Ru**	^{99}**Ru**	^{nat}**Ru**
Projectile	p	p	p	p	p	d	d	d	d
Ejectile	γ	$2n$	$3n$	$4n$	xn	n	$3n$	$4n$	xn

The reactions for the production of ^{97}Pd are given in table 3.4.

Table 3.4: *Possible reaction channels to produce ^{97}Pd generator.*

Target	^{96}**Ru**	^{96}**Ru**	^{98}**Ru**
Projecitle	α	^{3}He	^{3}He
Ejectile	$3n$	$2n$	$4n$

Due to the high number of possible reactions to produce ^{97}Ru as a generator, combined with the huge benefits to chemical separation provided by the generator, only generator reactions were considered going forwards, leaving a total of 24 reactions.

3.2 Products of Concern

As discussed in section 1.2, a tracer has several requirements. All of these requirements are used to determine a suitable tracer isotope. however, some of the requirements may also be used to determine an appropriate production route for the tracer. The tracer must not contain the analyte isotope, and the tracer must not contain isotopes with overlapping analytical characteristics.

This determines that any reaction should avoid the production of ^{99}Tc, however, using a ^{97}Ru generator, an initial chemical separation may be performed to remove any ^{99}Tc produced directly in the reaction — limiting the restriction on the irradiation. The main concern with generator production is the potential of other isotopes, which may eventually decay into ^{99}Tc or other unwanted technetium isotopes in a similar timeframe to the generator's decay, preventing chemical separation. For example, ^{99}Mo is of great concern as its half-life of $65.976(24)$ h [24] is very similar to the half-life of ^{97}Ru at $67.92(52)$ h [56]. An additional difficulty is the similar chemical properties of Ru and Mo, preventing the separation of the two elements.

Both ^{98}Tc and ^{100}Tc are of concern due to their proximity to ^{99}Tc, causing tailings in the mass spectrometry analysis. Both isotopes are shielded from both β^- decay of Mo and β^+ decay of Ru production by stable isotopes. Any of either Tc isotope produced directly in the reaction may be separated from the ruthenium by passing straight through a resin before collecting from the ruthenium in a subsequent step..

Other concerns would be the decay of ruthenium isotopes into technetium, preventing the collection of a pure generator. Several Ru isotopes are stable, including ^{96,98,99,100,101,102}Ru, which limits this problem greatly. The only isotopes of concern are ^{94}Ru and ^{95}Ru, however, with half-lives of $51.8(6)$ m and $1.634(13)$ h, these isotopes can be allowed to decay completely over a large number of half-lives before an initial separation of ruthenium from technetium is performed to isolate the generator from unwanted technetium. Optimising the reaction to limit the quantity of ^{94,95}Ru produced is still

desirable as this enables the separation to be performed sooner after the irradiation, retaining the highest possible quantity of ^{97}Tc decaying from the generator isotope.

3.3 Tc-97 Isomeric State Decay

In the branching ratio of the ^{97}Ru generator into ^{97}Tc, there is an excited state at 97 keV populated with a branching ratio of 0.0422%. This isomeric state has a half-life of 91.0(18) d and decays to the ground state with a branching ratio of 96.06% and the remaining 3.94% of the time the isomer decays to ^{97}Mo[56]. This is visualised in figure 3.3.

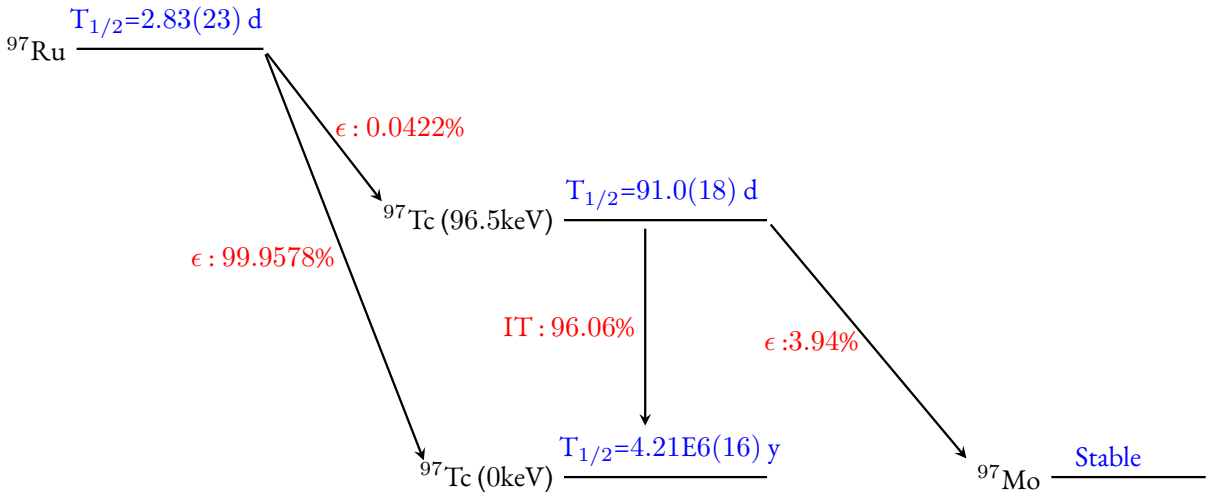


Figure 3.3: *Level scheme for the decay of ^{97}Ru, showing the branching of the isomeric state of ^{97}Tc into the ground state with a probability of 0.9606, with the remaining 0.0394 decaying via electron capture to ^{97}Mo. [56]*

The isomeric state of ^{97}Tc is not intrinsically of concern for mass measurements; however, the production of ^{97}Mo through the faster decay of the isomeric state is a challenge as this isotope is chemically different to the ^{97}Tc, and will be produced in greater quantities than expected through the half-life of ^{97}Tc, limiting the accuracy of the tracer. As the isomeric state is short-lived relative to the half-life of the ground state and within a reasonable working timescale, an additional separation could be performed between the Mo and Tc to remove any ^{97}Mo produced through the direct decay of the excited state of ^{97m}Tc. The isotopic and isomeric fractions over five years are displayed in figure 3.4 and 3.5 respectively.

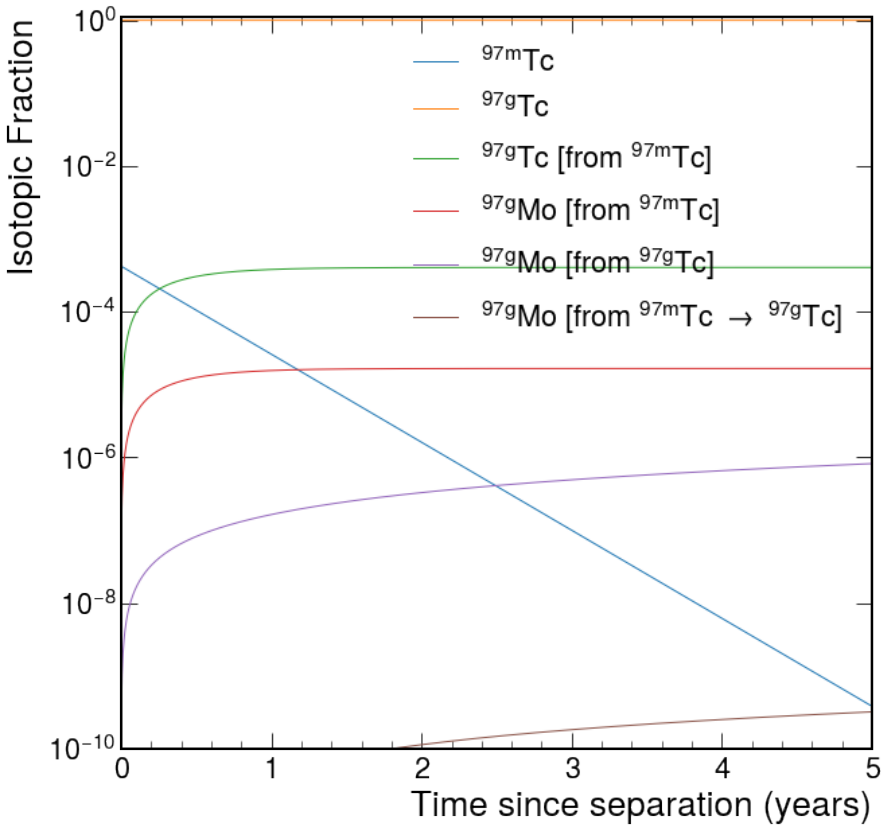


Figure 3.4: *Isotope fraction of ^{97}Tc and decay products of mass A=97 over a period of five years.*

It is clear from figure 3.4 that the fraction of ^{97}Tc in the isomeric state drops significantly, while there is no visible change in the ground state (near the top of the graph) over the same period of time.

A calculation was performed showing the ratio of ^{97}Tc to total ^{97}Mo and ^{97}Tc activities over time. This was performed with the additional separation occurring instantly, after one, two, three, and 1000 half-lives. This is visualised in figure 3.5. The quantitative results of the ratio are shown one year following the additional separation stage in table 3.5. As can be seen, the additional chemical separation has little impact on the overall isotopic purity.

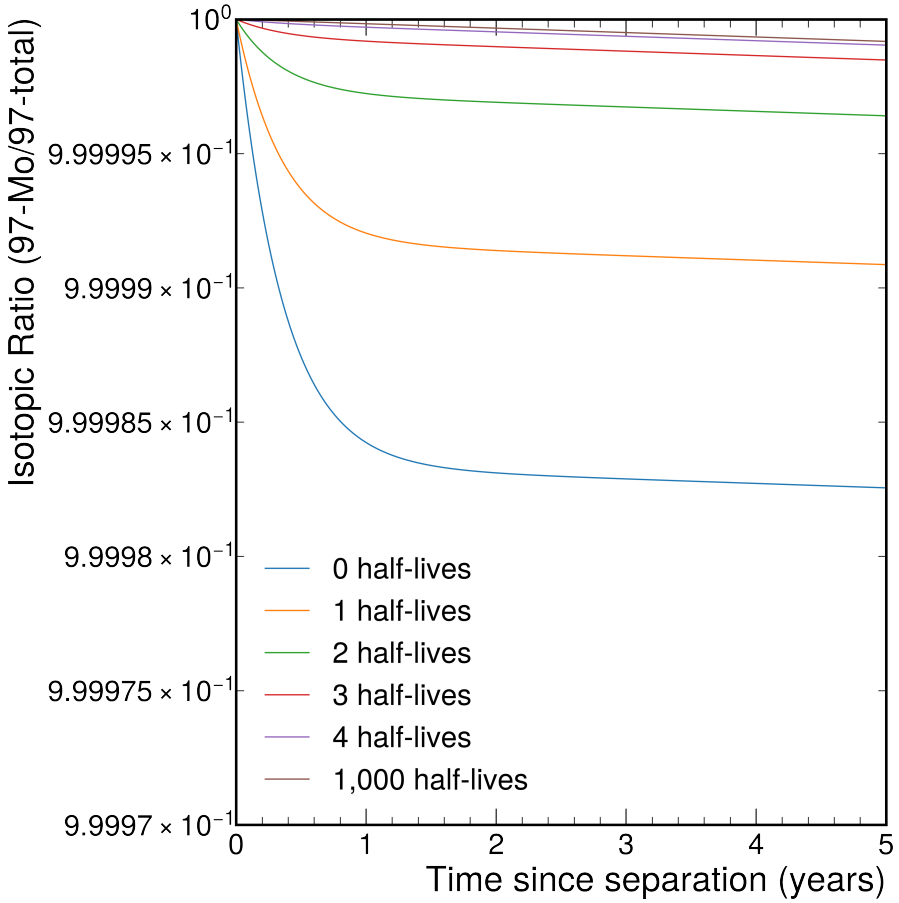


Figure 3.5: *Isomeric ratio of ^{97}Tc over total ^{97}Mo and ^{97}Tc over a period of five years.*

Table 3.5: *Atomic percentage of ^{97}Tc over the total atomic percentage of isotopes with mass A=97.*

Time (half-lives)	**0**	**1**	**2**	**3**	**4**	**1,000**
at% ^{97}**Tc/**$\sum_i(^{97}x_i)$	99.9983108	99.9991389	99.999691	99.9998981	99.9999533	99.9999671

3.4 Reaction Modelling

Nuclear Reaction calculations were performed to compare and determine the cross-section values using TALYS[84] and TASMAN[108], which are both described in section 2.6. These data were used to compare the relative merit of different reaction paths.

All reactions in this thesis were run using TALYS 1.96, run through TASMAN, running 1000 TALYS calculations for each reaction. The 'best' keyword was toggled to utilise improved nuclear parameteri-

sation for the reactions, along with `maxlevelsres=20` to increase the maximum number of energy levels calculated instead of the default value of 10.

While there are 27 possible reactions which could be considered, including all possible enriched isotopes, the natural abundance targets were first investigated as the target material is both cheaper and more easily sourced. Reactions using both molybdenum and ruthenium targets were considered; ^{nat}Mo-α, ^{nat}Mo-^{3}He, ^{nat}Ru-α, ^{nat}Ru-h, ^{nat}Ru-d, ^{nat}Ru-p and ^{nat}Ru-n. The main criteria is a high production cross-section of ^{97}Ru or an isotope which decays into ^{97}Ru (or ^{97}Rh, ^{97}Pd), as well as avoiding the production of ^{99}Mo.

3.5 Ruthenium Targets



Figure 3.6: *Isotopes of ruthenium near stability, showing A=95 to A=103, with the decay path for radioctive isotopes shown. [2].*

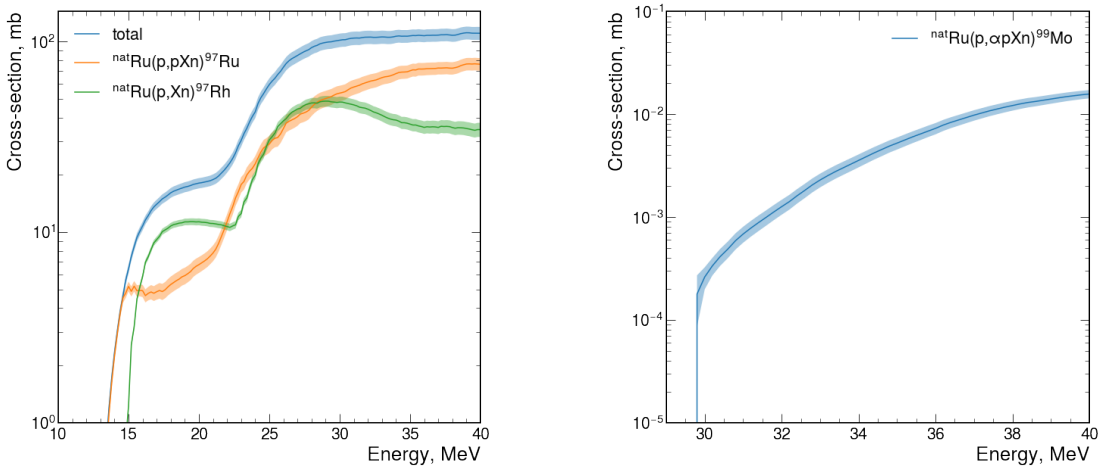
Ruthenium is a rare transition metal, being the 78^{th} most abundant element. The element naturally comprises seven stable isotopes shown in table 3.6. The high number of isotopes increases the difficulty in refining and optimising nuclear reactions, as even if one reaction mechanism were possible, seven discrete products would be produced. Ruthenium is chemically inert to most chemicals and has a high melting point of 2607 K, useful for long irradiations where thermal stability and resistance to oxidation is important.

Table 3.6: *Table showing the natural abundance of ruthenium isotopes, along with the error, extracted from NIST [104].*

	^{96}**Ru**	^{98}**Ru**	^{99}**Ru**	^{100}**Ru**	^{101}**Ru**	^{102}**Ru**	^{104}**Ru**
Abundance	0.0554(14)	0.0187(3)	0.1276(14)	0.1260(7)	0.1706(2)	0.3155(14)	0.1862(27)

3.5.1 Proton irradiation of ^{nat}Ru

Proton irradiation of ruthenium will produce ^{97}Ru, both directly through ^{nat}Ru(p,X)^{97}Ru reactions, as well as ^{97}Rh through ^{nat}Ru(p,X)^{97}Rh reactions which decay into ^{97}Ru The production cross-section of ^{97}Ru and ^{97}Rh are shown in figure 3.7 along with the production of ^{99}Mo through ^{nat}Ru(p,X)^{99}Mo reactions.



(a) *^{97}Ru production, including ^{97}Rh with 100% decay to ^{97}Ru.*

(b) *^{99}Mo production.*

Figure 3.7: *Production cross-sections for the Ru-p reaction.*

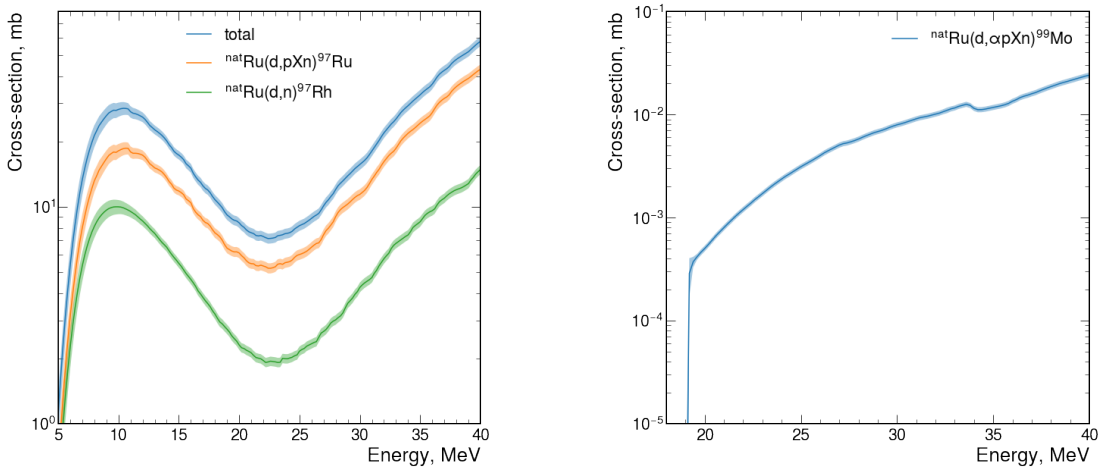
It may be seen that the ^{nat}Ru(p,pXn)^{97}Ru reaction has a lower threshold energy, produced from the ^{98}Ru(p,d)^{97}Ru reaction with a Q-value of -7.95 MeV. The production of ^{97}Ru is initiated at low energies by the ^{96}Ru(p,γ)^{97}Rh reaction with a positive Q-value of 3.81 MeV. This reaction channel peaks at 0.087 mb at 7.2 MeV. The higher mass isotopes of Ru contribute to the high production cross-section at higher energies.

The ^{99}Mo production reaction channel does not open until 29.8 MeV through the ^{104}Ru(p,αd)^{99}Mo pathway, with a Q-value of -10.4 MeV. The cross-section is not significant across the entire energy range up to 40 MeV, with a total maximum cross-section of 0.0164 mb at 40 MeV.

A full breakdown of the contributions to the cross-section to ^{97}Ru, ^{97}Rh and ^{99}Mo are in table C.1 in appendix C.

3.5.2 Deuteron irradiation of ^{nat}Ru

The production of ^{97}Ru through deuteron irradiation is facilitated through several neutron emissions for the production of ^{97}Rh and (d,pXn) and (d,dXn) reactions for the production of ^{97}Ru directly. The extra neutron in the deuteron greatly affects the reaction cross-sections for producing ^{97}Ru. The cross-section for production is shown for both the direct production of ^{97}Ru and ^{97}Rh, along with the production cross-section of ^{97}Mo.



(a) *^{97}Ru production, including ^{97}Rh with 100% decay to ^{97}Ru.*

(b) *^{99}Mo production.*

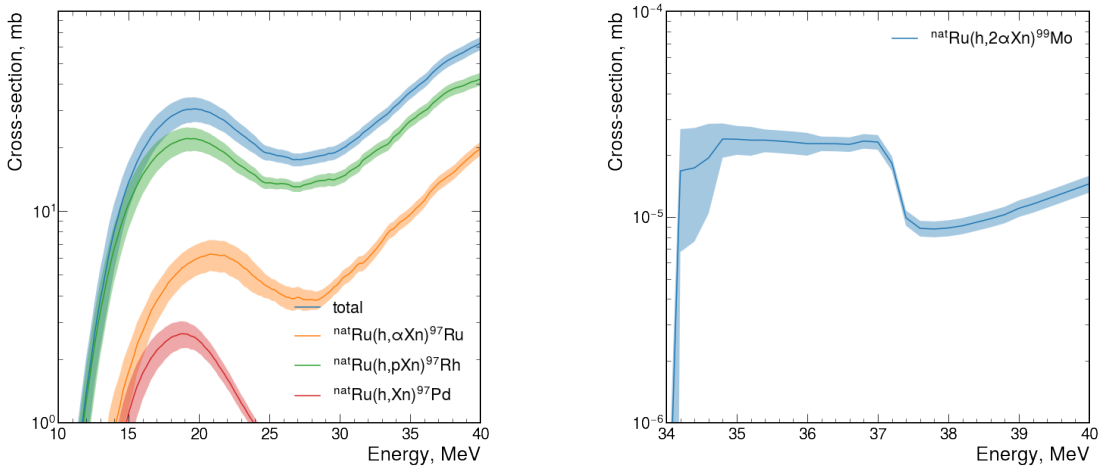
Figure 3.8: *Production cross-sections for the Ru-d reaction.*

The production of ^{97}Ru is dominated by the direct production of ^{97}Ru over the production of ^{97}Rh throughout the entire energy range. The energy-dependent trend is nearly identical for both isotopes, having a minimum threshold of around 2 MeV, however, the cross-section does not reach its low energy local-maxima until 9.8 MeV and 10.6 MeV for the ^{nat}Ru(d,X)^{97}Ru and ^{nat}Ru(d,xn)^{97}Rh respectively. The global maxima within the energy range up to 40 MeV are 63.0 mb and 2.0 mb for ^{97}Ru and ^{97}Rh respectively at 40 MeV.

The production of ^{99}Mo is low, with a maximum cross-section of 0.0263 mb at 40 MeV. The full production breakdown is shown in appendix C in table C.2.

3.5.3 Helium-3 irradiation of ^{nat}Ru

The helium-3 reaction will open extra reaction channels compared to the proton and deuteron reactions due to the extra proton in the projectile. Neutron emission mechanisms will produce an array of Pd isotopes. Palladium-97 decays into ^{97}Rh with a half-life of $3.10(9)$ m with ^{97}Rh decaying as shown in the previous reactions. The extra proton decreases the probability of producing ^{99}Mo as a compound nucleus as this would require the emission of four protons, which is suppressed in this energy range due to the Coulomb barrier and the neutron-to-proton ratio being greater than one. In high energy reactions, where four protons would be emitted, the mass lost through the emission prevents ^{99}Mo from being produced.



(a) ^{97}*Ru production, including* ^{97}*Rh with 100% decay to* ^{97}*Ru.*

(b) ^{99}*Mo production.*

Figure 3.9: *Production cross-sections for the Ru-*^{3}*He reaction, where h in the reaction denotes* ^{3}*He induced reactions.*

Throughout the entire energy range, the total residual production cross-section is predominated by the ^{97}Ru(^{3}He,pXn)^{97}Rh reactions with a minimum energy of 7 MeV, with a maximum cross-section (within the energy range) at 40 MeV, with a cross-section of 47.5 mb. The total residual production

cross-section at 40 MeV is 68.2 mb.

The cross-section for ^{97}Pd is very low, peaking at 2.64 mb at an energy of 18.8 MeV. When viewing the contributions from ^{97}Pd, as shown in figure 3.10, the high energies required for the (^{3}He,4n) and (^{3}He,5n) emission can be seen, which only begin to be populated at 40 MeV. The ^{98}Ru(^{3}He,4n)^{97}Pd reaction with a Q-value of −27.8 MeV does not begin to be populated until 29.6 MeV. The low abundance of ^{98}Ru at 0.0187(3) limits the magnitude of production, however, at 40 MeV the cross-section is 1.07 mb increasing with energy. The next reaction channel to open is ^{99}Ru(^{3}He,5n)^{97}Pd, with a Q-value of −35.2 MeV, and does not begin to be populated until 38.8 MeV.

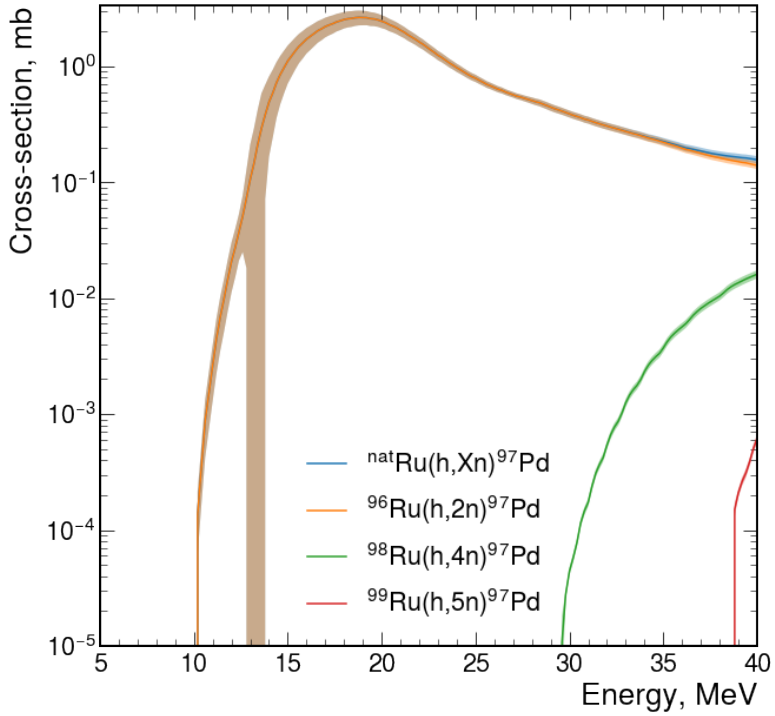


Figure 3.10: *Contributions to the production of ^{97}Pd from ^{nat}Ru(^{3}He,X) reactions. The natural reaction is nearly entirely dominated by the ^{96}Ru reaction, causing both the mean cross-section and the error margins to overlap over the entire energy range, diverting slightly above 35 MeV.*

Production of ^{99}Mo is only populated by the ^{104}Ru(^{3}He, 2α)^{99}Mo reaction. The emission of two alpha particles from any other natural abundance Ru isotope would reduce the atomic mass below 99. While the emission of four protons or a combination of protons and deuterons is possible and

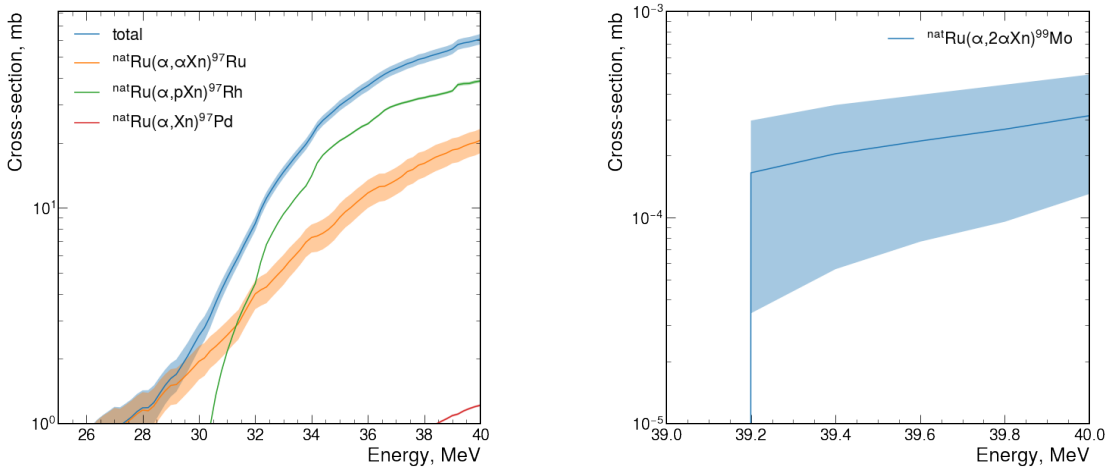
would enable higher mass ^{99}Mo isotopes to be produced, the probability of this is far too low due to the higher binding energy per nucleon of alpha particles.

The complete list of reaction contributions is in appendix C in table C.3.

3.5.4 Helium-4 irradiation of ^{nat}Ru

The production of ^{97}Ru through helium-4 irradiation of ^{nat}Ru is similar to the helium-3 reaction described in section 3.5.3, however, the addition of a second neutron in the projectile causes several differences. The cross-section increases gradually from 17.6 MeV for the production of ^{97}Ru. The ^{98}Ru(α, αn)^{97}Ru cross-section is the first reaction channel to open, with a Q-value of -10.2 MeV. The total direct production of ^{97}Ru, through the various isotopes of ruthenium ^{97}Ru(α,αXn)^{97}Ru increases gradually up to 40 MeV, where it has a value of 23.1 mb. The production of ^{97}Rh is populated through only one reaction within the energy range $0 - 40$ MeV ^{96}Ru(α, dn)^{97}Rh with a Q-value of -16.0 MeV and begins to be populated at 23.2 MeV. The cross-section increases to 39.57 mb at 40 MeV. The production of ^{97}Pd only occurs through a single reaction channel, ^{96}Ru(α, 3n)^{97}Pd with a Q-value of -30.1 MeV, increasing from 0 mb at 31.4 MeV to a value of 1.3 mb at 40 MeV. Due to the low neutron emission multiplicity, higher mass isotopes of Ru do not populate ^{97}Ru within the energy range. The total cross-section contributing to the production of ^{97}Ru directly or through decay increases gradually throughout the energy range, with its peak at 24.0 mb at 40 MeV.

The production of ^{99}Mo is also greatly affected by the extra neutron in the projectile. The reaction may only be fed by ^{104}Ru(α, 2α)^{97}Ru, with a Q-value of -12.6 MeV but does not begin to populate ^{99}Mo until 39.2 MeV. The cross-section of ^{97}Ru and its isobars as well as ^{99}Mo are given in figure 3.11



(a) ^{97}*Ru production, including* ^{97}*Rh and* ^{97}*Pd which both have 100% decay path to* ^{97}*Ru.*

(b) ^{99}*Mo production.*

Figure 3.11: *Plot of the residual production cross-sections for the Ru-α reaction, showing the production of* ^{97}*Ru and* ^{99}*Mo.*

A full breakdown of the residual production cross-sections for ^{97}Ru, its contributing isotopes (^{97}Rh and ^{97}Pd) as well as ^{99}Mo is given in table C.4 in appendix C.

3.6 Molybdenum targets



Figure 3.12: *Isotopes of molybdenum with stable isotopes in black [2].*

Molybdenum is a transition metal composed of seven stable isotopes with an even spread composition as shown in figure 3.12. The highest abundance isotope is ^{98}Mo at 24.39(37)%, with the full abundances shown in table 3.7. The high spread of isotopes increases the difficulty of avoiding the production of unwanted isotopes; however, molybdenum has several advantages. Having the 6^{th} highest melting point of any element at 2896 K, molybdenum targets are highly stable under high flux irradiations where temperatures can be significant. Weak oxidation of molybdenum does not occur until 600 K, not becoming significant until 900 K [109].

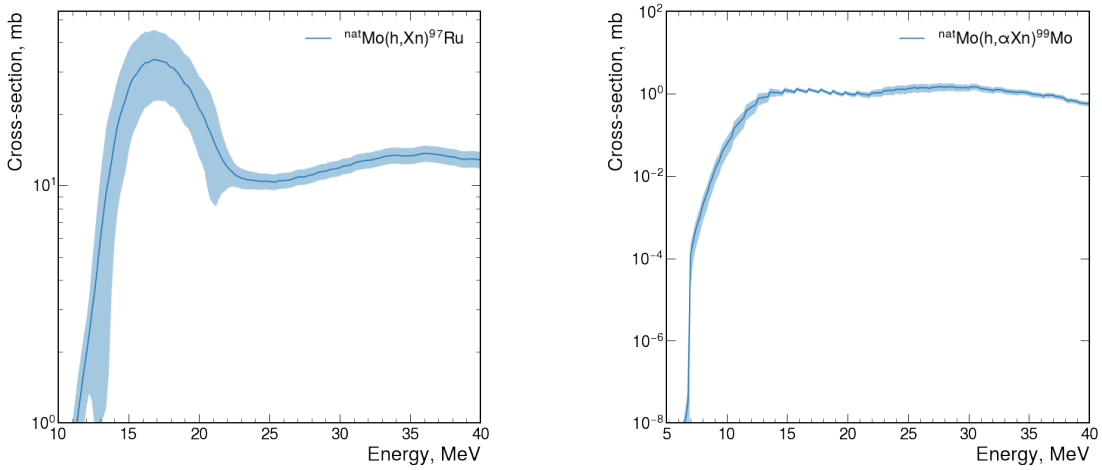
Table 3.7: *Natural abundance values of molybdenum isotopes, with errors, extracted from NIST [104].*

	^{92}**Mo**	^{94}**Mo**	^{95}**Mo**	^{96}**Mo**	^{97}**Mo**	^{98}**Mo**	^{100}**Mo**
Abundance	0.1453(30)	0.0915(9)	0.1584(11)	0.1667(15)	0.0960(14)	0.2439(37)	0.0982(31)

3.6.1 Helium-3 irradiation of ^{nat}Mo

The production of ^{97}Ru through the helium-3 bombardment of molybdenum is relatively simple, with the target-beam combination only being able to directly produce ^{97}Ru and not any higher Z products in the decay chain. Within the energy range $0 - 40$ MeV the maximum cross-section is 33.8 mb at 11.12 MeV. The lowest energy reaction ^{94}Mo(^{3}He,γ)^{97}Ru has a positive Q-value of 12.6 MeV. The highest contribution from a single reaction channel is ^{96}Mo(^{3}He,2n)^{97}Ru, which peaks at 23.1 mb at 16.2 MeV.

Due to the target element being molybdenum, there is a higher production probability of ^{99}Mo, with lower energy thresholds. The ^{nat}Mo(^{3}He,αXn)^{99}Mo reaction is predominantly populated by ^{100}Mo(^{3}He,α)^{99}Mo at lower energies, with a Q-value of 12.3 MeV being populated from 5.2 MeV, as shown in figure 3.13.



(a) *^{97}Ru production* ***(b)*** *^{99}Mo production*

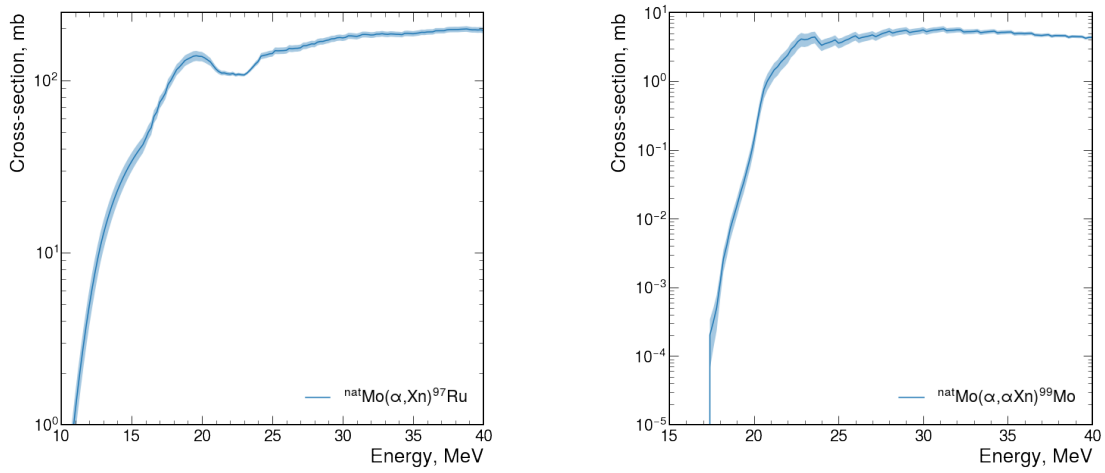
Figure 3.13: *Plot of the residual production cross-sections for the Mo-^{3}He reaction.*

A table of the full contributions is shown in appendix C in table C.5.

3.6.2 Helium-4 irradiation of ^{nat}Mo

The production of ^{97}Ru from the ^{4}He bombardment of ^{nat}Mo has a minimum energy of $8.4\,\mathrm{MeV}$. This is from the ^{94}Mo isotope with a reaction Q-value of $-7.94\,\mathrm{MeV}$. The highest contribution from a single isotope is ^{96}Mo peaking at $151.4\,\mathrm{mb}$ at $37.4\,\mathrm{MeV}$. Within the energy range $0-40\,\mathrm{MeV}$, the reaction peaks at $40\,\mathrm{MeV}$ with a total cross-section of $198.8\,\mathrm{mb}$.

The production of ^{99}Mo has a minimum threshold energy of $17.4\,\mathrm{MeV}$. The lowest energy component is populated from the transmutation of the ^{100}Mo isotope with a reaction Q-value of $-8.29\,\mathrm{MeV}$. The reaction cross-section increases gradually throughout the energy range of $0-40\,\mathrm{MeV}$ up to a maximum of $5.80\,\mathrm{mb}$ at $31.2\,\mathrm{MeV}$. The production of ^{97}Ru and ^{99}Mo can be seen in figure 3.14.



(a) ^{97}*Ru production* *(b)* ^{99}*Mo production*

Figure 3.14: *Plot of the residual production cross-sections for the production of* ^{97}*Ru and* ^{99}*Mo through the Mo-*α *reaction.*

A table containing the full contributions to the cross-section is given in appendix C in table C.6.

3.7 Reaction Comparison

The six reactions investigated have their merits, based on the magnitude of the production of both ^{97}Ru and ^{99}Mo, along with the energy thresholds for the reactions. This, along with the particle's range, enables a clear comparison between the different reactions. To decide on the optimum reaction for producing a high purity ^{97}Ru generator, avoiding the presence of ^{99}Mo, the reactions must be compared more directly. Due to the additional chemical benefits of a molybdenum target compared to a ruthenium target, the ruthenium and molybdenum reactions will first be compared separately, focusing solely on the nuclear reactions along with the stopping power of the various projectiles in the targets.

3.7.1 Stopping Power Comparison

For charged particles, stopping power is governed by the electromagnetic force and the particle's mass, affecting the energy lost in scattering events. This is described mathematically in the Bethe-Bloch equation in section 1.9.2. A projectile with a higher mass or charge will have a higher stopping power through a target. A target with a higher atomic number will also induce a higher stopping power in the target. As molybdenum and ruthenium are very close in mass and atomic number, the difference due to the different targets will be small. The significant differences will come from the projectiles being considered: proton, deuteron, helium-3 and helium-4. Figure 3.15 shows the range of different projectiles in the target.

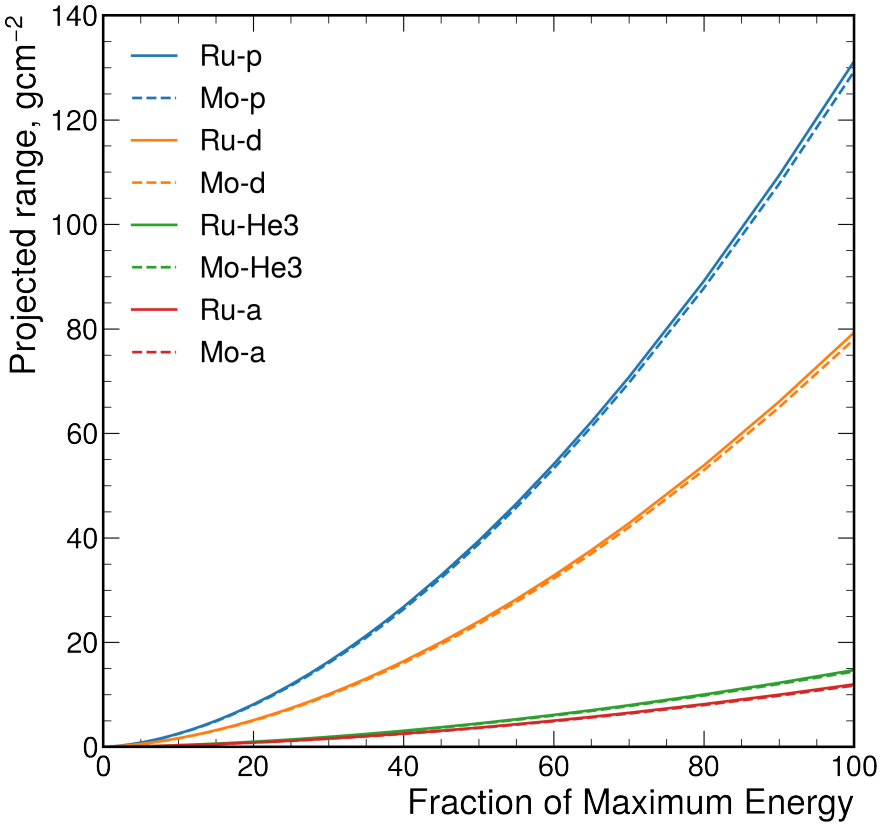


Figure 3.15: *Projected particle range of protons, deuterons, helium-3 and helium-4, through Ru and Mo targets.*

It can be seen that the proton has a significantly greater range than the deuteron, as the helium-3 does for helium-4, due to the difference in mass. The proton and deuteron have a much greater range than helium-3 and helium-4 due to the difference in charge. The projected range at 40 MeV is given in table 3.8. This is used as this is the maximum proton energy at the UoB MC40 cyclotron.

Table 3.8: *Projected particle range for different projectiles in Ru and Mo, in units of g.cm^{-2}.*

	Proton	**Deuteron**	**Helium-3**	**Helium-4**
Ru	26.78	16.38	3.08	2.55
Mo	26.33	16.06	3.01	2.49

As previously mentioned, the maximum projectile energy is based on the charge and mass of the projectile. At the University of Birmingham MC40 cyclotron, protons and alpha particles may be accelerated to 40 MeV, deuterons to 20 MeV and helium-3 to 53.3 MeV. For this reason, it may be

convenient to understand the range of the particle as a fraction of its maximum energy. Table 3.9 gives the range at the maximum energy of the various projectiles.

Table 3.9: *Projectile range for p, d, ^{3}He and α in Ru and Mo at their maximum energy in a K=40 cyclotron, in units of g.cm^{-2}.*

	Proton	**Deuteron**	**Helium-3**	**Helium-4**
Ru	26.78	5.11	5.01	2.55
Mo	26.33	5.0	4.9	2.49

A greater range is desirable, as the particles penetrate a greater depth and therefore per unit cross-section a particle beam of a given energy would cause a higher activity irradiation. This gives a great preference for proton reactions compared to deuteron and helium-3 reactions and a disadvantage to helium-4 reactions.

To quantitatively compare the reactions, the stopping power and cross-section component of the yield equation described in section 1.9.2, in equation 1.16 can be used to show the magnitude of the produced yield. The energy bounds on the equation will be from 0 MeV up to 3 MeV below the threshold energy of ^{99}Mo production for each reaction. By keeping 3 MeV below the threshold energy, this limits production of ^{99}Mo from particles at the high energy end of the distribution. The yield, Y, can be written mathematically as

$$Y \propto \int_0^{E_i} \frac{\sigma(E)}{\frac{dE}{dx}} dE, \tag{3.1}$$

where E_i is 3 MeV below the threshold energy of ^{99}Mo production, $\sigma(E)$ is the energy dependent cross-section and $\frac{dE}{dx}$ is the stopping power of the projectile through the target.

3.7.2 Ruthenium Target Reaction Comparison

The production of ^{97}Ru from the ^{nat}Ru target reactions is shown in figure 3.16, showing only the total production, which is a sum of the contributing cross-sections,

$$\sigma(^{97}Ru_{tot}) = \sum \left[\sigma(^{97}Ru) + \sigma(^{97}Rh) + \sigma(^{97}Pd)\right].$$

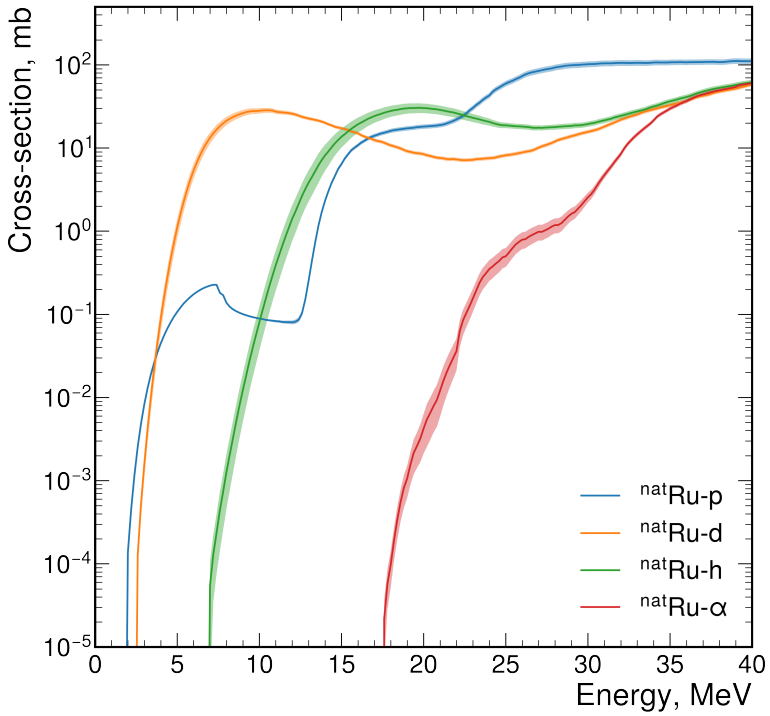


Figure 3.16: *Comparison of ^{97}Ru production for Ru target reactions.*

The maximum cross-section for each of the target-beam combinations is comparable, being 111.34(88) mb for protons, 63.04(32) mb for deuterons, 68.37(48) mb for ^{3}He and 63.98(361) mb for alphas. The threshold energy, however, differs greatly for the different reactions. Table 3.10 shows the Q-values, threshold energy and the first reaction channel to open for each of the four target-beam combinations.

Table 3.10: *Threshold energies for the various ruthenium target reactions.*

	Proton	**Deuteron**	**Helium-3**	**Helium-4**
Q-value, MeV	$+3.81$	$+5.89$	$+10.4$	-10.18
E_{min}, MeV	2.0	2.6	7.6	17.4
Target	^{98}Mo	^{96}Mo	^{98}Ru	^{98}Ru
Reaction	(p, d)	(d, p)	$(^{3}\mathrm{He},\alpha)$	$(\alpha,\mathrm{n}\alpha)$

The production threshold energies of ^{97}Ru, ^{97}Rh or ^{97}Pd are themselves not of absolute importance, provided that this threshold is below the maximum energy the particle can be accelerated to (which is true for all target-beam combinations) and that the ^{99}Mo production threshold energy is above that of the ^{97}Ru.

The production of ^{99}Mo from the four ^{nat}Ru target reactions is shown in figure 3.17.

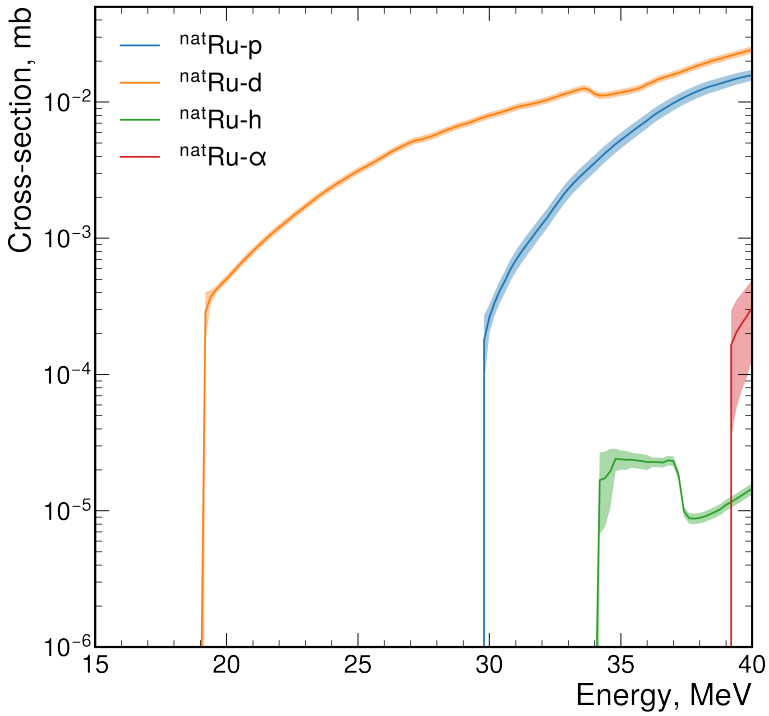


Figure 3.17: *Comparison of ^{99}Mo production for Ru target reactions*

As no ^{99}Mo production is tolerable, the beam energy must be run below the production energy threshold. The magnitude of ^{99}Mo population is therefore not important, only the threshold energy. Table 3.11 shows the Q-value, energy threshold, target isotope and reaction path for the lowest energy reaction for each target-beam combination.

Table 3.11: *Threshold for ^{99}Mo reactions with Ru targets.*

	Proton	**Deuteron**	**Helium-3**	**Helium-4**
Q-value, MeV	-10.4	$+0.29$	$+8.0$	-12.62
E_{min}, MeV	29.8	19.2	34.6	39.2
Target	^{101}Mo	^{100}Ru	^{104}Ru	^{104}Ru
Reaction	$(p, np\alpha)$	$(d, p\alpha)$	$(^3\text{He},2\alpha)$	$(\alpha,2\alpha n)$

All possible beam-target combinations have a ^{99}Mo production energy threshold higher than the energy threshold for ^{97}Ru production. To determine the optimum Ru target reaction, equation 3.1 is used to

determine the reaction rates, shown in table 3.12 for the four possible reactions. The maximum energy used for each calculation is 3 MeV below the ^{99}Mo threshold, which is 26.8 MeV, 16.2 MeV, 31.6 MeV and 36.2 MeV for the proton, deuteron, helium-3 and alpha, reactions respectively.

Table 3.12: *^{97}Ru scaled production reaction rate for each of the ruthenium reactions from 0 MeV to 3 MeV below the ^{99}Mo threshold energy. The production rate was calculated using the proportionality in equation 3.1.*

	Proton	**Deuteron**	**Helium-3**	**Helium-4**
$\mathbf{R}_{rate}$	26.35(190)	6.14(44)	3.32(40)	0.99(7)

It is clear from these calculations that the ^{nat}Ru-p is the optimum reaction with the ability to produce high quantities of ^{97}Ru without producing any ^{99}Mo.

3.7.3 Molybdenum Target Reaction Comparison

The two molybdenum reactions both show a significant residual production cross-section for ^{97}Ru. Figure 3.18 shows the ^{97}Ru production cross-sections overlaid.

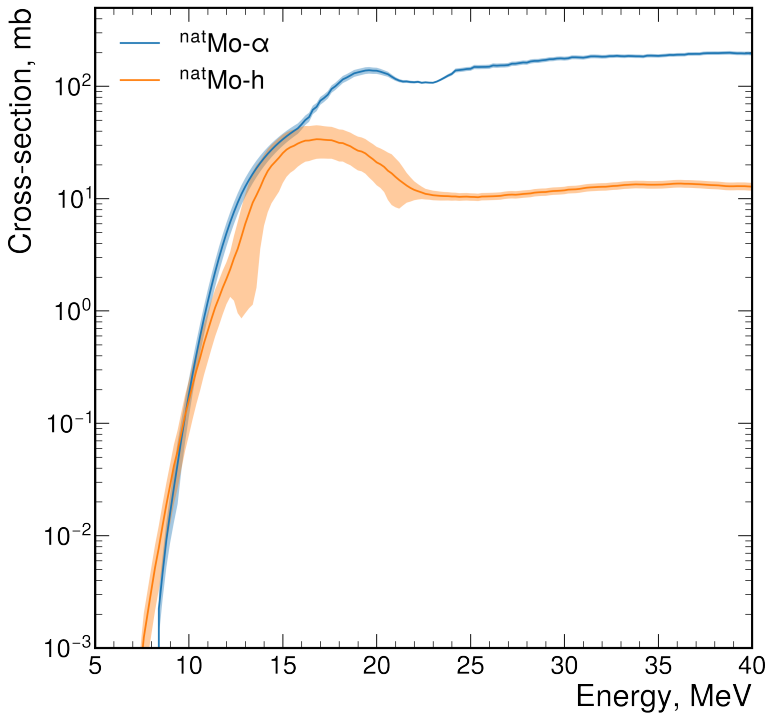


Figure 3.18: *Comparison of ^{97}Ru production for molybdenum target reactions.*

The reaction cross-sections are comparable over the energy range 0-40 MeV, however, the helium-3 reaction has a maximum energy of 53 MeV, which may favour the reaction, due to the increased target penetration compared to α particles, and higher energy reaction channels opening compared to all other available ion beams.

To determine the upper energy the reaction could be run at, it is first important to understand the threshold energy for the production of ^{99}Mo which the reaction must be run below. The cross-section for ^{99}Mo production is given in figure 3.19.

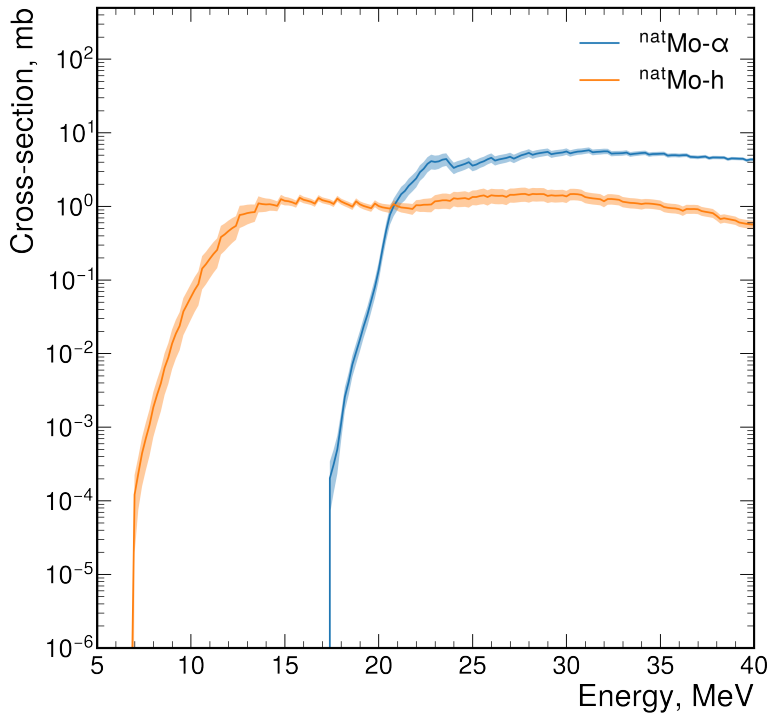


Figure 3.19: *Comparison of ^{99}Mo production for molybdenum target reactions.*

For the Mo-^{3}He reaction, ^{99}Mo is populated by ^{100}Mo(^{3}He,α)^{99}Mo at low energies. This reaction has a positive Q-value of 12.3 MeV meaning there is no threshold energy for this reaction. This may also be said for the production of ^{97}Ru which at low energies is populated by ^{94}Mo(^{3}He,γ)^{97}Ru with a Q-value of 12.6 MeV. It is therefore impossible to produce ^{97}Ru without ^{99}Mo using a ^{nat}Mo target and this reaction is not suitable.

The lowest energy contribution to the production of ^{97}Ru in the Mo-α reaction is ^{94}Mo(α,n)^{97}Ru with a Q-value of -7.94 MeV and a threshold energy of 8.4 MeV. In comparison to the production of ^{99}Mo which at low energies is populated by ^{100}Mo(α,αn)^{99}Mo with a Q-value of -8.29 MeV and has a threshold of 17.2 MeV. Taking the reaction rate from equation 3.1, the scaled yield of ^{97}Ru is $0.26(4)$.

3.7.4 Cross-Section Summary

The ^{nat}Ru-p reaction shows clear advantages over the other ruthenium reactions due to a combination of a low threshold energy for ^{97}Ru production, a high magnitude cross-section, and high threshold energy for ^{99}Mo. Molybdenum-α is the only molybdenum target reaction that produces ^{97}Ru without the production of ^{99}Mo, making it the obvious optimum reaction out of the Mo target reactions. When comparing ^{nat}Ru-p and ^{nat}Mo-α, the reaction rate for ^{nat}Ru-p is much higher than that for ^{nat}Mo-α, however, the use of a molybdenum target has distinct advantages in the chemical purification step, as discussed in detail in chapter 5. Both reactions are investigated in great detail throughout the coming sections of this thesis to determine the optimum route.

For both reactions, transmutation calculations are performed using the $\frac{dE}{dx}$ FISPACT-II program to calculate the production of all isotopes throughout an irradiation and subsequent cooling period. Additionally to this, in chapter 4 a high precision reaction cross-section measurement for Mo-α is performed, with results given. A greater understanding of the cross-section will give an increased understanding of the feasibility of the reaction and enable the beam energy to be tuned to give the maximum possible activity of ^{97}Ru without producing ^{99}Mo.

3.8 FISPACT-II Calculations

FISPACT-II was run for the Mo-α and Ru-p reactions, determining both the activity and the number of atoms of ^{99}Mo and ^{97}Ru, along with the production of ^{95}Ru and ^{94}Ru with half-lives of $1.643(13)$ h and $51.8(6)$ m respectively. These isotopes have half-lives much shorter than the generator isotope

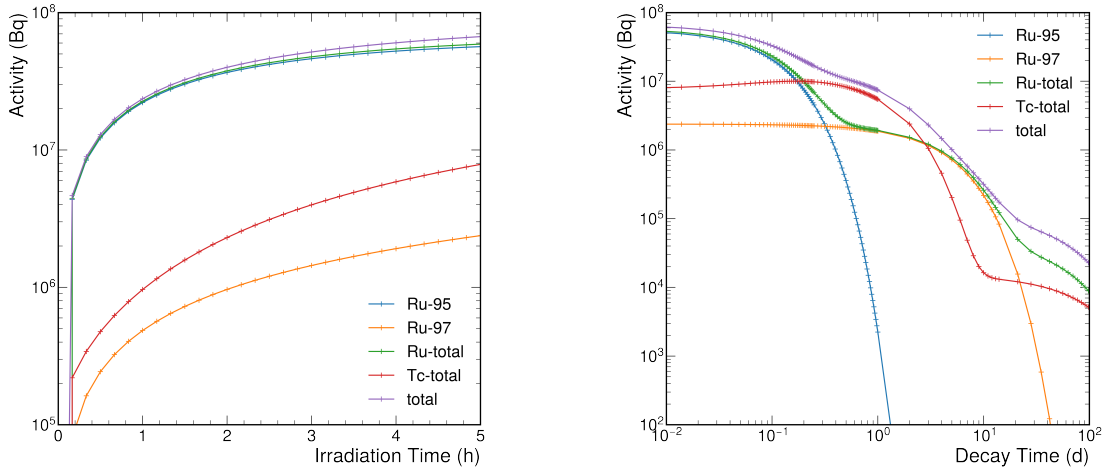
^{97}Ru, however, they must be fully depleted before the initial chemical purification of ^{97}Ru is completed, requiring an accurate understanding of their inventory evolution over time. The separation time should be optimised to avoid the presence of ^{95}Ru and ^{94}Ru, which decay into ^{95}Tc and ^{94}Tc, respectively, while maintaining the highest possible quantity of ^{97}Ru.

All calculations are performed using FISPACT-II with the additional $\frac{dE}{dx}$ extension developed during this project, as described in section 2.7.1.

3.8.1 Mo-α transmutation calculations

When modelling the Mo-α reaction, a number of assumptions were made: that the irradiation would be performed at the University of Birmingham cyclotron with a ^{4}He beam and that the reaction will be performed within one day, which assumes 6 hours of running. The cyclotron was assumed to have a maximum beam current of $5\ \mu$A. While the cyclotron could go higher, theoretically up to a maximum of $20\ \mu$A, this would require the ion source to be driven hard, potentially causing damage to the ion source. Some of the current would also be lost in steering and collimation, meaning this theoretical limit is unlikely achievable. A 6 h run at $5\ \mu$A gives a total irradiation of $30\ \mu$Ah.

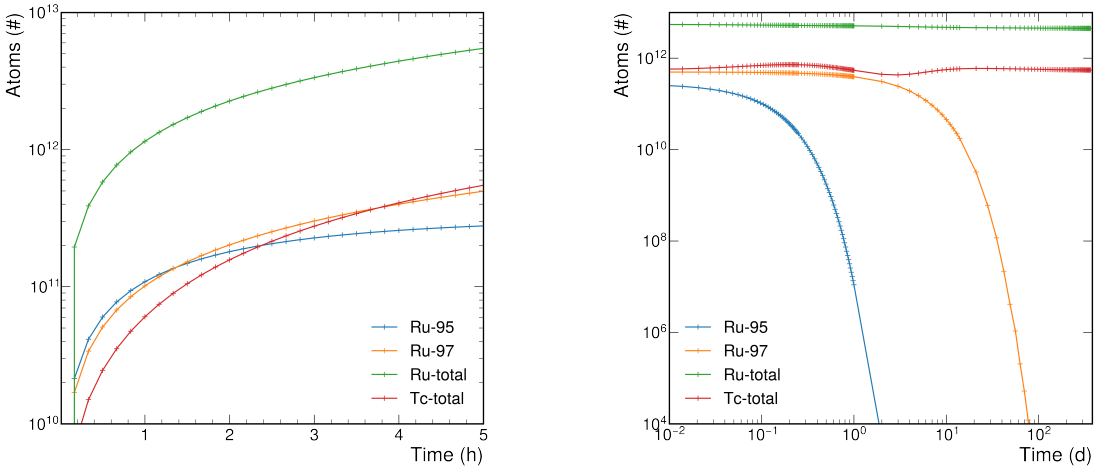
The main limiting factor of this reaction route is the production of ^{99}Mo limiting the beam energy to 15 MeV. There are no low energies that must be avoided (due to undesirable isotopes with low energy threshold reactions), so it is assumed for all calculations that the beam can be fully degraded within the target. Figure 3.20 gives the activity of isotopes through the irradiation and decay for the isotopes of interest.



(a) *Irradiatiation* ***(b)*** *Decay*

Figure 3.20: *Activity throughout the irradiation and during subsequent decay of Mo-α.*

As mass spectrometry is of interest in the analysis, it is important to not only understand the activity of the isotopes but the number of atoms present in the sample. The number of atoms of all of the isotopes of interest produced is shown in figure 3.21.



(a) *Irradiation* ***(b)*** *Decay*

Figure 3.21: *Number of production atoms throughout the irradiation and during subsequent decay of Mo-α.*

Table 3.13 gives the activity values and the number of atoms at the end of irradiation, τ_0, and the time at which ^{95}Tc has < 1 atom in the sample, τ_{95}, which is t_0+3 days. ^{94}Tc is not present in either the

plots or the data tables as no reaction channels that produce ^{94}Tc are open at 15 MeV.

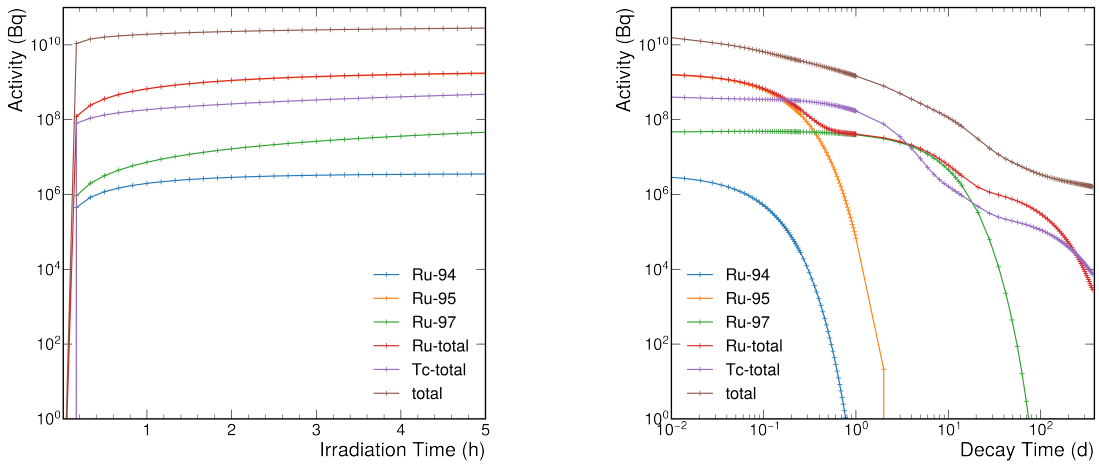
Table 3.13: *Production quantities for Mo-α initially following irradiation and after all ^{95}Ru has decayed*

		^{95}**Ru**	^{97}**Ru**	^{total}**Ru**	^{total}**Tc**	**total**
Activity (Bq)	τ_0	$3.25e+07$	$1.37e+06$	$3.39e+07$	$4.38e+06$	$3.84e+07$
	τ_{95}	0	$6.73e+05$	$7.12e+05$	$6.08e+05$	$1.36e+06$
Atoms (#)	τ_0	$2.78e+11$	$4.97e+11$	$5.47e+12$	$5.49e+11$	$3.08e+20$
	τ_{95}	0	$2.43e+11$	$4.93e+12$	$4.29e+11$	$3.08e+20$

3.8.2 Ru-p transmutation calculations

As with the Mo-α reaction, the reaction is assumed to be performed on a single day, giving an equal 6 h run. The proton beam current can be much higher than the ^{4}He current with a realistic beam-current of 20μA. This gives a total irradiation of 120μA.

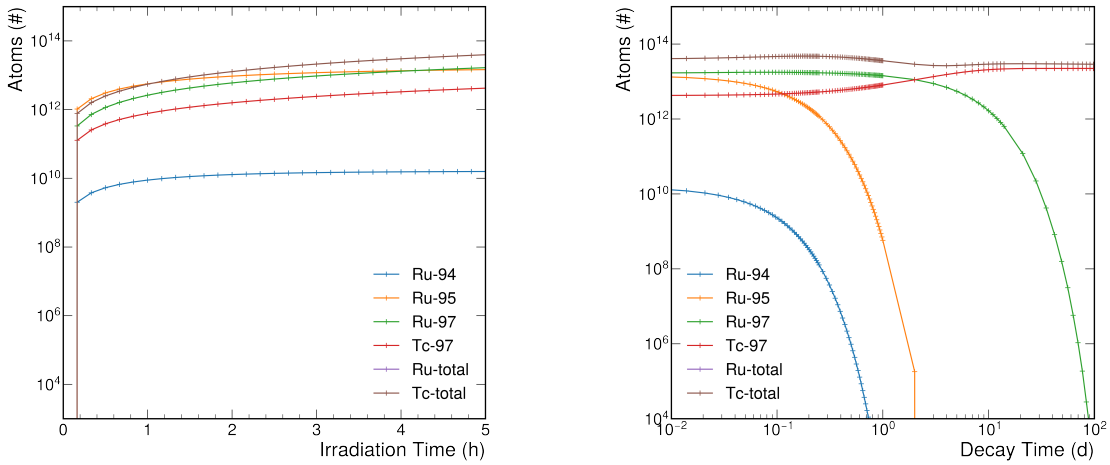
This reaction can run at a maximum energy of 26.8 MeV and the proton beam can be fully stopped within the target. Figure 3.22 shows the activity of the isotopes of interest throughout the irradiation and subsequent decay.



(a) *Irradiation* ***(b)*** *Decay*

Figure 3.22: *Activity throughout the irradiation and during subsequent decay of Ru-p.*

The number of atoms present for the isotopes and elements of interest is given in figure 3.23.



(a) Irradiation *(b) Decay*

Figure 3.23: *Number of atoms throughout the irradiation and during subsequent decay of Ru-p.*

Table 3.14 gives the activity and number of atoms present in the target both during and after the total number of atoms of ^{95}Ru and ^{94}Ru have decayed. As seen from the plots, the ^{95}Tc dictates this time due to its higher production and longer half-life. This time, $\tau_{94,95}$ is 3 days from the initial irradiation.

Table 3.14: *Production quantities for Ru-p initially following irradiation and after all ^{95}Ru has decayed*

		^{94}**Ru**	^{95}**Ru**	^{97}**Ru**	^{total}**Ru**	^{total}**Tc**	**total**
Activity (Bq)	τ_0	3.51E+06	1.71E+09	4.59E+07	1.76E+09	4.77E+08	2.80E+10
	τ_{95}	0	0	2.44E+07	2.61E+07	3.51E+07	5.03E+08
Atoms (#)	τ_0	1.58E+10	1.46E+13	1.66E+13	5.54E+21	3.95E+13	5.54E+21
	τ_{95}	0	0	8.83E+12	5.54E+21	2.66E+13	5.54E+21

3.9 Reaction Optimisation Conclusion

The transmutation calculations have extended the conclusion drawn from the cross-section calculations. Both reactions show high potential for producing a high purity ^{97}Tc radiotracer. The advantage of ^{nat}Ru-p compared to ^{nat}Mo-α is that the former has a higher threshold energy for ^{99}Mo production, leading to much high production activities and atom yields of ^{97}Ru. The time following irradiation when the separation can occur differs slightly for the two reactions, 2.9 d and 3.0 d for Mo and Ru targets, respectively. The activity of ^{97}Ru at this time is 24.4 MBq and 712 kBq for the Ru and Mo reactions, respectively, giving a yield of 339× for the Ru reaction. This is a huge advantage for the

^{nat}Ru-p reaction route.

The benefit of the ^{nat}Mo-α reaction is the lack of long-lived isotopes produced. The total activity of the irradiation sample 1 year after irradiation is 1.62 MBq and 19 kBq for the Ru-p and Mo-α reactions, both of which are dominated by ^{97}Tc.

Another consideration of reaction optimisation is chemical separation. As will be discussed later in the thesis in chapter 5, high quantities of the target material can swamp the chemical separation process, preventing the Tc from being able to bind to the separation matrix and be separated from the target. One of the advantages of the use of Mo with TK202 (the extraction chromatography resin used in this work), is that separation efficiency in the column increases with the quantity of Mo present, due to Mo creating binding sites on the resin. Again making both reactions possible at this stage and motivating a further investigation into the Mo-α cross-section to more precisely and accurately understand the probability of the reaction, especially the production of ^{99}Mo and to gain a clearer understanding of the separation of ^{97}Mo.

4

Experimental Mo-α Cross-Section Measurement

4.1 Introduction

This section details the development of a high-precision cross-section method at the University of Birmingham MC40 cyclotron [77], jointly achieved alongside a complementary project measuring Eu-α cross-sections for terbium medical isotope production by R. Trinder [110]. In this project, measurements were performed to elucidate the cross-section for the bombardment of a molybdenum target with an α beam with energies up to 40 MeV. These measurements were used to optimise the production of a technetium-97 tracer through a ruthenium-97 generator, as explained in previous chapters. In the literature, molybdenum-α cross-section measurements have previously been investigated by different groups [111, 112, 113], however, it was seen as valuable research to perform cross-section measurements due to the high variation found in these studies. This experiment is designed to enable greater precision in energy for each cross-section measurement than previous measurements, using thinner 1 μm

foils. The most precise previous measurement used foils of 10 μm, which results in higher levels of energy degradation through the target. Additionally to the specific cross-section being measured, the development of this method acts as a platform and pathway for future tracer development work at the University of Birmingham. A high-precision cross-section measurement enables a better understanding of the reaction rates directly, and the parameterisation of the nuclear reaction models. This allows an accurate understanding of the number of nuclei and activity of each product produced and the energy threshold of production. This enables the production of the isotope of interest (^{97}Ru) to be optimised while avoiding particular reaction channels which result in difficult-to-separate isotopes. For the production of ^{97}Tc through ^{nat}Mo-α reactions the production of ^{99}Mo must be avoided.

The University of Birmingham cyclotron is a Scanditronix MC40 cyclotron as explained in section 1.9.3, offering ^{4}He (α) beams accelerated up to an energy of 40 MeV. A stacked foil approach will be used whereby thin 1 μm Mo foils will be stacked within the beam line. As the incident α-particle's energy degrades through the foils, for a given initial beam energy, a number of cross-section measurements can be taken over a spread of energies, as the beam energy degrades through each successive target. The experiment was split into two individual irradiations, a higher-energy irradiation (39 MeV) and a lower-energy irradiation (29 MeV). By breaking the irradiations into two, the error on the energy through the later targets is reduced as beam energy smears as it passes through matter, degrading the precision of thick target foil stacks.

The experiment can be broken down into two discrete measurements: the calculation of the energy throughout the thickness of each target foil and the calculation of the measured cross-section within each target foil. The energy measurements were performed on an existing nuclear physics beam-line (4). The molybdenum foils were then irradiated on beam-line $4a$, a beam-line recommissioned and further developed for this project, to enable higher precision cross-section measurements, through improved beam current measurements. A schematic of the cyclotron with beam-line 4 and $4a$ labelled, is shown in figure 4.1.

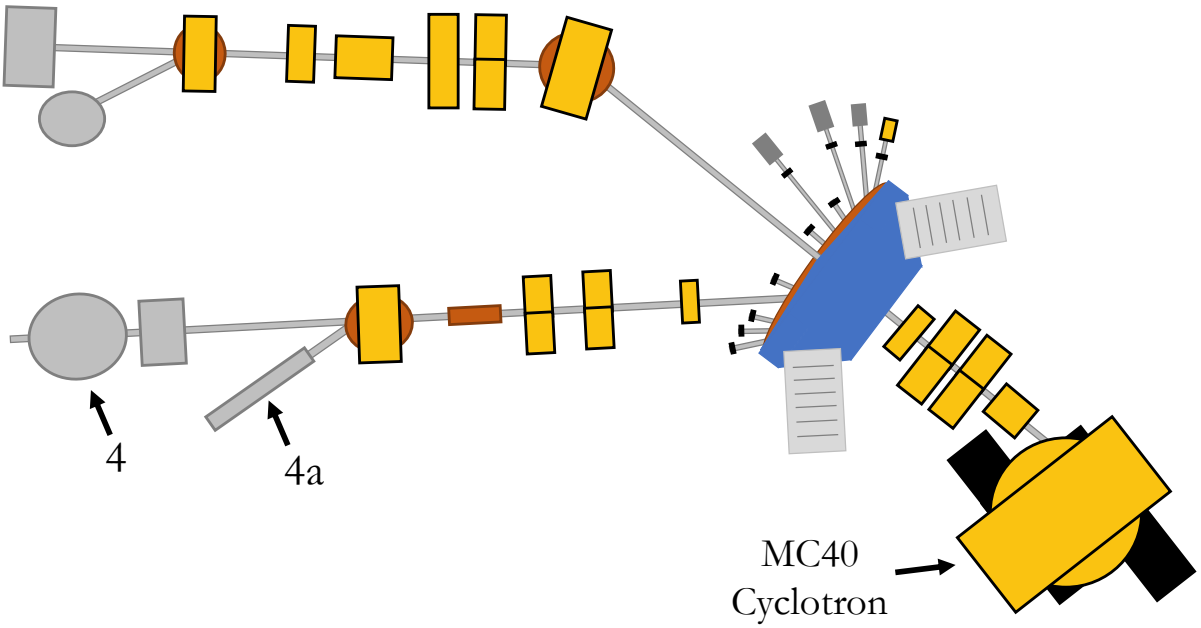


Figure 4.1: *A schematic aerial view of the University of Birmingham MC40 cyclotron, with beam-lines* 4 *and* 4a *used in this experiment highlighted.*

Cross-section is a derived quantity, and several parameters must be determined as given by

$$\sigma_i = \frac{A_i}{N_T \cdot [\Phi(1 - e^{-\lambda\tau_i}) \cdot e^{-\lambda\tau_c}]}. \tag{4.1}$$

The cross-section of a given isotope, i, is given as σ_i, A_i is the activity of the isotope, N_T is the number of target nuclei, Φ is the beam flux, λ is the decay constant and τ_i and τ_c are the irradiation and cooling time respectively. The determination of these parameters is described in detail in the proceeding sections of this chapter. Eight molybdenum foils were irradiated at a range of energies, with the experiment split into two separate irradiations, performed over two days, with four foils irradiated in each irradiation.

The initial stage involved analysing the energy of the α particle beam through high-precision scattering measurements, coupled with experimental foil thickness measurements, to perform calculations of how the energy of the beam will degrade through each target foil, using SRIM [76]. The cross-section was then analysed by calculating using the measured number of particles which passed through the foil and the number of nuclei produced using gamma-ray spectroscopy decay counting with HPGe

detectors.

4.2 Foil Thickness Measurement

The energy of an α particle degrades as it passes through a target. To calculate the energy spread of the α beam throughout the thickness of a foil, the foil thickness must be known with high precision. This enables the energy loss to be calculated using SRIM [76] stopping-power calculations. The method and results for the foil thickness measurement are described in this section, using the stopping power of α particles from a ^{239}Pu, ^{241}Am and ^{244}Cm triple-α source, with well characterised energies. The energy spread throughout the target can be translated to a foil thickness, using SRIM [76].

4.2.1 Experimental set-up

The foil thickness measurement was performed in the nuclear physics vacuum chamber on beam-line four of the University of Birmingham cyclotron, using a double-sided silicon strip detector (DSSD). The detector contains 16 silicon semi-conductor strips orientated vertically on the front and 16 strips orientated horizontally on the back of the detector. This leads to a positional array of 256 pseudo-pixels when a particle stops in the detector, with the energy signal being read twice; once from the front face and once from the back face. An image of a DSSD detector is shown in figure 4.2.

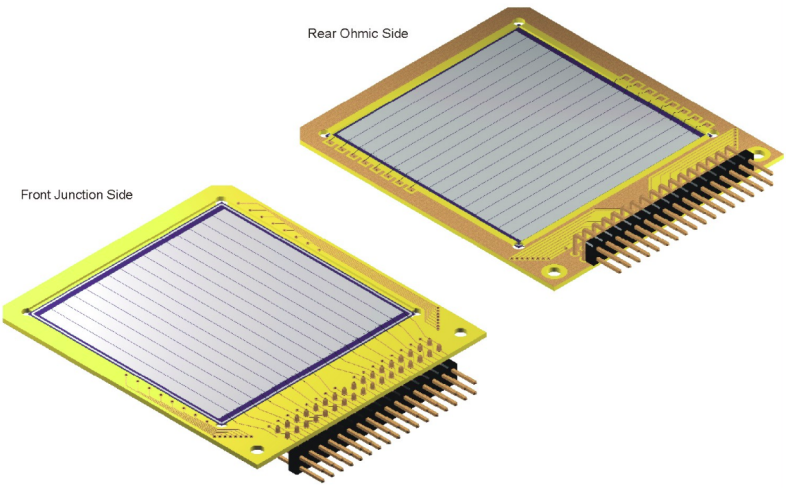


Figure 4.2: *A render of a DSSD detector highlighting the front vertical strips and rear horizontal strips of the detector. The 32 individual wires are seen, connecting to a 32-pin connector (including 2 ground pins) which can be connected to a pre-amplifier for signal processing [114].*

A triple-α source is placed into a collimator, custom-built and 3D printed in poly-lactic acid (PLA)

plastic for this project, placed perpendicular to the detector face. This enabled the isotropic α-source to be converted to a directional beam of three mono-energetic α particles. The CAD model is shown in figure 4.3.



Figure 4.3: *A render of the 3D printed collimator.*

The collimator is positioned to enable the directional beam of α particles to intersect a central detector channel perpendicular to the face of the detector. A slot was designed in the collimator to enable foils to be optionally inserted between the α-source and the detector. This enables the α particle energy to be measured, both with and without the foil present, enabling the energy difference due to the foil to be calculated. The detector was set up in a conventional coincidence circuit, enabling position to be determined on the detection of an alpha particle. The electronic set-up of the detector is shown in figure 4.4, with the single DSSD detector connected in series with a pre-amplifier and amplifier, ADC (analogue-to-digital converter), and VME (Versa Module Europa) control unit. The VME was connected to a computer via ethernet, where data acquisition was performed using MIDAS (a Multi-Instance Detector Acquisition System) [115]. An LED (leading-edge discriminator) was connected to the amplifier in series with a logic FiFo (Fan-In Fan-Out), gate and delay generator and trigger to produce a coincidence between the front and rear detector channels.

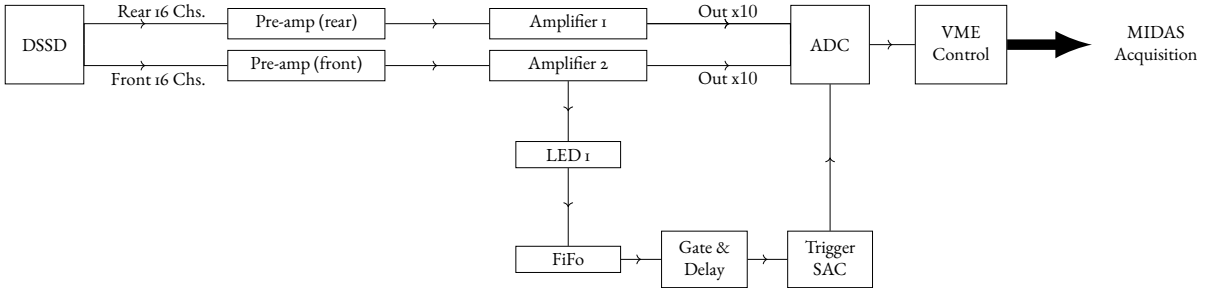


Figure 4.4: *Electronic set-up for the foil thickness measurement, showing a single DSSD detector connected to two pre-amplifiers, one for each of the front and rear channels, connected in series to an amplifier, ADC, VME and a computer with MIDAS software installed. The front detector channels were connected to the ADC additionally via an LED, FIFO, gate and delay, and trigger SAC all acting as a coincidence unit.*

A cross-sectional side view of the experimental set-up of the collimator, with a foil and α-source mounted along with the detector, is shown in figure 4.5. The set-up was placed inside the vacuum chamber of beam-line 4. The high vacuum is required to prevent interactions between the α particles and atmospheric atoms, which result in α energy loss, either causing a systematic error or completely preventing detection.

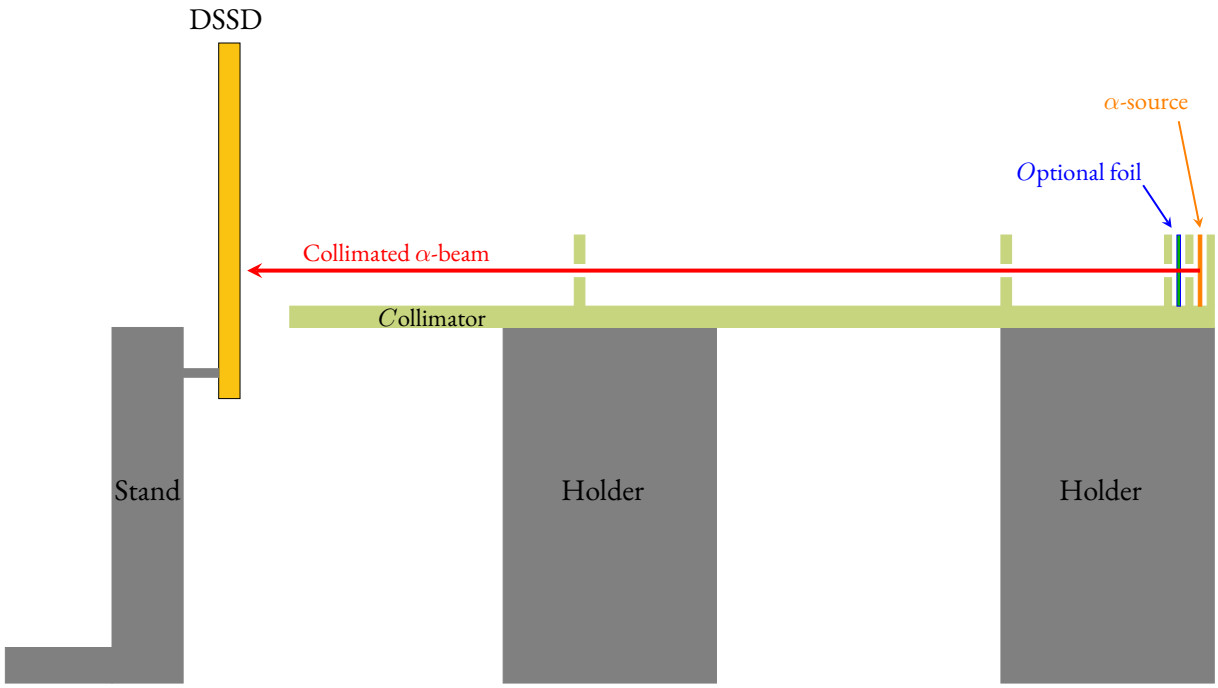


Figure 4.5: *A cross-sectional side view of the experimental set-up for alpha stopping power thickness measurements, showing the DSSD, collimator, foil and source set-up.*

4.2.2 Foil Thickness Experiment

Spectra were acquired for the triple-α calibration source. The α-energies of the source are given in table 4.1. The two ^{239}Pu peaks are too close in energy to be resolved, therefore, an average value of 5.15312 MeV is used by taking an intensity-weighted mean of their energies. The triple alpha source contains a 100 μgcm^{-2} thick coating of gold, which causes additional energy degradation from the ENSDF quoted values, and these lower energies are given alongside the emission energies in table 4.1.

Table 4.1: *Alpha energies of the triple-alpha calibration source, along with the degraded energy due to a thin gold flashing, labelled as calibration energy.*

Isotope	Energy (MeV)	Branching Ratio (%)	Calibration Energy (MeV)
^{239}Pu	5.1443 (8)	17.11 (14)	5.13
^{239}Pu	5.15659 (14)	70.77 (14)	5.13
^{241}Am	5.48556 (12)	84.8 (5)	5.46
^{244}Cm	5.80477 (5)	76.90 (10)	5.78

The detector was lined-up perpendicular to the collimator as shown in figure 4.5, with the vertical and lateral displacement along the detector set to enable the collimated α-beam to be directed at strip 8 on the front and strip 24 on the back, as both are strips which have previously been confirmed as having a high resolution. Only events that passed through strips 8 and 24 were used in the analysis as these alpha particles will have passed through the foil as close to normal to the surface as possible. Alpha particles which pass through the foil at any non-zero angle from the perpendicular would give an overestimate of the thickness

$$x_{rel} = \frac{x}{\cos\theta}, \tag{4.2}$$

where x is the actual thickness of the foil, θ is the angle through the foil, and x_{rel} is the perceived thickness of the foil.

Once the initial spectrum was taken with the α-source with no foil, two separate spectra were acquired, one with the Mo foil and another with the Al foil. The measurement times for both were roughly 4 days to account for the low count-rate due to the highly collimated source.

A linear calibration of the detector channel to α energy was produced from the spectra collected without foils present. This calibration was used to calculate the energy of the particles in the following spectra with foils present. Only the front detector channel was used for the energy measurement, as the rear channel has increased capacitive noise due to the bias being applied on the rear of the detector, however, the rear channel was used in the analysis to determine the position of the particles.

The thickness was calculated for each of the energy peaks by taking the difference in energy for each of the measured peaks, with and without the foil present. Using the SRIM stopping-power code [76], the thickness of material travelled through was calculated using particle range calculations. Figure 4.6 shows a spectrum with and without Mo foils present. The energy loss and also the increased energy straggling can clearly be seen.

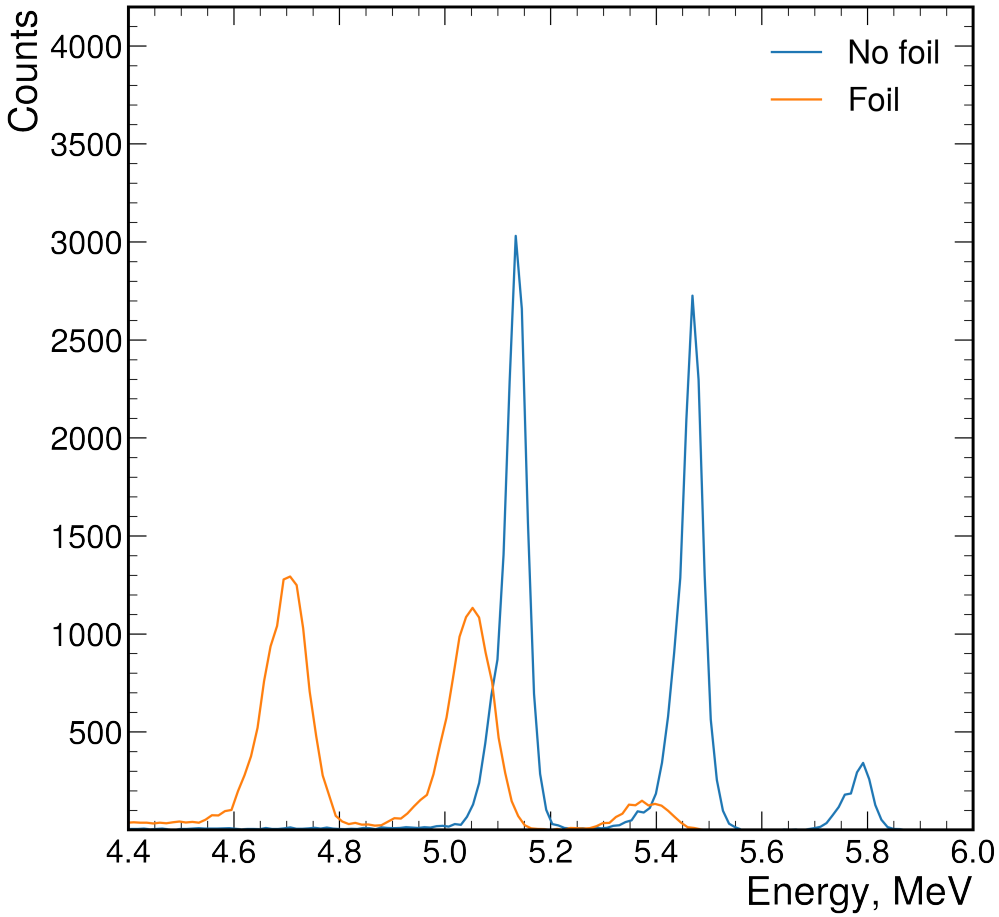


Figure 4.6: *Triple-α spectra recorded on the DSSD charged particle detector, with recorded spectra overlaid both with and without a Mo foil present.*

Three energy loss values are calculated for each foil, one for each of the three α-emission energies. The final thickness value was calculated by taking the weighted mean of the three values. Figure 4.7 shows the relationship between the energy loss and the particle range for the three α energy peaks annotated on a plot of α particle range in Mo against energy.

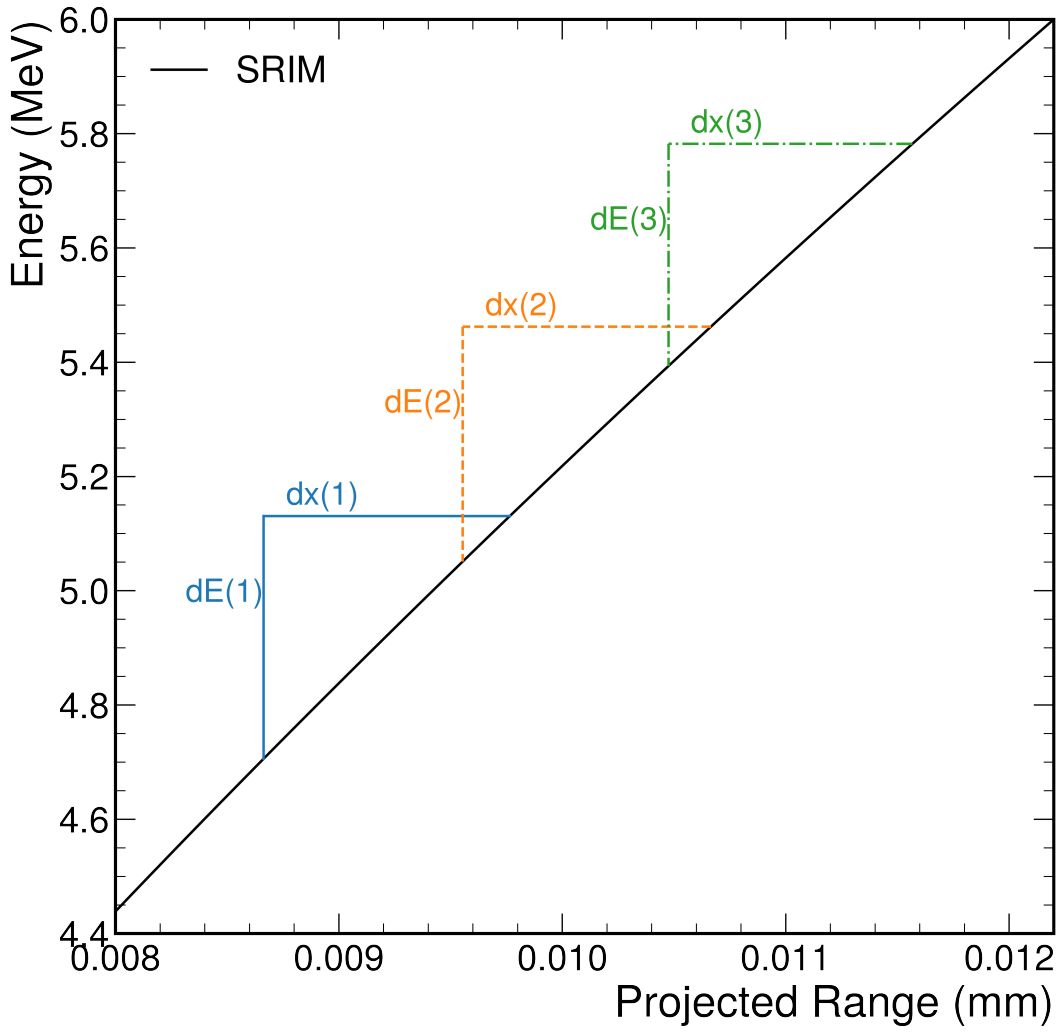


Figure 4.7: *A plot showing particle energy against projected range in mm for an α particle travelling through a Mo foil, calculated using SRIM. Three annotations have been made to the plot, highlighting the change in energy caused by passing through a 1 μm Mo foil.*

4.2.3 Results

The foil thickness results are given in table 4.2 and 4.3 for Mo and Al foils respectively, showing the energy following the foil, the change in energy and the calculated thickness with error on each of the values.

Table 4.2: *Calculation of the thickness of the molybdenum foils, taken as a weighted average of the values calculated from each triple-α result, along with the mean thickness, $\bar{x}$. Energy values are all given in units of MeV and thicknesses in units of μm. The error on the thicknesses are given for both positive and negative values as $\delta(x)_{upp}$ and $\delta(x)_{low}$ respectively.*

	5.13MeV	**5.46 MeV**	**5.78 MeV**	$\bar{\mathbf{x}}$
$\mathbf{E_f}$	$4.706(51)$	$5.051(41)$	$5.393(58)$	
$\mathbf{E_i - E_f}$	$0.425(51)$	$0.411(41)$	$0.389(58)$	
$\mathbf{x}$	1.102	1.111	1.092	1.104
$\delta(x)_{low}$	0.129	0.108	0.160	0.073
$\delta(x)_{upp}$	0.128	0.108	0.159	0.074

The measured Mo foil thickness of $1.104(^{+74}_{-73})$ μm is within the quoted errors given by the manufacturer of $1.00(25)$ μm. The magnitude of the upper and lower error differ slightly due to the change in stopping power, however, this is seen to have a negligible effect on the results.

Table 4.3: *Calculation for the thickness of the aluminium foils, taken as a weighted average of the values calculated from each triple-α result. Energy values are given in units of MeV and distances in units of μm.*

	5.13MeV	**5.46 MeV**	**5.78 MeV**	$\bar{\mathbf{x}}$
$\mathbf{E_f}$	$2.855(191)$	$3.346(146)$	$3.787(214)$	
$\mathbf{E_i - E_f}$	$2.275(191)$	$2.116(146)$	$1.995(214)$	
$\mathbf{x}$	9.214	9.232	9.269	12.050
$\delta(x)_{low}$	0.839	0.701	1.097	0.483
$\delta(x)_{upp}$	0.867	0.718	1.133	0.497

The results for the Al foil thickness measurement is $12.050(^{+483}_{-497})$ μm.

4.3 Beam Energy Measurements

The foil thickness has been measured to a high precision in section 4.2, enabling the energy loss through each foil to be calculated to high precision. While it is essential to understand the energy loss through each target, if the beam energy is not accurately characterised, the high precision and accuracy of the thickness measurements provide little benefit. The energy profile of a cyclotron beam is usually Gaussian [116]. The mean and distribution of this are calculated using a nuclear physics method of kinematic reconstruction, using scattering of the beam describing a general method for a cyclotron beam.

4.3.1 Kinematic Reconstruction

For a particle beam incident on a stationary tagrt, as the mass of the target and beam nuclei are known, and the energy and scattering angle of the scattered nuclei can be determined with the DSSD detectors, the energy of the incident beam can be determined using two-body kinematics, as shown schematically in figure 4.8.

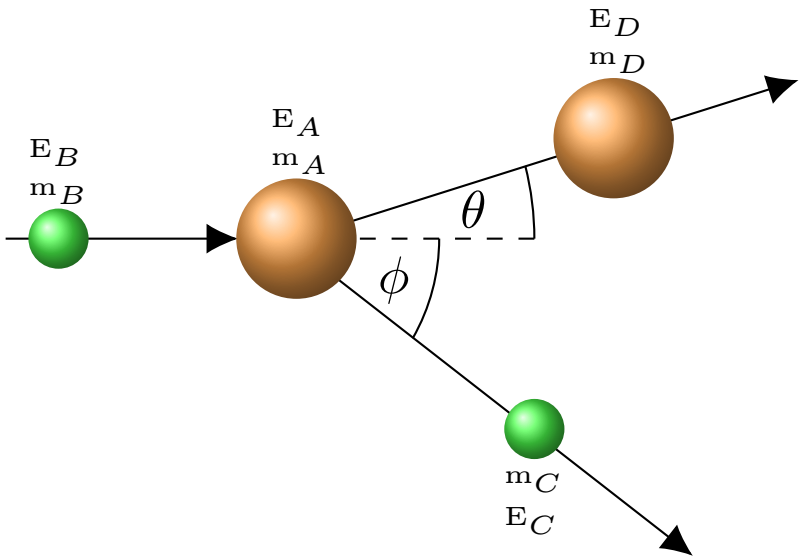


Figure 4.8: *Schematic of two-body kinematic scattering of a projectile from a stationary target, where θ is the scattering angle of the target nucleus nucleus from the beam axis and ϕ is the scattering angle of the projectile particle from the beam axis.*

Equation 4.3 shows the kinematic relationship between the parameters in the form of a quadratic equation in $\sqrt{E_B}$

$$\left(1-\frac{m_C}{m_B}\right)E_B - 2\sqrt{\frac{m_D}{m_B}E_D}\cos\theta\sqrt{E_B} + \left(\frac{m_D}{m_B}+\frac{m_C}{m_B}\right)E_D + \frac{m_C}{m_B}(E_x - Q) = 0. \quad (4.3)$$

Here m_A and m_B are the mass of the stationary target and beam particle, m_C and m_D are the mass of the recoil nucleus and ejectile, respectively, E_B is the beam energy, and E_D is the energy of the ejectile particle. This equation can be solved to give the beam energy as a function of ejectile scattering angle, θ

$$\sqrt{E_B} = \frac{2\sqrt{\frac{m_D}{m_B}E_D}\cos\theta \pm \left[4\frac{m_D}{m_B}E_D\cos^2\theta - 4\left(1-\frac{m_C}{m_B}\right)\left(\frac{m_D}{m_B}+\frac{m_C}{m_B}\right)E_D + \frac{m_C}{m_B}(E_x-Q)\right]^{1/2}}{2\left(1-\frac{m_C}{m_B}\right)} \quad (4.4)$$

The full kinematic derivation is given in appendix D.

The beam was incident on an Au target in the centre of the chamber, where the beam scattered both elastically and in-elastically, with the scattered particles measured by energy-calibrated double-sided silicon strip detectors (DSSDs) in a set-up previously described. The kinematic curves were then modelled to investigate the optimum positioning of the detectors. An angle of the detector must be such that the rate of change of energy with respect to angle is the greatest, enabling the most accurate fitting of the kinematic lines to data. The distance of the detector from the point reaction point must also be optimised. A detector close to the foil will cover a greater range of scattering angles; however, the angular resolution will improve for greater radial distances from the scatter.

The particle energy at the detectors will have degraded as it passes through the Au foil, and the reconstructed beam energy will be the energy at the scattering point, not accounting for any energy degradation before the scattering reaction. It is assumed that scattering is as likely to occur at any point through the Au foil, therefore a reasonable correction is to assume that the scattering has occurred halfway through the foil. The scattering is highlighted in figure 4.9.

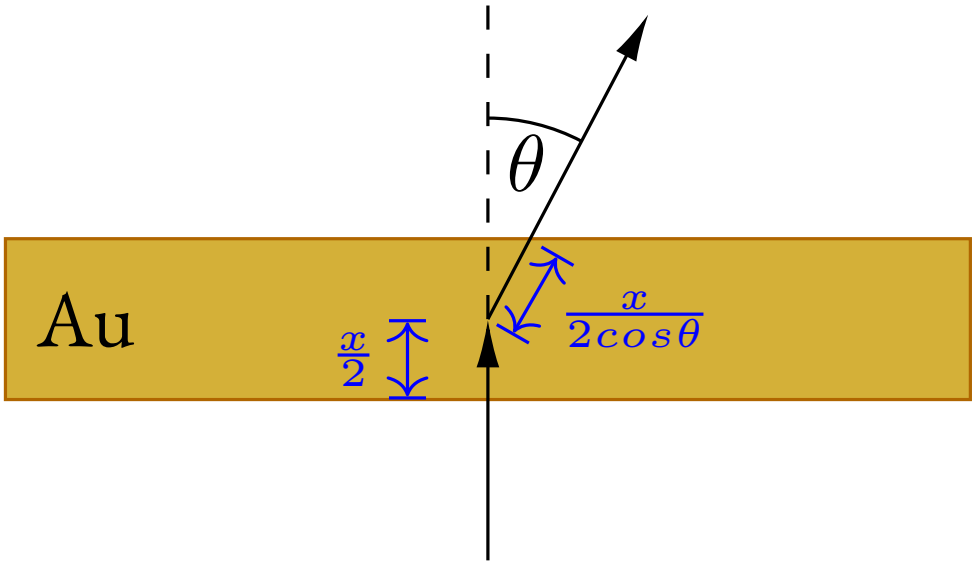


Figure 4.9: *Schematic of a beam passing through the Au foil, scattering at $\frac{x}{2}$, halfway through the foil.*

This requires stopping power corrections to be performed within the beam-energy calculations. The energy E_D must be corrected for energy loss through $\frac{x}{2\cos\theta}$ of Au, and the value of E_B must be corrected for energy loss through $\frac{x}{2}$ of Au. The Au foil used in the experiment has a thickness of 200 μgcm^{-2}

4.3.2 Experimental set-up

The experiment was set up in a vacuum chamber, with two DSSD charged-particle detectors. A thin Au foil was placed in the centre of the chamber in the beam path to cause scattering. The two detectors were positioned perpendicular to the scattering paths from the centre of the chamber, set at angles out of the main beam's path to enable the higher angle scatters to be measured while preventing damage to the detector from the high beam current. Both detectors were positioned at different angles to enable a greater spread of angles to be analysed. The detectors were positioned at 210 mm radially out from the interaction point, with detector 1 centered at $51.5°$ and detector 2 at $-24.5°$, which was determined using a 2D kinematic model. The scattering of an α particle from a gold foil was modelled, with the detectors placed where the $\frac{dE}{dx}$ was greatest to better constrain the fits. Provided the detectors do not overlap it is not essential whether they are both on the same side of the beam or not. Both detectors were positioned at the furthest possible distance in the scattering chamber, 210 mm radially out to give

the best angular resolution to each individual detector pixel. The set-up is shown in figure 4.10.

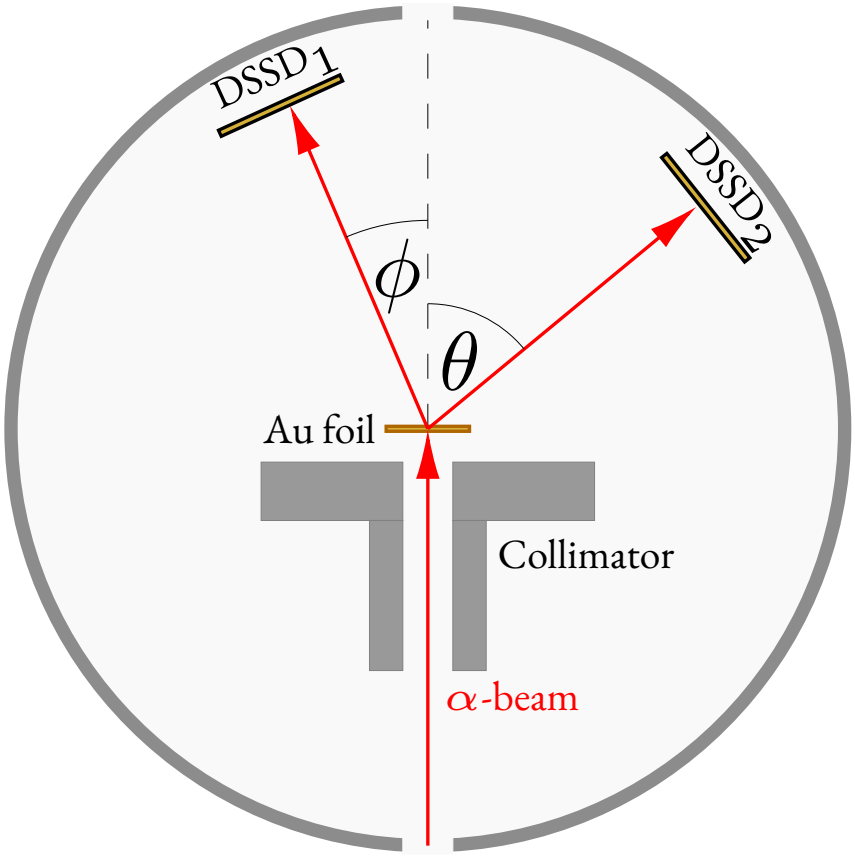


Figure 4.10: *Birmingham cyclotron's beam-line 4 vacuum chamber, with two DSSD detectors set up at 210 mm from the Au foil. The two detectors were set up at different angles of $\theta = 51.5°$ and $\phi = -24.5°$. Collimators are present prior to the scattering point to maintain a clean beam profile for scattering and detection.*

This electronic set-up is similar to the experimental set-up shown in section 4.2 for the foil thickness measurements, with additions and modifications. In this experiment, two DSSD detectors were connected in a circuit as shown in figure 4.11. Each detector was connected to a pre-amplifier, amplifier and analogue to digital converter (ADC) and a VME module connected to a computer. This set-up enables the current pulses to be maximised relative to noise and interpreted by computer software, as the peak amplitude is proportional to the energy of the incident particle.

A coincidence circuit was set up between the front and back strips on the detector to enable the pixelated position to be determined from the intersection of both strips (front ∩ rear). When a pulse

was registered in the front, followed by the back detector in quick succession, the pulses could be associated as a 'coincidence'. The coincidence circuit was composed of a leading edge discriminator (LED), a Fan-in Fan-out (FiFo) module, a gate and delay generator and a trigger SAC.

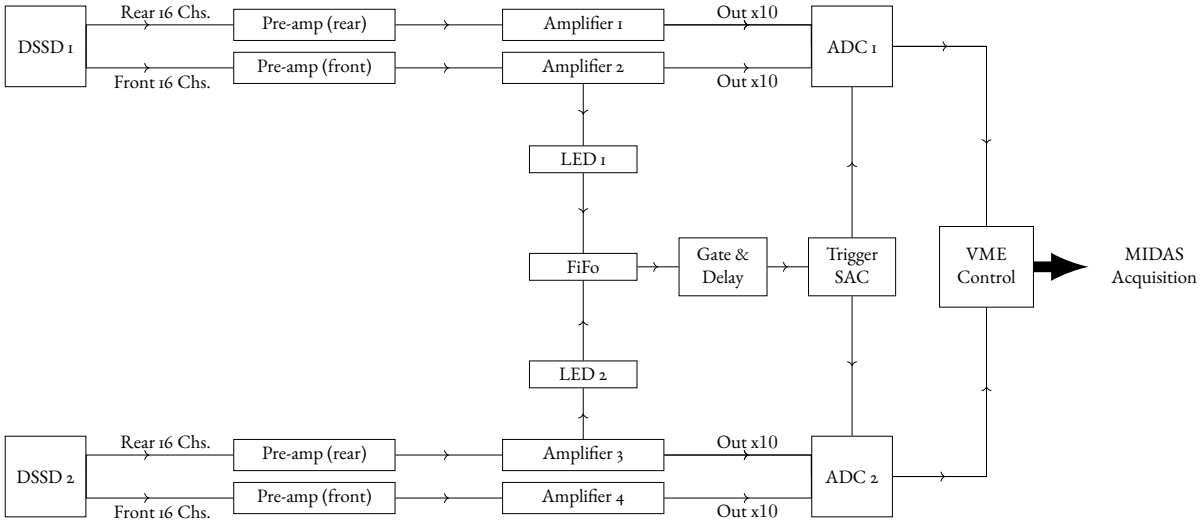
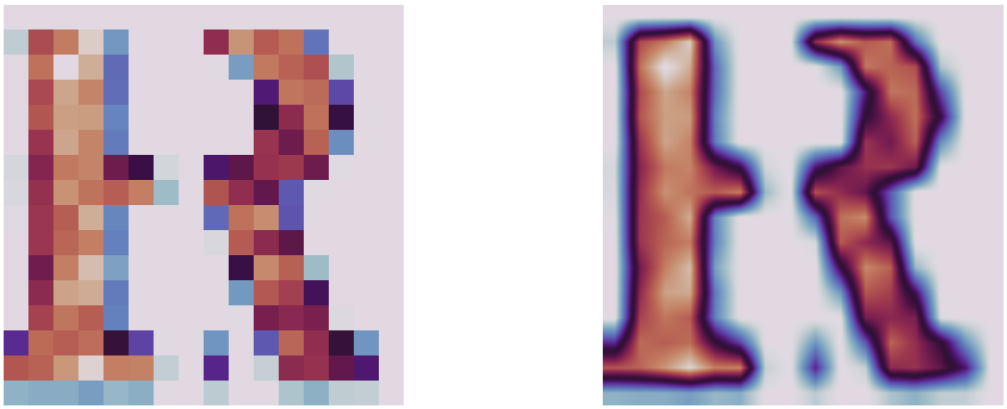


Figure 4.11: *Electronic set-up of the DSSD detectors.*

4.3.3 Calibration

A calibration was performed to produce a conversion from channel number to energy for each detector strip. There is both an energy and position calibration. Positional calibration involves the correct orientation and position of the detectors, enabling the right location in the space of each pixel to be determined. Each strip in the detector correlates to a single ADC channel. To confirm which detector channel aligns with which ADC, a mask with an R-shaped hole is placed over the detector. When viewed as a 2D heat map, if the ADC channels are configured correctly in the analysis code, a correctly orientated 'R' shape will be present. Smearing is performed on the channels to enhance the shape, enabling it to be more easily seen. The output of the R-mask is shown for detector one, both without and with smearing.



(a) *No smearing effects* ***(b)*** *With smearing effects*

Figure 4.12: *Detector* 1 *with an attenuating R-mask overlaid, to enable the orientation of the channels to be determined.*

An alpha calibration source is used for these measurements. This is a source composed of three isotopes, ^{239}Pu, ^{241}Am and ^{244}Cm. The energy of the alpha particles is shown in table 4.1. The two peaks from ^{239}Pu are so close in energy that the peaks cannot be resolved, and instead, a weighted mean is taken of the peaks. There is also a thin metallic film in front of the source isotopes, which causes slight degradation in energy.

The three energy peaks from the alpha particle enable a relationship to be produced between the detector ADC channel and the energy of the α particle. The measurement was performed with the triple-α source in front of the detector. Fitting the channels to the energy enables the detector channels to be converted to energy using a linear fit. Figure 4.13 displays all 64 of the ADC channels overlaid in energy against counts with the alpha-energies annotated.

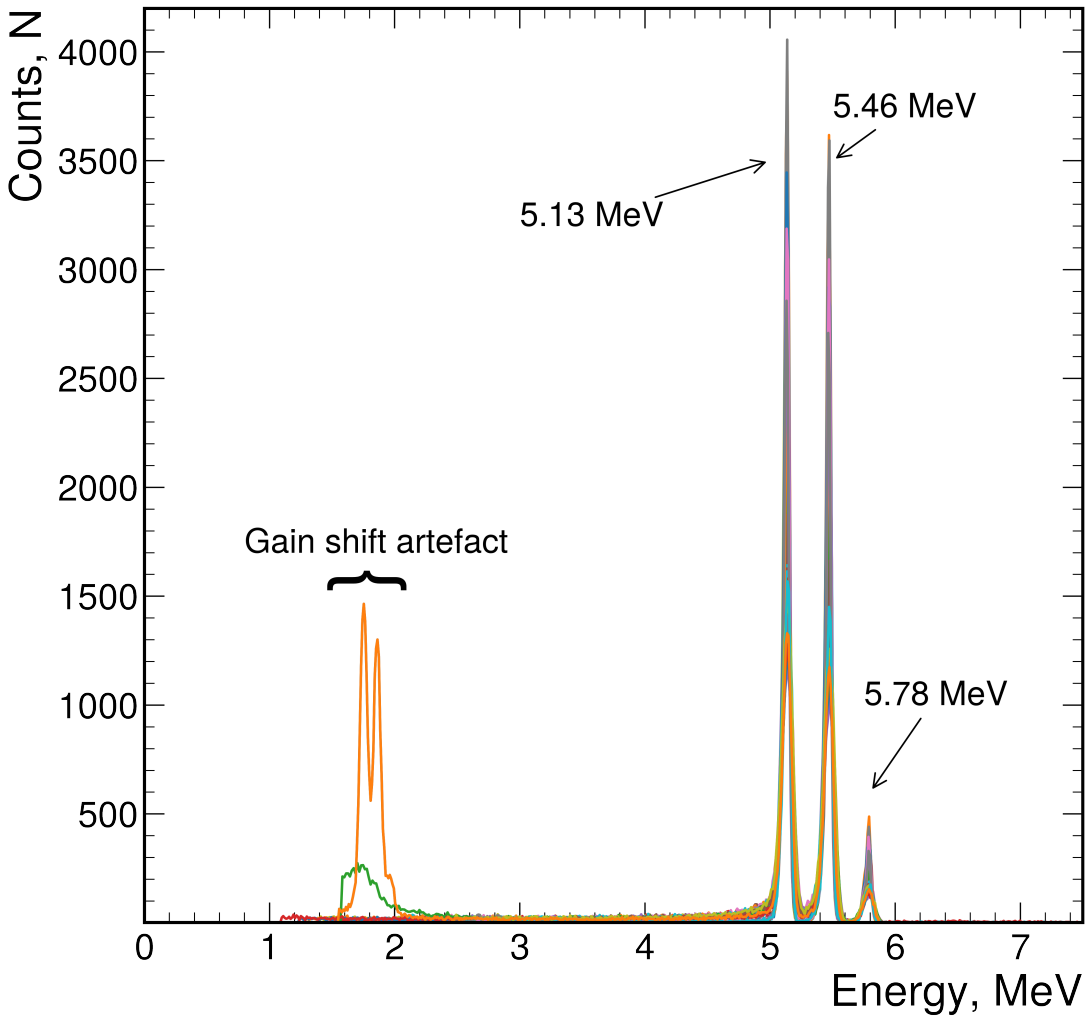
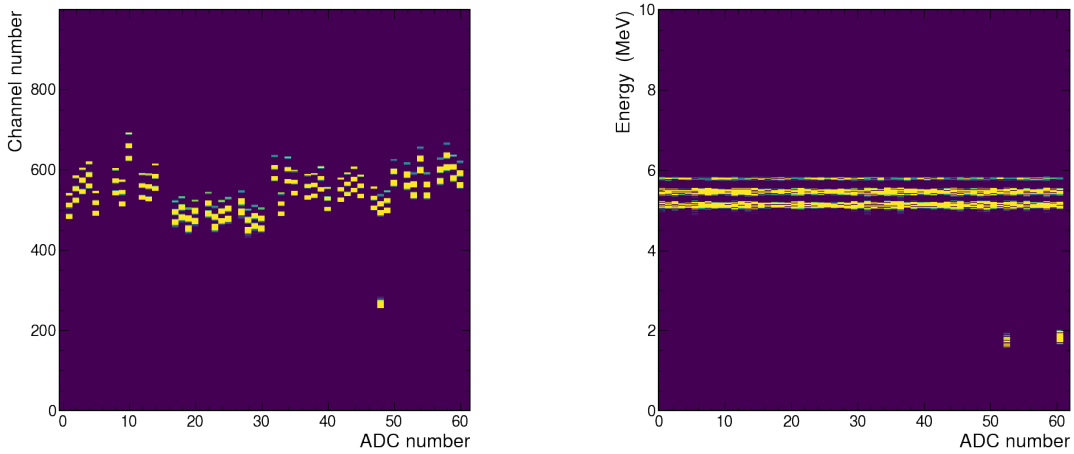


Figure 4.13: *Plot of counts against energy with triple-α peaks highlighted with each of the channels overlaid for all* 64 *channels in both detectors. The three energies of the triple-α are annotated along with the low-energy noise.*

The process of calibrating the ADC channels can also be shown in figure 4.14 in 2D, showing the energy channels with the triple-alpha peaks present both uncalibrated and calibrated.



(a) *Uncalibrated DSSDs* ***(b)*** *Energy calibrated DSSDs*

Figure 4.14: *Both DSSD detectors, measuring a triple alpha-source, showing both uncalibrated and calibrated.*

4.3.4 Results

The detectors being at the furthest possible distance of 210 mm had a benefit in terms of the angular resolution of the detector, however, this results in a lower count rate, due to the smaller solid angle of each detector pseudo-pixel. With greater angles, there is a considerable drop-off in the Rutherford scattering cross-section, which must be considered for the detector at a wider angle. Calculations were performed independently for the two detectors. The forward detector ($DSSD_1$) had $400\times$ statistics in the Gaussian peak of the beam energy compared to the outer detector ($DSSD_2$), however, the spread of the data is greater in $DSSD_1$, causing a greater error than $DSSD_2$.

The results for the $\sim$ 40 MeV irradiation are given in table 4.4, and the results for the $\sim$ 29 MeV irradiation are given in table 4.5.

Table 4.4: *Beam energy calculation using kinematic reconstruction for the* 40 *MeV* α *beam.*

	Beam Energy, MeV	**Beam Energy Error, MeV**
$DSSD_1$ (24.5°)	38.92	0.19
$DSSD_2$ (51.5°)	39.10	0.46
Weighted mean	39.01	0.18

Table 4.5: *Beam energy calculation using kinematic reconstruction for the* 29 *MeV* α *beam.*

	Beam Energy, MeV	**Beam energy Error, MeV**
$DSSD_1$ (24.5°)	26.89	0.17
$DSSD_2$ (51.5°)	26.81	0.34
Weighted mean	26.84	0.15

The final value for the beam energies of the two irradiations were $39.01(18)$ MeV and $26.84(15)$ MeV.

4.4 Calculation of Beam Energy Through Each Foil

The calculation of energy through each foil is used to determine the energy range of the particle beam as it passes through the foil. The particle beam will have an incident energy at the front of the foil, and degrade through the foil, either stopping in the foil or leaving the rear of the foil at a reduced energy. Utilising the foil thickness measurements in section 4.2 and the beam energy calculations in section 4.3, along with stopping calculations in SRIM, the energy through each of the foils can be calculated.

A total of eight foils were irradiated, in two independent irradiations of four foils each. Breaking the irradiation into a higher energy ($\sim$ 39 MeV) and lower energy ($\sim$ 27 MeV) irradiation is helpful to limit energy straggling and additional reactions from secondary particles. Each foil was stacked with two Al energy-degrader foils between them, as shown schematically in figure 4.15. The stack was identical for the two irradiations.

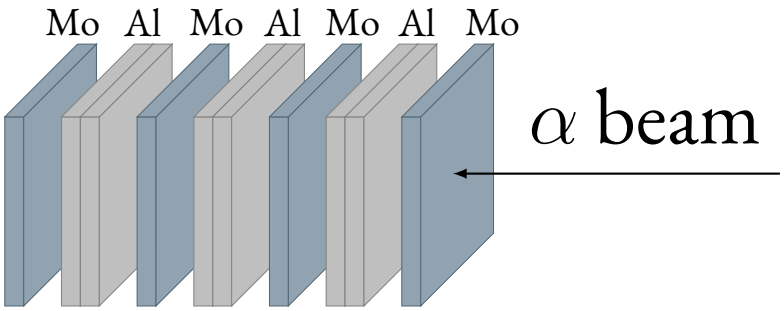


Figure 4.15: *Schematic of the foil stack with alternating Mo and Al.*

4.4.1 Stopping power and alpha particles ranges

The stopping power and projected range of α particle passing through Mo and Al has been calculated. Figures 4.16 and 4.17 show the stopping power and projected range overlaid against energy for Mo and Al foils, respectively.

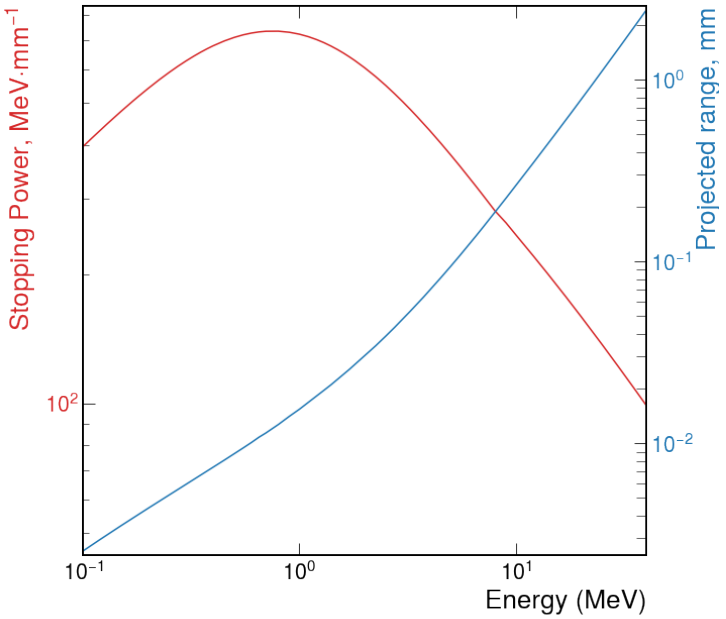


Figure 4.16: *Stopping power and projected range for an α particle passing through Mo, calculated using SRIM.*

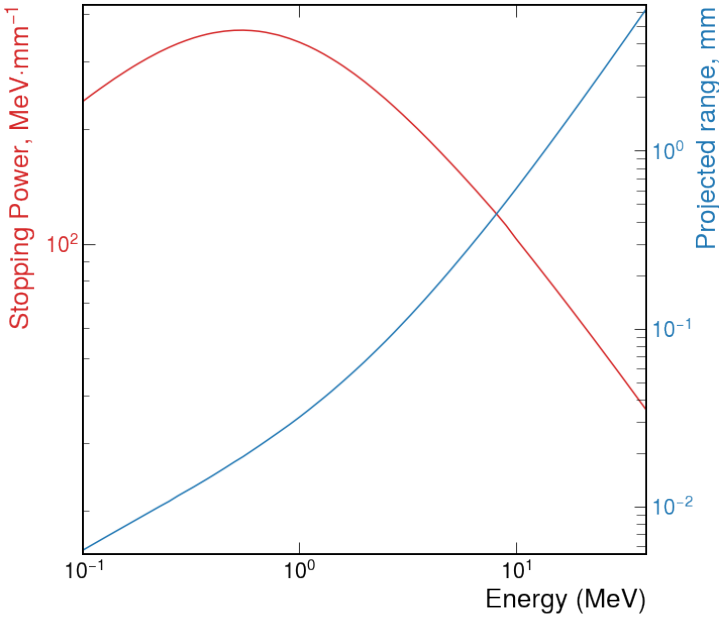


Figure 4.17: *Stopping power and projected range for an α particle passing through Al, calculated using SRIM.*

4.4.2 Calculations of alpha particle energies at the centre of each foil

The foil energy was calculated by taking the mean energy at half the thickness of each Mo foil. The error in the energy was calculated by taking the absolute limits from the error on the beam energy, Mo thickness and Al thickness. The minimum energy of the beam in each of the foils was calculated by taking the mean beam energy minus the error. This was propagated by using the maximum thickness of Mo and Al through each foil, which was taken as the mean value plus the error. The maximum energy of the beam in each of the foils was calculated by taking the mean beam energy plus the error. As with the minimum error this was propagated through the foils by making the minimum thickness of each foil which is the average thickness minus the error.

The foil energies for irradiation 1 performed at $39.01(18)$ MeV are given in table 4.6.

Table 4.6: *Table of the foil energies for the* 1*st irradiation performed with foils* 1-4 *at* $39.03(15)$ *MeV. The mean energy is the average energy at* $x/2$ *distance through the target, while the upper and lower energies are the limits at the edge of the target, using the error bounds of the energy and thicknesses.*

Foil Number	**E at** $x/2$	E_{min}	E_{max}
1	38.954	38.795	39.113
2	36.236	36.058	36.635
3	33.599	33.166	34.034
4	30.684	30.086	31.285

The foil energies for irradiation 2 performed at $26.84(15)$ MeV are given in table 4.7.

Table 4.7: *Table of the foil energies for the* 2*nd irradiation performed with foils* 5-8 *at* $26.84(15)$ *MeV. The mean energy is the average energy at* $x/2$ *distance through the target, while the upper and lower energies are the limits at the edge of the target, using the error bounds of the energy and thicknesses.*

Foil Number	**E at** $x/2$	E_{min}	E_{max}
5	26.778	26.617	26.938
6	23.317	22.976	23.659
7	19.469	18.896	20.040
8	15.035	14.129	15.924

The data for the foil energy at the centre of each foil and the error is given in figure 4.18. The advantage of splitting the irradiation into two separate irradiations is clear, as the uncertainty on the error explodes as the beam is propagated through more foils.

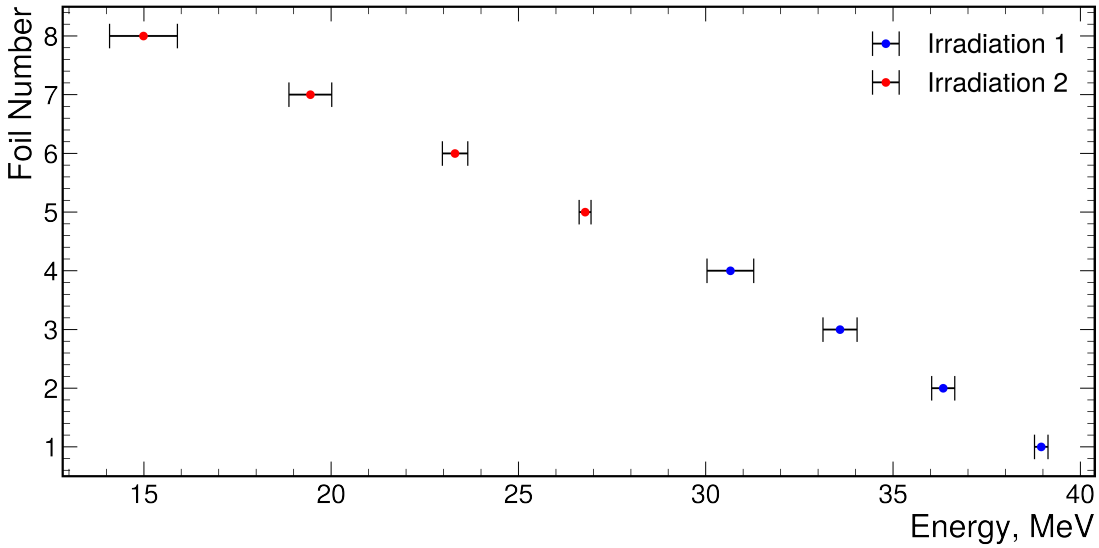


Figure 4.18: *This plot shows the energy at which each foil was irradiated. The data point for each foil is the mean energy halfway through the thickness of the target, while the errors are taken from propagating the maximum beam energy ($E + dE$) and the minimum thicknesses ($x - \sigma x$) for the upper bound, and taking the minimum beam energy ($E - dE$) and the maximum thicknesses ($x + \sigma x$) for the lower bound.*

4.5 Current Measurement

Beam current measurements are essential to understand the intensity of the accelerator beam. The irradiation time and the time the irradiation finished are also needed.

4.5.1 Experimental set-up

Previously to this project at the University of Birmingham cyclotron, cross-section measurements were performed on a standard water-cooled target mounting as shown in figure 4.19. This was composed of a 3 mm thick aluminium plate on the front and a 5 mm aluminium plate on the back. The front plate contained a 10×22 mm hole for the target to be inset.

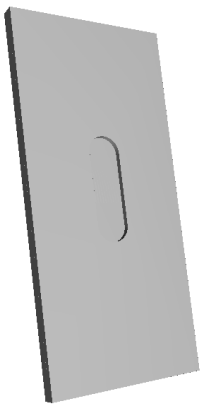


Figure 4.19: *A CAD output of the water-cooled target used for cross-section measurements at the University of Birmingham cyclotron. This is mounted externally to beamline* 3*.*

While this was a convenient set-up, there were several issues which negatively impacted the precision and accuracy of the experiment beyond the disadvantages mentioned in section 4.3.2. The current was measured by connecting a cable to the conducting target plates. The current could then be converted to particle flux by dividing by the charge of the incident particles.

The first disadvantage is that the set-up did not possess collimators along the beamline, causing a large beam spread, resulting in some of the collected charge coming from particles which were incident on the target mounting rather than the target itself. The second and larger issue was that the target mount enabled secondary (delta) electrons to escape, causing the measured positive charge to be

higher than the true value. The effect of this is deemed to cause a $\sim$ 20% divergence in the current value.

The new set-up moved the irradiation to beam-line $4a$ shown in figure 4.1, a previously unused beam-line in the nuclear physics vault. A beamline section was assembled as shown in figure 4.20, including three collimators to limit the beam spread. The target was then housed in an isolated section at the end of the beam line. This was a deep cavity, greatly limiting the secondary electron loss, and the beam-current could be measured from here. While this set-up does not contain a solenoid magnet to divert the electrons, it is functionally a Faraday cup.

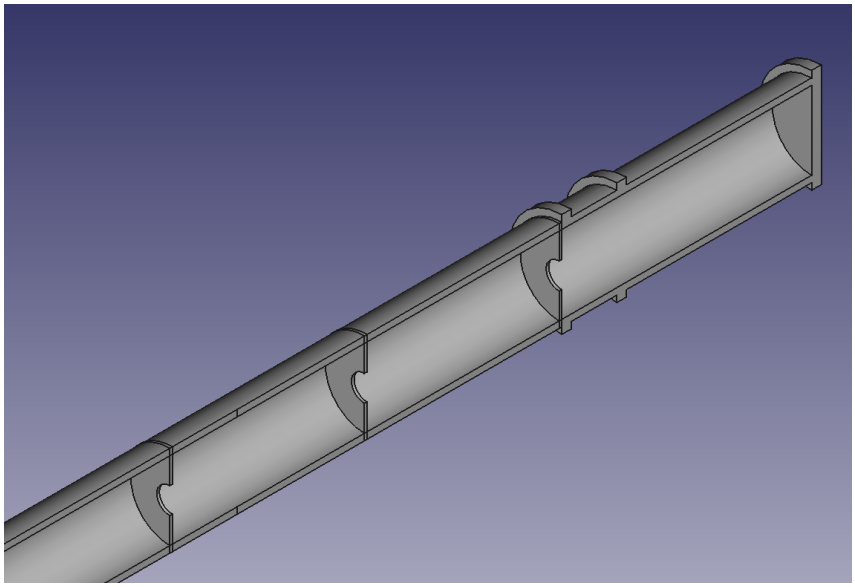


Figure 4.20: *A CAD render of beam-line* $4a$ *at the University of Birmingham cyclotron. The beamline was commissioned for high-precision cross-section measurements.*

A further schematic of the beam-line is shown in figure 4.21, with a cross-sectional view of the beamline, collimators, insulating section and target holder, with all respective dimensions, with a mock beam profile highlighted in purple throughout the beamline.

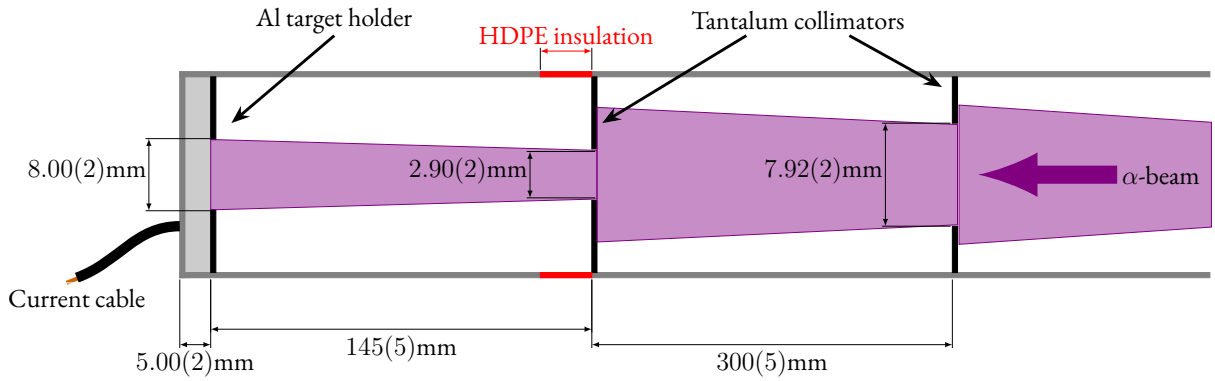


Figure 4.21: *A schematic side-profile cross-section of beamline 4a at the University of Birmingham MC40 cyclotron, with the beamline, collimators, target holder and insulating section highlighted with all relevant dimensions. A mock beam profile is shown in purple.*

4.5.2 Data Analysis

The cyclotron beam current was measured using an Arduino Mega micro-controller connected to an INA219 current sensor, which logged the cyclotron beam current every second throughout the irradiation period, appending the timestamped values to a .csv file.

In an ideal scenario, the foils would be irradiated by a constant current, I, for a period of time between t_0 and t_{irrad}. This can be modelled as a top-hat function,

$$T(t) = \begin{cases} 0 & \text{if } t < t_0 \\ I & \text{if } t_0 \geq t \leq t_{irrad} \\ 0 & \text{if } t > t_{irrad} \end{cases} . \tag{4.5}$$

The activity of an isotope at time t following irradiation, $A(t)$, can be given as

$$A_i = \sigma_i N_T I(1 - e^{-\lambda_i \tau_{irrad}}) \tag{4.6}$$

where σ_i is the cross-section, N_T the number density, I, the beam current, λ, the decay constant and, τ_{irrad}, the irradiation time.

The activity is proportional to the current, I. However, due to the pulsed nature of a cyclotron's beam, combined with the imperfect nature of an ion source and the inability to maintain magnets with perfectly constant field strength, the cyclotron current is transient throughout the irradiation time, τ_{irrad}. This can be seen in figure 4.22 for irradiation one.

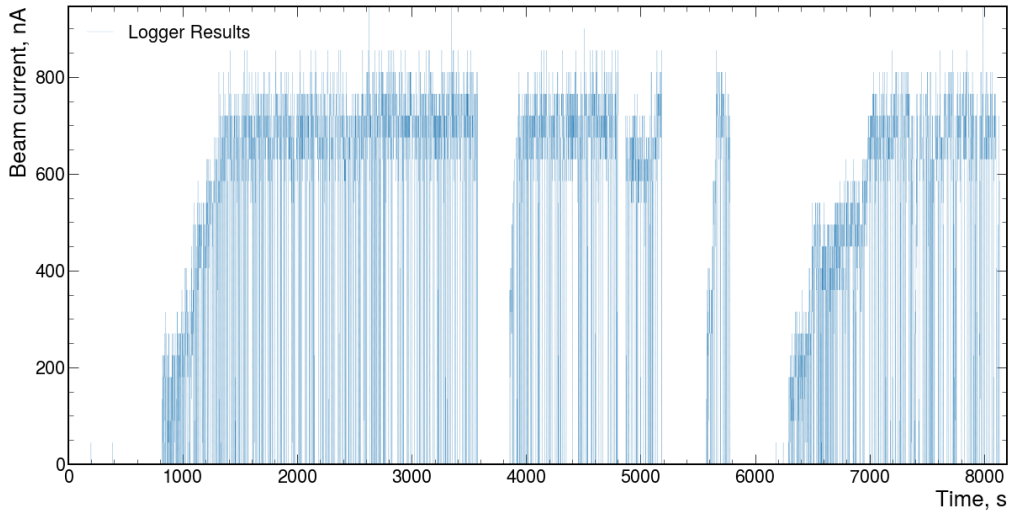


Figure 4.22: *The output of the cyclotron current logger for the day* 1 *irradiation of foils* 1-4*. The electrical current is measured* nA*, and the time is seconds from the start of the measurement.*

It would be inaccurate to model this as a single step-function as the beam is seen to have several prolonged periods of outage along with great variance between the current at different times. Equation 4.6 may then be modified for the irradiation to be the sum of a series of discrete irradiation steps

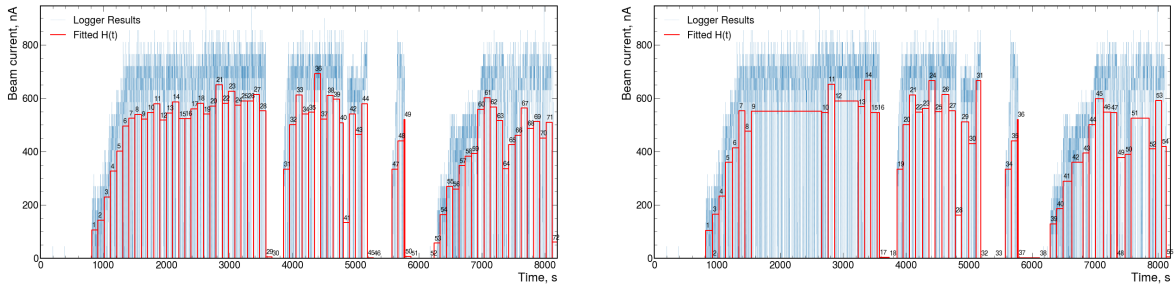
$$A_i(T) = \sigma_i N_T \sum_{k=1}^{n} I_k \left[1 - e^{-\lambda_i(\tau_k^f - \tau_k^i)}\right] e^{-\lambda(T-\tau_k^f)}, \tag{4.7}$$

where the symbols have their usual meaning and τ_k^i and τ_k^f are the time at which the irradiation step begins and finishes, and T is the time at the end of the entire irradiation.

An algorithm was therefore developed to calculate the optimum irradiation steps. A higher resolution offers greater accuracy and precision, however, this increases the computational complexity.

The algorithm takes in three parameters; the logged current data, a minimum width of step and a minimum current difference. The algorithm starts at $t = 0$ and initiates two directly successive step functions. The initial width of these step functions is determined by the 'minimum step' parameter, which is the minimum width of the step in seconds. The mean current is calculated for each of the steps. If the difference in the mean current between the two-step functions is greater than the 'minimum current difference' parameter, the first of the two step functions is stored to file, and the process will continue by creating a new step function adjacent and in front of the remaining step function. If the mean current values are below this threshold, the width of the first step is increased in one-second steps, until the difference in the mean current between the two step functions is above the threshold. At this point, the first step function is stored. The algorithm continues until the second step function reaches the end of the irradiation $t = \tau_{irrad}$, at which point the two-step functions are appended to the file and the process is killed.

Examples of the algorithm are shown for the day one irradiation in figure 4.23.



(a) *min. step*=0 *nA, min. width*=100 *s* ***(b)*** *min. step*=70 *nA, min. width*=100 *s*

Figure 4.23: *The output of the current logger for the day* 1 *irradiation at the MC*40 *cyclotron, showing current in nA against time since the start of the measurement in seconds. The two panels show outputs from the current algorithm, which converts a current spectrum to a series of step functions. Different parameters were used for each to highlight the flexibility of the algorithm.*

Decreasing the minimum width of the steps greatly increases the accuracy of measurements. This can be seen when modelling the irradiation of a nuclide with a half-life of 1800 s. As the step size is decreased, the value for the final activity produced converges. This is shown in figure 4.24.

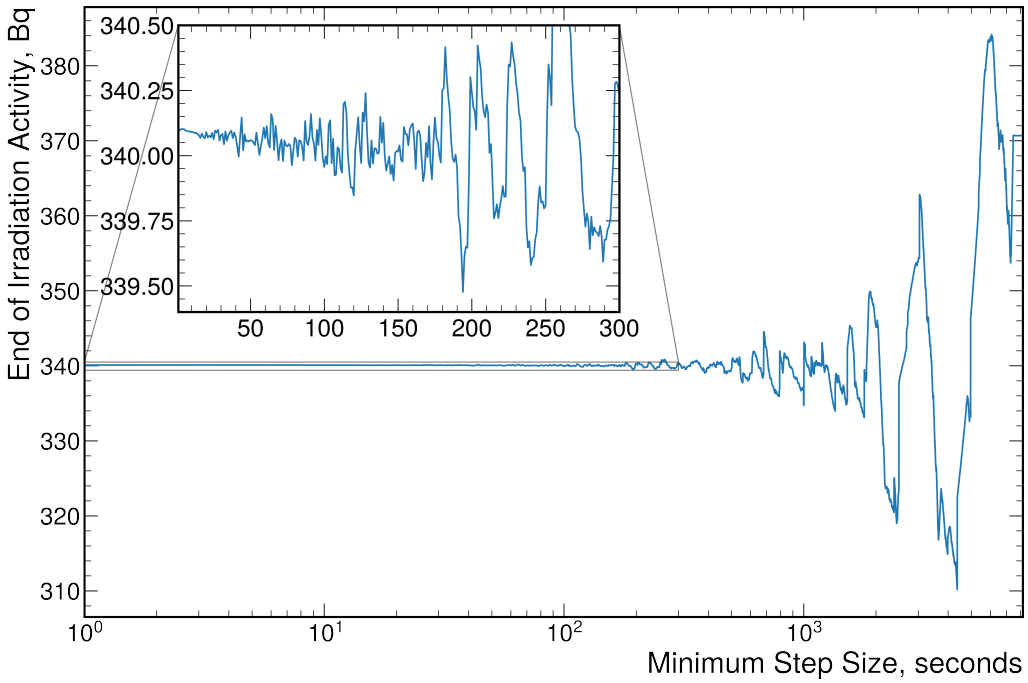


Figure 4.24: *The calculated final activity of a* 1800*s half-life isotope irradiated using the day* 1 *current profile at the MC40 cyclotron, where the irradiation is broken into n discrete constant-current irradiations. Along the horizontal axis is the step-size, measured in seconds, used in the algorithm, showing a clear improvement in accuracy with decreasing step size and large oscillations around this value at high values of step size.*

4.5.3 Results

For the final calculations of beam-current, the minimum width was set to 1 s and the minimum step set to 0 nA. This produced a series of irradiations, each with the finest granularity to give the greatest precision. The results for irradiation one and two are shown in table 4.8.

Table 4.8: *The current results for the two Mo foil irradiations, showing the data, start and end time of the irradiation, the number of* 1 *second non-zero steps and the integrated current in μAh with error.*

Session	Foils	Date	Start time	End time	No. of steps	Integrated Current
1	1, 2, 3, 4	09/03/2021	14:03:04	16:21:20	5524	0.8159(255)μAh
2	5, 6, 7, 8	10/03/2021	13:28:15	15:40:35	7475	1.40370(21)μAh

4.6 High-Resolution gamma-ray Spectroscopy

The decay of a radioactive nucleus may result in the emission of one or more characteristic γ rays, as it decays to a more stable state. Due to the energy levels being quantised and unique to the structure of the nucleus of different isotopes, these γ emissions act as a fingerprint. Measuring particular energy γ rays or a combination of γ rays can confirm the presence of a particular isotope, which, particularly with shorter-lived isotopes, can be verified by the decrease in emissions over time, in accordance with the decay constant, λ. Accurate measurement of gamma-ray emissions (through accurate counting and accounting for the efficiency of detection) and the decay constant, enables the quantity of a particular isotope present in a sample to be determined, which can, along with the parameters calculated in previous sections of this chapter, be used to calculate the cross-section of production.

This section of the thesis covers the experimental set-up, data acquisition, and both the online data analysis used to optimise the acquisition and high precision offline analysis and corrections to elucidate the cross-sections and results.

4.6.1 Experimental Set-Up

The experiment involved two HPGe detectors with nearly identical dimensions, connected in identical circuits. The detectors were connected to a built-in (cold) pre-amplifier, which matches the high impedance of the detector output with the low impedance of the successive electronic units, while also amplifying the voltage signal. The benefit of the pre-amplifier being built into the detector is the short distance the signal must travel, limiting the effects of capacitative pick-up noise. The pre-amplifier was connected to an Ortec 572A amplifier with a dual function of amplifying the voltage signal, while also shaping the pulse. The pre-amplifier pulse has a sharp rise followed by an exponential decay. The pulse that leaves the amplifier has a Gaussian form, with a positive magnitude when operated in unipolar mode, as was done in the present work. The amplitude of the signal is proportional to the energy of the photon energy deposited in the HPGe detector. From detection to after the amplifier, the pulse is analogue, while computational analysis requires the signal to be converted to a digital

signal. This conversion is performed using an analogue-to-digital converter (ADC) connected in series to the amplifier. The conversion process is performed by binning the pulse into a channel based on the magnitude of the pulse. The ORTEC ADCs used in this experiment contained 8192 channels (2^{13}), and accept voltages in the range 0-10 V. The gain of the amplifier was adjusted to prevent any high-energy photons from being above the threshold while increasing the gain as much as possible to spread the photon emissions over a broader range of channels, which is important when differentiating between two photons with similar energy. The ADC was connected directly to a computer with ORTEC's Maestro acquisition software, with all spectra collected in .Chn format. A benefit of the Maestro software is the ability to run batch files, enabling multiple spectra to be collected automatically. The set-up is shown schematically in figure 4.25.

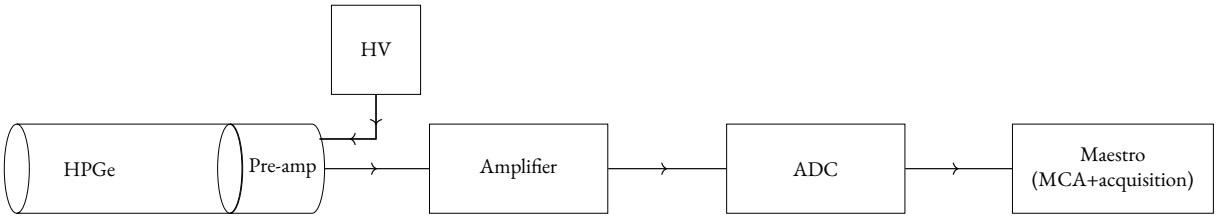


Figure 4.25: *The electronic setup of the Hyper-Pure Germanium detector, showing the detector with the high voltage (HV) power supply, and the signal sequence consisting of an inbuilt pre-amplifier, amplifier, analogue-to-digital convertor (ADC) and MCA, connected in series to a PC with Maestro acquisition software.*

To accurately set the distance of the foils from the detector, they were placed on perspex sheets in a 3D-printed foil holder with grooves at defined distances, shown in figure 4.26. This enabled the distance to be accurately and precisely noted for each spectrum. Many grooves were designed into the holder to enable the foils to be placed in predefined positions closer to the detector, as the activity of the source reduced over time. The fact these are 3D printed grooves increases the accuracy in the foil position, while also reducing the time needed to position the foils between measurements.

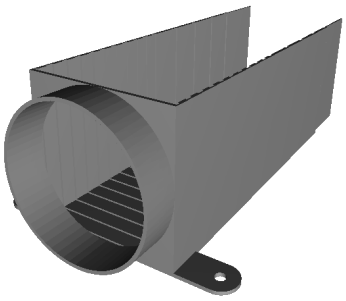
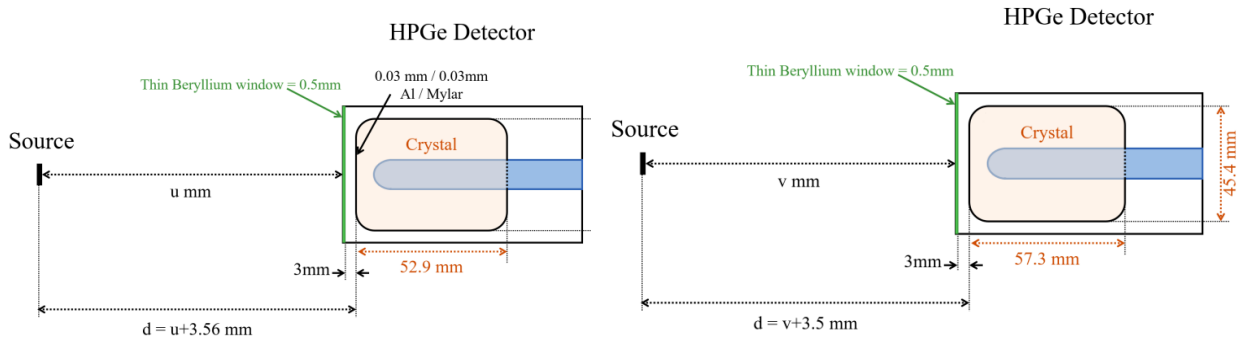


Figure 4.26: *A render of the 3D printed target holder, containing a circular hole for the HPGe detector to slide into. There are then several slits at various distances throughout the device to enable perspex plates holding the irradiated foils to be placed.*

4.6.2 HPGe Detector

Hyper Pure Germanium (HPGe) detectors were used in this experiment due to their high energy resolution. Two detectors were used in two different locations to enable simultaneous measurements without the activity of one source interfering with the other. The location of the two detectors will be referred to by their room names G11 and B15, used predominantly for the analysis of foils 1-4 and 5-8, respectively. Both detectors are p-type semi-conductors with coaxial crystals. Schematics of the detectors in G11 and B15 are shown in figure 4.27 and the specification is given in the appendix.



(a) *G11* ***(b)*** *B15*

Figure 4.27: *Schematic of both HPGe detectors used in the experiment with dimensions overlaid [110].*

Characteristics usually used to differentiate different spectroscopy detectors are, the timing resolution, energy resolution and efficiency of detection. In this set-up, coincidence counting was not used,

making timing resolution less critical. Therefore, the detector's ability to resolve a γ-ray's energy and the efficiency of detection of the γ ray are the two important characteristics in this set-up.

4.6.3 Energy Resolution

The energy resolution is the relative energy width of a detector's γ ray response. This parameter is important as it is correlated to the ability to distinguish one energy peak from another. The energy of an emitted γ-ray is quantised and therefore mono-energetic, provided that the lifetime isn't short enough that Heisenberg's uncertainty principle dominates ($\Delta E \Delta t \approx \frac{\hbar}{2}$), in which case the detected energy has a Lorentzian shape. For states with lifetimes longer than a few femtoseconds, this effect is negligible, being less than 1 μeV, compared to the 1-2 keV resolution of an HPGe detector. Therefore, for these longer-lived decays, the resolution response is determined only by the detector's intrinsic ability to resolve the energy.

Resolution can be written mathematically as

$$R = \frac{\text{FWHM}(E)}{E}, \tag{4.8}$$

where E is the energy of the γ ray and FWHM(E) is the full width at half-maximum of the detector response, which is the convolution of: a normal Gaussian, low energy skewed Gaussian and often a lower energy Compton edge as shown in figure 4.28, however, the normal Gaussian component is the most significant contribution.

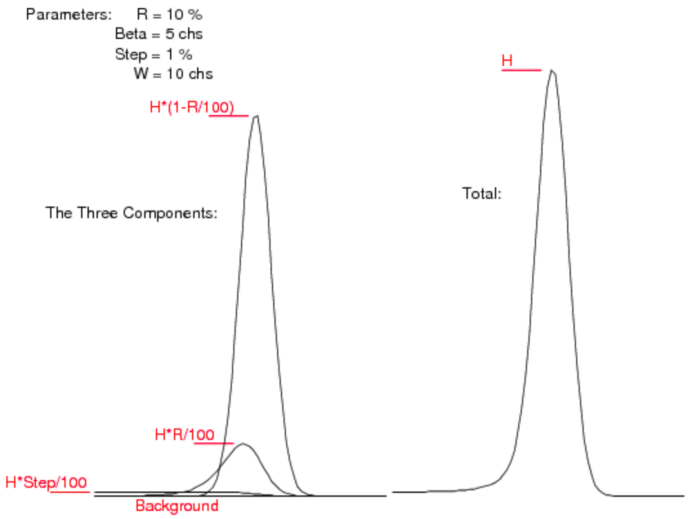


Figure 4.28: *The detector response of a γ ray, broken down into its constituent contributions, including a normal Gaussian, skewed Gaussian and Compton edge labelled as 'Step' in the above image [117].*

The FWHM can be related to the standard deviation for a Gaussian distribution as FWHM=$2\sigma\sqrt{2ln(2)}$. The total FWHM of the response, $\text{FWHM}_{overall}$ is given as the sum in quadrature of the statistical, noise and drift-related variance

$$\text{FWHM}^2_{overall} = \text{FWHM}^2_{statistical} + \text{FWHM}^2_{noise} + \text{FWHM}^2_{drift}. \tag{4.9}$$

In the majority of cases, it is the statistical variance which limits the resolution of a detector. The variance comes from the number of signal carriers produced in a gamma-ray interaction within a detector. The number of signal carriers, N, is related to the energy of the gamma-ray, E, and the energy to create a single signal carrier, ω, $N = \omega E$. A single signal carrier is produced by a single electron-hole pair in a semiconductor detector. While it is true that the γ-ray emission is quantised and every emission from a particular decay channel contains a discrete amount of energy, the interaction process within the detector is random. Therefore, there are random fluctuations in the number of signal carriers produced inside the detector. According to Poisson statistics, this variance is related to the square root of the number of signal carriers, $\sqrt{N}$. This enables the statistical fluctuation to be defined in terms of the energy of the γ-ray, E, the energy to produce a single signal carrier, ω, and a

constant of proportionality, K.

$$\text{FWHM}(E)_{statistical} = K\sqrt{E\omega}. \tag{4.10}$$

With the statistical effects being the predominant influence on the width, $\text{FWHM}_{overall} \approx \text{FWHM}_{statistical}$, the relationship between the energy, E, the γ ray and the resolution, R may be given as

$$R_{statistical} = \frac{K\sqrt{\omega E}}{E}. \tag{4.11}$$

On a log-log plot, this gives a relationship of $\ln(R)$ to $\ln(E)$ as a linear line with a gradient of $-\frac{1}{2}$. However, with semiconductors such as HPGe detectors, the production of each electron-hole pair is not random, so the standard deviation is smaller than predicted Poisson statistics. This is accounted for by a factor known as the Fano factor

$$F = \frac{\text{Observed variance in } N}{\text{Poisson predicted variance}}, \tag{4.12}$$

which gives a correction to the resolution equation 4.11, as

$$R_{statistical} = \frac{K\sqrt{F}\sqrt{\omega E}}{E}. \tag{4.13}$$

In semiconductors, such as HPGe detectors,the Fano factor is well below unity, usually around 0.1. This causes the electrical noise to become dominant and, thus, FWHM is constant as a function of energy. In this case, when resolution is plotted against energy on a log-log plot, the gradient is -1 as

$$R = \frac{Kc}{E}, \tag{4.14}$$

where the variables have the same meaning as before, and c is a constant variance due to electrical noise.

The gamma-spectrometry analysis code used in this project, Radware gf3, can store the fitted data into a .sto file. Edits were made to the source code of Radware, to output the widths of fitted peaks in

the .sto files. This enabled the resolution characteristics of the detector to be understood, as well as validating the fits. Any peaks with a resolution significantly higher than the established trend would indicate that a double peak has been incorrectly fitted as a single peak. The resolution against energy was plotted on a log-log plot for the two detectors used in the experiment, in G11 for foils 1-4 and B15 for foils 5-8. This plot includes the resolution of every peak fitted for the two detectors. These plots are shown in figure 4.29 and 4.30 for the detector in G11 and B15 respectively.

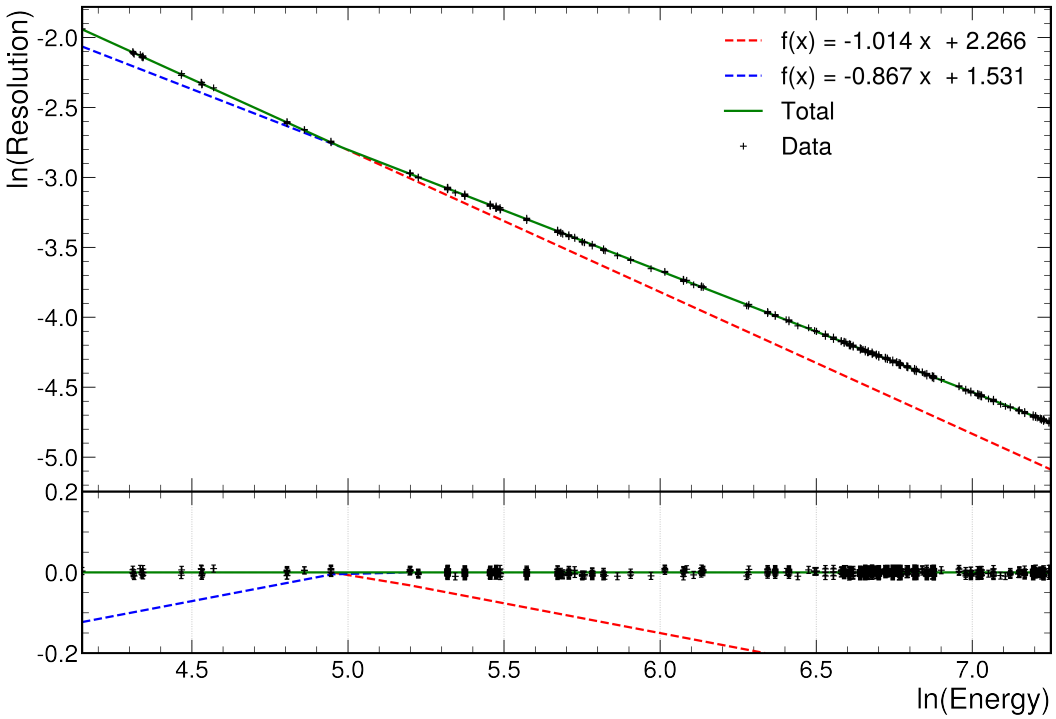


Figure 4.29: *Resolution against gamma-ray energy for the G11 HPGe detector, shown on a log-log plot, with the two fit lines shown, for the respective energy regions in red and blue and the dominating resolution shown in green. The cross-over between the two lines is at* 148 *keV, the energy at which the number of signal carriers is sufficient not to be resolution limiting.*

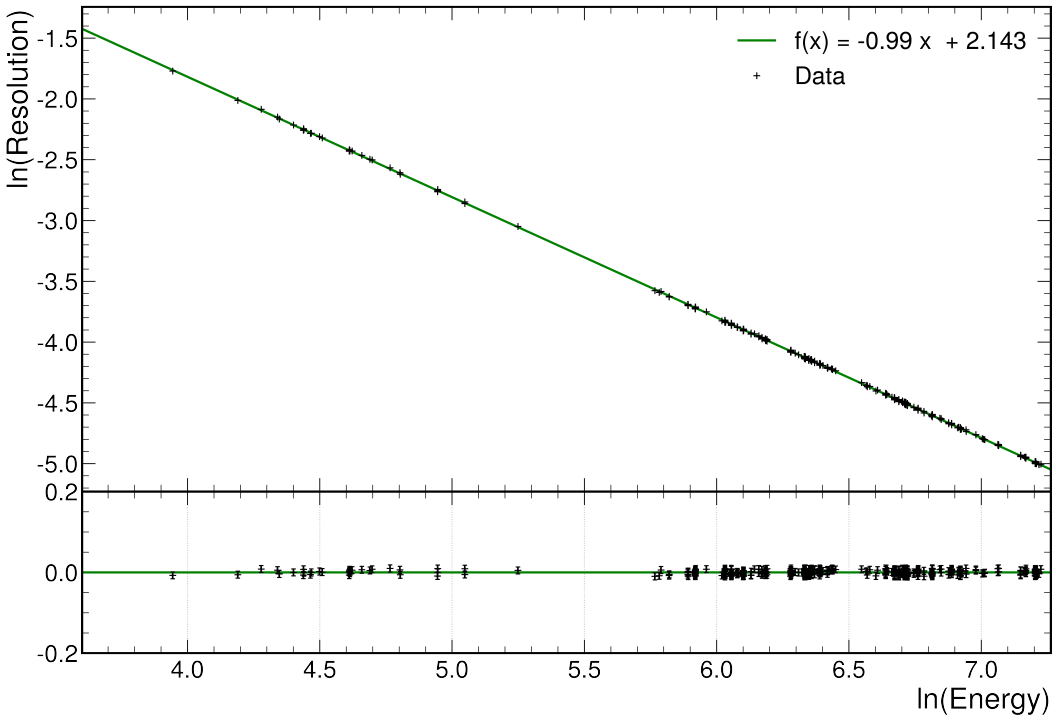


Figure 4.30: *Resolution against gamma-energy for the B15 HPGe detector, shown on a log-log plot, with a linear fit line shown in green, with a gradient of* -0.99.

It is clear from the figures that both detector resolutions are dominated by noise at lower energies, with gradients of -1.08 and -0.99 for the G11 and B14 detectors, respectively. At higher energies, the effects of noise become the dominant factor for the G11 detector due to the E^{-1} dependency, resulting in a greatly reduced number of signal carriers, giving a gradient of -0.867.

4.6.4 Detector Efficiency

Another important characteristic of a γ-ray detector is intrinsic photo-peak efficiency, the probability of a γ-ray that passes through the detector, having its entire energy measured, known as a photo-peak detection. When a γ ray, or any photon, passes through a detector, there are three possible interactions: Compton scattering, the photo-electric effect and pair production. The cross-section of these three interaction mechanisms is a function of the photon energy E and the atomic number of the material, Z. The energy and atomic number at which these interactions dominate are shown in figure 4.31. The absolute value and the competition between these effects are what results in a detector's efficiency.

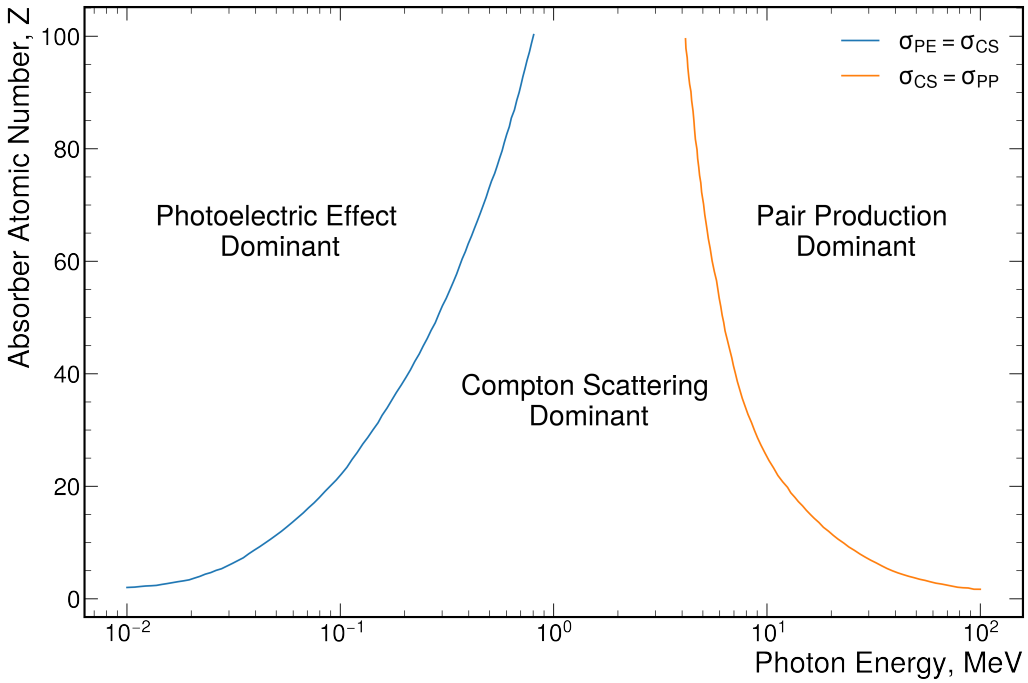


Figure 4.31: *The relative probability of any particular detection mechanism occurring for photon energy, E and detector atomic number, Z [118].*

Photons that interact through the photo-electric effect are detected and counted in the analysis and approximately form a Gaussian distribution around the mean photon energy. A fraction of photons will Compton scatter with electrons in the detection material, depositing energy to the electron as they scatter away. If the scattered photon and the recoil electron are both detected, the whole energy of the photon is measured, and the response will contribute to the photo peak. If the scattered photon passes through the detector without being absorbed, only the energy deposited on the recoil electron is measured. The energy carried by the recoil electron is a function of the energy of the incident photon and the scattering angle. This gives a spread of detected Compton energies E_{comp}

$$E_{comp} = E_i - \left(\frac{E_i}{(1 + \frac{E_i}{m_e c^2}(1 - \cos\theta)} \right), \tag{4.15}$$

where E_i is the incident photon energy, θ is the scattering angle of the photon, m_e is the rest mass of an electron and c is the speed of light. The maximum energy deposited on the recoil electron is when

$\theta = \pi$, giving an artefact seen on the Compton continuum known as the Compton edge as it is the highest energy detected in the Compton continuum. This means the energy of Compton scattering stops below the photo-peak, and there is no interference between the continuum and the photo-peak for a high-resolution detector and single scatters. The Compton scattering contributions overlap with lower energy photo-peaks and detriment the counting accuracy and increase the limit of detection. Compton scattering can be limited by increasing the detector volume, thus increasing the probability of a scattered photon being absorbed rather than leaving the detector.

The third effect that can be seen is from pair production, where a photon interacts in the field of an atom and produces an electron-positron pair. This requires the photon to have a minimum energy of the sum of the electron and positron rest mass, $E = 2m_e c^2 = 1.022$ MeV. While this is the minimum energy of the effect, it becomes increasingly likely at higher photon energies. Any additional energy above the rest energy is converted to the kinetic energy of the electron-positron pair, which is transferred to the detector medium over a very short range. The positron then forms a short-lived exotic atom with an electron which, once all kinetic energy is lost, annihilates, forming two 511 keV photons. The loss of either or both of these photons causes escape peaks. A single escape peak is 511 keV below the photo peak, and the double escape peak is 1022 keV below the photo peak due to one or both of the annihilation photons leaving the detector without interacting.

It should be noted that at lower energies, the probability of a photon interacting before it reaches the active detection volume is high, reducing the probability of the photon interacting within the detector. Additionally, high-energy photons have low cross-sections of interaction meaning the photons are more likely to pass through the detector without interacting.

When analysing a γ-ray spectrum, trying to determine the activity of a source, it is essential to accurately determine the probability of a photon interacting and giving rise to a response within the photo-peak of the detector. This is known as the intrinsic photo-peak efficiency, ϵ_{int} and is the proba-

bility of a photon that is incident on the detector being counted in the photo peak

$$\epsilon_{int} = \frac{N}{A\gamma\frac{\Omega}{4\pi}t}, \tag{4.16}$$

where N is the number of counts in the photo-peak, t is the length of time the spectrum was recorded for, A and γ are the source activity and the photon emission branching ratio, respectively, and Ω is the solid-angle subtended by the detector for a given source. This enables a correction from the isotropic gamma-emission to account only for the photons which are incident on the detector, assuming the source is point-like.

4.6.4.1 Solid Angle Calculation

The solid angle, Ω, accounts for the area of emitted photons that will intersect the detector face. This, as a fraction of 4π, gives the fraction of photons which will intersect the detector face, assuming photon emission to be isotropic. For a point source incident on a detector with a circular face

$$\Omega = 2\pi\left(1 - \frac{d}{\sqrt{d^2 + r^2}}\right), \tag{4.17}$$

where d is the distance from the front of the detector crystal to the source, and r is the radius of the detector crystal.

4.6.4.2 Efficiency Fitting

A detector's efficiency with respect to energy is determined by the attenuation of the photons through the detector window, and the interaction probability in the detector via the competing effects of photo-electric and Compton scattering, and at higher energies pair production. It is therefore hard to describe the shape of the efficiency by a simple mathematical function of energy. There are, however, several routines which utilise splice functions, including RadWare's empirical solution [119], taking a splice of lower energy and higher energy components,

$$\epsilon = e^{[(A+Bx+Cx^2)^{-G}+(D+Ey+Fy^2)^{-G}](-1/G)}, \tag{4.18}$$

where A-G are fit parameters, and

$$x = \ln\left(\frac{E_\gamma}{100\ \text{keV}}\right) \tag{4.19}$$

$$y = \ln\left(\frac{E_\gamma}{1\ \text{MeV}}\right). \tag{4.20}$$

The efficiencies of the detectors used in this experiment were initially calculated by collecting a spectrum for a long period to gain high statistics at a well-defined location from the detector. A ^{152}Eu γ-source was used due to its many emission peaks over a wide range of energies. The source had a low uncertainty of 5.7% on the activity. The efficiency was calculated using equation 4.16.

The efficiency calculated should be an intrinsic function of the detector, and the geometric efficiency of emissionf from the foils at any given point should be easily derived from this. During the analysis, it was noticed that the decay plots had clear dislocations in the activity values when the distance of the source was changed. Upon further inspection, this was determined to be due to the solid angle calculation not accurately accounting for the changing probability of interaction. The solid angle accounts for the probability of a photon being incident on the detector surface. At distances far from the detector face, the incident angle is much smaller than when the source is close to the face, affecting the thickness of the detector crystal, through which the photon will pass, and changing the probability of detection. The correction is explained in detail in section 4.6.6.2.

4.6.4.3 Efficiency Measurement Results

The efficiency was measured with a ^{152}Eu calibration source with an activity of $210(12)$ kBq for a live time of 12 hours at a distance of 15 cm from the detector face. The spectra were analysed in RadWare gf3 [119] with the fitting performed using the trf (trust region reflective) algorithm in the SciPy python package Optimize class. The efficiency plots produced for the detectors labelled as G11 and B15 are shown in figures 4.32 and 4.33 respectively.

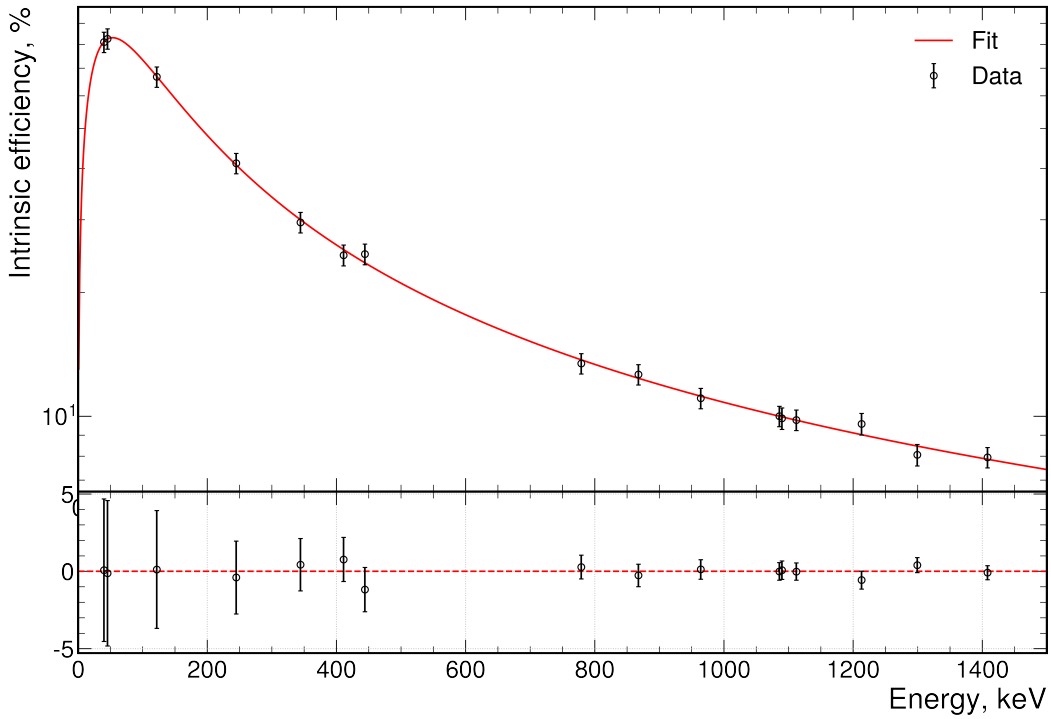


Figure 4.32: *Efficiency plot for the GII HPGe detector, taken for a* ^{152}*Eu calibration source at* 15 *cm for* 12 *hours.*

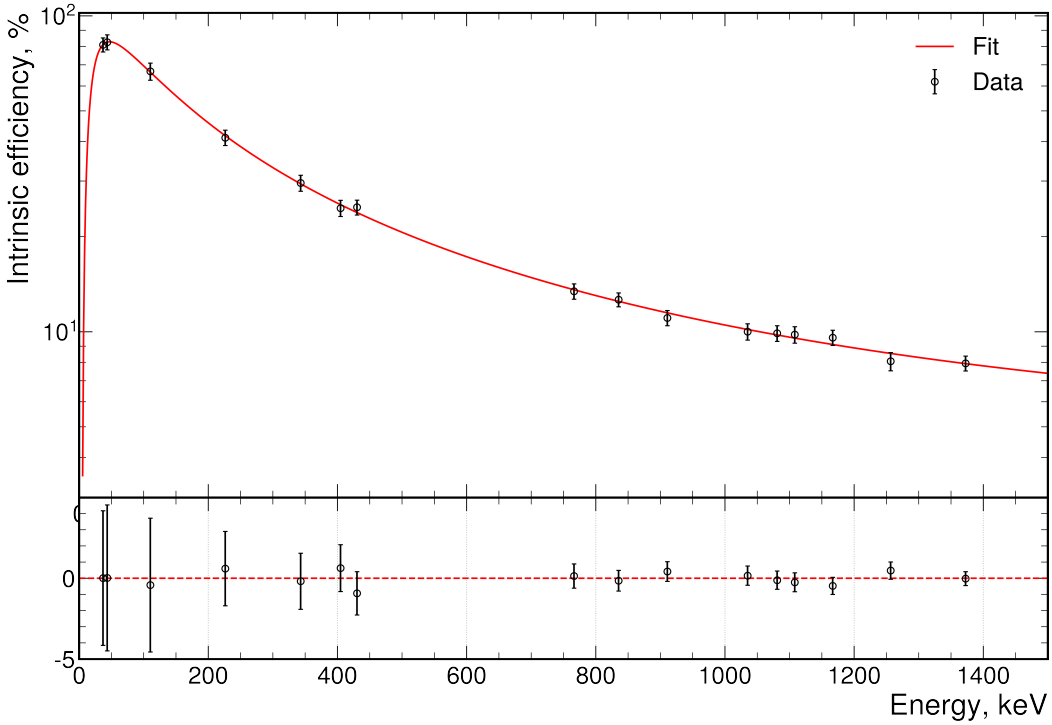


Figure 4.33: *Efficiency plot for the B15 HPGe detector, taken for a* ^{152}*Eu calibration source at* 15 *cm for* 12 *hours.*

4.6.5 Data Analysis

Analysis of the data acquired from the gamma-spectra had two main branches, online analysis, which was used to adjust the experiment as it proceeded, enabling the distance of the sources from the detectors to be adjusted and the live-time of the runs to reach the desired statistics, as well as the second component of the analysis which was off-line, which occurred after the data were taken and followed a much more rigorous process of fitting spectra and corrections to produce accurate and precise results.

For both the online and offline analysis, the data were analysed through identical steps for the majority of processing, with the only difference being the data fitting was automated in the online analysis. Figure 4.34 shows a flowchart of the analysis framework.

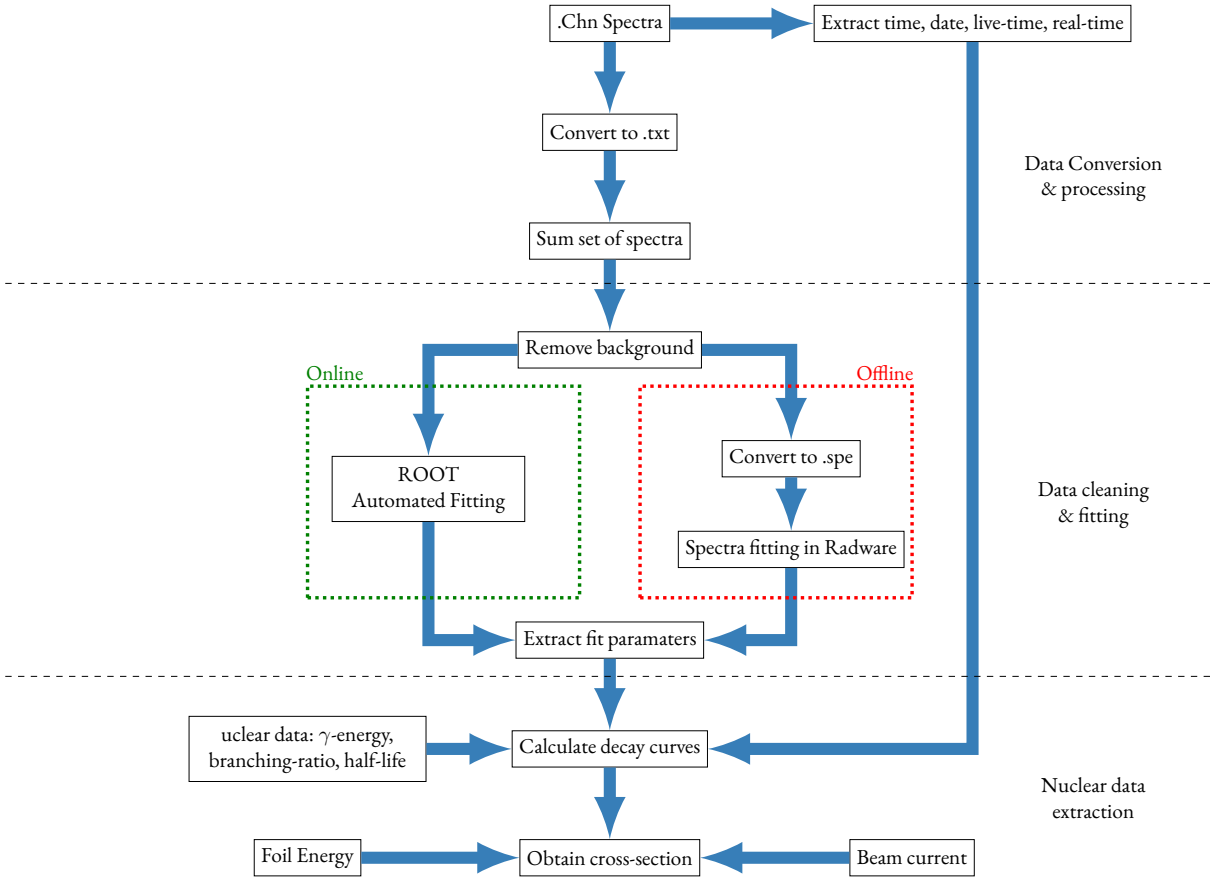


Figure 4.34: *A flowchart of the gamma-ray spectrometry analytical framework developed through this project, offering options for both online automated and offline data fitting.*

It can be seen that the analytical framework can be broken down in its simplest form into three main stages; data conversion and procession, data cleaning and fitting and nuclear data extraction.

4.6.5.1 Data Cleaning

Data were collected using Maestro gamma-spectrometry software, with spectra saved in the Ortec binary Chn format. Throughout the experiment, the summed spectra corresponded to times ranging from 5 minutes (for high activities and short half-lives) to 24 hours (for lower activities and longer half-lives). Individual spectra in a set were executed through batch files, enabling a series of successive spectra to be automatically collected. Each of the individual spectra were 300 seconds long throughout the entire experiment. The benefit of breaking the spectra into shorter spectra was that the effects of gain shift could be easily corrected, along with having to remove less data if data corruption occurred.

Data are stored in a folder hierarchy; day #, set #, foil #. At the beginning of the experiment, this folder structure is created automatically along with the batch scripts. This helps to maintain rigorous data structure and format, which enables smoother automatic analysis. Each spectrum within the foil # folder increments numerically starting with 000.Chn. Having day first, then set # second before foil # is convenient for data acquisition, however, for analysis, it is more convenient to group the data by the foil #. For this, a script was created which converted the folder hierarchy to foil #, day #, set #.

Once the overall data structure has been established, the first step of analysis involves the conversion of the spectra from Chn to txt, which is done using an open-source spec_conv script run as a subprocess. The .txt spectrum format is column-wise data with each row accounting for a channel. Spec_conv outputs important meta-data, including the real-time, live-time, start-time and date to the terminal. As the analysis code runs spec_conv as a sub-process, these data are read and stored in a file called spec_data.txt in the same folder as the spectra. Each row of the file contains all of the meta-data for a spectrum. The script preemptively creates a row at the bottom containing the data for a summed spectrum. This uses the start-time and date of the first spectrum along with the sum of real-time and live-time for each spectrum.

The spectra are then summed to give a total.txt file stored in the same folder as the individual spectra.

4.6.5.2 Online Data Visualisation

The online components of the analysis enable the data to be processed, cleaned and visualised in real-time. This enables any potential gain shift to be understood, or to determine whether the statistics of the spectra being recorded are still reasonable, or whether alterations must be made to either the geometry or the live time of the spectra being collected. Figure 4.35 shows an online data visualisation showing each spectrum successively along the y-axis. The x-axis shows the channel number or energy depending on whether a calibration has been input into the analysis software. The counts or count rate is shown on the z-axis.

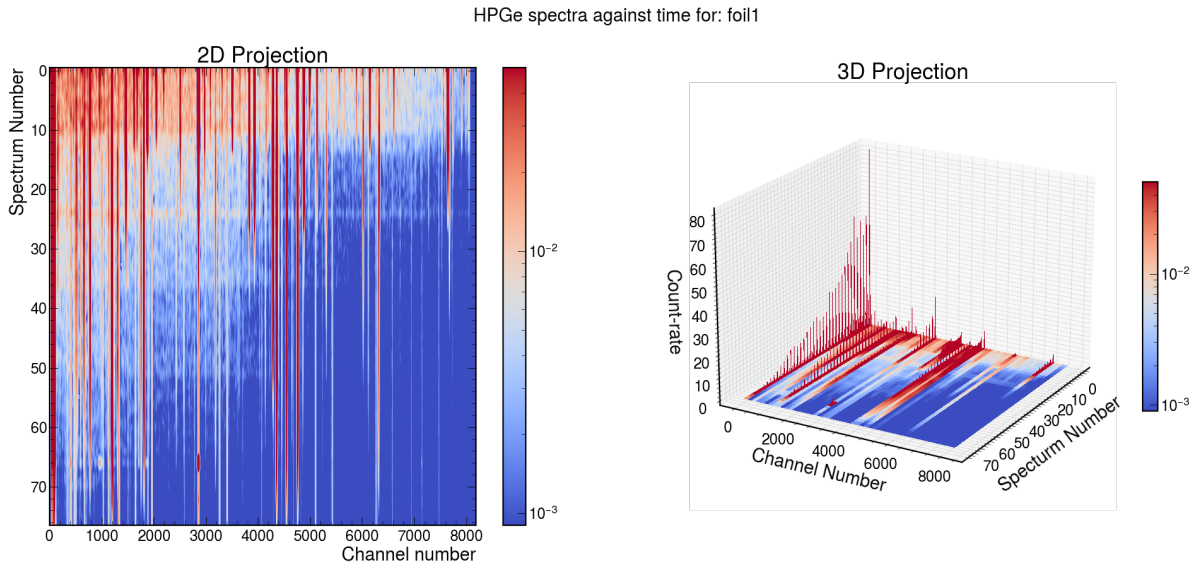


Figure 4.35: *Online gamma-ray spectra visualisation, showing a 2D and 3D representation of channel and counts for each successive spectrum.*

Work was undertaken to produce online decay curves, which rely on automated peak fitting of pre-determined peaks of interest with their half-life indicated. The advantage of this is that a warning could be generated in the analysis software to indicate that a count rate or the expected summed counts in a spectrum are below a statistical threshold, indicating when adjustments are needed to the spectrum measurement time or geometry. This is an adaptation to the offline analysis software, which would require a more robust peak fitting routine if automation were to be used.

4.6.5.3 Peak Fitting

Peak fitting is the most important stage of the analysis, and the chosen method greatly impacts the precision of the analysis. The centroid, peak area and width, and corresponding errors must be stored at this stage. While the width of the peaks is not required in the analysis, it is an important tool in validating the goodness of fit. The width can be used to calculate the resolution. If there are any outliers, this may be due to improper fitting such as a double peak being fit as a single peak. There are many possible analysis methods, however, two have been used in this work, ROOT for automated online analysis and RadWare for high-precision manual fitting following the experiment.

The .txt files are imported into ROOT for online analysis using the pyROOT interface. Background subtraction is performed, which accounts for Compton effects as this was seen to improve the fit's accuracy significantly. A peak-finding algorithm is then used to find peaks before a Gaussian fitting routine is performed. The algorithm has a high rate of false positives, interpreting spectrum noise as a peak. These can be filtered by setting constraints on the width of the peaks as well as the minimum area. An extra filtration step involves only accepting peaks which line up in energy with peaks which are looked for. This requires the spectrum to have a calibration. The count rate is output for each of the gamma-ray peaks. This can determine the number of counts produced if a spectrum was run for a certain time at any given distance from the detector. The fitted data are stored as a file called fitted_data.txt containing the centroid, area, and width matched energy, and their respective errors.

On the other hand, manual offline analysis is used for the final offline analysis due to the much higher precision and accuracy attainable for the fitted areas. All offline analysis was performed using the RadWare [119] gamma-ray spectroscopy analysis software. This is a program developed by D.C. Radford at Oak Ridge National Laboratory to analyse HPGe gamma-ray spectra. The program accurately fits the peaks as a convolution of a skewed Gaussian with a low-energy Gaussian contribution. To perform fitting in RadWare the spectra must be converted into RadWare's own spectrum format (.spe). This process was performed again using the spec_conv program. The process of manual fitting was optimised by editing the RadWare source code to enable the addition of widths to 'Store Areas' function. The function now outputs the fitted areas, centroids, widths and respective errors to be written to file, stored as gf3.sto files. These files are then parsed into python, with the peaks matched to expected gamma-ray peaks and the file stored as fitted_peaks.txt.

4.6.5.4 Calculating Decay Curves

Once the fitted data have been stored and parsed into the fitted_peaks.txt format, the code reads through all files with this name within a foil #, simultaneously extracting the live-time, real-time, start-time and date. At the top level within the foil # folder, a file is created for each of the gamma-energies, containing the area, error on area, live-time, real-time, date and distance between the foil and the detector for each

spectrum.

The decay curves can then be calculated by converting the number of counts under a peak to the activity

$$A(t) = \frac{N}{\epsilon_{int}(E)\gamma\frac{\Omega}{4\pi}t}. \tag{4.21}$$

The activity of the isotopes will decay exponentially, meaning the logarithm of the activity against time gives a straight line

$$\ln\big(A(t)\big) = -\lambda t + \ln(A_0), \tag{4.22}$$

where A is the activity at a time, t following the irradiation, λ is the decay constant, and A_0 is the activity at the end of the irradiation. Converting the decay to a linear line simplifies the extraction of the parameters, A_0 and λ. Fitting of a linear line is mathematically more simple and improves the accuracy of fitting. All linear fits were accomplished using the Scipy python package Optimize class fitting routine, using the trf (trust region reflective) algorithm. A decay curve for ^{97}Ru is shown in figure 4.36

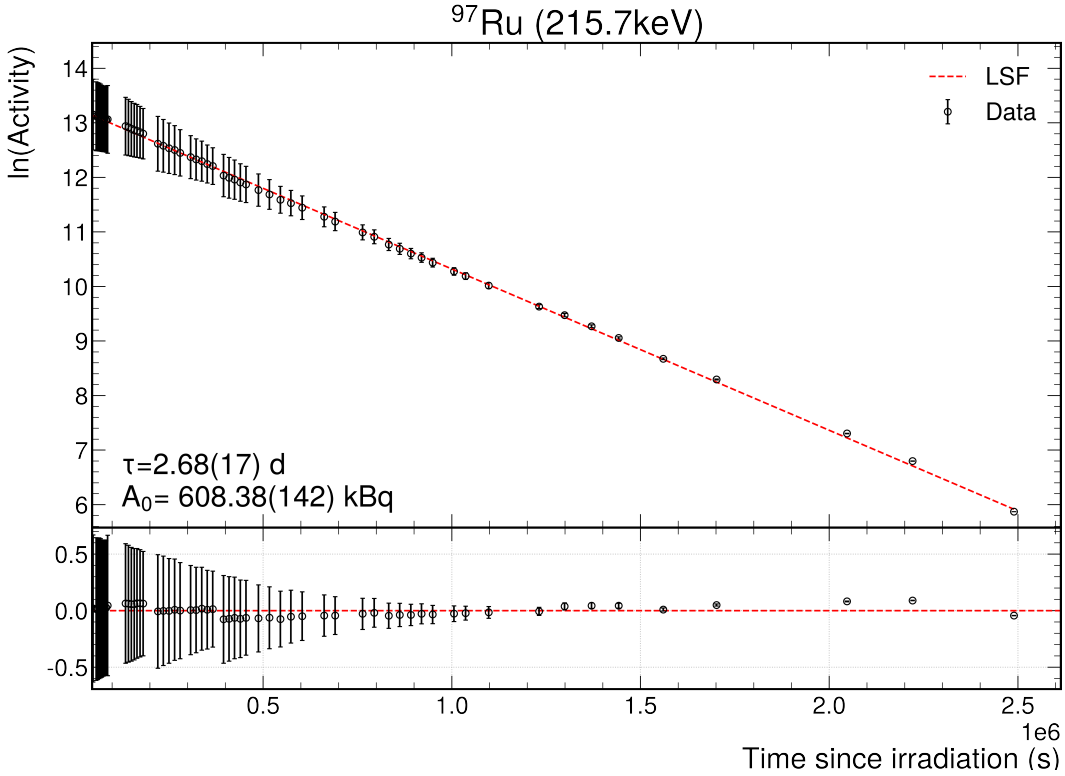


Figure 4.36: *A decay curve for* ^{97}*Ru measured using the* $215.70(3)$ *keV* γ*-emission for foil* 1.

4.6.5.5 Cross-Section Calculation

Once the activity has been calculated, the cross-section, σ_i, can be calculated as

$$\sigma_i = \frac{A_i(0)}{N_T \sum_{k=1}^{n} I_k \left[1 - e^{-\lambda_i(\tau_k^f - \tau_k^i)}\right] e^{-\lambda(T-\tau_k^f)}}, \tag{4.23}$$

where $A_i(0)$ is equal to A(t) given in equation 4.21, for a given isotope, i and at time, $t = 0$. I_k is the beam current for an individual step in the irradiation, λ_i is the decay constant of isotope, i, τ_k^i and τ_k^f are the start and end times of a given irradiation step, k and τ is the time at the very end of the irradiation, and N_T is the target areal number density which can be calculated as

$$N_T = \frac{\rho N_A}{A_r} x, \tag{4.24}$$

where ρ is the mass density of the target, N_A is Avogadro's constant, A_r is the atomic weight of the target and, x, is the target thickness for which the beam is above the reaction threshold. For all of the

calculations, N_T was calculated as $7.12(47) \times 10^{18}$ cm^{-2}.

4.6.6 Data Correction

Following the initial cross-section analysis, several errors were discovered that needed to be addressed. This section details these corrections and the effects these had on the output data.

4.6.6.1 Counts corrections

When calculating the half-lives from the decay curves, shorter half-lives had a greater discrepancy from the quoted values on ENSDF, along with spectra collected over greater periods. This shows a divergence from quoted values with increased spectrum collection time to half-life ratios.

For each spectrum, the counts over the entire collection time was attributed to the start time of the spectrum. As the isotope is decaying throughout the collection time, the average count rate over the time of the spectrum is lower than the count rate at the start time. Rather than calculating the count rate by simply dividing the number of counts by the live time, a correction that accounts for the isotope's decay throughout the spectrum length can be applied:

$$A(t) = \frac{A}{1 - e^{-\lambda\tau}}, \tag{4.25}$$

where $A(t)$ is the corrected count rate, A is the spectrum count rate, λ is the decay constant, and τ is the real-time of the spectrum. The derivation of the correction is given in appendix E.

4.6.6.2 Efficiency Corrections

When calculating decay curves, clear dislocations were observed in the residuals, as seen in figure 4.36. The cause of these shifts was investigated, and by differentiating the data points at different distances between the source and the detector, the cause can clearly be seen, as in figure 4.37.

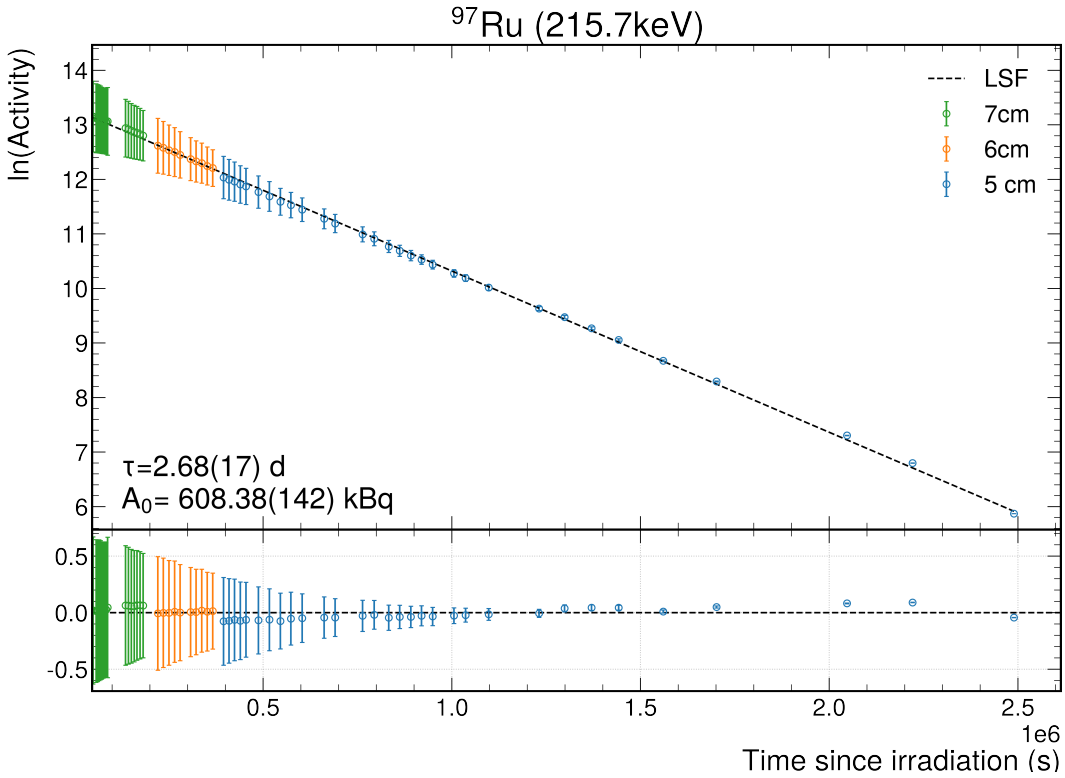


Figure 4.37: *Plot of the decay of ^{97}Ru measures on foil 1, with the data points taken at different distances given in different colours to highlight the dislocation in the count rate.*

This indicated an error in the geometric efficiency calculation. Upon further investigation, this comes down to the efficiency being calculated simply by dividing the count rate by the geometric efficiency to get the activity, where the geometric efficiency is calculated as

$$\epsilon_{geo} = \epsilon_{int}\left(\frac{\Omega}{4\pi}\right)^{-1}, \tag{4.26}$$

where ϵ_{geo} is the geometric efficiency, ϵ_{int} is the intrinsic efficiency and Ω is the solid angle. The limitation of this approach is that it only considers the probability of a photon being incident on the detector face. Taking the two extreme cases, a photon from a source an infinite distance from the detector will only pass through the detector if it is perfectly parallel to, and centered on, the axis of the detector, whereas a photon from a source which subtends the detector would pass through the detector over a 2π coverage, meaning a photon is more likely to pass through the edge of the detector, where the distance the photon travels through the detector may be much shorter. The probability of

an interaction occurring is proportional to the distance travelled through the detector.

Efficiency measurements were performed using a ^{152}Eu calibration source for each source position used in the experiment: 5 cm, 6 cm, 7 cm, 8 cm, 9 cm, 10 cm, 12.5 cm, 15 cm, and 17.5 cm. The analysed results are shown overlaid for each of the positions in figure 4.38.

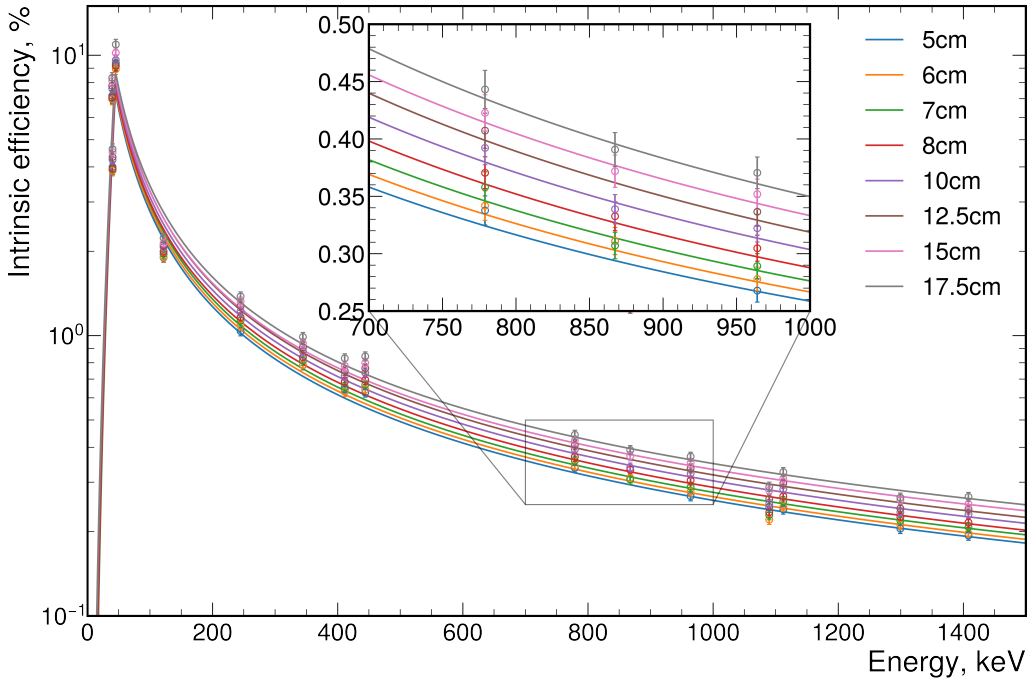


Figure 4.38: *A plot of the intrinsic efficiency calculations performed using a ^{152}Eu calibration source for each source position used in the experiment.*

The corrected distance-dependent efficiency calculations were then applied independently to each data point at each respective distance.

Applying this efficiency to the decay curve for ^{97}Ru shown in figure 4.37 above, the correction resolved the dislocations seen at each distance, enabling a more accurate value for initial activity and the half-life to be determined. The corrected decay curve is shown in figure 4.39.

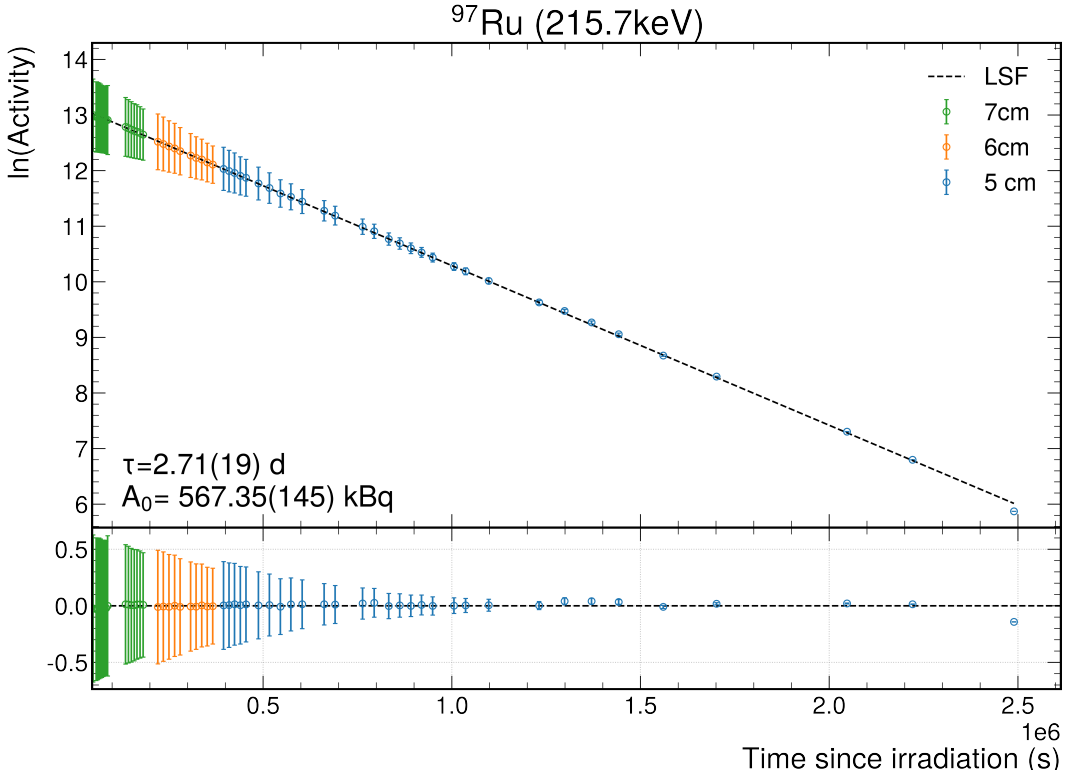


Figure 4.39: *Plot of the decay of ^{97}Ru measures on foil 1, with the data points taken at different distances given in different colours, with the new efficiency correction applied.*

The benefit of the correction can be seen in the improved half-life measurement. The ENSDF published value for the half-life of ^{97}Ru is $2.83(32)$ days [56]. The decay curve without the correction had a value of $2.68(17)$ days and with the correction, the half-life was calculated as $2.71(19)$ days. The half-life obtained here is within one standard deviation of the published value but has a smaller uncertainty. The error on the half-life is slightly higher for the corrected decay curve at 0.19, compared to 0.17 for the uncorrected curve. This is due to the greater alignment of the data points enabling greater variance allowed in the least-squares fit, however, this is a more realistic value.

The correction has had an effect on the initial activity value, from $608.3(14)$ kBq in the uncorrected analysis to $567.3(14)$ kBq in the corrected analysis, which will affect the calculated cross-section value. In both of the decay curves, the count rate error is very high in the initial measurements compared to the longer measurement times. This is due to the shorter measurement times compared to the half-life of the isotope. At earlier points in the experiment, the set-up was optimised to capture short-lived

isotopes with greater fidelity on the collection time, resulting in shorter measurement times. In future experiments, this could be improved by using continuous measurements, whereby the spectra could be segmented at different rates depending on the half-life of the isotope being analysed.

4.6.7 Sequential decays

There are several isotopes which are analysed in this measurement, where the product will be both produced directly and through the decay of another isotope. A good example of this is the decay of ^{99m}Tc, which decays with a half-life of $6.0067(5)$ h through a $140.511(1)$ keV γ-ray emission with a branching ratio of $89(4)\%$. This isomer is also populated by the 100% beta decay of ^{99}Mo, with a half-life of $65.976(24)$ h. When analysing the decay curve produced from the 140.511 keV γ-ray emission the log of activity against time is not linear, as shown in figure 4.40.

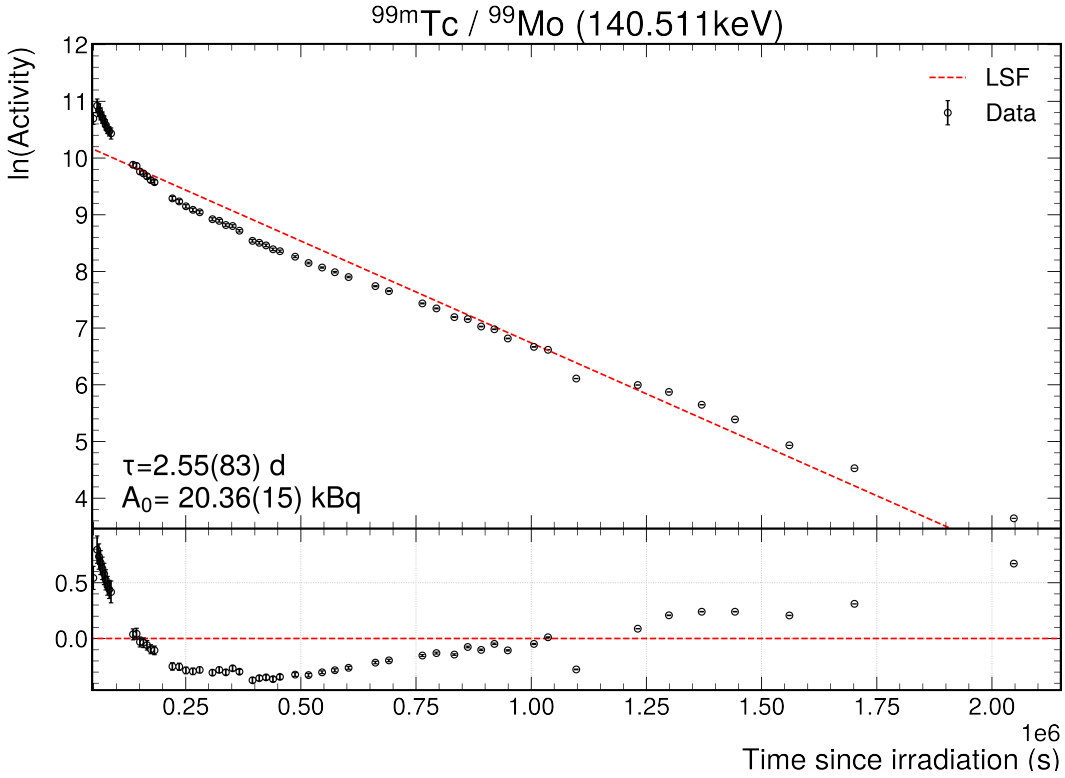


Figure 4.40: *Plot of the decay of the* 140.511 *keV* γ*-emission, showing a non-linear trend due to the contributions from* ^{99m}*Tc produced directly in the reaction, exhibiting the intrinsic half-life of* $6.0067(5)$ *h, dominated at longer decay times by the* ^{99}*Mo half-life of* $65.976(24)$ *h due to the equilibrium between the* ^{99}*Mo and* ^{99m}*Tc.*

This was resolved by stating two isotopes in the analysis code, for decays which had contributions from multiple decays. The data was a sum of two linear fits, where the half-lives of the two isotopes were placed as the initial estimates of the gradient to force the desired fit. The results of this can be seen in figure 4.41.

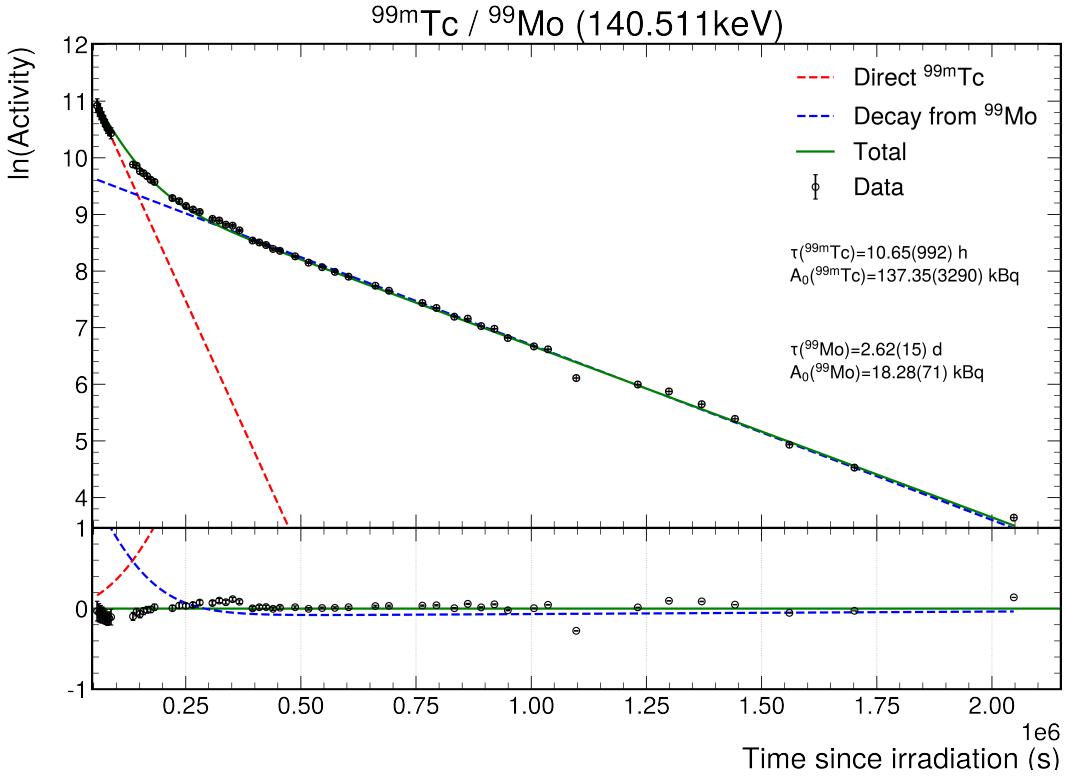


Figure 4.41: *Plot of the decay of the* 140.511 *keV* γ*-emission, showing a non-linear trend due to the contributions from* ^{99m}*Tc produced directly in the reaction, with a half-life of* $6.0067(5)$ *h, dominated at longer decay times by the* ^{99}*Mo half-life of* $65.976(24)$ *h due to the equilibrium between the* ^{99}*Mo and* ^{99m}*Tc.The data have been fit as the sum of two exponential decays, one for the short-lived* ^{99m}*Tc and one for the longer lived* ^{99}*Mo.*

From the residuals, the fitting of two decays is reasonable, comprising of short-lived ^{99m}Tc with the longer-lived ^{99}Mo. The ^{99m}Tc half-life was measured to be $10.65(992)$ h, which is within errors of literature values, $6.0067(5)$ h [24], however, the mean value is 77% larger. The longer-lived decay rate controlled by the decay of ^{99}Mo decaying into ^{99m}Tc resulted in a half-life of $2.62(15)$ d, which is within errors of the literature values of $2.749(1)$ d [24]. What is additionally evident from this plot is the reduced accuracy for shorter half-lives, such as the direct decay of ^{99m}Tc, which is expected to be due to the reduced measurement time and greater distance from the detector. For the improvement of

nuclear data for the development of a ^{97}Tc radiotracer through the production of a ^{97}Ru generator, this is not a concern as the isotopes of the greatest importance are ^{99}Mo with a half-life of $2.749(1)$ d [24] and ^{97}Ru with a half-life of $2.83(23)$ d [56].

4.6.8 Predicted isotopes and γ emissions produced in the Mo-α reaction

Determining the isotopes which could be analysed through γ-spectrometry decay analysis is a two-stage process. From the TALYS and FISPACT-II calculations, the expected products are known. Importing the γ-energies and intensities from ENSDF gave insight into the expected spectrum. Once analysis began, any peaks which were found, that were not already accounted for either through the ENSDF list or as known background peaks were investigated using the NuDat γ search tool [120]. As decay curves were produced in the analysis, the energy of the peak and the half-life could be used to determine the parent decay of any peaks.

A known background contaminant is ^{40}K, present in humans as a natural radiation source. Potassium-40 has a half-life of $1.248(3) \times 10^9$ years and has a gamma-ray at $1460.820(5)$ keV, with branching ratio of $0.1066(17)$.

The list of gamma-energies investigated in the analysis includes an array of isotopes of Nb, Mo, Tc and Ru. The full list of isotopes are: ^{90}Nb, ^{93m}Mo, ^{99}Mo, ^{93}Tc, ^{94}Tc, ^{94m}Tc, ^{96}Tc, ^{99m}Tc, ^{94}Ru, ^{95}Ru, ^{97}Ru and ^{103}Ru. Short-lived isotopes were only present in the initial spectra, while the longer-lived isotopes often have lower activity, meaning these isotopes were only picked up later in the analysis when the spectra' live times were increased. Spectra from day 1 and day 7 are shown for foils 1 and 8 in figures 4.42—4.45 breaking the spectrum into four sections; E $<$ 350 keV, 350 keV $\leq$ E $<$ 700 keV, 700 keV$\leq$ E $<$ 1050 keV, 1050 keV$\leq$ E. Overlaid are the published gamma-ray energies.

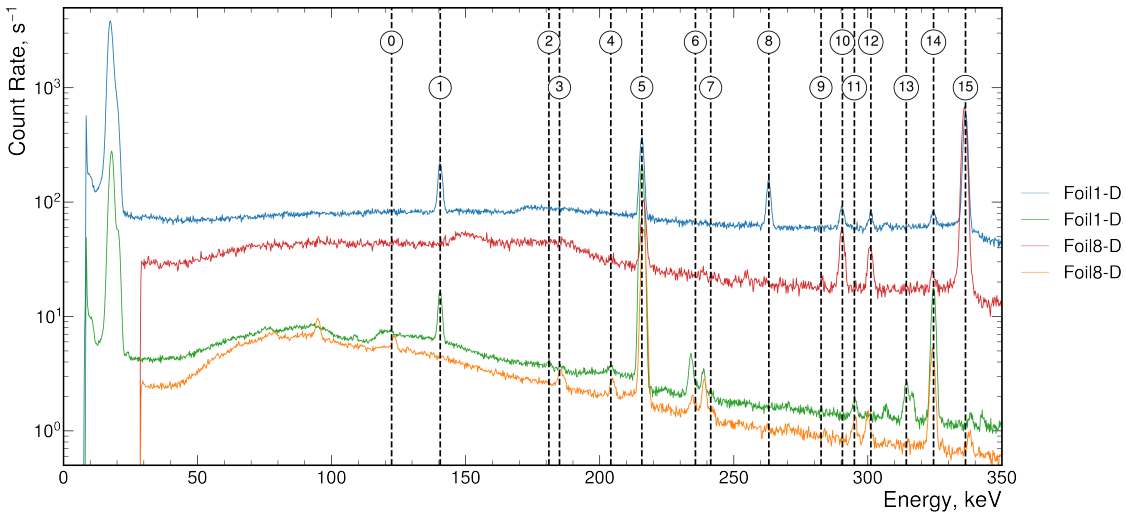


Figure 4.42: *Spectra with peaks highlighted for energy* < 350 *keV for foils* 1 *and* 8 *on days* 1 *and* 7. *The highlighted peaks can be found in table 4.9 and 4.10.*

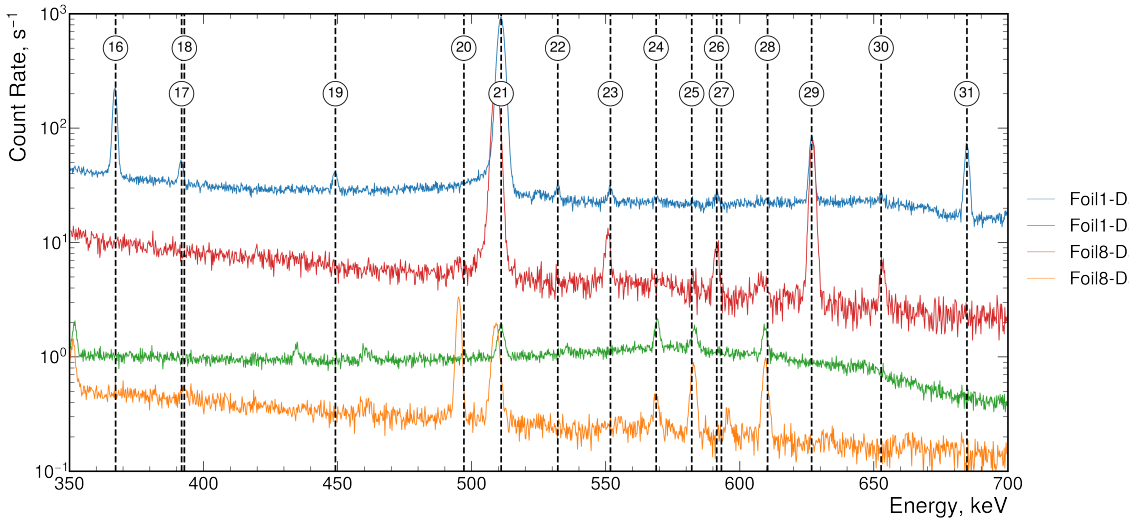


Figure 4.43: *Spectra with peaks highlighted for energy* 350-700 *keV for foils* 1 *and* 8 *on days* 1 *and* 7. *The highlighted peaks can be found in table 4.9 and 4.10.*

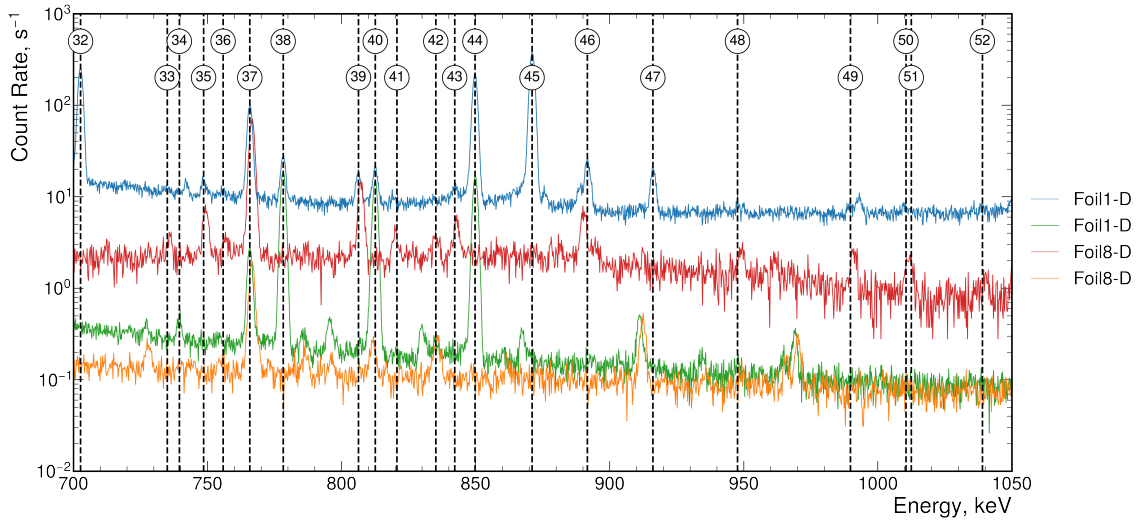


Figure 4.44: *Spectra with peaks highlighted for energy* 700-1050 *keV for foils* 1 *and* 8 *on days* 1 *and* 7. *The highlighted peaks can be found in table 4.9 and 4.10.*

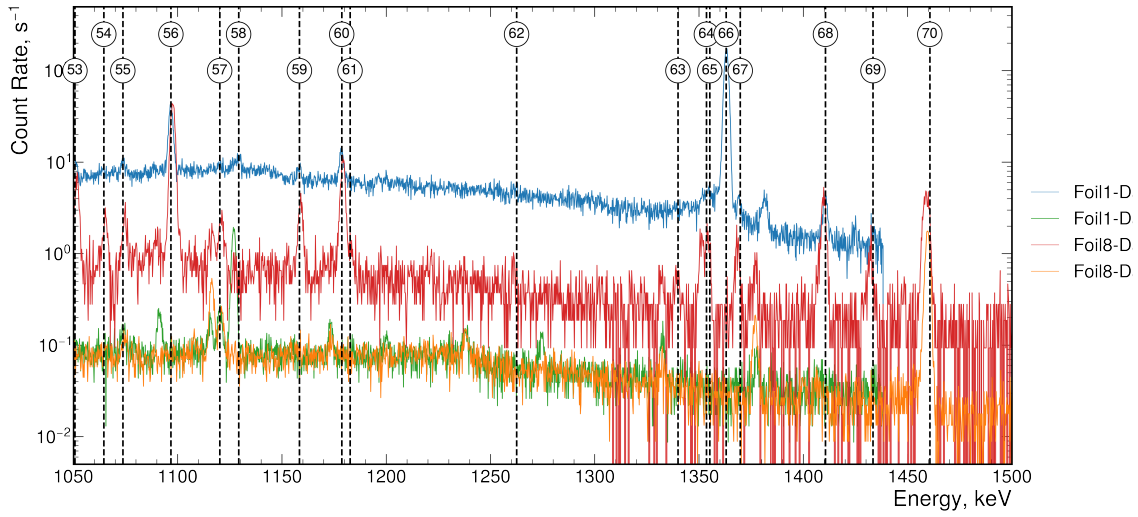


Figure 4.45: *Spectra with peaks highlighted for energy* $>$ 1050 *keV for foils* 1 *and* 8 *on days* 1 *and* 7. *The highlighted peaks can be found in table 4.9 and 4.10.*

The peaks highlighted in the spectra can be seen in table 4.9 and 4.10, showing the energy, intensity and respective errors.

Table 4.9: *Table of predicted gamma-ray energies* 0-35 *from the* ^{nat}*Mo-α reaction, extracted from ENSFD [25].*

Peak #	E, keV	ΔE, keV	Isotope	I, %	ΔI, %
0	122.37	0.022	^{90}Mo	64.2	2.3
1	140.511	0.01	^{99m}Tc	89	4
2	181.068	0.08	^{99}Mo	6.05	0.12
3	185.0	0.1	^{97}Ru	0.0046	0.0021
4	204.117	0.01	^{95m}Tc	63.2	0.8
5	215.7	0.03	^{97}Ru	85.62	x
6	235.69	0.02	^{95m}Nb	24.9	0.8
7	241.377	0.015	^{96}Tc	0.09	0.02
8	263.049	0.021	^{93m}Mo	57.4	1.1
9	282.52	0.1	^{98m}Nb	0.04	0.007
10	290.48	0.06	^{95}Ru	3.7	0.1
11	294.978	0.02	^{103}Ru	0.303	0.005
12	301.11	0.06	^{95}Ru	2.11	0.06
13	314.337	0.071	^{96}Tc	2.43	0.24
14	324.48	0.03	^{97}Ru	10.79	0.17
15	336.4	0.1	^{95}Ru	69.9	0.5
16	367.2	0.5	^{94}Ru	75	8
17	391.83	0.08	^{93m}Tc	58.3	x
18	392.87	0.09	^{88}Zr	97.29	x
19	449.2	0.3	^{94}Tc	3.3	0.3
20	497.085	0.1	^{103}Ru	91.0	1.2
21	511.0	x	Multiple	100	x
22	532.1	0.3	^{94}Tc	2.35	0.25
23	551.76	0.05	^{95}Ru	1.71	0.06
24	568.8	0.12	^{96}Nb	58	0.3
25	582.082	0.003	^{95m}Tc	30.0	4
26	591.36	0.07	^{95}Ru	1.19	0.05
27	593.16	0.06	^{95}Tc	0.022	0.007
28	610.333	0.1	^{103}Ru	5.76	0.06
29	626.77	0.03	^{95}Ru	17.8	0.5
30	652.72	0.05	^{95}Ru	1.02	0.04
31	684.693	0.021	^{93m}Mo	99.9	0.8
32	702.67	0.07	^{94g}Tc	99.6	1.8
33	734.98	0.13	^{95}Ru	0.466	0.02
34	739.5	0.017	^{99}Mo	12.2	x
35	748.55	0.05	^{95}Ru	1.62	0.06

Table 4.10: *Table of predicted gamma-ray energies* 36-70 *analysed from the* ^{nat}*Mo-α reaction.*

Peak #	E, keV	ΔE, keV	Isotope	I, %	ΔI, %
36	755.83	0.07	^{95}Ru	0.218	0.02
37	765.789	0.009	^{95g}Tc	93.8	0.3
38	778.224	0.015	^{96g}Nb	96.45	19
39	806.32	0.05	^{95}Ru	4.05	0.17
40	812.581	0.015	^{96}Tc	82	4
41	820.63	x	^{95m}Tc	26.63	0.19
42	835.149	0.005	^{95m}Tc	26.63	0.19
43	842.18	0.06	^{95}Ru	1.27	0.05
44	849.74	0.07	^{94g}Tc	95.7	1.8
45	871.05	0.07	^{94m}Tc	94.2	x
46	891.68	0.1	^{94}Ru	25	5
47	916.1	0.15	^{94g}Tc	7.6	0.4
48	947.67	0.02	^{95}Tc	1.951	0.19
49	989.76	0.05	^{95}Ru	0.7	0.03
50	1010.5	0.07	^{95}Ru	0.72	0.03
51	1012.47	0.38	^{101}Mo	13.0	0.7
52	1039.264	x	^{95m}Tc	2.78	x
53	1050.75	0.05	^{95}Ru	2.61	0.11
54	1064.59	0.11	^{101}Mo	0.275	0.015
55	1073.71	0.02	^{95g}Tc	3.74	0.04
56	1096.76	0.06	^{95g}Ru	21.0	1.0
57	1120.15	0.09	^{95}Ru	0.94	0.05
58	1129.224	0.015	^{90g}Nb	92.7	0.5
59	1158.38	0.04	^{95}Ru	0.84	0.2
60	1178.66	0.06	^{95}Ru	5.16	0.25
61	1182.65	0.21	^{95}Ru	0.22	0.03
62	1262.5	0.3	^{95}Ru	0.038	0.009
63	1339.87	0.25	^{95}Ru	0.00047	x
64	1353.5	0.2	^{95}Ru	0.023	0.003
65	1355.1	0.14	^{95}Ru	0.78	0.05
66	1362.94	0.07	^{93g}Tc	66.2	x
67	1369.75	0.15	^{95m}Tc	0.00013	3e-05
68	1410.6	0.07	^{95}Ru	2.49	0.16
69	1433.4	0.3	^{95}Ru	0.029	0.006
70	1460.63	x	^{40}K	10.66	0.17

4.7 Cross-Section Results

The final cross-section results are given in the following section, broken down by product isotope. The data are given in table format for each foil, accompanied by a visualisation of the data alongside TALYS nuclear reaction models, run using TASMAN to extract parameter sensitivity. All simulations were plotted using the UoB-TIP plotting functions, developed during this project. For isotopes with multiple measurable gamma-ray emissions, an intensity-weighted mean was calculated for each of the cross-sections with respect to their associated error.

4.7.1 Ruthenium-103

The cross-section measurement for ^{103}Ru, with a published half-life of $39.247(13)$ days [121], was tracked throughout the whole 30 days of the measurement. There are two main gamma-ray emission lines for the decay of ^{103}Ru: $497.085(10)$ keV with a branching ratio of $91.0(12)$%, and $610.333(10)$ keV with a branching ratio of $5.76(6)$%, however, only the lower energy peak was used in the measurement due to the significantly higher branching ratio and higher detector efficiency at the lower energy. The results are given in tables 4.11 and 4.12 for foils 1-4 and 5-8 respectively.

Table 4.11: *Molybdenum-α cross-section results for ruthenium-103, for the $497.085(10)$ keV emission, for foils 1-4. All cross-section values are in units of millibarns (mb).*

	Foil 1	**Foil** 2	**Foil** 3	**Foil** 4
497.085(10) keV	1.48(10)	2.44(16)	1.12(7)	1.91(13)

Table 4.12: *Molybdenum-α cross-section results for ruthenium-103, for the $497.085(10)$ keV emission, for foils 5-8. All cross-section values are in units of millibarns (mb).*

	Foil 5	**Foil** 6	**Foil** 7	**Foil** 8
497.085(10)	1.60(18)	2.18(25)	4.84(55)	10.3(12)

The data are visualised in figure 4.46 for the eight cross-section points, plotted alongside the TALYS results for the ^{nat}Mo(α,xn)^{103}Ru reaction. The plot makes the increase in cross-section at foil 2 clear. Due to the high mass of ^{103}Ru, the production is only possible through the ^{100}Mo(α,n)^{103}Ru reaction,

which explains the low energy peak, as at higher energies the reaction is suppressed due to more probable multiple neutron emission reactions.

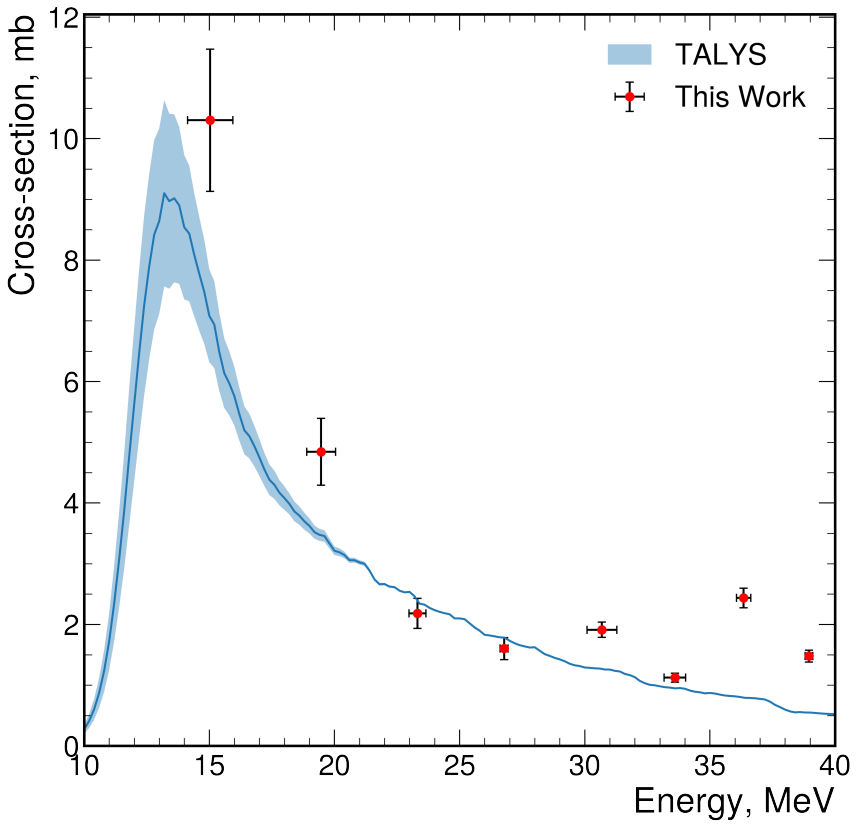


Figure 4.46: *Plot of the eight experimental cross-section results, with associated errors, overlaid with cross-section calculations for* ^{nat}*Mo(α, xn)*^{103}*Ru calculated using TALYS and TASMAN up to* 40 *MeV.*

4.7.2 Ruthenium-97

The cross-section for ^{97}Ru was measured throughout the entire 30 days of the measurement period, due to its long half-life of 2.83(23) days in the literature [56]. Two independent γ emission channels were measured: the 215.70(3) keV line with a branching ratio of 85.62(1)%, and the 324.48(3) keV emission with a branching ratio of 10.79(17)%. The isotope was present for all eight foils, given in tables 4.13 and 4.14, for foils 1-4 and foils 5-8 respectively, showing the individual cross-sections, their respective errors and the calculated intensity-weighted mean.

Table 4.13: *Molybdenum-α cross-section results for ruthenium-97, for the* 215.70(3) *keV and* 324.48(3) *keV emissions, along with the weighted mean, for foils* 1-4*. All cross-section values are in units of millibarns (mb).*

	Foil 1	**Foil** 2	**Foil** 3	**Foil** 4
215.7 keV	216(14)	222(15)	240(16)	228(15)
342.6 keV	200(13)	205(14)	225(15)	212(14)
Mean	208(10)	213(10)	232(11)	219(10)

Table 4.14: *Molybdenum-α cross-section results for ruthenium-97, for the* 215.70(3) *keV and* 324.48(3) *keV emissions, along with the intensity-weighted mean, for foils* 5-8*. All cross-section values are in units of millibarns (mb).*

	Foil 5	**Foil** 6	**Foil** 7	**Foil** 8
215.7 keV	145(16)	137(15)	100(11)	23.9(27)
342.6 keV	134(15)	126(14)	88(10)	24.6(28)
Mean	139(11)	131(10)	92.5(74)	24.2(19)

The cross-section data are visualised in figure 4.47, displayed against modelled data using TALYS and TASMAN.

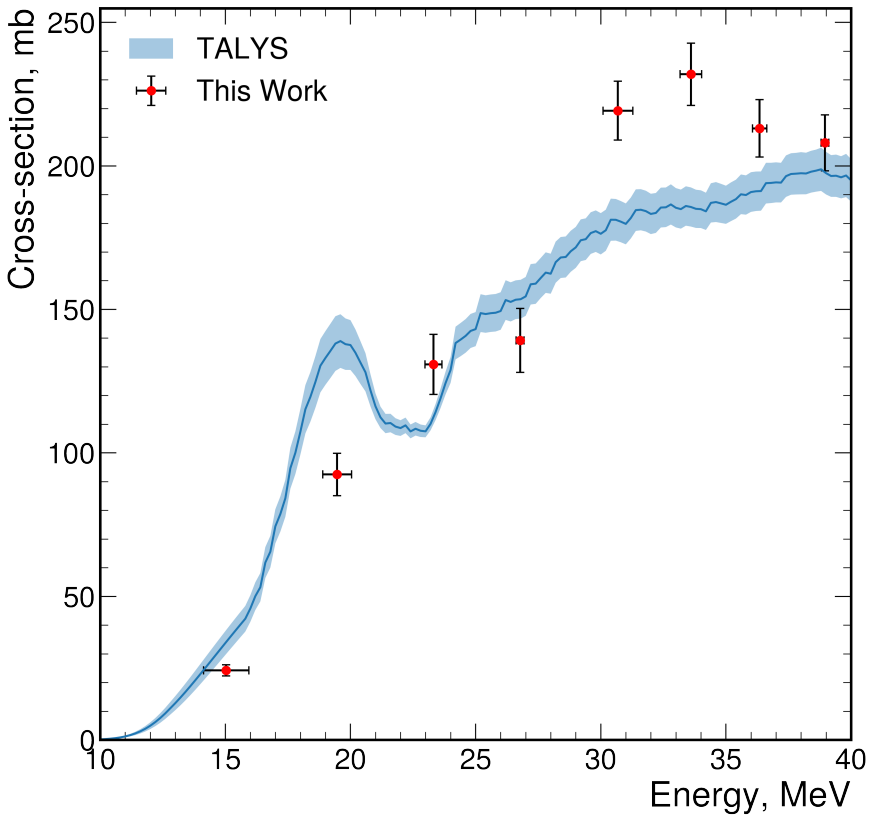


Figure 4.47: *Plot of the eight cross-section data points, with errors, overlaid with cross-section calculations for* $^{nat}Mo(\alpha, xn)^{97}Ru$ *calculated using TALYS and TASMAN up to* 40 *MeV.*

4.7.3 Ruthenium-95

The production cross-section of ruthenium-95 was measured through the $336.40(10)$ keV gamma-ray emission with a branching ratio of $69.9(5)$%, as well as $626.83(10)$ with a branching ratio of $17.8(5)$%. Due to the isotope's short half-life of $1.643(13)$ hours, data for ^{95}Ru was only detected for the first 3 days of the measurement [54]. The data are shown in table 4.15 and 4.16 for the results of foils 1-4 and 5-8 respectively. Due to the low statistics for foils 3-6, only the higher branching ratio $336.40(10)$ keV peak is used.

Table 4.15: *Molybdenum-α cross-section results for ruthenium-95, for the* 336.40(10) *keV and* 626.83(10) *keV emissions, along with the intensity-weighted mean, for foils* 1-4*. All cross-section values are in units of millibarns (mb).*

	Foil 1	**Foil** 2	**Foil** 3	**Foil** 4
336.40(10) keV	42.1(28)	34.2(23)	13.14(87)	5.79(38)
626.83(10) keV	37.9(25)	30.5(20)	0.29(2)	2.43(16)
Mean	39.8(19)	32.1(15)	13.14(87)	5.79(38)

Table 4.16: *Molybdenum-α cross-section result for ruthenium-95, for the* 336.40(10) *keV and* 626.83(10) *keV emissions, along with the intensity-weighted mean, for foils* 5-8*. The mean cross-section for foils* 3-6 *was taken only from the* 336.40(10) *keV peak due to much higher statistics. All cross-section values are in units of millibarns (mb).*

	Foil 5	**Foil** 6	**Foil** 7	**Foil** 8
336.40(10) keV	2.40(21)	9.62(84)	90.0(79)	34.2(30)
626.83(10) keV	2.03(18)	1.59(14)	80.5(71)	30.1(26)
Mean	2.40(21)	9.62(84)	84.7(53)	31.9(20)

The data are visualised in figure 4.48 for the mean calculated cross-section for the eight foils, overlaid with the TALYS and TASMAN calculations.

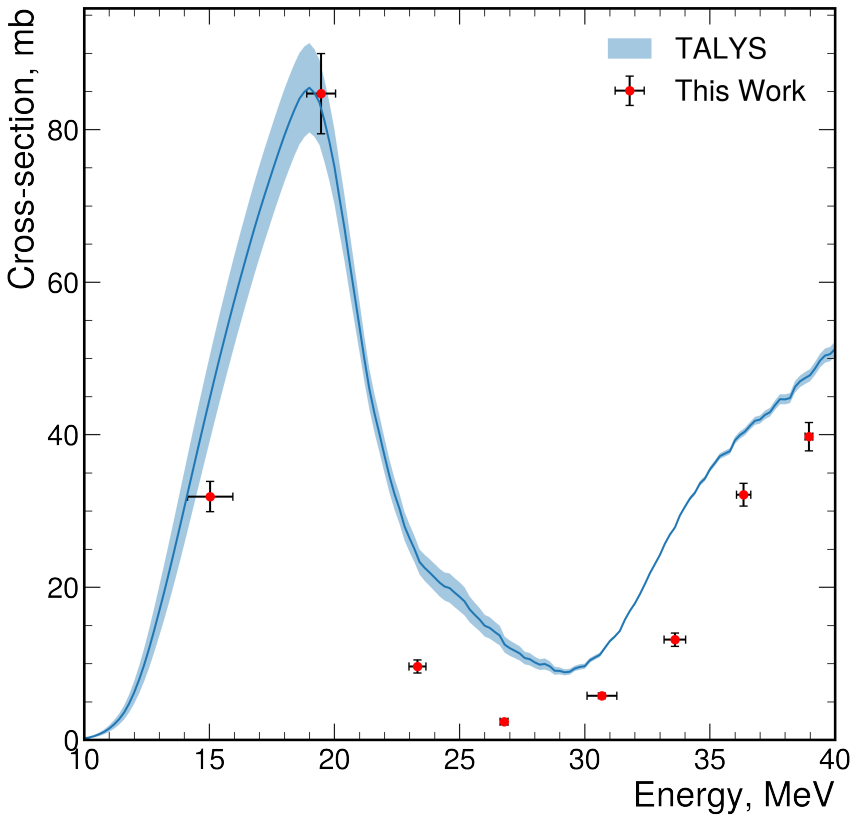


Figure 4.48: *Plot of the mean production cross-section for $^{nat}Mo(\alpha, xn)^{95}Ru$ calculated for the eight energies using data acquired through gamma-ray spectrometry analysis. The data are overlaid with cross-section models, calculated using TALYS and TASMAN up to 40 MeV.*

4.7.4 Ruthenium-94

The presence of ruthenium-94, a short-lived isotope, with a half-life in literature of 51.8(6) minutes, was measured in the sample through a single high-probability gamma-ray emission at 367.2(5) keV, with a branching ratio of 75(8)%. Due to the short half-life, data were only analysed for the first 2 days following irradiation, before statistics were too low. The data are shown in table 4.17 and 4.18 for the results of foils 1-4 and 5-7 respectively. No peaks were observed above statistical noise for foil 8 at any point in the measurement.

Table 4.17: *Molybdenum-α cross-section results for ruthenium-94, for the* 367.2(5) *keV emission, for foils* 1-4*. All cross-section values are in units of millibarns (mb).*

	Foil 1	**Foil** 2	**Foil** 3	**Foil** 4
336.40(10) keV	12.86(85)	22.9(15)	33.0(22)	31.2(21)

Table 4.18: *Molybdenum-α cross-section results for ruthenium-94, for the* 367.2(5) *keV emissions for foils* 5-7*. All cross-section values are in units of millibarns (mb).*

	Foil 5	**Foil** 6	**Foil** 7
336.40(10) keV	11.87(82)	6.78(47)	0.23(2)

The data are visualised in figure 4.49 for the mean calculated cross-section for the seven energies of foils 1-7, overlaid with TALYS calculations for ^{nat}Mo-α, run with TASMAN to determine parameter sensitivity.

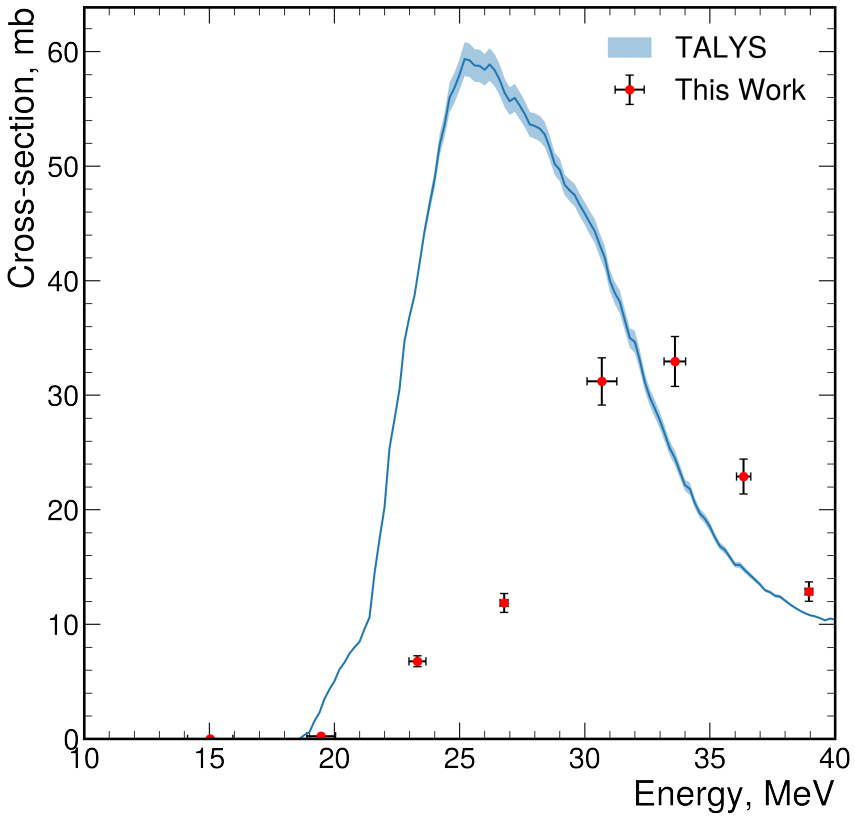


Figure 4.49: *A plot of the mean production cross-sections for ruthenium-94 using data acquired through gamma-ray spectrometry analysis. The data are overlaid with cross-section models, calculated using TALYS and TASMAN up to* 40 *MeV.*

4.7.5 Technetium-99m

Technetium-99m, an isomeric state with an excitation energy of 0.1427 MeV and a half-life of $6.0067(5)$ hours is produced both directly in the reaction and through the decay of ^{99}Mo, which itself has a half-life of $65.976(24)$ hours [24]. To measure the reaction cross-section of ^{99m}Tc, the measurement was optimised to enable a large number of short measurements to be collected in quick succession soon after the irradiation had finished. The measurement started 1 hour after the irradiation finished. This enabled 30 minutes to allow the short-lived aluminium products to decay, which would have resulted in high dose rates from the target. Over the subsequent 30 minutes, the foils were removed from the beamline, and placed onto the perspex foil mounts, which are sized to fit at defined distances from the detector, and positioned centrally. It was seen that after roughly 24 hours, the decay of ^{99}Mo dominated the decay rate of ^{99m}Tc, as the decay reached equilibrium through the decay of ^{99m}Tc. The state was measured using a single high probability gamma-ray emission at $140.511(1)$ keV, with a branching ratio of $89(4)$%. The results are given in table 4.19 for foils 1-6, where the signal was detectable above the noise. The data are visualised in figure 4.50.

Table 4.19: *Molybdenum-α cross-section results for technetium-99m, for the $140.511(1)$ keV emission, for foils 1 and 6. All cross-section values are in units of millibarns (mb).*

	Foil 1	**Foil** 2	**Foil** 3	**Foil** 4	**Foil** 5	**Foil** 6
140.511(1) keV	56.5(37)	81.2(54)	86.0(57)	81.0(54)	18.0(19)	10.2(11)

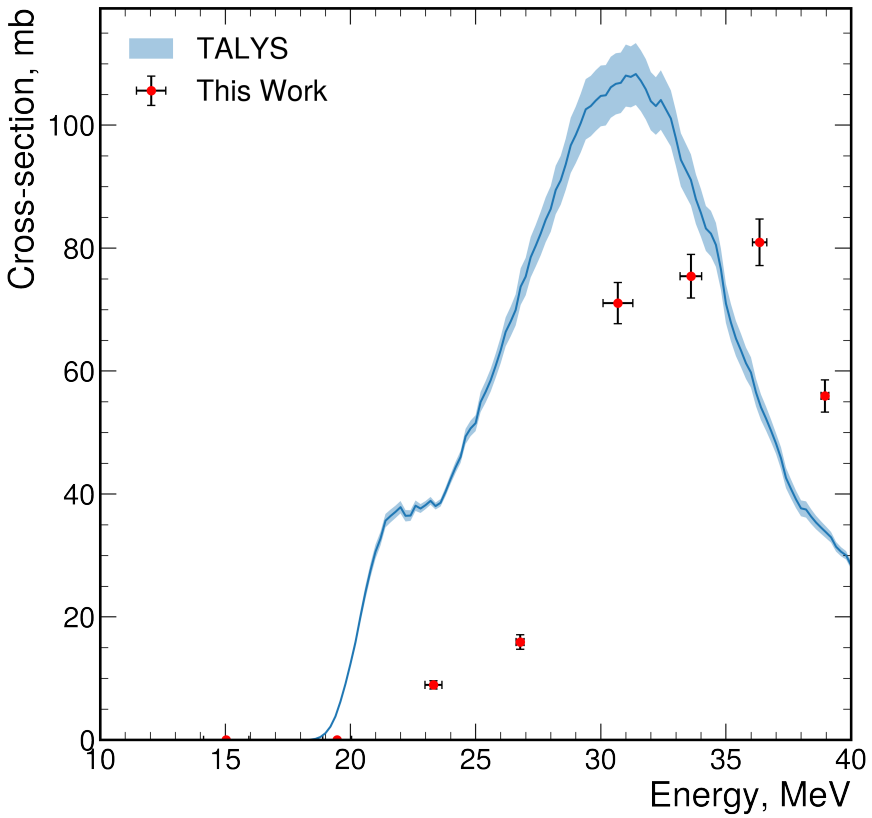


Figure 4.50: *A plot of the mean production cross-section of ^{99m}Tc, calculated for foils* 1-6*, with associated error. The data are overlaid with cross-section models for ^{nat}Mo(α, pxn)^{99m}Tc, calculated using TALYS and TASMAN up to* 40 *MeV.*

4.7.6 Technetium-96

The production of technetium-96 results in the production of the ground state with a half-life of $4.28(7)$ days, along with an isomeric state ^{96m}Tc with an excitation energy of 34.234 keV, and a half-life of $51.5(10)$ minutes [55]. The isomer decays with a $98.0(5)$% branching ratio into the ground state state, and $2.0(5)$% to ^{96}Mo. Due to the short half-life of the isomer and the low excitation energy, the cross-section of the ground state and isomer could not be measured separately. The measurement was taken as a total production cross-section of the ground state and isomer. There are three high-probability gamma-rays which can be used to measure the ground state's decay: $778.22(4)$ keV with a branching ratio of 99.760%, $812.54(4)$ keV with a branching ratio of $82(3)$% and $849.86(4)$ keV

with a branching ratio of 98(4)%. Due to the overlap of the 812.54(4) keV peak with the 810.8(2) keV of ^{96}Nb and overlap of the 849.86(4) keV peak with the 847.687(22) keV peak of ^{96}Nb, only the 778.22(4) keV emission was used. The results for the two gamma-rays along with the intensity-weighted mean are given in table 4.20 for foils 1-6, as the isotope was below the experiment's limit of detection for foils 7 and 8. The data are also visualised in figure 4.51, showing the intensity-weighted mean cross-section overlaid with the total ^{96}Tc production cross-section, calculated using TALYS and TASMAN.

Table 4.20: *Table of results for the total technetium-96 production cross-section. The results are for the* 778.22(4) *keV gamma-ray emission for foils* 1-6. *All cross-section values are in units of millibarns (mb).*

	Foil 1	**Foil** 2	**Foil** 3	**Foil** 4	**Foil** 5	**Foil** 6
778.22(4) keV	69.5(46)	55.6(37)	41.8(28)	28.7(19)	13.0(15)	4.27(48)

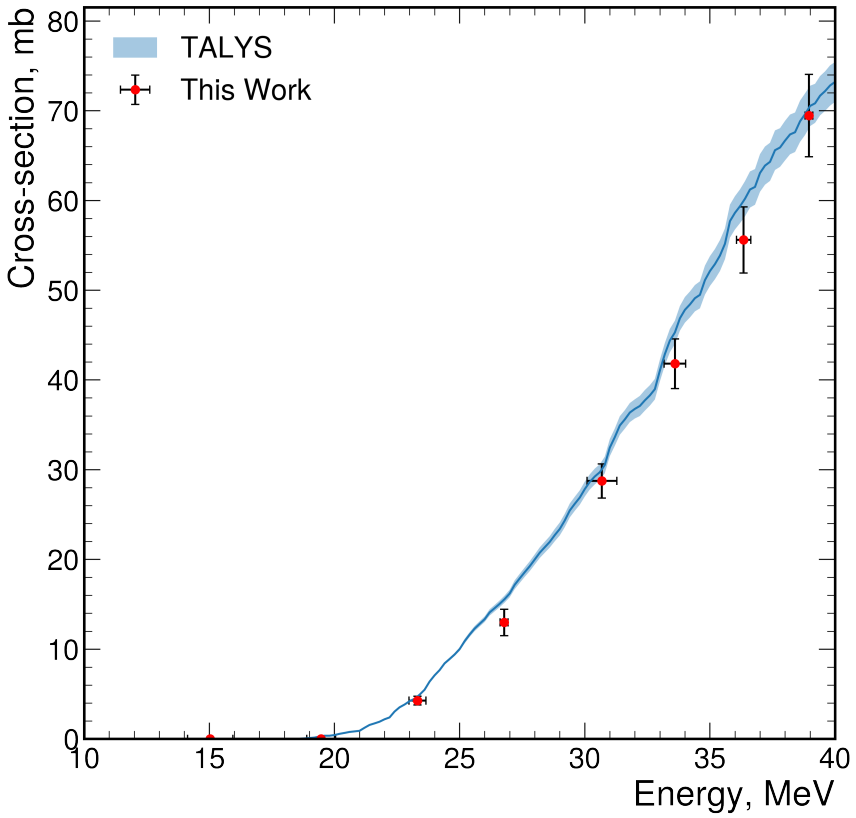


Figure 4.51: *Plot of the mean production cross-section of ^{96}Tc, calculated for foils* 1-6, *with error. The data are overlaid with cross-section models for ^{nat}Mo(α, pxn)^{96}Tc, calculated using TALYS and TASMAN up to* 40 *MeV.*

It is clear from the plot that the data have strong agreement with the predictions of TALYS over the entire energy range up to 40 MeV.

4.7.7 Technetium-95g

The ground state of technetium-95 is produced both directly in the reaction, as well as through the decay of ^{95m}Tc with a half-life of 61 days and a branching ratio of 3.88%. The long half-life of the excited state limits the effect of the decay on the cross-section of the ground state produced directly in the reaction. The decay of ^{95}Ru is a much greater problem, with a half-life of 1.643(13) hours and a decay probability of 97.4% to ^{95g}Tc, with the rest decaying into ^{95m}Tc, of which 3.88% decays into ^{95g}Tc. The short half-life of ^{95}Ru eliminates the possibility of obtaining the measurement before the effect of ^{95}Ru becomes dominant. The cross-section calculated for the ^{95}Ru must therefore be used to adjust the result in the analysis. The presence of ^{95g}Tc with a half-life of 20.0(1) hours was measured using two gamma-ray emission lines, the 765.789(9) keV emission with a branching ratio of 93.8(3)% and the 1073.71(2) keV emission, with a branching ratio of 3.74(4)%. The results, as expected, were significantly higher than the TALYS models predict. To correct for the calculated cross-section of ^{95}Ru (given in section 4.7.3), the calculated ^{95}Ru cross-section was multiplied by the decay branch of 97.4% and subtracted from the measured value of ^{95g}Tc, given as the corrected mean. This gives a much stronger agreement with the model. The results are given in table 4.21 and 4.22 for foils 1-4 and 5-8 respectively. The data are visualised in figure 4.52.

Table 4.21: *Molybdenum-α cross-section results for technetium-95g, for the 765.789(9) keV and 1073.71(2) keV emissions, along with the intensity-weighted mean, for foils 1-4. All cross-section values are in units of millibarns (mb).*

	Foil 1	**Foil** 2	**Foil** 3	**Foil** 4
765.789(9) keV	94.4(62)	64.1(42)	38.0(25)	12.3(8)
1073.71(2) keV	92.6(61)	62.6(41)	39.0(26)	16.9(11)
Mean	93.5(44)	63.3(30)	38.5(18)	13.9(7)
Corrected Mean	54.8(47)	32.0(33)	25.7(20)	8.3(8)

Table 4.22: *Molybdenum-α cross-section results for technetium-95g, for the* 765.789(9) *keV and* 1073.71(2) *keV emissions, along with the intensity-weighted mean, for foils* 5-8. *All cross-section values are in units of millibarns (mb).*

	Foil 5	**Foil** 6	**Foil** 7	**Foil** 8
765.789(9) keV	2.8(20)	47.5(64)	102.2(43)	42.0(25)
1073.71(2) keV	18.3(20)	43.3(70)	109.2(48)	48.1(31)
Mean	10.0(14)	45.6(47)	105.3(32)	44.3(19)
Corrected Mean	7.7(14)	36.2(48)	17.6(83)	11.0(35)

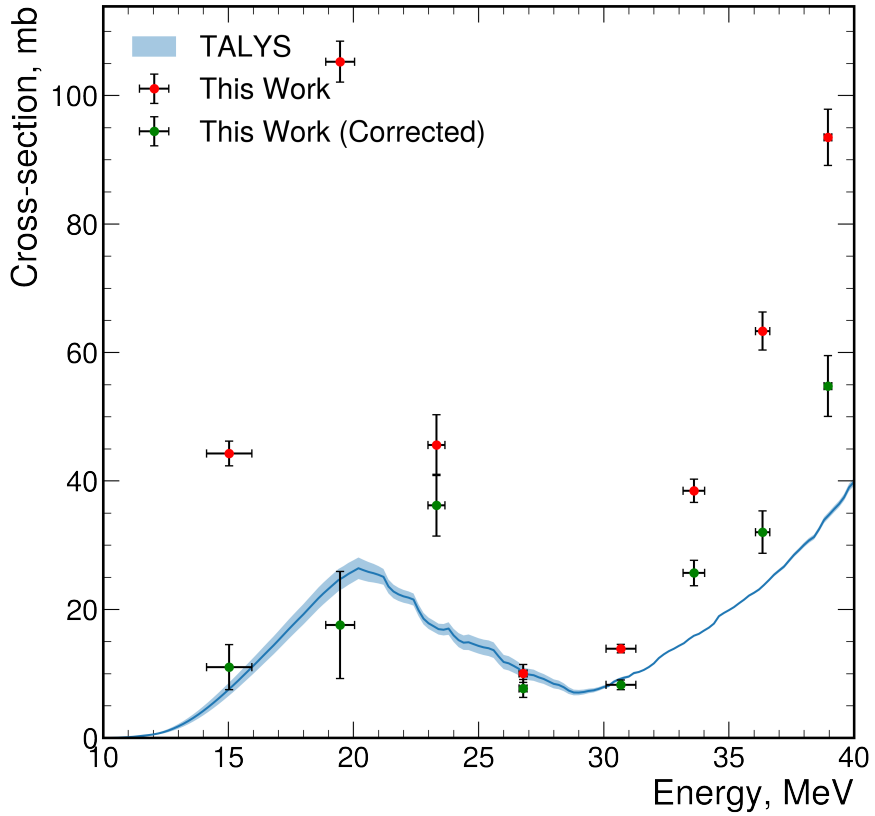


Figure 4.52: *Plot of the mean* ^{95g}*Tc production cross-section, calculated for the eight energies with their associated error. The data are overlaid with cross-section models calculated using TALYS and TASMAN up to* 40 *MeV. The corrected value uses the calculated value of cross-section, subtracting the calculated production of* ^{95}*Ru, multiplied by the probability of decay into* ^{95g}*Tc (*97.4*%).*

4.7.8 Technetium-94g

Technetium-94 is predominantly produced directly in the reaction, with only 0.1% of ^{94m}Tc decaying into the ground state. The presence of ^{94g}Tc can be measured through three high probability gamma-ray emission lines: $702.67(7)$ keV with a branching ratio of $99.6(18)\%$, $849.74(7)$ keV with a branching ratio of $95.7(18)\%$ and $817.05(7)$ keV with a branching ratio of $95.7(18)\%$. The $702.67(7)$ keV and $817.05(7)$ keV peaks were used in the analysis, as the $849.74(7)$ keV overlaps with a 849.9 keV gamma-ray emission from the decay of ^{96}Tc. The results for the two gamma-ray emissions along with a intensity-weighted mean are shown in table 4.23 for foils 1-6. The peaks were not detected in foils 7 and 8. The data are visualised in figure 4.53.

Table 4.23: *Molybdenum-α cross-section results for technetium-94, for the $702.67(7)$ keV and $817.05(7)$ keV emissions, along with the intensity-weighted mean, for foils 1 and 6. All cross-section values are in units of millibarns (mb).*

	Foil 1	**Foil** 2	**Foil** 3	**Foil** 4	**Foil** 5	**Foil** 6
702.67(7) keV	56.5(37)	81.2(54)	86.0(57)	81.0(54)	18.0(19)	10.2(11)
817.05(7) keV	55.4(37)	80.70(53)	68.7(45)	64.7(43)	14.60(152)	8.13(85)
Mean	56.0(26)	80.9(38)	75.4(36)	71.0(33)	15.94(118)	8.94(66)

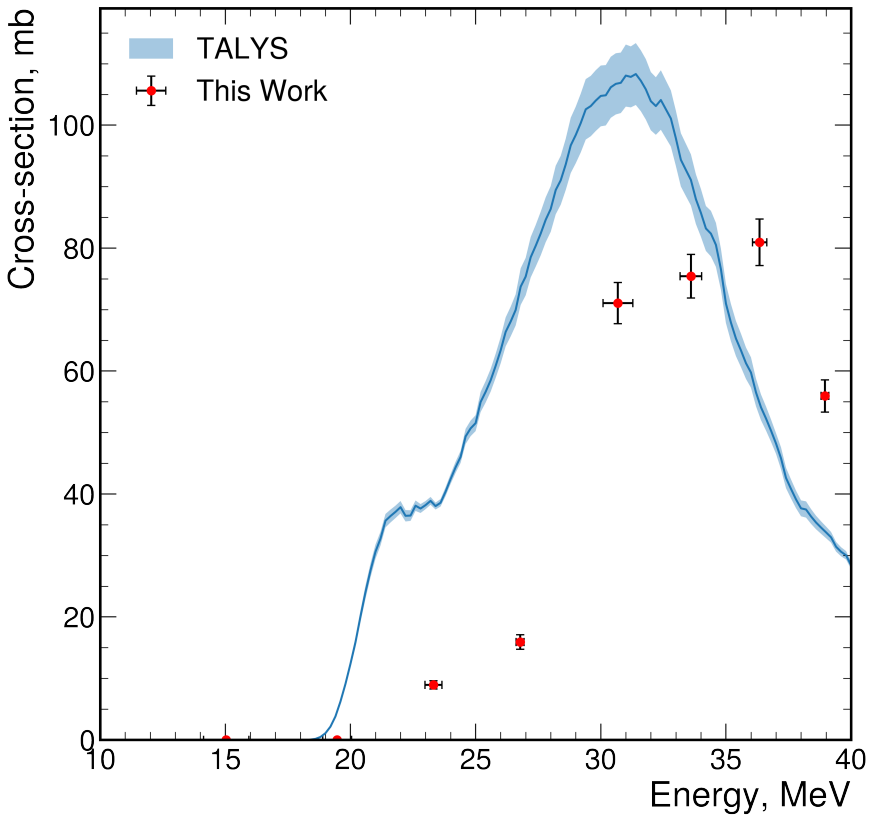


Figure 4.53: *Plot of the mean cross-section calculated for foils* 1-6*, with error. The data are overlaid with cross-section models for* ^{nat}*Mo(*α*, pxn)*^{94}*Tc, calculated using TALYS and TASMAN up to* 40 *MeV.*

4.7.9 Technetium-93m

The production of technetium-93m, with an excitation energy of 391.838 keV is populated directly in the reaction, and through the decay of ^{93}Ru. Ruthenium-93 has a half-life of 59.7(6) seconds, meaning all of the products will have decayed into technetium-93m by the time the measurement is taken. The technetium-93m cross-section is therefore measured as a sum of the ^{93m}Tc and ^{93}Ru cross-sections. Technetium possesses a half-life of 43.5(10) minutes and is measured from a single gamma-ray emission at 391.83(8) keV, with a branching ratio of 58.3%. The results for this reaction are given in table 4.24 and the data visualised in figure 4.54, showing the results alongside the TALYS prediction for the production of ^{93m}Tc, ^{93}Ru and the sum total.

Table 4.24: *Molybdenum-α cross-section results for technetium-93m, for the* 391.83(8) *keV emissions, along with the intensity-weighted mean, for foils* 1 *and* 2*. All cross-section values are in units of millibarns (mb).*

	Foil 1	**Foil** 2
391.83(8) keV	1.47(97)	0.44(28)

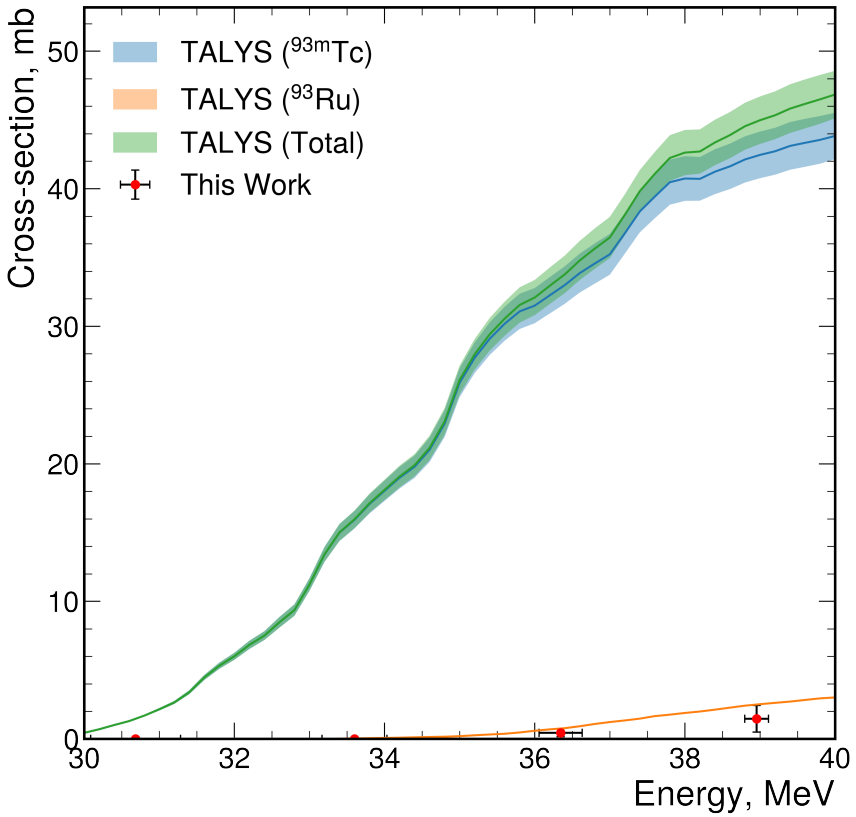


Figure 4.54: *Plot of the production cross-section of* ^{93m}*Tc and short lived* ^{93}*Ru, calculated for foils* 1 *and* 2*, with error. The data are overlaid with cross-section models for* ^{nat}*Mo(α, pxn)*^{93}*Tc,* ^{nat}*Mo(α, xn)*^{93}*Ru, and the sum of these calculated using TALYS and TASMAN up to* 40 *MeV.*

4.7.10 Technetium-93

The cross-section for technetium-93 production was detected for foils 1 and 2 only due to the high energy threshold of the reaction, predominantly populated by the ^{92}Mo(α,p2n)^{93}Tc reaction channel with a Q-value of -24.209 MeV. The isotope has a half-life of 2.75(5) hours, enabling the peak to be measured for 4 and 3 days for foil 1 and 2 respectively. The measurement was taken from a 1362.94(7)

keV gamma-ray emission, with a branching ratio of 66.2%. The results are given in table 4.25. The cross-section results are far below the predicted value, however, this is consistent with values in literature [112]. The data closely match the modelled predictions for the production from the decay of ^{93}Ru, which could indicate that the ^{93m}Tc state is not as heavily populated as predicted by the models, but only via the decay of ^{93}Ru.

Table 4.25: *Molybdenum-α cross-section results for technetium-93, for the* 1362.94(7) *keV emissions, for foils* 1 *and* 2. *All cross-section values are in units of millibarns (mb).*

	Foil 1	**Foil** 2
1362.94(7) keV	75.8(50)	45.7(30)

The results are shown in figure 4.55.

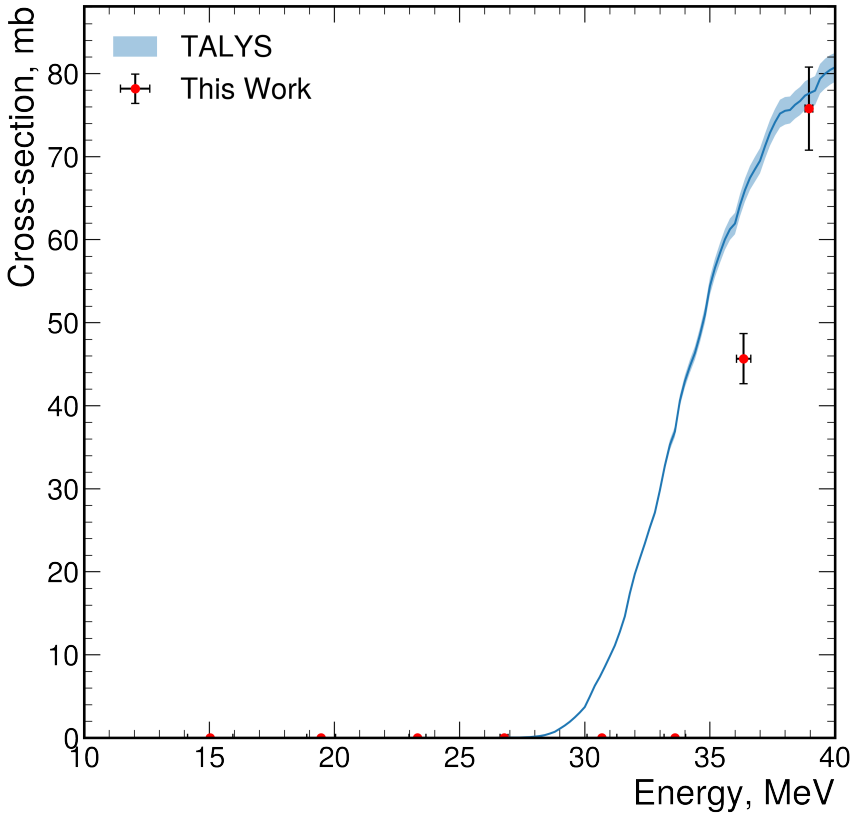


Figure 4.55: *Plot of the mean cross-section calculated for the two energies, with their associated error. The data are overlaid with cross-section models for* ^{nat}*Mo(α, pxn)*^{94}*Ru, calculated using TALYS and TASMAN up to* 40 *MeV.*

4.7.11 Molybdenum-99

The production cross-section of molybdenum-99, with a half-life of $65.976(24)$ hours has two possible detectable gamma-rays. There is a $89(4)$% emission of a $140.511(1)$ keV gamma-rays from the successive decay of ^{99m}Tc, which itself has a half-life of $6.0067(5)$ hours. The difficulty with analysing this peak is deconvolving the decay of ^{99m}Tc produced directly in the reaction and that produced from the decay of ^{99}Mo. Due to the much longer half-life of ^{99}Mo, over time as the directly produced ^{99m}Tc decays, the rate of decay reaches equilibrium with the production from the decay of ^{99}Mo. This equilibrium enables the initial activity of the longer-lived parent to be traced back, provided the ^{99}Mo production was sufficient to be detectable following the decay of ^{99m}Tc directly produced in the reaction. The second detection mechanism involves the detection of a direct gamma-ray in the decay of ^{99}Mo at $739.500(17)$ keV, with a branching ratio of 12.20%. The results for the two peaks are given in table 4.26. For foil 6 as no significant ^{99}Mo activity was detectable in the $140.511(1)$ keV peak, only the $739.500(17)$ keV result was used to calculate the mean.

Table 4.26: *Molybdenum-α cross-section results for ^{99}Mo, for the 140.511 keV from the successive ^{99m}Tc decay and $739.500(17)$ keV emissions, along with the intensity-weighted mean, for foils 1-6. All cross-section values are in units of millibarns (mb).*

	Foil 1	**Foil** 2	**Foil** 3	**Foil** 4	**Foil** 5	**Foil** 6
140.511(1) keV	5.00(33)	4.72(31)	3.79(25)	2.69(18)	1.13(13)	0.0(0)
739.500(17) keV	6.95(46)	5.46(36)	4.65(31)	3.15(21)	1.54(17)	0.66(7)
Mean	5.66(27)	5.04(24)	4.13(19)	2.89(14)	1.27(10)	0.66(7)

The cross-section results are visualised in figure 4.56 overlaid with TALYS calculations run using TASMAN.

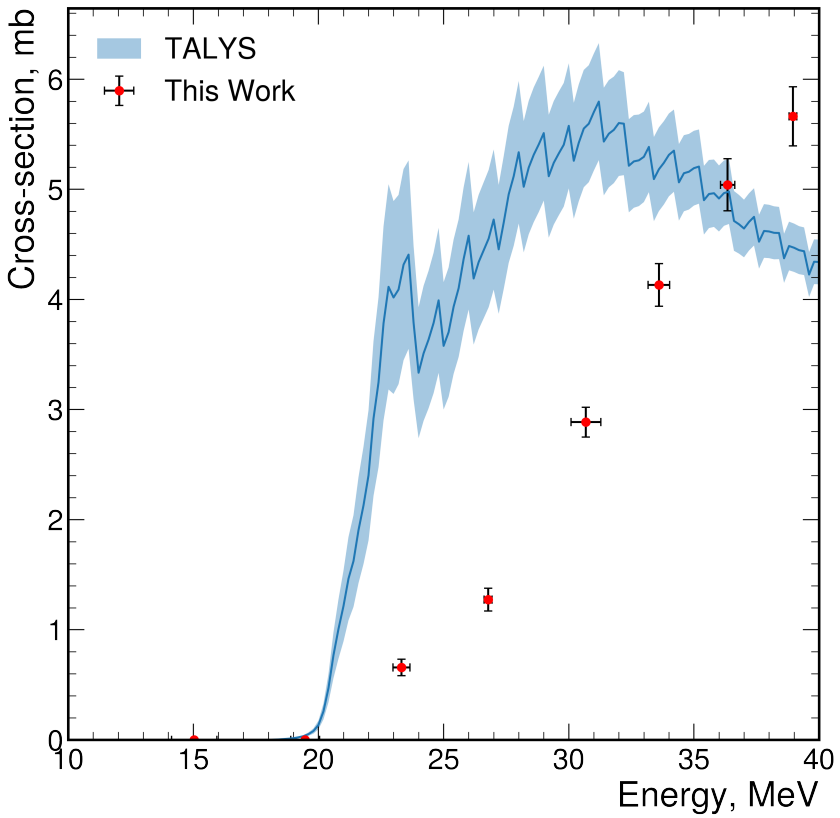


Figure 4.56: *Plot of the mean cross-section calculated for foils* 1-6*, with error. The data are overlaid with cross-section models for* ^{nat}*Mo(α, αxn)*^{99}*Mo, calculated using TALYS and TASMAN up to* 40 *MeV.*

4.7.12 Molybdenum-93m

The production of molybdenum-93m, with an excitation energy of 2424.974 keV, was measurable for the first 7 days following the irradiation, with a half-life of 6.85(7) hours. There are two strong gamma-ray emissions which can be effectively measured; 263.049(13) keV with a branching ratio of 57.4(11)%, 684.693(21) keV with a branching ratio of 99.9(8)%. The results are given for the two peaks in table 4.27.

Table 4.27: *Molybdenum-α cross-section results for ^{93m}Mo, for the 263.049(13) keV and 684.693(21) keV emissions, along with the intensity-weighted mean, for foils 1-5. All cross-section values are in units of millibarns (mb).*

	Foil 1	**Foil** 2	**Foil** 3	**Foil** 4	**Foil** 5
263.049(13) keV	13.09(87)	6.89(46)	2.32(15)	0.86(6)	0.57(6)
684.693(21) keV	14.71(99)	6.29(46)	2.31(30)	0.91(8)	0.12(8)
Mean	13.79(65)	6.59(32)	2.32(14)	0.87(5)	0.41(5)

The results are visualised in figure 4.57 showing the results for foils 1-5, overlaid with TALYS and TASMAN calculations up to 40 MeV.

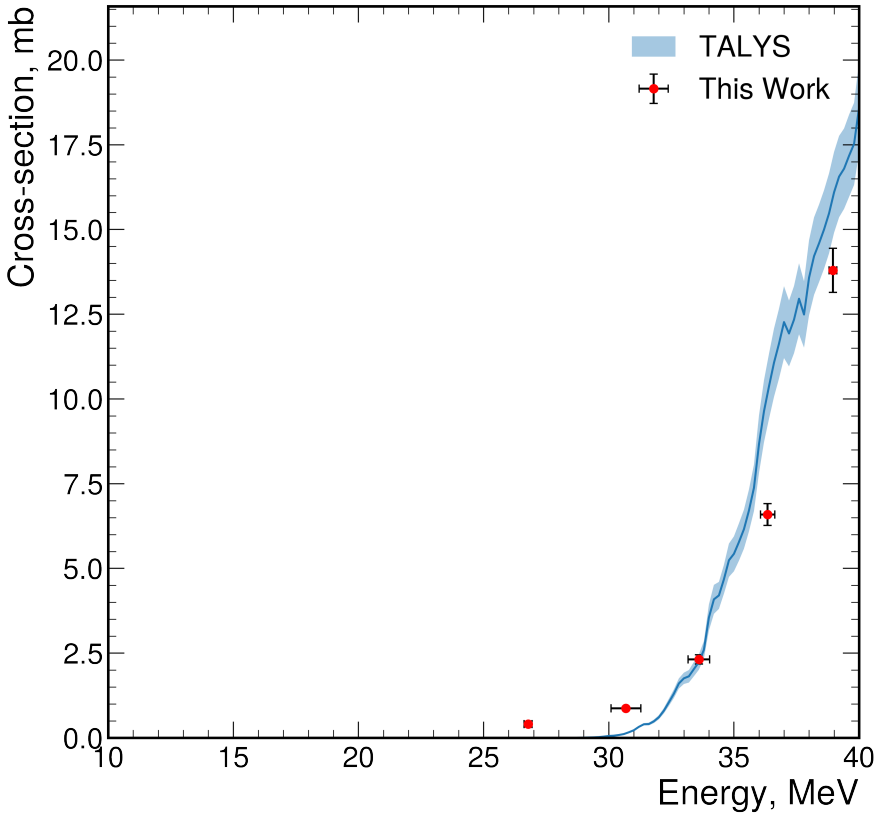


Figure 4.57: *Plot of the mean cross-section calculated for foils 1-5, with error. The data are overlaid with cross-section models for ^{nat}Mo(α, αxn)^{93m}Mo, calculated using TALYS and TASMAN up to 40 MeV.*

4.7.13 Niobium-90

The cross-section for niobium-90, has a low cross-section in the region up to 40 MeV, only becoming dominant above 30 MeV. This is due to its Q-value of -19.509 MeV, being populated most commonly by the ^{92}Mo(α,αpn)^{90}Nb reaction. There are three high-probability gamma-rays which the measurement could be taken from; $132.716(18)$ keV with a branching ratio of $4.13(4)$%, $141.178(15)$ keV with a branching ratio of $66.8(7)$% and $1129.224(15)$ keV with a branching ratio of $92.7(5)$%. Due to the low branching ratio of the first peak, the low cross-section of the reaction and the high levels of Compton scattering background at low energies, the $132.716(18)$ keV peak could not be detected. The $141.178(15)$ keV peak overlaps with the 140.511 keV emission of ^{99m}Tc, causing large uncertainty in the fitting. For this reason, this peak was not used in the analysis. The result for the $1129.224(15)$ keV peak for foils 1 and 2, where the isotope was detectable are given in table 4.28. The data are visualised in figure 4.58 alongside the TALYS cross-sections.

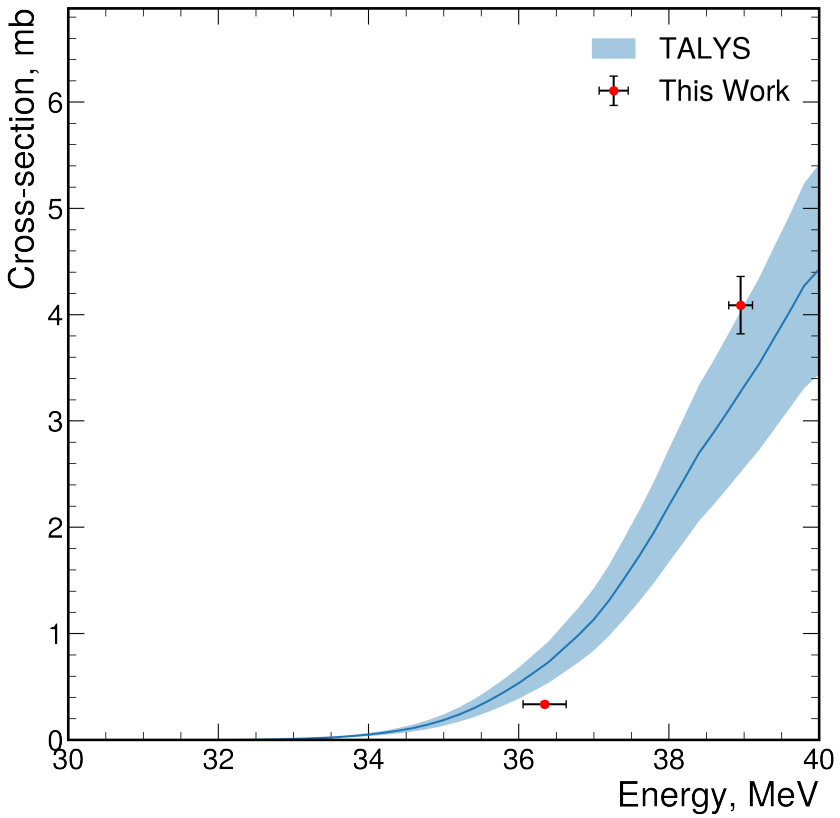


Figure 4.58: *Plot of the mean cross-sections calculated for foils* 1 *and* 2*, with error. The data are overlaid with cross-section models for* $^{nat}Mo(\alpha, \alpha xn)^{90}Nb$*, calculated using TALYS and TASMAN up to* 40 *MeV.*

Table 4.28: *Molybdenum-*α *cross-section results for* ^{90}Nb*, for the* 1129.224(15) *keV emission for foils* 1 *and* 2*. All cross-section values are in units of millibarns (mb).*

	Foil 1	**Foil** 2
1129.224(15) keV	4.09(27)	0.34(2)

4.7.14 Conclusion

The cross-section results overall show good agreement with the models for most isotopes, however, there is some discrepancy for particular isotopes. The ^{99}Mo production line shows a much lower production than TALYS had predicted. Ruthenium-94 has a lower production cross-section than TALYS predicted up to 32 MeV, before increasing above the prediction. Ruthenium-95 also showed a

lower cross-section than TALYS for energies above 19 MeV, however, the predicted trend with energy was seen. The technetium isotopes showed strong agreement with the models, however, the results were more difficult, due to the short-lived ruthenium and molybdenum isotopes feeding into them. The cross-sections for the isotopes analysed shown together in figure 4.59. The results show strong agreement with the previous work, particularly the work of F. Tárkányi et al. [112].

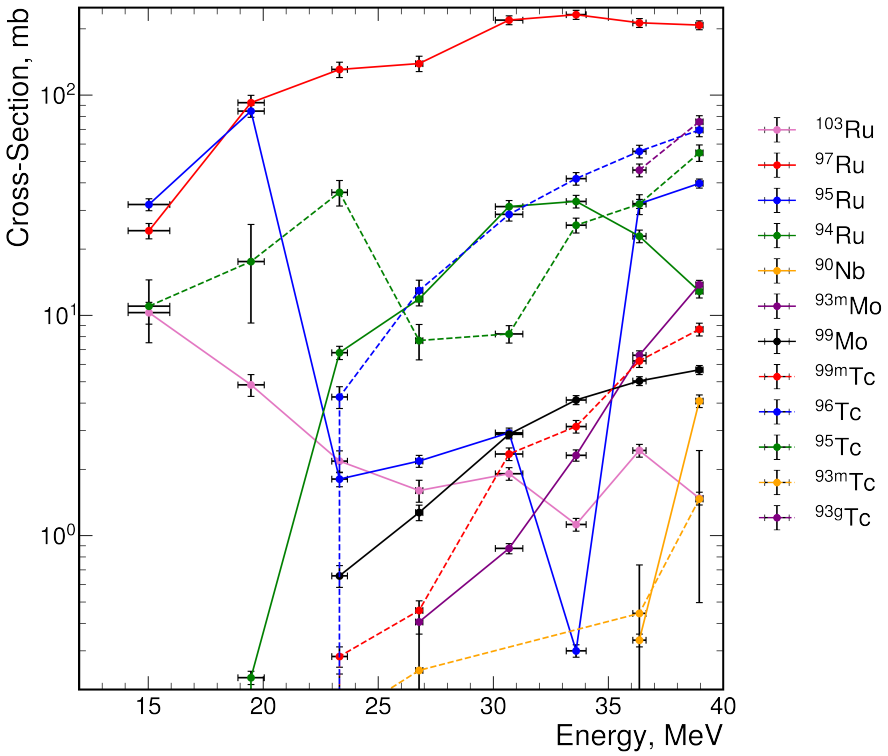


Figure 4.59: *Plot of the cross-sections of all analysed isotopes.*

5

Tc-97 Chemical Purification

5.1 Introduction

Chemical separation is an essential step in the purification of a radiotracer. Work on chemical separation method development and validation was all performed at the UK National Physical Laboratory's Nuclear Metrology group. Chemical separation can be performed through various techniques, including anion exchange, liquid extraction, selective precipitation, extraction chromatography, and even combustion techniques that have been used previously [122]. This project focused on separating technetium using TK202, an extraction chromatography resin developed by Triskem International [123], with characterisation of the resin. This chapter details the different applications of technetium separation, different separation methods and the development of a chemical separation method for a technetium tracer. The final stages of the work involved the processing of an active Mo target irradiated at the University of Birmingham cyclotron, and separated and analysed at the National Physical Laboratory using an optimised chemical separation technique.

5.2 Technetium separation

Chemical separation of technetium is ubiquitous in various technical fields, including environmental monitoring, nuclear medicine and nuclear decommissioning. The most commonly used technetium separation is the separation of ^{99m}Tc from ^{99}Mo in medical isotope generators. Environmental monitoring often requires the processing of aqueous samples, investigating the presence and transport of ^{99}Tc through the biosphere, which is commonly related to the discharge of technetium from reprocessing plants and nuclear disasters due to the high solubility of TcO_4^- ions. The third application, nuclear decommissioning, overlaps with environmental monitoring; with the closure of many old nuclear reactors, vast amounts of environmental monitoring are required to enable remediation and eventual release of nuclear sites from regulatory control along with monitoring the presence of technetium contamination on reactor components.

5.2.1 Medical Isotopes

The use of ^{99}Tc in medicine accounts for 80% of medical isotope use globally [124], providing huge demand for technetium separation, traditionally extracted from ^{99}Mo generators. Medical technetium is traditionally produced using uranium targets irradiated in nuclear reactors, where the ^{99}Mo is produced in fission, and is chemically separated using UTEVA extraction chromatography resin [125], and the ^{99}Mo is loaded into an alumina column, binding due to Mo's high affinity. The ^{99}Mo decays with a half-life of 6.0067(5) h, allowing the product ^{99m}Tc with its low affinity to alumina to be collected by passing saline solution through the column.

There is a strong desire within the political and technical sphere to move away from uranium targets for the production of ^{99m}Tc, due in part to the closure of old nuclear reactors and the high associated waste and security risk. Several alternative production routes are being developed using Mo targets. Two neutron production reactions enable the production of ^{99}Mo using enriched Mo targets in research reactors; the ^{98}Mo(n,γ)^{99}Mo reaction with thermal neutron spectra or ^{100}Mo(n,2n)^{99}Mo with fast neutron spectra, however, these production routes do not remove the need for research reac-

tors, only the use of fissile material. There are accelerator-driven production routes to remove the need for nuclear reactors, utilising γ-ray and proton-induced reactions. The γ-induced reactions require the production of a high flux γ-ray beam produced by the bombardment of high energy electrons on a thick target. These γ-rays drive the ^{100}Mo(γ,n)^{99}Mo or ^{238}U(γ,f)^{99}Mo reaction, however, the latter does not remove the use of fissionable material. Proton-induced reactions cause the direct production of ^{99m}Tc, using the bombardment of a Mo target, ^{100}Mo(p,pn)^{99}Mo, however, direct production has disadvantages that the material must be transported and used in quick succession of production due to the short half-life of ^{99m}Tc compared to the generator isotope ^{99}Mo.

The novel Mo target production methods using either enriched ^{98}Mo or ^{100}Mo result in low specific activity of Mo of the irradiated target, compared to the isolation of ^{99}Mo from fission products. The mass of resin required for separation is proportional to the amount of sample requiring binding with a capacity of around 50 μg of binding analyte to 1 g of resin [126]; the required mass of alumina and the size of the columns would be impractical.

For this reason, a reverse generator approach has been adopted, whereby the chemistry is optimised to bind the Tc and enable the high quantities of Mo to pass through the resin, greatly reducing the quantity of resin required. The technetium is flushed out of the extraction resin by passing through a clean solution with differing reagent concentrations, optimised for the Tc to be eluted out of the matrix. This new method has been employed by NorthStar [127] and SHINE [128] in the United States. Both of these methods adopt Triskem's TK202 resin.

5.2.2 Environmental Monitoring and Nuclear Decommissioning

Environmental monitoring and nuclear decommissioning samples are very similar, with often low levels of ^{99}Tc in the form of contamination. Commonly, these samples are contaminated steel or concrete. These samples are far more variable compared to medical applications, being formed of varied and complex matrices that must be separated. The resin and conditions used depend entirely on the sample's constituents and will vary greatly from sample to sample. Environmental samples

have very low concentrations of technetium, requiring the processing of large masses or volumes of samples [129]. The complex environmental samples require large amounts of processing to enable the low concentrations of technetium to be detected free of interference requiring concentration, sample separation and purification [130].

5.3 Triskem Technetium Resins

Triskem International is a company that develops a range of extraction chromatography resins for radiochemical applications. Several of these resins have been designed specifically for the separation of technetium, while others have been retrospectively discovered to have beneficial technetium separation characteristics. Determining the optimum resin to purify the ^{97}Tc tracer depends on the resin's ability to separate ruthenium and high levels of Mo in the target material. The development of a chemical separation process was not a retrospective thought to the production method, but was an active part in the choice of reaction, as highlighted in section 3.9.

All of the Triskem resins have been characterised by Triskem International, with validation and further testing at the National Physical Laboratory (NPL).

5.3.1 TEVA

TEVA is an acronym of **TE**tra**V**alent **A**ctinides and technetium, and as the name suggests, is used for the separation of actinides and technetium [131]. The resin is formed of a quaternary ammonium salt known as Aliquat336. At low concentrations of both HNO_3 and HCl, TEVA has high retention of Tc, decreasing significantly with increased concentrations.

5.3.2 TK-TcScint

TK-TcScint is a relatively novel resin, with the extractant itself being Aliquant-336, a known technetium separation resin used in TEVA [132]. The interesting aspect of the resin is the binding of the extractant to plastic scintillation microspheres; however, this resin is only applicable to liquid-scintillation counting.

5.3.3 **TK**200

Based on TriOctylPhosphine Oxide (TOPO), the extractant is used extensively to extract various metal ions, designed for separating uranium, plutonium and thorium [133]. A unique use of the attractant is the separation of Ga from Zn, particularly useful in separating the medical isotope ^{68}Ga from a Zn target. NPL has worked extensively on extending the current specification of TK200 to enable the separation of Tc. The retention of Tc is high over a wide range (0.1M-10M) of concentrations of HCl, whereas retention is high at low concentrations of HNO_3, decreasing significantly at high concentrations.

5.3.4 **TK**201

A resin based on tertiary amine, it is specifically designed for radiolysis stability by adding long-chained alcohols, which are scavengers of free radicals produced from ionising radiation [134]. This resin has application in the separation of Cu from Ni targets, but more notable is the resin's technetium separation, showing high retention at low acidic concentrations and lower retention of Tc at higher acidic concentrations, particularly in HNO_3.

5.3.5 **TK**202

A high molecular weight resin based on Polyethyleneglycol covalently bound onto a polymer support [123]. This resin was designed specifically for the separation of technetium from high concentrations of molybdenum. The main application of TK202 is the separation of ^{99m}Tc from molybdenum targets for nuclear medicine. One of the main advantages is that TK202 acts as a biphasic system and has the ability to retain chaotropic ions, including TcO_4^-, when in the presence of kosmotropic anions (anions which enhance H-bonding in water molecules), including MoO_4^{2-}. This makes TK202 further suited for the separation of Tc from high concentrations of Mo, such as Mo target irradiations.

Studies have shown very high retention of Tc and low retention of Mo, particularly at alkaline concentrations of 7 M-9 M NaOH [135], as shown in figure 5.1. An additional point of note from the plot is

the divergence in the retention of Tc and Re - highlighting the limitations of Re as a radiotracer for Tc and the importance of a true Tc radiotracer being developed.

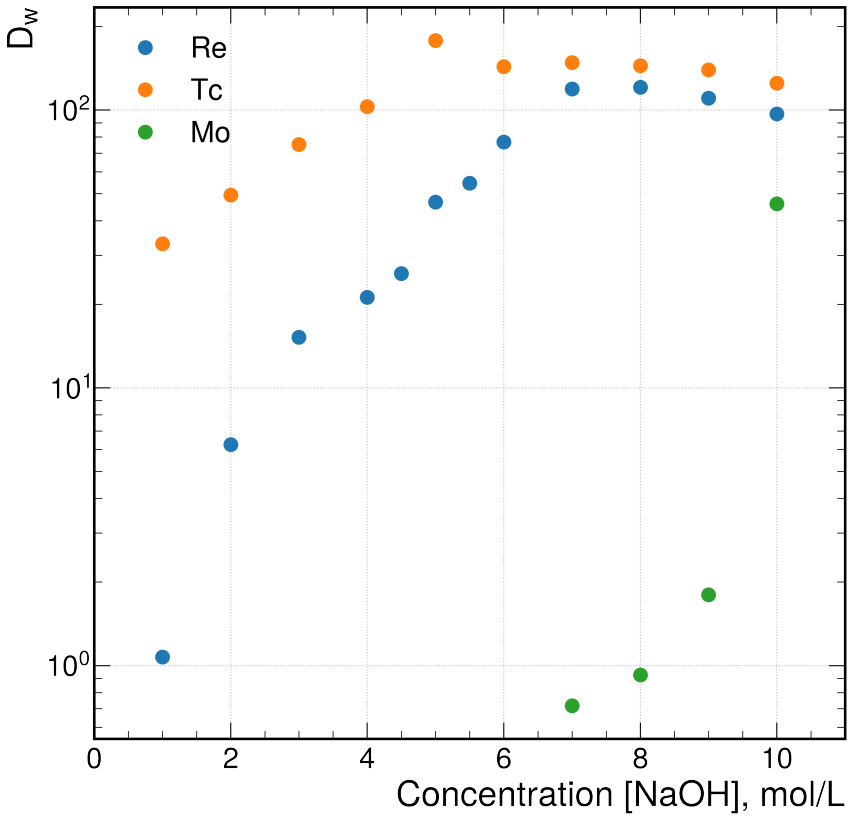


Figure 5.1: *Affinity of Tc, Re and Mo to TK202 over a range of NaOH alkaline conditions from 1 M-10 M as published by Triskem [123].*

Validation of the kosmotropic nature of the resin is published by Polatom, where the retention of Tc was measured as a function of Mo in the sample [135]. The results are shown in figure 5.2.

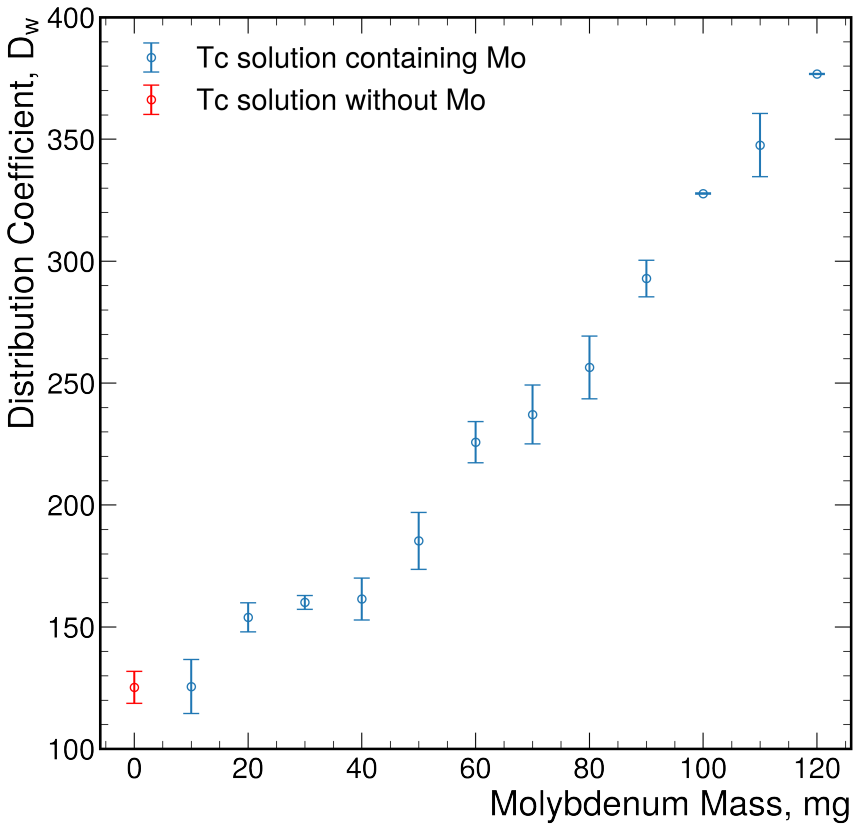


Figure 5.2: *Distribution coefficients for Tc in 5M NaOH on TK202 resin versus molybdenum mass [135].*

Due to its proven ability to deal with the separation of technetium in high concentrations of molybdenum, TK202 instantly became a key candidate for the purification of ^{97}Tc in tracer development. The aim is to optimise the separation procedure for the dissolution of a Mo target, the separation of Mo and Tc and to establish Ru behaviour on TK202, which has not previously been investigated.

5.4 Method Development

A method was developed for the chemical separation of Tc from a Mo target based on TK202, adapting the method used for the separation of medical ^{99m}Tc from low-specific activity molybdenum targets. The main reason is the huge advantage of the kosmotropic nature of the resin benefitting from high concentrations of Mo, a significant reason for the ^{nat}Mo(α,xn)^{97}Ru production route being inves-

tigated. Work was undertaken to validate the increased retention with high levels of molybdenum, the optimum alkali conditions for Tc retention and the effects of high levels of Ru, important due to the prevalence of the generator isotope ^{97}Ru. Prior to this study, there was no information on the behaviour of Ru on TK202.

5.4.1 Reverse Generator

A reverse generator was determined as a potential route for isolating Tc from the Mo and Ru in the target, modifying the method developed for Mo target medical isotope production. The aim was to develop a method to retain technetium within the resin, with the Mo and Ru passing through. An initial separation will be used to separate any Tc produced in the reaction from the Ru and Mo including the ^{97}Ru generator. This first stage enables the separation of any Tc produced directly in the reaction to be separated from the desired Ru generator. Following a period of time, in the order of several half-lives of ^{97}Ru (2.83(23) d), allowing the ^{97}Ru to decay into ^{97}Tc, a second separation is made, retaining only the ^{97}Tc, followed by a wash to collect the isotope. This second step is essential to separate the ^{97}Tc which has decayed from ^{97}Ru from the stable isotopes of ruthenium. A schematic showing the reverse generator method is shown in figure 5.3.

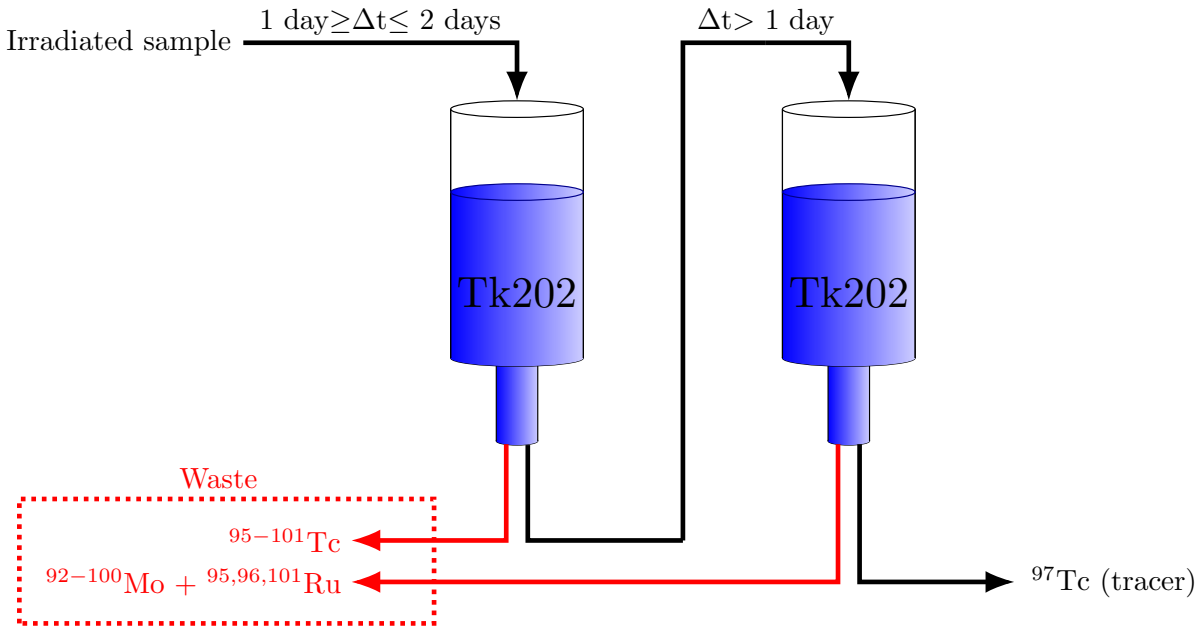


Figure 5.3: *A schematic of the reverse generator approach for the isolation of ^{97}Tc.*

5.4.2 Sample Preparation

Molybdenum is in two common forms, metallic Mo and oxide as MoO or MoO_3. To enable the highest possible production yield, metallic Mo is preferred as the integrated cross-section over the target depth will be higher compared to the oxide, as the O isotopes will degrade the energy of the beam (according to the Bethe Bloche charged particle stopping power formula) without increasing the yield of ^{97}Ru.

Metallic Mo has high thermal stability, with a melting point of $2,623$ °C [109] and high chemical stability, with no visible reaction with oxygen or water at room temperature. At temperatures above 300 °C, slight oxidation occurs, and bulk oxidation above 600 °C. Molybdenum also shows little desire to form cations in aqueous solutions[136]. These factors make the dissolution of a metallic Mo target non-trivial, requiring highly reducing agents to break down the metallic structure.

Acid dissolution can be effective but is not practical if column separation requires alkaline conditions. Previous work suggested hydrogen peroxide (H_2O_2) as an effective means of dissolving the metallic targets [137]. Initial tests were performed by dissolving unirradiated targets of Mo with a range of masses of Mo of 40 mg, 120 mg, 280 mg and 550 mg in 6 ml of 30 % H_2O_2. The initial dissolution rate was slow for all of the samples while heating the samples on hotplates to temperatures of around 70 °C caused a notable increase in the reaction rate [138]. As the target dissolved, the colourless hydrogen peroxide gained a yellow hue. During the evaporation of the H_2O_2, the process was optimised to prevent the evaporation of technetium. A cover was placed on the top of the container to increase refluxing and prevent losses of the solution. The sample was heated but maintained below 80°C, and the beaker was removed from the hot plate before the solution reached complete dryness.

Once the dissolution was complete, the samples were left on the hot plates allowing the hydrogen peroxide to evaporate, leaving an orange molybdenum oxide precipitate. The process from adding the peroxide to obtaining the evaporated precipitate took between 30 minutes to 1 hour - however this is affected by the beaker geometry, volume of solution and temperature. Dissolution was successful for

all of the Mo masses tested.

For the next stage of method development, ~ 0.2g strips of Mo were dissolved in $1-5$ M NaOH and $5-6$ M KOH in 1 M intervals. All samples redissolved readily in approximately 6 ml of alkaline solution; however, the higher concentrations of NaOH (7M) required slight heating to around $50\,^{\circ}$C and the use of magnetic stirrers to remove any residual precipitate.

Both prepackaged cartridges of TK202 and bulk resin used in the experiments were provided directly by Triskem International. When using bulk resin, packing the resin columns was significantly easier with the resin preconditioned overnight in a small volume of 1M NaOH solution pipetted into the resin.

5.4.3 Optimising Separation Conditions

To determine the optimum separation conditions, elutions were performed with simulated targets. These were formed of 500 mg quantities of Mo, dissolved using the target preparation method described above, and doped with standards of Ru and stable Re, a chemical analogue of Tc. The advantage of using Re in the method development was the similar chemical properties of Re to Tc, while preventing the interference between ^{99}Ru and ^{99}Tc and the handling of active material during method development.

The range of alkaline concentrations of both KOH and NaOH was used to validate the work performed by Polatom for 3 M, 4 M and 5 M NaOH for both Re and Mo, with the addition of Ru [135]. The work was extended to include 1 M and 2 M NaOH and 1 M-5 M KOH for Mo, Ru and Re. These tests were performed using 0.2 g samples of Mo doped with low concentrations of Re and Ru. Following the dissolution process and conversion to alkaline solution, the samples were passed through the prepacked TK202 columns using a partial vacuum to assist in drawing the solution through the column as assistance at a flow rate of $\sim$ 2 mL per minute. While no quantitative trend was drawn on the effect of flow rate, early tests with different flow rates showed huge variations in the retention

of Tc. The recommended flow rate in the method is 1 mL per minute. For all tests, the Mo foil was dissolved in 5 mL of the selected alkali and loaded onto the column. This was followed by a 10 mL wash with the same alkali conditions, with the aim of collecting the Mo and Ru in the load and wash. For all tests, a 10 mL deionised water elution stage was added to collect Re. A 0.1 mL aliquot of the load collected, wash and elution stages was collected and diluted to 10 mL with deionised water for ICP-MS measurement. A 0.1 mL aliquot of the load solution was also collected prior to adding this to the column to calculate the Mo, Ru and Re recovery in each fraction.

The results for the recovery of Ru, Re and Mo for NaOH are shown in figures 5.4, 5.5 and 5.6 for the load collected, wash and elution respectively. All analysis was performed using an Agilent 8800 ICP-MS [42].

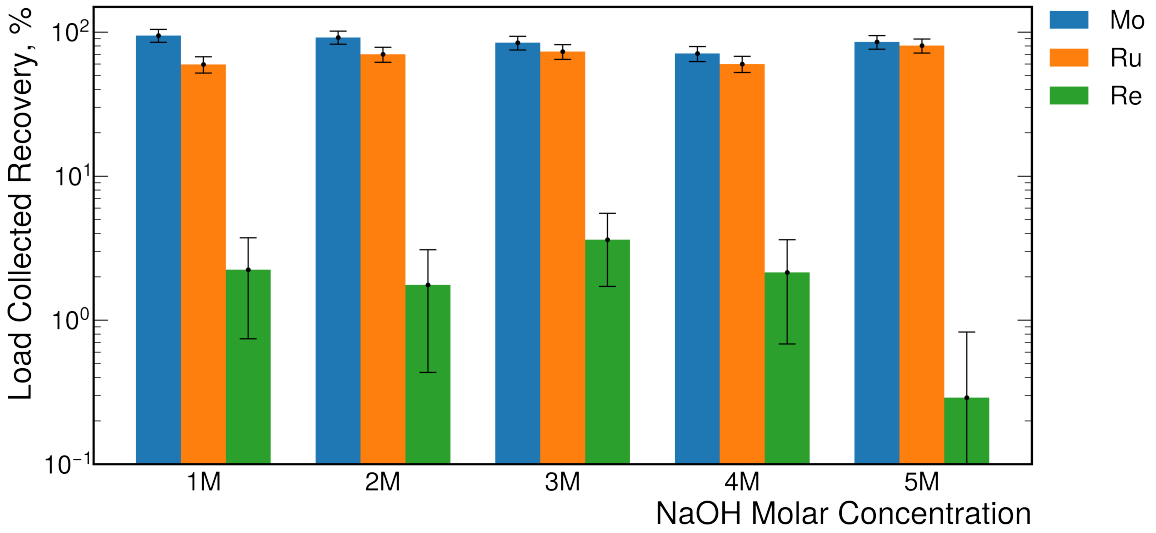


Figure 5.4: *Percentage recovery in the load collected of Mo, Ru and Re in varying NaOH molar concentrations through TK*202.

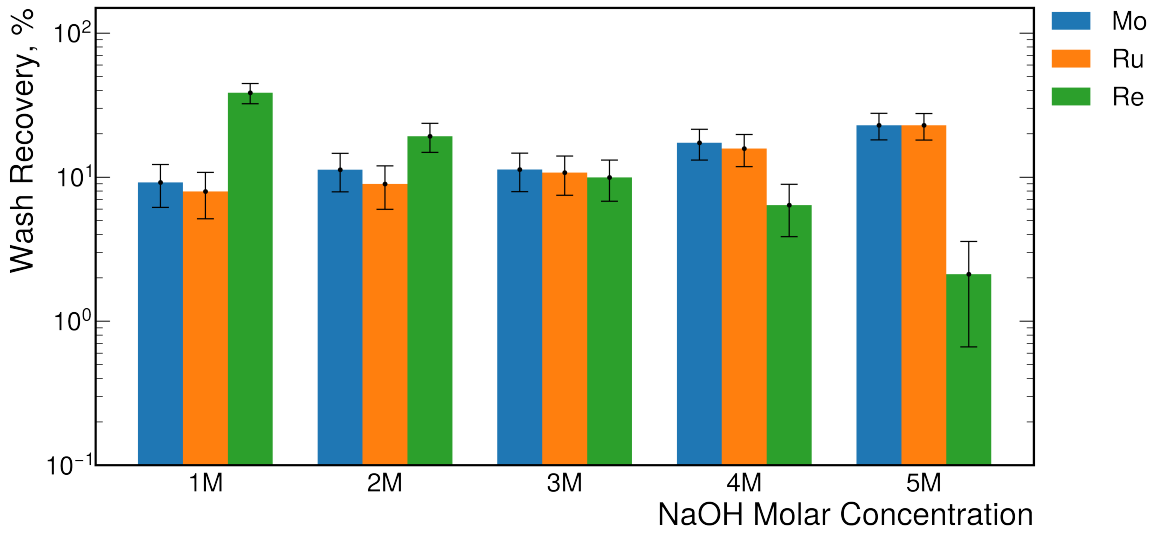


Figure 5.5: *Percentage recovery in the wash of Mo, Ru and Re in varying NaOH molar concentrations through TK*202.

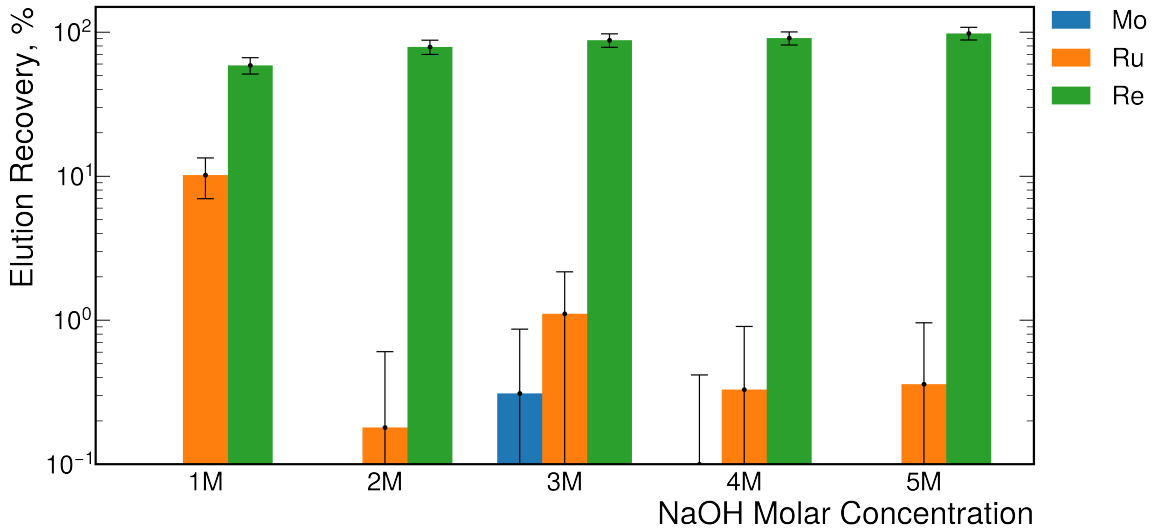


Figure 5.6: *Percentage recovery in the elution of Mo, Ru and Re in varying NaOH molar concentrations through TK*202.

The results are also tabulated in table 5.1. 5 M was shown to be the optimal solution for NaOH with a high recovery of Ru at 22.88% in the wash, 80.48% in the load collected and only 0.36% in the elution fraction. For Mo, 22.94% was in the wash, 85.35% in the load collected and 0.06% in the elution, showing similar chemical properties to Mo. The Re (a surrogate of Tc) acted significantly differently,

with 2.12% in the wash, 0.29% in the load collected and 97.93% in the elution fraction, showing high retention at the alkaline conditions.

Table 5.1: *Percentage recovery of Mo, Ru and Re in the elution using de-ionised H_2O, following running the samples through the TK202 extraction chromatography resin with varying molar concentrations of NaOH.*

	Load Collected			Wash			Elution		
	Mo	**Ru**	**Re**	**Mo**	**Ru**	**Re**	**Mo**	**Ru**	**Re**
1M NaOH	94.61	59.69	2.24	9.2	7.96	38.5	0.07	10.17	58.8
2M NaOH	91.83	70.10	1.76	11.27	8.98	19.26	0.08	0.18	78.92
3M NaOH	84.30	73.21	3.62	11.3	10.75	9.96	0.31	1.11	87.88
4M NaOH	70.96	60.08	2.15	17.31	15.81	6.39	0.1	0.33	90.77
5M NaOH	85.35	80.48	0.29	22.94	22.88	2.12	0.06	0.36	97.93

The recovery for 1 M-5 M KOH for Mo, Ru and Re in the load collected, wash and elution for 5.9, 5.7 and 5.8 respectively.

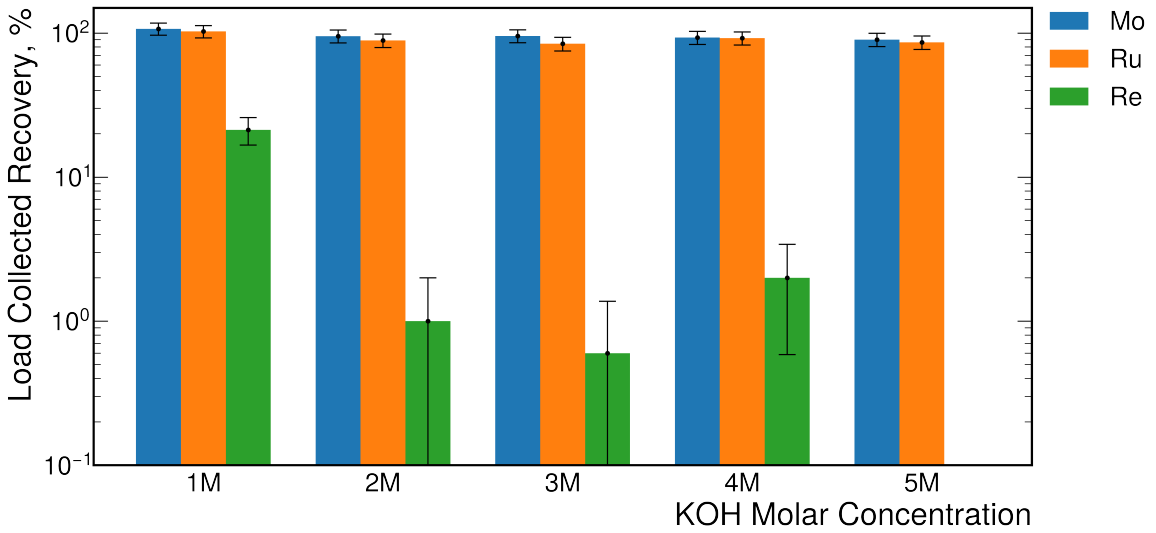


Figure 5.7: *Percentage recovery in the load collected of Mo, Ru and Re in varying KOH molar concentrations through TK202.*

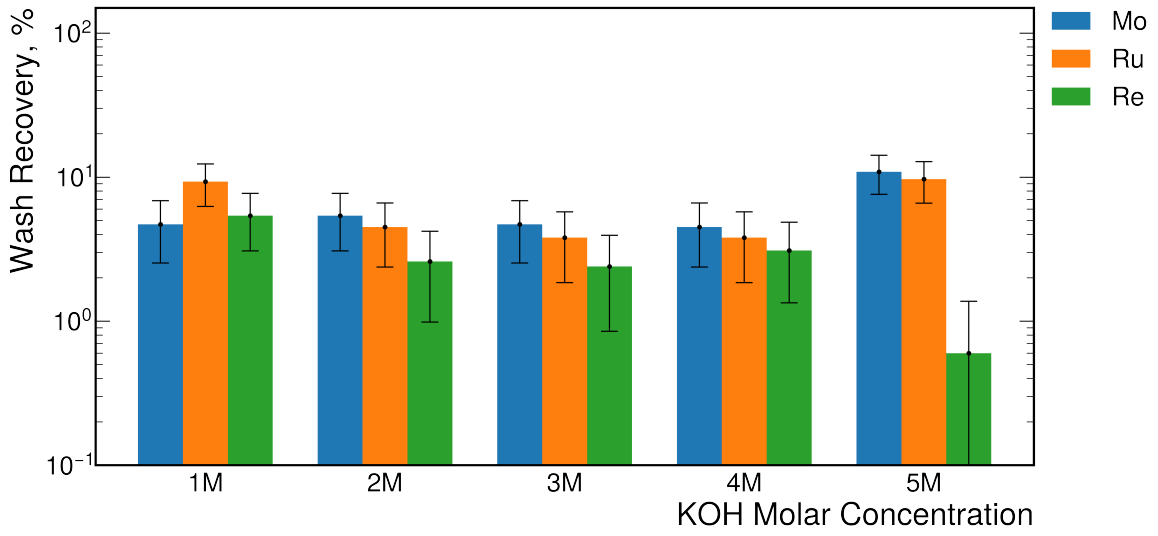


Figure 5.8: *Percentage recovery in the wash of Mo, Ru and Re in varying KOH molar concentrations through TK202.*

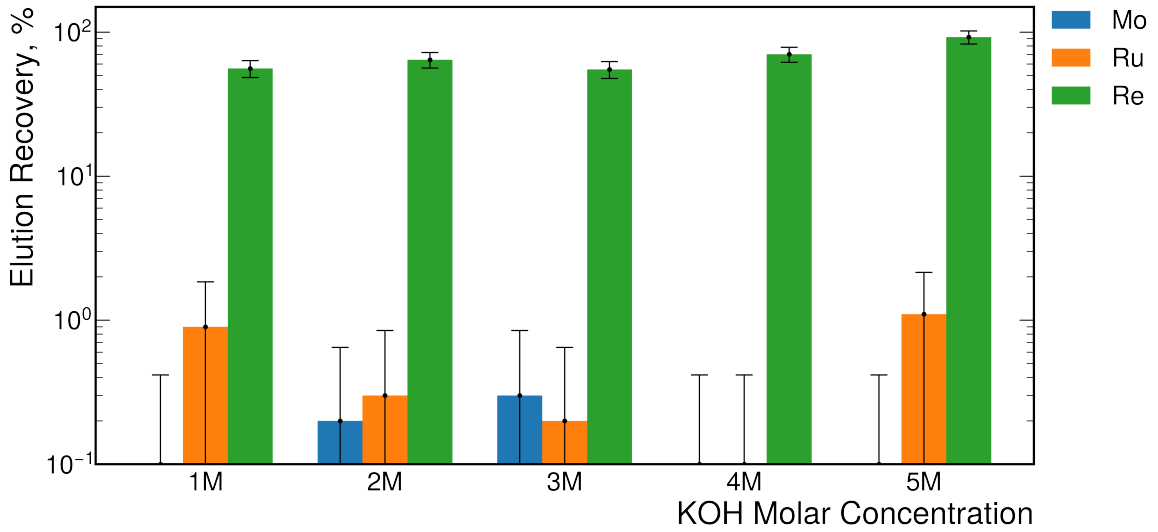


Figure 5.9: *Percentage recovery in the elution of Mo, Ru and Re in varying KOH molar concentrations through TK202.*

The percentage recovery values for Mo, Ru and Re at molar concentrations of KOH between 1 M and 5 M are tabulated in table 5.2.

Table 5.2: *Percentage recovery of Mo, Ru and Re at varying molar concentrations of KOH through TK202 extraction chromatography resin.*

	Load Collected			Wash			Elution		
	Mo	**Ru**	**Re**	**Mo**	**Ru**	**Re**	**Mo**	**Ru**	**Re**
1M KOH	107.1	102.7	21.3	4.7	9.3	5.4	0.1	0.9	55.9
2M KOH	95.3	88.9	1.0	5.4	4.5	2.6	0.2	0.3	64.2
3M KOH	95.4	84.3	0.6	4.7	3.8	2.4	0.3	0.2	55.0
4M KOH	93.1	92.2	2.0	4.5	3.8	3.1	0.1	0.1	70.1
5M KOH	90.1	86.2	0.0	10.9	9.7	0.6	0.1	1.1	92.2

For KOH the optimum alkaline condition was determined to be 5 M KOH due to the low levels of Re in the wash at 0.6 % and 0.0 % in the load collected. 92 % was detected in the elution fraction. There was high retention of Mo with 10.9 % in the wash and 90.1 % in the load collected, with only 0.1 % detected in the elution fraction. The results were similar for the Ru with 9.7 % in the wash, 86.2 % in the load collected, with only 0.1 % detected in the elution fraction. The same tests were performed for 6 M-8 M KOH but significantly higher Re recovery was detected in the load and wash. In the load collected the recovery was 25.7%, 30.7% and 63.2% for 6 M, 7 M and 8 M respectively. In the wash the recovery was 7.5%, 7.4% and 59.9% for 6 M, 7 M and 8 M respectively.

From the KOH and NaOH elution plots at 1 M-5 M concentrations, it is clear that the 5 M NaOH is the optimum chemistry enabling high retention of technetium and low retention of both ruthenium and molybdenum as desired. The results for 5 M HaOH are collated in figure 5.10.

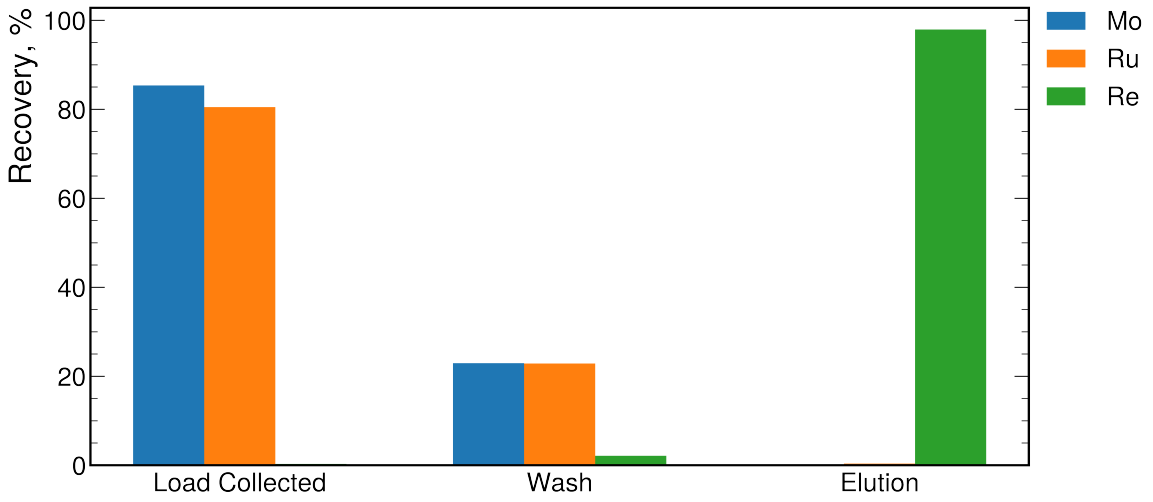


Figure 5.10: *The recovery of Ru, Mo and Re under the optimum conditions of 5M NaOH*

5.5 Chemical Separation Scheme

An optimised chemical separation scheme was developed from the work performed, detailing the steps to take an irradiated target and convert it into a high purity tracer of ^{97}Tc. The separation scheme is shown in figure 5.11

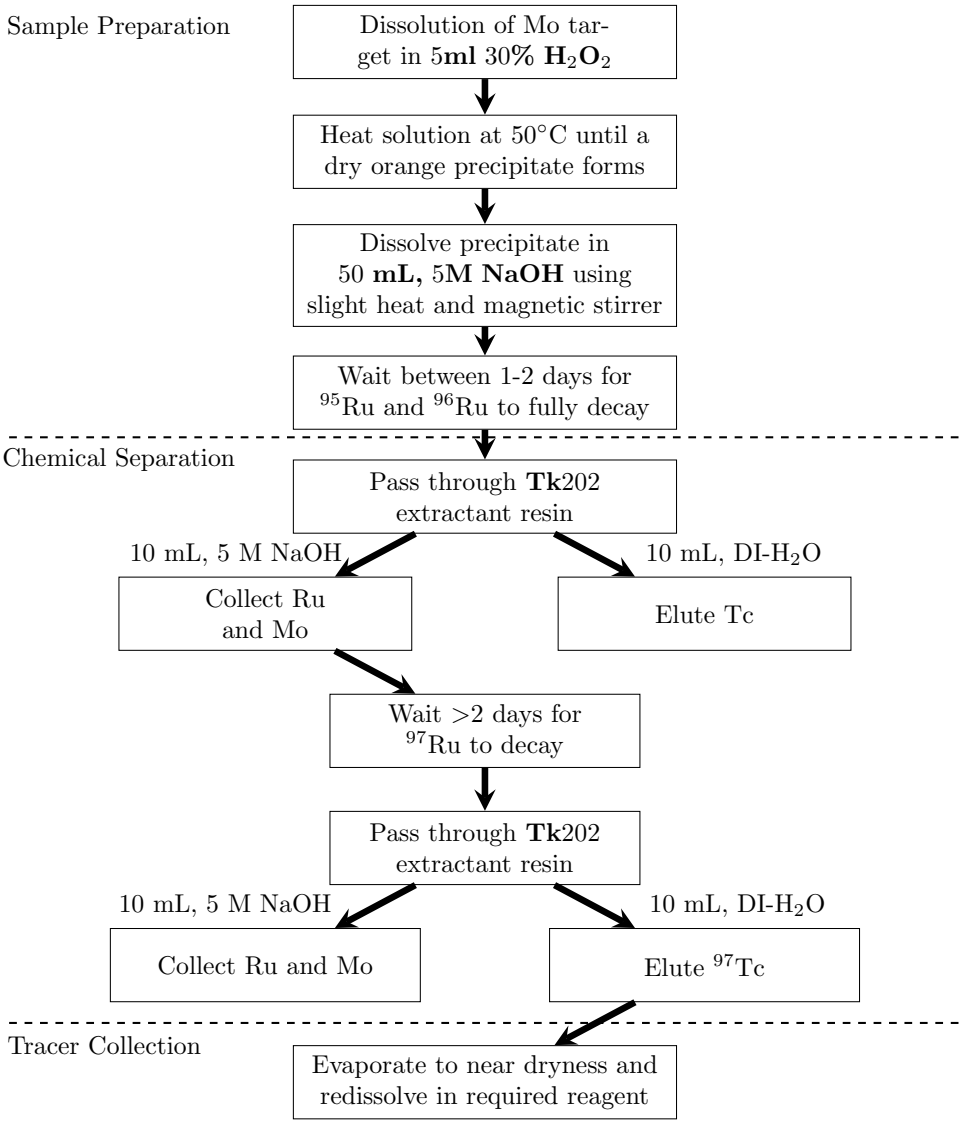


Figure 5.11: *Chemical separation scheme for isolating ^{97}Tc from a Mo irradiated target through a ^{97}Ru generator isotope.*

5.6 Surrogate Target Experiment

Prior to the use of an activated target, a surrogate was used, where the concentrations of each of the elements could be controlled by doping them into a pure-unirradiated Mo target, dissolved in the 5 M NaOH alkaline solutions, determined to be the optimum separation conditions.

The separation was performed as described by the method developed in figure 5.11.

5.6.1 Mass Spectrometry Measurement

Samples were collected after each stage of both separations. These samples were measured using ICP-MS/MS, with Tc monitored at mass 99 and Ru at mass 102. There is an isobaric overlap at mass 99 from ^{99}Ru, which was corrected using the counts at mass 102, assuming natural Ru abundances in the spiked samples. This correction does not account for instrument mass bias, however, this is predicted to be low relative to the uncertainty in the measurement. The percentage recovery was calculated relative to the counts in the aliquot at time 0 i.e. before the sample was loaded onto the column. Each fraction was corrected for the dilution before mass spec measurement and for the mass of the aliquot taken from the sample.

5.6.2 Mass Spectrometry Results

This test was used to verify the results obtained using stable Re as an analogue of Tc. Spiking Mo foils with stable Ru and ^{99}Tc was run in the optimised mode described (load and wash in 5 M NaOH). The results were in good agreement with those obtained using Re. In the first separation stage, Ru was only detected in the load and wash fractions. In separation stage 2, the majority of ^{99}Tc was detected in the elution fraction, with a recovery on the order of 60%.

5.7 Active Sample Validation

Following the successful elution tests and development of an optimised chemical separation scheme, it was important to validate the method with a radioactive, irradiated target. The irradiation was performed at the University of Birmingham MC40 cyclotron, with the sample transported to the National Physical Laboratory for chemical separation and radiometric and mass analysis.

5.7.1 Irradiation

A 250μm thick foil of metallic Mo was α irradiated at the University of Birmingham cyclotron with a beam-current of 5 μA for a total of 6 hours, giving an integrated irradiation of 30 μAh. The beam

energy at the front of the target was 15.5 MeV, below the threshold for ^{99}Mo production, even considering the beam's energy spread.

FISPACT-II calculations were performed to determine the activity and atom count of the sample and its constituent isotopes following the irradiation. These calculations were essential for radiation safety, transport and sample analysis.

The activity of various products of interest from the end of the irradiation to 1 year following the irradiation are shown in figure 5.12.

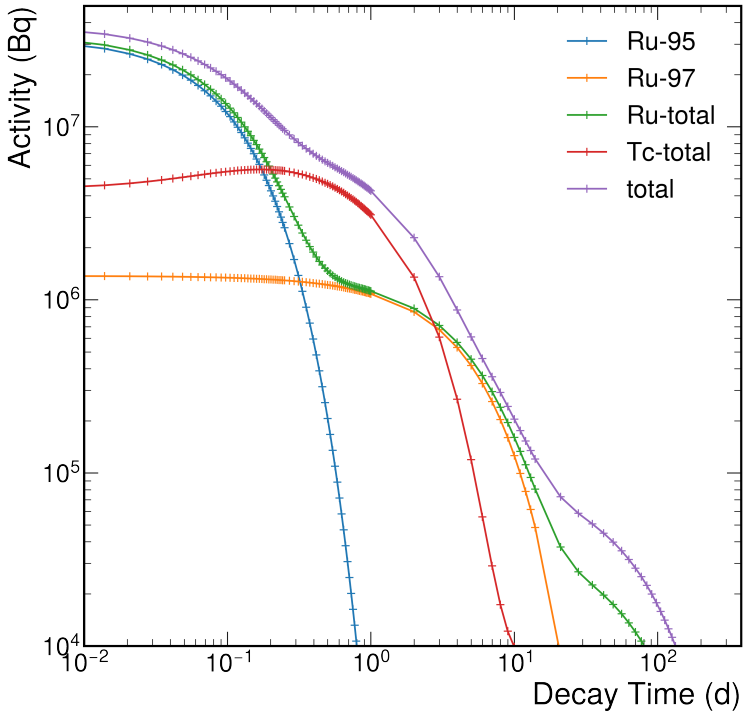


Figure 5.12: *The activity of various products of interest from the end of the irradiation to 1 year of decay time, for a fully-depleted* 15.5 *MeV* α *beam in a* 250μ*m Mo target.*

The lack of presence of ^{99}Mo and ^{96}Tc is due to the beam energy being run below the threshold energy of production of either isotope.

For mass applications, the number of atoms is of more importance than the activity. The number of atoms of a range of isotopes of interest is shown in figure 5.13.

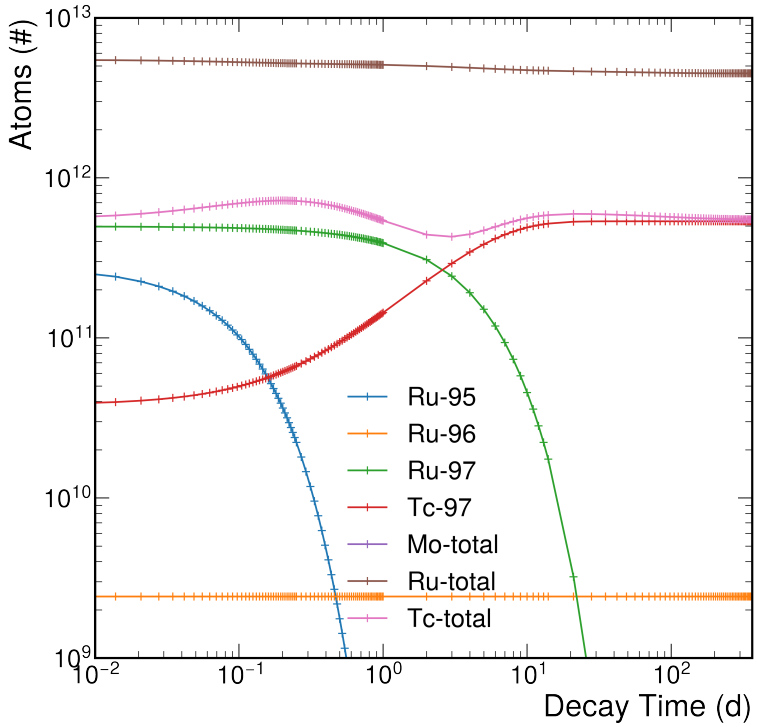


Figure 5.13: *The number of atoms of various products of interest from the end of the irradiation to* 1 *year, for a fully-depleted* α *beam in a* 250 μ*m Mo target.*

These calculations' main focus was confirmation of the lack of ^{99}Mo production at 15.5 MeV, as expected, and determining the quantities of the isotopes of interest. The presence of ^{95}Tc can be handled in two ways, either by separating in an additional separation step, or by leaving the target to decay to remove ^{95}Ru, separating once it has decayed to ^{95}Mo.

At the end of the irradiation, the total activity of the target was calculated to be 66.8 MBq, with 2.38 MBq coming from ^{97}Ru. Immediately after the irradiation, the majority of the activity was predicted to be from the shorter-lived products, including ^{95}Ru, with a half-life of 1.643(13) h [54], responsible for 56.5 MBq of the total activity initially. The sample's activity rapidly drops due to the decay of such short-lived isotopes, with the total activity dropping to 48.5 MBq after 1 hour and 36.4

MBq 2 hours after the irradiation, an important consideration when handling the targets. All target handling was performed the morning after the irradiation was finished to lower the dose, which, as the irradiation was finished at 4 pm, allowed the sample to cool for 17 hours by 9 am. At 9 am the following morning, the total activity of the target was predicted to be 9.39 MBq.

The quantity of ^{95}Ru drops to zero between 2 and 3 days following the irradiation, at which point the ^{97}Ru generator would have lost half of its activity. For this reason, separation was performed at the earliest convenient time, roughly 22 hours after the end of the irradiation.

It is essential to determine the yield of ^{97}Tc from the irradiation and separation. Figure 5.14 shows the ingrowth of ^{97}Tc and the corresponding decay of ^{97}Ru. Once an irradiation has been performed and the quantity of ^{97}Ru has been set, the most important factor in increasing the extractable yield of ^{97}Tc is the timing of the initial separation stage, separating ^{97}Ru from any Tc isotopes produced directly in the reaction, or decay products of short-lived isotopes. The quantity of tracer is calculable as the quantity of ^{97}Tc at the second irradiation minus the quantity of ^{97}Tc at the first separation. The second separation was performed 1 month after the irradiation, which works out as 6.76×10^{11} atoms of ^{97}Tc.

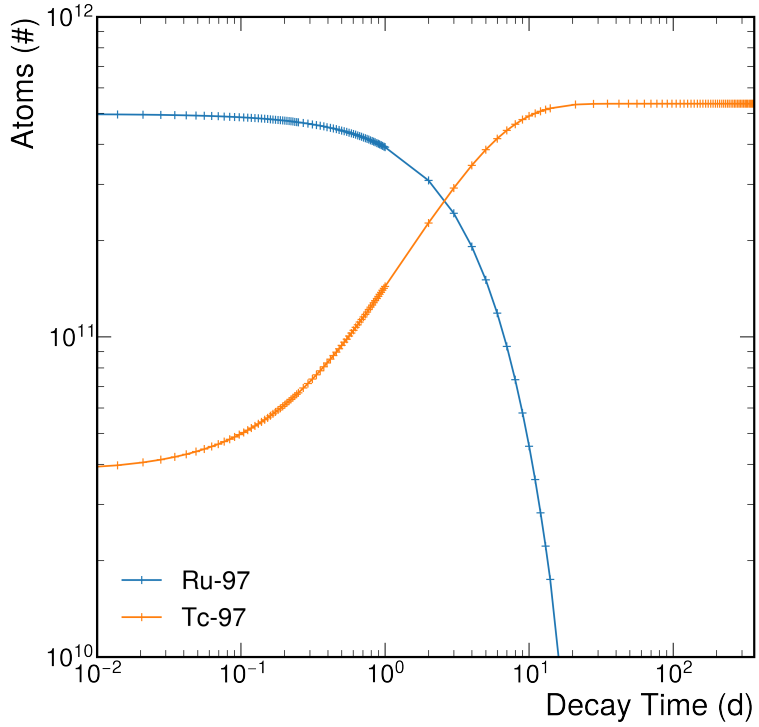


Figure 5.14: *A plot showing the number of atoms of ^{97}Tc and ^{97}Ru following a Mo-α irradiation, with the in-growth of the ^{97}Tc from the decay of ^{97}Ru evident.*

5.7.2 Chemical Separation

Chemical separation was performed using the chemical separation scheme described in section 5.5. All resins used were 2 mL TK202 columns, either prepacked or from bulk resin. All resins were preconditioned in 1M NaOH overnight before the separation.

Following the first separation stage, 0.1mL fractions were taken from the pre-separation, load, wash and elution and placed into 15mL centrifuge tubes ready for mass spectrometry analysis of stable and long-lived radionuclide composition.

Additional sample preparation was performed for gamma-ray spectrometry analysis, with 1g of the sample being dispensed into 2 mL ISO ampoules.

5.7.3 Gamma-ray Spectrometry Measurement

Gamma-ray spectrometry was performed to investigate the short-lived radioisotopes produced in the reaction and gain insight into their quantities and, most importantly, the effectiveness of the separation stages.

A set of 1 g fractions of the aqueous samples was prepared in 2 mL ISO ampoules. Due to the low quantity of sample present, the "LANCELOT" environmental gamma-spectrometer was used. This is a semi-planar HPGe γ detector with a carbon fibre detector window to improve low energy efficiency. The relative efficiency of the detector (the ratio of the absolute efficiency of the detector to that of a sodium iodide detector) is 65%. The samples were mounted concentrically 10mm above the detector face, in a shielded chamber with graded Pb, Cd and Cu to reduce background.

The ISO ampoules analysed are given in table 5.3 showing the sample ID, separation stage and expected elements.

Table 5.3: *Table containing the 2 mL ISO ampoules containing 1 g fractions of the aqueous samples of the dissolved target.*

Separation stage	Expected elements
Pre-separation	(Tc, Mo, Ru)
Load	(Mo+Ru)
Wash	(Mo+Ru)
Rinse	Tc

Using these samples, several spectra were collected over a period of time following the sample separation. The spectra collected are highlighted in table 5.4.

Table 5.4: *Table of the measurements performed on the "LANCELOT" HPGe gamma-ray spectrometer at the National Physical Laboratory.*

Measurement ID	1	2	3	4	5	6
Stage	Wash	Load-Collected	Wash	Pre-sep	Rinse	Rinse
Mmnt Time (s)	65414.86	241965.67	262286.79	180179.29	59414.47	156958.04
Start Date	8/11/2022	8/12/2022	8/19/2022	8/16/2022	8/23/2022	8/24/2022
Start Time	16:02	13:44	9:05	9:55	18:00	14:44
Mass	1	1	1	1	1	1

The acquired spectra are shown in figure 5.15 for spectra of measurement 1-6.

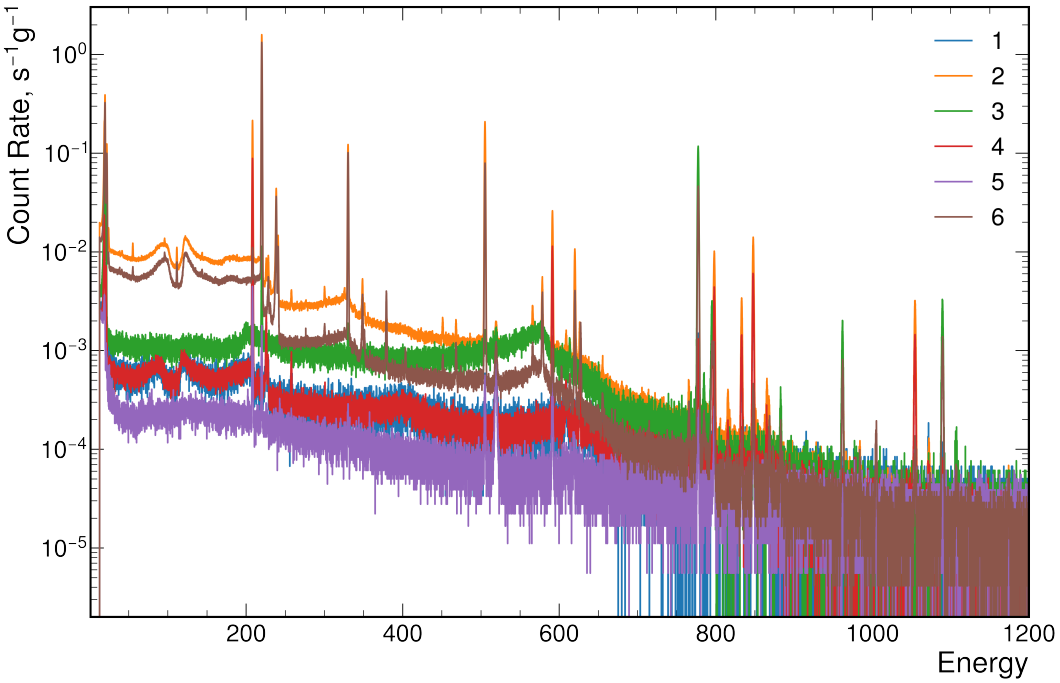


Figure 5.15: *Gamma-ray spectra acquired on LANCELOT HPGe detector at the National Physical Laboratory for six measurements of* 2 *mL ISO ampoules of* 1 *g sample fractions, taken from a separated, irradiated Mo-*α *foil at different times and stages.*

5.7.3.1 Gamma-Ray Spectrometry Results

The decay corrected counts for five key isotopes ^{95}Tc, ^{95m}Tc, ^{97}Ru, ^{99}Mo and ^{103}Ru are given for the 6 measurements in table 5.5, with these visualised in figure 5.16.

Table 5.5: *Decay corrected gamma-spectrum counts per second per gram using the "LANCELOT" detector for the six measurements of a separated Mo-*α *target at varying separation stages.*

Measurement ID	**1**	**2**	**3**	**4**	**5**	**6**
^{95}**Tc**	3.102	1.237	0.003	3.569	0.037	0.034
^{95m}**Tc**	0.030	0.036	0.004	0.458	0.123	0.123
^{97}**Ru**	0.224	48.445	0.209	200.687	0.140	0.129
^{99}**Mo**	0.000	0.022	0.000	0.087	0.000	0.000
^{103}**Ru**	0.009	1.754	0.007	7.315	0.005	0.006

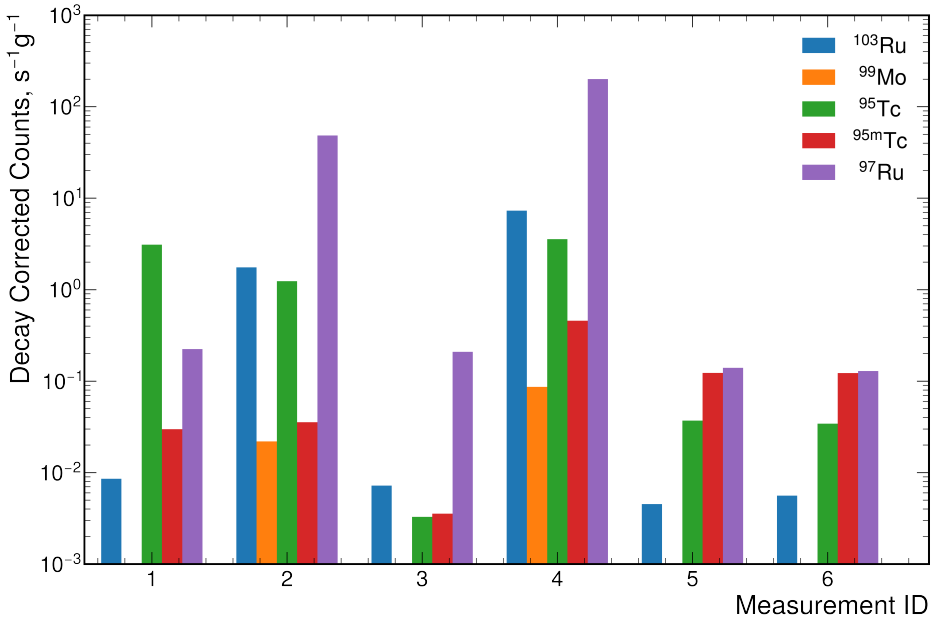


Figure 5.16: *Decay corrected counts per second per gram for the six measurements taken on the "LANCELOT" HPGe gamma-ray detector at the National Physical Laboratory for the separated sample.*

For all of the key isotopes excluding ^{97}Ru, the ratio of counts over the ^{97}Ru counts was calculated.

The results are given in table 5.6 and in figure 5.17.

Table 5.6: *Decay corrected counts per second per gram for each of the six measurements for each isotope of interest as a ratio over the decay corrected counts per second per gram of ^{97}Ru.*

Measurement ID	**1**	**2**	**3**	**4**	**5**	**6**
^{95}Tc	13.8256	0.0255	0.0157	0.0178	0.2652	0.2660
^{95m}Tc	0.1329	0.0007	0.0170	0.0023	0.8804	0.9493
^{99}Mo		0.0005		0.0004		
^{103}Ru	0.0382	0.0362	0.0345	0.0365	0.0325	0.0434

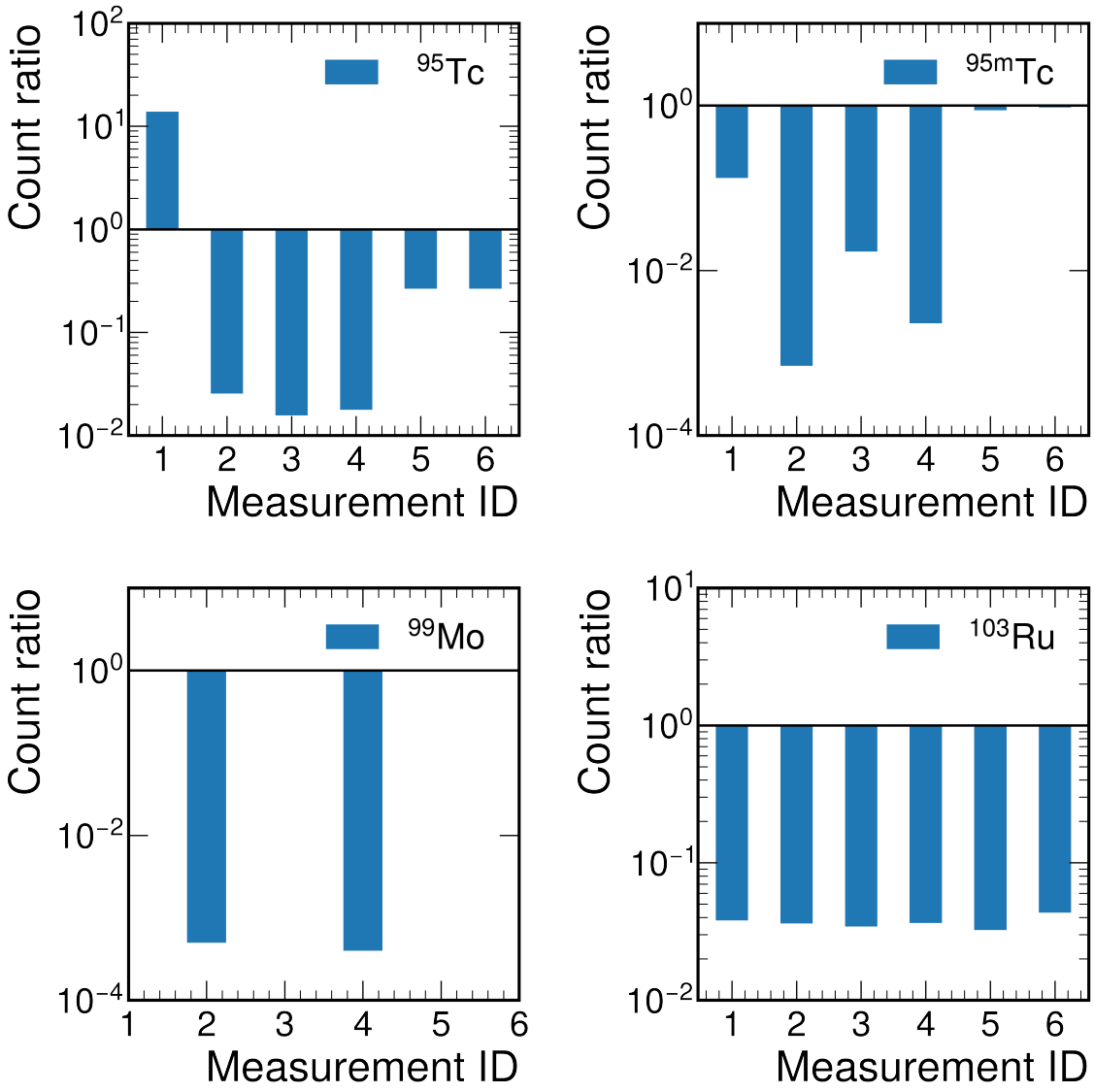


Figure 5.17: *Ratio of counts of four key isotopes ^{95}Tc, ^{95m}Tc, ^{99}Mo and ^{103}Ru over ^{97}Ru for the Mo-α irradiated target separated at NPL, analysed under the "LANCELOT" gamma-ray spectrometer.*

The ^{99}Mo contamination is only found in measurements two and four, which are samples X220488 and X220487. This is a feature which should be avoided if possible, however this contaminant was not expected in the reaction according to both the simulations and cross-section experiment. This could be a product of neutrons produced by interactions at the 25 μm Ti beam-line window. It is hard to be certain on these results as, for example, measurement 1 and 4 were both from the wash, and there is a high level of disagreement with none showing in measurement 1 and a count ratio of 0.0004 in measurement 4.

^{99}Tc was found in all of the samples, which indicated there should be another separation step following the two which have been performed. The concentration was very high in measurement 1, which is taken from the wash collection, however this contradicts the results from fraction 4, which was also taken from the wash.

^{103}Ru shows relatively consistent results over the four measurements, with values of 0.0382, 0.0362, 0.0345, 0.0365, 0.0325 and 0.0434 for measurements 1-6 respectively. This result is surprising as the Ru concentration is expected to be much lower in the wash and elution than in the load collected.

5.7.3.2 Presence of ^{99}Mo

^{99}Mo was detected in the samples through the 140.5 keV γ-peak from ^{99m}Tc. ^{99m}Tc has a short half-life of 6.0 h and would all have fully decayed by the time the measurement was taken, alluding to its presence through the decay of the longer-lived ^{99}Mo with a half-life of 60.0(1) h. The low quantities may have been below the limit of detection to be measured in the cross-section measurement, however with the increased target mass and beam current and use of a high efficiency set-up the peak was detected. It is believed that the reaction was run at energies below the reaction threshold for ^{nat}Mo(α, X)^{99}Mo.

5.7.3.3 Molybdenum Saturation

In the mass spectrometry measurement, it was not possible to detect ^{97}Tc due to the presence of high quantities of stable molybdenum, namely ^{97}Mo, with the formation of hydrides (MoH^+) with ^{96}Mo causing additional contamination to the mass 97 peak. Future method development to reduce this is described in section 6.3.1.

5.8 Conclusion

The development of a novel ^{97}Tc chemical separation scheme showed high promise, utilising a reverse generator offered the ability to separate Tc from Ru and Mo with high concentrations of Mo with

small volumes of resin. The ability to separate Ru from Mo would have huge benefits in running the reaction at higher energies, separating any ^{99}Mo produced in the reaction from the ^{97}Ru generator. The kosmotropic nature of the TK202 resin enabled high retention of Tc with high quantities of Mo present in an initial separation stage, particularly ^{99}Tc, which must be avoided completely in the tracer.

Completing a full-scale irradiation highlighted issues not seen with a controlled surrogate target. The presence of ^{99}Mo was unexpected, however in the Geant4 Monte Carlo simulations, these appear to have come from the interaction of the α-beam with the aluminium target holder. This can be suppressed or removed by improving the target holder design. The saturation of Mo in the separated sample was also unexpected as the chemical properties of the surrogate, and real targets were expected to be more similar, with the decay products being a larger variable. There have been ongoing discussions with Triskem International on how to further improve the Mo reduction. The levels of Mo were significantly reduced by a factor of 10^6, however, for a high-purity tracer more work is needed.

6

Conclusions

This thesis contains a broad range of work, predominantly focusing on the optimisation of accelerator-driven nuclear reactions for isotope production of industry-relevant isotopes, including software developed for nuclear reaction modelling and isotope production calculations, experimental cross-section measurements for the production of a ^{97}Tc tracer and subsequent chemical separation work.

Due to the strong connections with the nuclear industry, facilitated through project funding by the Nuclear Decommissioning Authority and supervision at the National Physical Laboratory Nuclear Metrology Group as well as the National Nuclear Laboratory Nuclear Physics Group, the project was guided throughout to maintain relevance to the industry, maximising the impact of the project. The following sections detailed the relative success of the research, future improvements and how this work can be used as a template for developing a range of other important tracer isotopes for the nuclear industry.

6.1 Nuclear Data Software Development

Early in the project, many nuclear reaction calculations were performed to enable a quantitative comparison of different beam-target combinations and experimental parameters, including energy. It was clear that while the nuclear reaction tools are very powerful, the ability to effectively and easily run large numbers of simulations was missing, along with ordered data output. Each simulation produces 20+ output files, one for each residual nucleus, each exclusive cross-section and several other nuclear reaction parameters. This is not a problem when only running a single nuclear reaction, however, the problem becomes increasingly inhibiting with increasing numbers of reactions. A visualisation suite enabled intuitive comparisons of different nuclear reactions as well as the ability to optimise both the energy of a particular reaction as well as the optimum time for chemical separation of isotopes based on isotopic or activity ratios.

The program has been converted into a python package enabling users to install the program, with example files available to allow somebody with no experience of the interface to run the code. To make sure the code and the ambitions line up with the view and direction of TALYS, conversations were had with Arjan Koning, the TALYS lead developer. Future integration of components of the code into the core of TALYS has been discussed, and the actual implementation will be explored following the conclusion of this project. UoB-TIP can be further developed in several directions depending on the future needs of users, however, UoB-TIP has served the functional purpose and reached all of the initial goals of the project. While the program reached all of the initial objectives, there are ambitions which came to light throughout the development process:

- Implementation of a graphical user interface (GUI);
- Addition of an EXFOR data reader to enable measured reaction cross-sections to be overlaid on plots;
- Ability to convert nuclear reaction simulation data into a format that can be interpreted by FISPACT-II for direct transmutation and activation calculations, accounting for sensitivity of

the cross-section calculations, something not currently possible using the inbuilt nuclear data libraries.

6.2 Technetium Radiotracer Development

Several radionuclides lacking suitable yield tracers were explored at the start of the project, including ^{239}Pu, ^{59}Ni, ^{237}Np and ^{226}Ra. Through extensive conversations with the industry, including the National Physical Laboratory, National Nuclear Laboratory, and several other organisations within the industry, the lack of a mass spectrometry tracer for ^{99}Tc was seen as a high-impact research area. This worked well due to NPL's ongoing work developing technetium separation methods, analysis using both mass spectrometry and liquid scintillation counting and history in producing tracable standards for a range of end users.

The project has made progress in the development of a commercially available tracer for ^{99}Tc, optimising the irradiation of ^{99}Mo to produce ^{97}Ru, which acts as an effective generator of ^{97}Tc, the tracer isotope. The generator stage enables effective chemical separation of unwanted isotopes.

To bring the tracer to a commercially viable level (TRL 9), standardisation is required. This is a rigorous process using multiple analytical techniques on a sample to determine the quantity of the tracer in the sample and the quantification of any impurities. This would be completed following the completion of the chemical separation process, determining the limits of how pure the sample can be made. In a case where the sample did not reach the optimum purity level, enriched molybdenum targets could be explored, avoiding, in particular, any potential production of ^{99}Mo.

6.2.1 Future Method Improvements

When measuring ^{97}Tc by mass methods, the signal from ^{97}Mo (present from the fraction of target material remaining) signal is too high and the ^{97}Tc signal cannot be detected at mass 97. When measuring ^{99}Tc by ICP-MS/MS, the Tc is shifted to a double oxide to overcome Mo and Ru interferences.

However, a large proportion of the Tc signal remains on mass, whilst the majority of Mo shifts to form single and double oxides. Therefore, measuring ^{97}Tc on mass in the separated target using O_2 reaction gas may be beneficial. The next step for ICP-MS/MS is to re-measure the separated target in this way to see if online Mo separation can be achieved to further prove the presence of ^{97}Tc.

6.3 Cross-Section Method Development

This project shows the development of a high-precision cross-section measurement at the University of Birmingham cyclotron, with a wide range of applications in decommissioning, waste management, medicine, nuclear astrophysics, fusion and fission energy.

The cross-section experimental station was advanced greatly by utilising a previously unused beam-line spur, beamline $4a$, at the Birmingham Cyclotron Facility. The improvements are clearly seen in the cross-section data with small errors of the order of a few percent due to a much higher certainty in the beam energy. The automated current logger was a useful addition in terms of enabling the experiment to be more hands-off, however, the difference in precision with data readings taken every 1 minute as previously or every 1 second now was seen to be negligible. However, it is hard to obtain an exact value of the total beam exposure due to remaining uncertainties in the accuracy of measuring the beam current.

The development of an automated analysis software package is a powerful tool, enabling the handling and manipulation of large numbers of data files in the formats required, including Maestro software. The main benefit of the system is the ability to analyse the results online, enabling validation that the measurement is as expected. Simple calculations can then be performed to determine the optimum measurement times to acquire a certain level of statistical certainty.

6.3.1 Future Method Improvements

As with all experiments, there are still large areas for improvement, enabling higher precision and accuracy of data. The most easily achievable method would be full automation of the peak fitting. This would enable a higher throughput of experiments due to the reduced human resources required to acquire and analyse data. Development of an accurate automation tool would also enable the results to be more easily reproducible and the sensitivity to different paramaterisations of the fit could be easily assessed, which leads to a better quantification of errors. A couple of attempts were made using both ROOT and RadWare gf3 to automate data fitting, however, due to the significant and varying background, this proved challenging, particularly where doublet-peaks were found.

Experimentally, the most obvious improvements would involve upgrades to the decay counting set-up. Currently, two HPGe detectors are used, however, due to the large number of foils being analysed, this was a labour-intensive process, especially a short time following the irradiations where the changing between the foils was more frequent. Increasing the number of detectors would improve this, or multiple irradiations, where the foils are irradiated and analysed successively rather than in parallel. This method would improve the data as the foils could be analysed continuously, with the data broken down into certain measurement windows retrospectively, enabling the optimum balance between statistics in a single spectrum and the total number of spectra. Alternatively, digitisers could be used, whereby the data are collected as timestamped datums, which can be broken down into individual spectra, with measurement times suited to each individual peak decay.

The use of coincidence counting and Compton suppression using thick lead shielding around the detector would be an advantageous addition to the experimental set-up, enabling the low probability photo-peaks peaks to be distinguished more easily. It was seen that manually removing the background using algorithms greatly improved the accuracy of automated fitting, and it is expected that a reduction in the background in acquisition would have an equal effect.

6.4 Technetium Chemical Separation

Partnership with the National Physical Laboratory enabled the development of a robust chemical separation scheme for the production of ^{97}Tc as a tracer, using the expertise and experience of both NPL and its collaborations with Triskem International Ltd (a company which develops extraction chromatography resins), to limit the parameter space for the isotope production.

6.4.1 Future Work

Based on the current results, several future steps are being prepared to enable a higher purity of ^{97}Tc to be separated, including the use of additional stages of separation with the TK202 resin and the use of alumina columns.

6.5 Additional Benefits of Mo-α Nuclear Data

The focus of the Mo-α cross-section modelling and experimental validation in this thesis was to develop a novel ^{97}Tc radiotracer, however, with research, it is important to understand and appreciate the wider applications and impact of the work undertaken.

6.5.1 Nuclear Medicine

The use of ^{97}Ru as a medical isotope is well described in the literature. The emission of a clear γ-ray at $215.70(3)$ keV with a branching ratio of 85.62% [56] makes ^{97}Ru a leading candidate for single-photon emission computed tomography (SPECT)[139, 113]. While the purity levels of ^{97}Ru required for medical applications using Mo-α reactions would require enrichment to prevent the population of a large spread of Ru isotopes, improved data on ^{nat}Mo assists in showing the feasibility of the method. Further work on the development of a ^{97}Tc tracer using a ^{97}Ru generator may lead to improved nuclear data on the decay of ^{97}Ru and that of ^{97}Tc. The work in this project on the separation of Ru and Tc contributes through the development of a purification method of Ru from Tc.

6.5.2 Fusion Energy

Molybdenum is a potential candidate material for use in fusion reactors. The chemical properties of molybdenum are incredibly promising for fusion. Molybdenum has the fifth highest melting temperature of any element at $2,623°C$ [109], only behind tungsten, rhenium, osmium and tantalum, all of which are far more scarce than molybdenum. The ease of fabrication of Mo and low neutron-induced embrittlement compared to the leading candidate, tungsten, assist Mo's candidacy in fusion energy. Molybdenum has a low sputtering yield, the number of atoms released per incident ion on the material. Sputtering causes degradation to plasma performance due to the energy required to ionise the atom, therefore, the low sputtering yield of Mo further assists in its potential. In plasma-facing components, alpha-induced reactions on molybdenum are highly important in the radioactive products produced. The limiting factor in implementing Mo in fusion energy is the reactions with neutrons, producing long-lived waste, including ^{99}Tc [140]. While neutron-induced reactions on Mo are most important due to the high neutron flux and no Coulomb barrier to overcome, a better definition of α induced cross-sections can be used to gain a better understanding of the nuclear structure parameters of Mo isotopes, leading to the better predictive power of nuclear reaction models for molybdenum.

6.6 Future Tracer Development

This work focused on developing a technetium radiotracer; the method developed will act as a template for future collaboration between the University of Birmingham and the National Physical Laboratory on developing tracers of high importance in the nuclear industry. This study takes insight and direction directly from industry on what isotopes would add significant value to the analysis of difficult-to-measure radionuclides and determine one or more candidate radio-isotopes along with any radionuclides which must be avoided. Nuclear reaction models can then be executed for all possible beam-target energies. The elements produced can then be assessed on the ability to chemically separate them. A chemical separation method can then be developed, and nuclear data improved where applicable. Once these steps have been concluded and a high-purity radiotracer has been produced, standardisation is required, where the concentration of the radionuclide is quantified to a high standard.

The process of radiotracer development is visualised in figure 6.1.

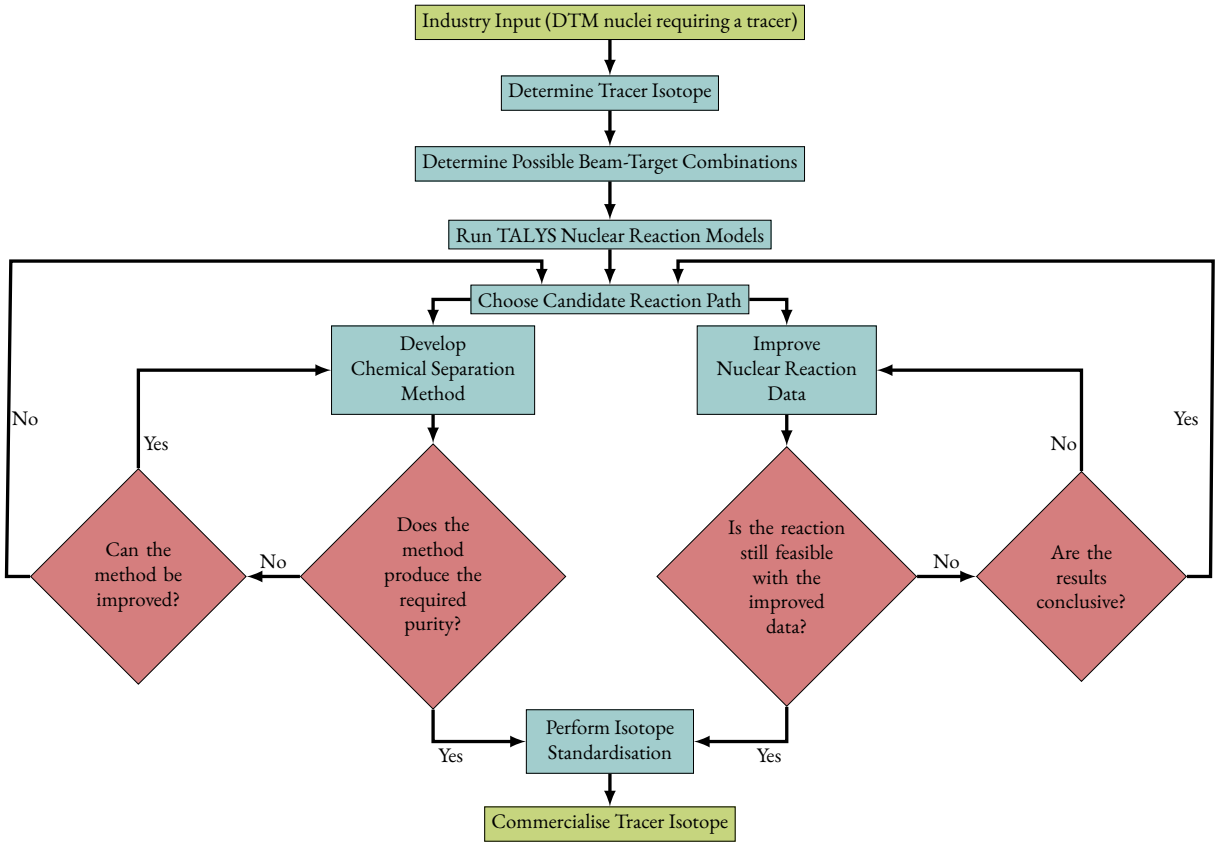


Figure 6.1: *Flowchart for developing a novel radio-isotope tracer for difficult-to-measure (DTM) nuclides, taking input from industry, followed by an iterative research and development project and final standardisation and commercialisation.*

Several tracers with a strong desire from the industry have already been highlighted, including radium-228 for radium-226, plutonium-236, 242 or 244 as a tracer for plutonium-239 and 240. Another tracer of interest is neptunium-236 for neptunium-237, which NPL have pursued previously, with little success [14], however, it is believed the cross-section measurement capabilities along with the improved reaction optimisation modelling tools developed during this project, could significantly assist in optimising this tracer development work.

A

Conference Presentations

- Production of 95mTc radiotracer for the analysis of ^{99}Tc

  Nuclear Decommissioning Authority PhD Seminar, January 2019: Oral

- Production of Novel Radioisotopes for Tracking of Long-Lived Fission Products

  UK Nuclear Physics Summer School, August 2019: Oral

- Production of Novel Radioisotopes for the Analysis of Technetium-99

  Conference of Applied Radio-Metrology, December 2019: Oral

- Production of Novel Radiotracers to Characterise Technetium-99 in Spent Nuclear Fuel

  10th International Conference on Isotope, February 2020: Oral

- Optimisation of isotope production using computational modelling - Development of an interface code for TALYS and EMPIRE

  Institute of Physics - Nuclear Physics Lockdown Seminar, August 2020: Oral

- Development of Novel Radio Isotope Tracers : A Computational Approach

Virtual- Conference of Applied Radio-Metrology 2020, Jan 2020: Oral

- Developing a Tc tracer: from cross-section to Characterisation

  TRANSCEND & NDA PhD Conference, Dec 2020: Oral

- The Optimisation Of Nuclear Reactions For The Production of Industrial Deodorizers Using the UOB-TIP Computational Package

  2nd International CBRNe, December 2020: Poster

- Development of UoB-TIP (University of Birmingham - Tool for Isotope Production) A computational tool for rapid comparison in isotope production

  Institute of Physics APP/HEPP/NP, May 2021: Poster (Award winner)

- The development of a novel ^{97}Tc radiotracer: the pursuit of nuclear data

  International Nuclear Physics Conference, Sept 2022: Oral

B

Variable Cross-Section Reaction Rate Derivation

The reaction rate for an infinitesimally thin foil may be given as

$$R_R = \phi N_T \sigma A dx, \tag{B.1}$$

where ϕ is the fuel, σ is the cross-section, N_T is the target number density, A is the beam surface area, and dx is a thin slice of the target thickness. For thick targets, we can integrate dx, while the cross-section can no longer be assumed to be constant, and is given as $\sigma(x)$, a function of distance into the target. The reaction rate is then

$$R_R = \phi N_T A \int \sigma(x) dx, \tag{B.2}$$

Multiplying the beam area, A, and the flux, ϕ, gives the reaction rate as a function of beam current, I_B. A more relevant parameter in accelerator physics

$$R_R = I_B N_T \int \sigma(x) dx, \tag{B.3}$$

Cross-section is usually a function of energy. To convert the variables one can use the inequality

$$dx = \frac{dx}{dE} dE, \tag{B.4}$$

which when applied to the reaction rate gives

$$R_R = \phi N_T A \int_{E_0}^{E_1} \sigma(E) \frac{dx}{dE} dE. \tag{B.5}$$

The factor of $\frac{dx}{dE}$ is the inverse of the stopping power. Calculating the reaction rate for a target between energies E_1 and E_0 gives

$$R_R = \phi N_T A \int_{E_0}^{E_1} \sigma(E) \left(\frac{dE}{dx} \right)^{-1} dE. \tag{B.6}$$

C

Nuclear Reaction Modelling Results

Table C.1: *TASMAN reaction results for Ru-p, showing the residual production cross-section and exclusive cross-section along with key values: Q-value, energy threshold, maximum cross-section and the energy of the maximum. The values of Q, E_thres, and E(XS$_{max}$) are in units of MeV, and σ_{max} and error(σ_{max}) are in units of mb.*

Product	Target	Ejectile	Q	E$_{thres}$	σ_{max}	error(σ_{max})	E(XS$_{max}$)
^{97}Ru	^{101}Ru	d3n	-25.641	25.897	8.8675	0.84966	40
^{97}Ru	^{99}Ru	dn	-9.16565	9.25899	460.563	36.978	34.2
^{97}Ru	^{98}Ru	d	-7.95106	8.03286	526.075	41.206	24.8
^{97}Ru	^{100}Ru	d2n	-18.839	19.0289	243.834	23.887	40
^{97}Ru	^{102}Ru	d4n	-34.8607	35.2052	0.0036	0.00024	40
^{97}Ru	^{nat}Ru	pXn	x	8.03286	76.8742	5.94196	40
^{97}Rh	^{96}Ru	γ	3.80615	0.0	4.0962	0.08695	7.2
^{97}Rh	^{101}Ru	5n	-38.4282	38.8118	2.3245	0.26391	40
^{97}Rh	^{99}Ru	3n	-21.9528	22.1764	357.42	23.803	29.2
^{97}Rh	^{98}Ru	2n	-14.481	14.63	604.093	24.138	19.4
^{97}Rh	^{100}Ru	4n	-31.6261	31.945	156.013	15.651	40
^{97}Rh	^{nat}Ru	γXn	x	0.0	48.7417	3.18043	29.0
^{99}Mo	^{101}Ru	αp	-16.5659	16.7313	0.0012	0.00034	40
^{99}Mo	^{104}Ru	αd	-10.3973	10.4981	0.0875	0.00787	40
^{99}Mo	^{nat}Ru	αpXn	x	10.4981	0.0164	0.00159	40

Table C.2: *TASMAN reaction results for Ru-d, showing the residual production cross-section and exclusive cross-section along with key values: Q-value, energy threshold, maximum cross-section and the energy of the maximum. The values of Q, E_thres, and E(XS_{max}) are in units of MeV, and σ_{max} and error(σ_{max}) are in units of mb.*

Product	Target	Ejectile	Q	E_{thres}	σ_{max}	error(σ_{max})	E(XS_{max})
^{97}Ru	^{96}Ru	p	5.88693	0.0	336.198	22.1	10.6
^{97}Ru	^{101}Ru	d4n	-27.8656	28.4216	0.3044	0.01553	40
^{97}Ru	^{99}Ru	d2n	-11.3902	11.6221	247.883	12.393	40
^{97}Ru	^{98}Ru	dn	-3.91838	3.99897	732.349	38.396	40
^{97}Ru	^{100}Ru	d3n	-21.0635	21.4881	11.6171	0.7813	40
^{97}Ru	^{nat}Ru	pXn	x	0.0	47.2099	2.41782	40
^{97}Rh	^{96}Ru	n	1.58158	0.0	180.501	14.247	9.8
^{97}Rh	^{99}Ru	4n	-24.1774	24.6696	83.8739	3.9549	40
^{97}Rh	^{98}Ru	3n	-16.7056	17.0491	249.017	12.522	40
^{97}Rh	^{100}Ru	5n	-33.8507	34.533	2.2182	0.15582	40
^{97}Rh	^{nat}Ru	n	x	0.0	15.8288	0.76788	40
^{99}Mo	^{104}Ru	αdn	-6.36464	6.48798	0.0743	0.0047	40
^{99}Mo	^{100}Ru	αp	-11.9885	12.2301	0.0006	6e-05	40
^{99}Mo	^{102}Ru	αp	0.28551	0.0	0.0401	0.00224	40
^{99}Mo	^{nat}Ru	αdXn	x	0.0	0.0263	0.00159	40

Table C.3: *TASMAN reaction results for Ru-^{3}He, showing the residual production cross-section and exclusive cross-section along with key values: Q-value, energy threshold, maximum cross-section and the energy of the maximum. The values of Q, E_thres, and E(XS_{max}) are in units of MeV, and σ_{max} and error(σ_{max}) are in units of mb.*

Product	Target	Ejectile	Q	E_{thres}	σ_{max}	error(σ_{max})	E(XS_{max})
^{97}Ru	^{96}Ru	α	0.393444	0.0	68.6759	10.5212	21.2
^{97}Ru	^{101}Ru	α3n	-13.5452	13.9501	2.4855	0.17647	40
^{97}Ru	^{99}Ru	αn	2.93015	0.0	127.15	9.337	40
^{97}Ru	^{98}Ru	α	10.402	0.0	169.744	12.807	39.4
^{97}Ru	^{100}Ru	α2n	-6.74318	6.94675	6.6772	0.47909	40
^{97}Ru	^{102}Ru	α4n	-22.7649	23.4386	0.2037	0.01616	40
^{97}Ru	^{nat}Ru	αXn	x	0.0	20.68	1.51811	40
^{97}Rh	^{96}Ru	d	-1.68734	1.7404	397.811	51.28	19.2
^{97}Rh	^{99}Ru	d3n	-21.1891	21.8352	271.253	18.633	40
^{97}Rh	^{98}Ru	d2n	-13.7172	14.1398	580.004	40.602	36.4
^{97}Rh	^{100}Ru	d4n	-30.8624	31.7941	4.2965	0.30335	40
^{97}Rh	^{nat}Ru	dXn	x	1.7404	47.5449	3.26515	40
^{97}Pd	^{96}Ru	2n	-9.48597	9.78428	47.5872	6.9489	18.8
^{97}Pd	^{99}Ru	5n	-35.2449	36.3197	0.0101	0.00083	40
^{97}Pd	^{98}Ru	4n	-27.7731	28.6287	1.004	0.08041	40
^{97}Pd	^{nat}Ru	Xn	x	9.78428	2.6363	0.385	18.8
^{99}Mo	^{104}Ru	2α	7.95572	0.0	0.0001	5e-05	34.8
^{99}Mo	^{nat}Ru	2αXn	x	0.0	0.0	3e-05	34.8

Table C.4: *TASMAN reaction results for Ru-α, showing the residual production cross-section and exclusive cross-section along with key values: Q-value, energy threshold, maximum cross-section and the energy of the maximum. The values of Q, E_thres, and E(XS_{max}) are in units of MeV, and σ_{max} and error(σ_{max}) are in units of mb.*

Product	Target	Ejectile	Q	E_{thres}	σ_{max}	error(σ_{max})	E(XS_{max})
^{97}Ru	^{96}Ru	α	-12.4661	12.9864	168.737	4.113	40
^{97}Ru	^{99}Ru	α2n	-17.6475	18.3616	96.844	19.65	40
^{97}Ru	^{98}Ru	αn	-10.1756	10.5916	108.833	17.386	34.2
^{97}Ru	^{100}Ru	α3n	-27.3208	28.4154	0.7963	0.25799	40
^{97}Ru	^{nat}Ru	αXn	x	10.5916	23.1188	2.90792	40
^{97}Rh	^{96}Ru	dn	-16.0077	16.6758	714.235	12.39	40
^{97}Rh	^{nat}Ru	dXn	x	16.6758	39.5686	0.68642	40
^{97}Pd	^{96}Ru	3n	-30.0636	31.3183	23.4196	0.2634	40
^{97}Pd	^{nat}Ru	Xn	x	31.3183	1.2974	0.01464	40
^{99}Mo	^{104}Ru	2αn	-12.6219	13.1081	0.0025	0.0012	40
^{99}Mo	^{nat}Ru	2αXn	x	13.1081	0.0005	0.00019	40

Table C.5: *TASMAN reaction results for Mo-^{3}He, showing the residual production cross-section and exclusive cross-section along with key values: Q-value, energy threshold, maximum cross-section and the energy of the maximum. The values of Q, E_thres, and E(XS_{max}) are in units of MeV, and σ_{max} and error(σ_{max}) are in units of mb.*

Product	Target	Ejectile	Q	E_{thres}	σ_{max}	error(σ_{max})	E(XS_{max})
^{97}Ru	^{97}Mo	3n	-10.7069	11.0401	124.955	59.787	18.2
^{97}Ru	^{95}Mo	n	5.26857	0.0	9.1887	0.67462	14.8
^{97}Ru	^{94}Mo	γ	12.6377	0.0	0.0014	0.00058	15.0
^{97}Ru	^{100}Mo	6n	-33.5692	34.5826	0.8447	0.07608	40
^{97}Ru	^{96}Mo	2n	-3.88577	4.00797	138.78	41.131	16.2
^{97}Ru	^{98}Mo	4n	-19.3495	19.9456	41.1093	3.328	39.6
^{97}Ru	^{nat}Mo	Xn	x	0.0	33.7964	11.17735	16.8
^{99}Mo	^{100}Mo	α	12.2834	0.0	14.98	3.2933	27.8
^{99}Mo	^{98}Mo	α	-1.79261	1.84783	0.1164	0.01149	40
^{99}Mo	^{nat}Mo	αXn	x	0.0	1.4776	0.32244	27.8

Table C.6: *TASMAN reaction results for Mo-α, showing the residual production cross-section and exclusive cross-section along with key values: Q-value, energy threshold, maximum cross-section and the energy of the maximum.The values of Q, E_thres, and E(XS_{max}) are in units of MeV, and σ_{max} and error(σ_{max}) are in units of mb.*

Product	**Target**	**Ejectile**	**Q**	**E_{thres}**	σ_{max}	**error(σ_{max})**	**E(XS_{max})**
^{97}Ru	^{97}Mo	4n	-31.2845	32.5767	383.659	8.709	40
^{97}Ru	^{95}Mo	2n	-15.309	15.9547	917.661	40.847	26.2
^{97}Ru	^{94}Mo	n	-7.93993	8.27836	617.873	52.528	18.0
^{97}Ru	^{96}Mo	3n	-24.4634	25.4844	907.796	35.672	37.4
^{97}Ru	^{nat}Mo	Xn	x	8.27836	198.8132	7.53106	38.8
^{99}Mo	^{97}Mo	α	-13.7276	14.2946	0.0566	0.00097	39.2
^{99}Mo	^{100}Mo	αn	-8.29425	8.62654	59.0988	5.4511	31.2
^{99}Mo	^{98}Mo	α	-14.6522	15.2512	2.5128	0.0017	40
^{99}Mo	^{nat}Mo	αXn	x	8.62654	5.7965	0.5312	31.2

D

Non-relativistic two-body kinematic scattering

The interaction between a stationary target nucleus A with a particle beam B often leads to the production of two products C and D where the beam's momentum is distributed between the two products ejected at angles θ and ϕ respectively from the azimuthal beam angle [141] as shown in figure D.1.

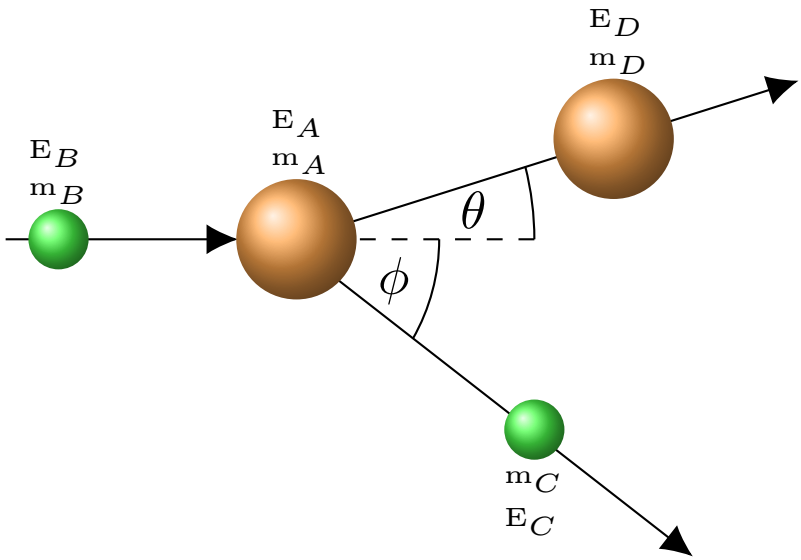


Figure D.1: *Schematic of two-body kinematic scattering of a projectile on a stationary target.*

An additional consideration to the reaction is the possibility of the daughter nucleus residing in an excited state E_x and the conversion of energy and mass equal the reaction Q-value

$$Q = \left(\sum_{i=A,B} m_i - \sum_{k=C,D} m_f \right) c^2, \tag{D.1}$$

where c is the speed of light. This leads to the construction of energy conservation equations for the reaction

$$Q + E_B = E_C + E_D + E_x \tag{D.2}$$

and complementary momentum conservation equations

$$P_B = P_D cos\theta + P_C cos\phi, \tag{D.3}$$

and

$$0 = P_D sin\theta - P_C sin\phi \tag{D.4}$$

Equation D.3 can be rearrange and squared to give

$$P_C^2 \cos^2 \phi = (P_B - P_D \cos\theta)^2. \tag{D.5}$$

Squaring and rearranging equation D.4 gives

$$P_D^2 \sin^2\theta = P_C^2 \sin^2\phi, \tag{D.6}$$

with the substitution of the trigonometric identity $\sin^2\theta + \cos^2\theta = 1$ we get

$$P_C^2 \cos^2\phi = P_C^2 - P_D^2 \sin^2\theta. \tag{D.7}$$

Rearranging and equating equation D.6 and D.7 gives

$$P_C^2 = P_B^2 + P_D^2(\cos^2\theta + \sin^2\theta) - 2P_B P_D \cos\theta \tag{D.8}$$

$$= P_B^2 + P_D^2 - 2P_B P_D \cos\theta, \tag{D.9}$$

where the momenta can be written in terms of their energy using the non-relativistic energy-momentum relationship of $P = \sqrt{2mE}$ yielding

$$2m_C E_C = 2m_B E_B + 2m_D E_D - 4\sqrt{m_B m_D E_B E_D}\cos\theta, \tag{D.10}$$

which now in terms of energy, can have equation D.2 rearranged and substituted to remove E_C, while also dividing by $2m_B$

$$\frac{m_C}{m_B}(E_B + Q - E_D - E_x) = \frac{m_D}{m_B}E_D - 2\sqrt{\frac{m_D}{m_B}E_B E_D}\cos\theta. \tag{D.11}$$

The equation can now conveniently be converted into the quadratic form of $Ax^2 + Bx + C = 0$, where $x = \sqrt{E_B}$ by rearranging and dividing by $2m_B$

$$\left(1 - \frac{m_C}{m_B}\right)E_B - 2\sqrt{\frac{m_D}{m_B}E_D}\cos\theta\sqrt{E_B} + \left(\frac{m_D}{m_B} + \frac{m_C}{m_B}\right)E_D + \frac{m_C}{m_B}(E_x - Q) = 0. \tag{D.12}$$

The equation could have been rearranged in several ways to make different energies the subject; however, it is the beam-energy which requires determining in this instance, as the energies, E_D and the angle of

scatter, θ of product D can be accurately determined with DSSD detectors, as is done in this method. Equation D.12 can be solved to give

$$\sqrt{E_B} = \frac{2\sqrt{\frac{m_D}{m_B}E_D}\cos\theta \pm \left[4\frac{m_D}{m_B}E_D\cos^2\theta - 4\left(1-\frac{m_C}{m_B}\right)\left(\frac{m_D}{m_B}+\frac{m_C}{m_B}\right)E_D + \frac{m_C}{m_B}(E_x - Q)\right]^{1/2}}{2\left(1-\frac{m_C}{m_B}\right)} \tag{D.13}$$

E

Spectrum Decay Count Correction

The activity, A of a radioactive nucleus is given as the rate of change in counts over time

$$A = \frac{dN}{dt}, \tag{E.1}$$

where N is the number of counts and t is time. The activity of a nucleus over time can also be calculated as

$$A(t) = A_0 e^{-\lambda t}, \tag{E.2}$$

where λ is the decay constant, t is time, and A_0 is the activity at time $t = 0$. Equation E.1 can be substituted into equation E.2 to give

$$\frac{dN}{dt} = A_0 e^{-\lambda t}, \tag{E.3}$$

whereby multiplying by dt, the counts on both sides can be integrated:

$$\int dN = A_0 \int_0^t e^{-\lambda t} dt \tag{E.4}$$

$$N = A_0 \Big[-\frac{e^{-\lambda t}}{\lambda} \Big]_0^{\tau}, \tag{E.5}$$

$$= A_0 \Big[-\frac{e^{-\lambda \tau}}{\lambda} - -\frac{1}{\lambda} \Big], \tag{E.6}$$

$$= A_0 \Big[\frac{1 - e^{-\lambda \tau}}{\lambda} \Big], \tag{E.7}$$

where τ is the real-time of the spectrum. This can be rearranged to give the count rate at the start of the spectrum

$$A_0 = \frac{\lambda N}{1 - e^{-\lambda \tau}} \tag{E.8}$$

$$= \frac{A}{1 - e^{-\lambda \tau}}, \tag{E.9}$$

where A is the count rate calculated by simply dividing the spectrum counts by the live-time of the spectrum, τ_L to give $A = N/\tau_L$ [118].

F

Statistics

This section details a number of statistical equations used throughout the analysis method in this thesis.

F.1 Error Propagation

For the propagation of errors, the general method of error propagation error was used, taking the total differential of the function. For a function

$$z = f(w, x, y, z...), \tag{F.1}$$

where z is a function of a number of independent variables, in this case, w, x, y, and z. The error on z, given as σz can be given as the partial sum of the function with respect to each variable in the function

multiplied by the error on that variable

$$\sigma z^2 = \left(\frac{\partial f}{\partial w}\right)^2 \sigma w^2 + \left(\frac{\partial f}{\partial x}\right)^2 \sigma x^2 + \left(\frac{\partial f}{\partial y}\right)^2 \sigma y^2 + ... \tag{F.2}$$

where σw, σx, σy and, σz are the errors of the respective variables [142].

F.2 Weighted average of value with errors

When determining the average of a set of values x_i to give $\bar{x}$, each with their own error σ_i. The average value should be weighted to favour values with smaller errors as shown

$$\bar{x} = \frac{\sum_i^n (x_i/\sigma_i^2)}{\sum_i^n (1/\sigma_i^2)}. \tag{F.3}$$

To calculate the error of the mean $\bar{x}$, each value of x_i is treated as an independent variable, with the general method of error propagation shown in equation F.2. This can be written as

$$\sigma\bar{x}^2 = \left(\frac{\partial \bar{x}}{\partial x_1}\right)^2 \sigma x_1^2 + \left(\frac{\partial \bar{x}}{\partial x_2}\right)^2 \sigma x_2^2 + ... + \left(\frac{\partial \bar{x}}{\partial x_n}\right)^2 \sigma x_n^2 \tag{F.4}$$

$$= \sum_j^n \left(\frac{\partial \bar{x}}{\partial x_j^2}\right)^2 x_j^2 \tag{F.5}$$

$$= \sum_j^n \left(\frac{1/\sigma_j}{\sum_i^n 1/\sigma_i^2}\right)^2 \sigma_j^2 \tag{F.6}$$

$$= \frac{1}{\sum_i^n 1/\sigma_i^2} \tag{F.7}$$

$$\sigma\bar{x} = \sqrt{\frac{1}{\sum_i^n 1/\sigma_i^2}} \tag{F.8}$$

References

[1] A. J. Plompen et al. "The joint evaluated fission and Fusion Nuclear Data Library, jeff-3.3". In: *The European Physical Journal A* 56.7 (2020). DOI: 10.1140/epja/s10050-020-00141-9.

[2] *Colourful nuclide chart*. URL: https://people.physics.anu.edu.au/~ecs103/chart/.

[3] "The existence of a Neutron". In: *Proceedings of the Royal Society of London. Series A, Containing Papers of a Mathematical and Physical Character* 136.830 (1932), pp. 692–708. DOI: 10.1098/rspa.1932.0112.

[4] I Curie. *Artificial Production of Radioactive Elements*. 1935.

[5] American Physical Society. *December 1938: Lise Meitner &; Otto Frisch discover nuclear fission*. URL: https://www.aps.org/publications/apsnews/200712/physicshistory.cfm.

[6] Robert Vandenbosch. In: *Nuclear fission*. Elsevier Science, 2012, p. 6.

[7] Published by Statista Research Department and Aug 1. *Operational Nuclear Reactors Worldwide 2022*. 2022. URL: https://www.statista.com/statistics/1203469/operating-nuclear-reactors-worldwide/.

[8] Dragoslav PopoviÄ‡. "Validity of the inverse velocity law for the fission cross section of 235 u". In: *Physica* 20.1-6 (1954), 406â€“412. DOI: 10.1016/s0031-8914(54)80055-3.

[9] A.S. Soldatov et al. "Quadrupole fission of U238". In: *Physics Letters* 14.3 (1965), 217â€“219. DOI: 10.1016/0031-9163(65)90596-2.

[10] *Argonne National Laboratory*. URL: https://www.anl.gov/topic/spent-nuclear-fuel.

[11] Robert Mills. Private Communication. National Nuclear Laboratory, 2022.

[12] David W Shoesmith. "CHEMISTRY/ELECTROCHEMISTRY OF SPENT NUCLEAR FUEL AS A WASTEFORM". In: *Surface Science Western and Department of Chemistry* ().

[13] Maria Garcia Miranda, Ben Russell, and Peter Ivanov. "Measurement of 151SM in nuclear decommissioning samples by ICP-MS/MS". In: *Journal of Radioanalytical and Nuclear Chemistry* 316.2 (2018), pp. 831–838. DOI: 10.1007/s10967-018-5764-x.

[14] S.M. Jerome et al. "The production of neptunium-236G". In: *Journal of Environmental Radioactivity* 138 (2014), pp. 315–322. DOI: 10.1016/j.jenvrad.2014.02.029.

[15] B. R. Harvey et al. "Determination of technetium-99 in environmental material with rhenium as a yield monitor". In: *Journal of Radioanalytical and Nuclear Chemistry Articles* 158.2 (1992), pp. 417–436. DOI: 10.1007/bf02047127.

[16] Th. B Unger. "Standard Test Method for Radiochemical Determination of Uranium Isotopes in Soil by Alpha Spectrometry". In: (1029). DOI: 10.1520/c1000-00.

[17] Chang Kyu Kim. 2010.

[18] Ivan K. Kressin et al. "Plutonium-242 vs plutonium-236 as an analytical tracer". In: *Health Physics* 28.1 (1975), pp. 41–47. DOI: 10.1097/00004032-197501000-00007.

[19] Matthew Gott, Jörg Steinbach, and Constantin Mamat. "The radiochemical and radiopharmaceutical applications of radium". In: *Open Chemistry* 14.1 (2016), pp. 118–129. DOI: 10.1515/chem-2016-0011.

[20] B.T. Kenna and P.K. Kuroda. "Technetium in nature". In: *Journal of Inorganic and Nuclear Chemistry* 26.4 (1964), pp. 493–499. DOI: 10.1016/0022-1902(64)80280-3.

[21] Jonathan P. Icenhower et al. "The geochemistry of technetium: A summary of the behavior of an artificial element in the natural environment". In: (2008). DOI: 10.2172/1010487.

[22] Keliang Shi et al. "Determination of technetium-99 in environmental samples: A Review". In: *Analytica Chimica Acta* 709 (2012), pp. 1–20. DOI: 10.1016/j.aca.2011.10.020.

[23] C. Perrier and E. Segrè. "Some chemical properties of element 43". In: *The Journal of Chemical Physics* 5.9 (1937), pp. 712–716. DOI: 10.1063/1.1750105.

[24] E. Browne and J.K. Tuli. "Nuclear data sheets for A = 99". In: *Nuclear Data Sheets* 145 (2017), pp. 25–340. DOI: 10.1016/j.nds.2017.09.002.

[25] M. R. Bhat. "Evaluated Nuclear Structure Data File (ENSDF)". In: *Nuclear Data for Science and Technology* (1992), pp. 817–821. DOI: 10.1007/978-3-642-58113-7_227.

[26] K.S. Leonard et al. "Distribution of technetium-99 in UK coastal waters". In: *Marine Pollution Bulletin* 34.8 (1997), pp. 628–636. DOI: 10.1016/s0025-326x(96)00185-3.

[27] Environment Agency. *Radioactivity in Food and the Environment, 2009*. 2010. URL: https://assets.publishing.service.gov.uk/government/uploads/system/uploads/attachment_data/file/750770/Radioactivity_in_food_and_the_environment_2009_RIFE_15.pdf.

[28] Yasmin Sheng Yu. "Development of an optimised procedure for measurement of 99Tc in aqueous samples by ICP-MS/MS". MA thesis. Royal Holloway, 2018.

[29] S. Uchida et al. "Determination of 99Tc deposited on the ground within the 30-km zone around the Chernobyl Reactor and estimation of 99Tc released into atmosphere by the accident". In: *Chemosphere* 39.15 (1999), pp. 2757–2766. DOI: 10.1016/s0045-6535(99)00210-6.

[30] P. Bailly du Bois et al. "Estimation of marine source-term following Fukushima Dai-ichi accident". In: *Journal of Environmental Radioactivity* 114 (2012), pp. 2–9. DOI: 10.1016/j.jenvrad.2011.11.015.

[31] P. Lindahl et al. "Long-term study of 99Tc in the marine environment on the Swedish West Coast". In: *Journal of Environmental Radioactivity* 67.2 (2003), pp. 145–156. DOI: 10.1016/s0265-931x(02)00176-5.

[32] S. Uchida and K. Tagami. "Separation and concentration of technetium using a TC-selective extraction chromatographic resin". In: *Journal of Radioanalytical and Nuclear Chemistry* 221.1-2 (1997), pp. 35–39. DOI: 10.1007/bf02035239.

[33] Hsin-Chieh Wu et al. "Rapid determination of technetium-99 by automatic solid phase extraction and inductively coupled plasma mass spectrometry". In: *RSC Adv.* 4.74 (2014), pp. 39226–39230. DOI: 10.1039/c4ra06591c.

[34] Zi-lu Zhang et al. "Preconcentration and separation of 99Tc in groundwater by using Teva Resin". In: *Journal of Radioanalytical and Nuclear Chemistry* 314.1 (2017), pp. 161–166. DOI: 10.1007/s10967-017-5425-5.

[35] Hans Sahli, Stefan Röllin, and José A. Corcho Alvarado. "Determination of 99Tc in environmental samples and depleted uranium penetrators using ICP-MS". In: *Journal of Radioanalytical and Nuclear Chemistry* 311.3 (2016), pp. 1633–1642. DOI: 10.1007/s10967-016-5145-2.

[36] Kamila Kołacińska et al. "A comparison study on the use of Dowex 1 and Teva-resin in determination of 99Tc in environmental and nuclear coolant samples in a SIA system with ICP-Ms Detection". In: *Talanta* 184 (2018), pp. 527–536. DOI: 10.1016/j.talanta.2018.03.034.

[37] E. Kabai et al. "Separation technique for the determination of 99Tc in milk and dairy products in case of emergency". In: *Applied Radiation and Isotopes* 81 (2013), pp. 36–41. DOI: 10.1016/j.apradiso.2013.03.031.

[38] Lian-Song Chen et al. "Accurate technetium-99 determination using the combination of Teva Resin Pretreatment and ICP-MS Measurement and its influence on the TC-99/CS-137 scaling factor calculation". In: *Journal of Radioanalytical and Nuclear Chemistry* 299.3 (2014), pp. 1883–1889. DOI: 10.1007/s10967-014-2931-6.

[39] Mumtaz Khan and Wooyong Um. "Liquid scintillation counting methodology for 99Tc analysis: A remedy for radiopharmaceutical waste". In: *Analytical Chemistry* 87.17 (2015), pp. 9054–9060. DOI: 10.1021/acs.analchem.5b02279.

[40] Eliane S. Temba et al. "Separation and determination of the difficult-to-measure radionuclide 99Tc in radioactive wastes from nuclear power plants by using extraction chromatography and radiometric techniques". In: *Journal of Radioanalytical and Nuclear Chemistry* 307.2 (2015), pp. 1453–1458. DOI: 10.1007/s10967-015-4359-z.

[41] Xiaolin Hou and Per Roos. "Critical comparison of radiometric and mass spectrometric methods for the determination of radionuclides in environmental, biological and nuclear waste samples". In: *Analytica Chimica Acta* 608.2 (2008), pp. 105–139. DOI: 10.1016/j.aca.2007.12.012.

[42] URL: https://www.agilent.com/cs/library/technicaloverviews/public/5991-1708EN_TechOverview_ICP-MS_8800_ORS_mode.pdf.

[43] B Russell. *Applications of novel resins for Technetium separation from environmental and target samples*. 2021.

[44] P. E. Warwick et al. "Evaluation of inductively coupled plasma tandem mass spectrometry for radionuclide assay in nuclear waste characterisation". In: *Journal of Analytical Atomic Spectrometry* 34.9 (2019), pp. 1810–1821. DOI: 10.1039/c8ja00411k.

[45] Martin McCartney et al. "Development of a novel method for the determination of 99Tc in environmental samples by ICP-MS". In: *Journal of Analytical Atomic Spectrometry* 14.12 (1999), pp. 1849–1852. DOI: 10.1039/a905274g.

[46] Keiko Tagami and Shigeo Uchida. "Soil-to-plant transfer factors of technetium-99 for various plants collected in the Chernobyl area". In: *Journal of Nuclear and Radiochemical Sciences* 6.3 (2005), pp. 261–264. DOI: 10.14494/jnrs2000.6.3_261.

[47] D. M. Beals. "Determination of technetium-99 in aqueous samples by isotope dilution inductively coupled plasma-mass spectrometry". In: *Journal of Radioanalytical and Nuclear Chemistry Articles* 204.2 (1996), pp. 253–263. DOI: 10.1007/bf02060314.

[48] N CHU. "Radiochemical determination of Technetium?99". In: *Talanta* 31.10 (1984), pp. 809–813. DOI: 10.1016/0039-9140(84)80203-9.

[49] F Wigley et al. "Optimised method for the routine determination of technetium-99 in environmental samples by Liquid Scintillation counting". In: *Analytica Chimica Acta* 380.1 (1999), pp. 73–82. DOI: 10.1016/s0003-2670(98)00676-x.

[50] Fano Chen et al. "A simple two-strip method to determine the radiochemical purity of technetium-99m mercaptoacetyltriglycine". In: *European Journal of Nuclear Medicine* 20.4 (1993). DOI: 10.1007/bf00169810.

[51] J.C. Butterworth, F.R. Livens, and P.R. Makinson. "Development of a method for the determination of low levels of technetium-99". In: *Science of The Total Environment* 173-174 (1995), pp. 293–300. DOI: 10.1016/0048-9697(95)04774-3.

[52] Keliang Shi et al. "Determination of technetium-99 in environmental samples: A Review". In: *Analytica Chimica Acta* 709 (2012), pp. 1–20. DOI: 10.1016/j.aca.2011.10.020.

[53] J.K. Tuli. "Nuclear data sheets update for A = 94". In: *Nuclear Data Sheets* 66.1 (1992), pp. 1–67. DOI: 10.1016/s0090-3752(05)80028-6.

[54] S.K. Basu, G. Mukherjee, and A.A. Sonzogni. "Nuclear data sheets for A = 95". In: *Nuclear Data Sheets* 111.10-11 (2010), pp. 2555–2737. DOI: 10.1016/j.nds.2010.10.001.

[55] D. Abriola and A.A. Sonzogni. "Nuclear data sheets for A = 96". In: *Nuclear Data Sheets* 109.11 (2008), pp. 2501–2655. DOI: 10.1016/j.nds.2008.10.002.

[56] N. Nica. "Nuclear data sheets for A = 97". In: *Nuclear Data Sheets* 111.3 (2010), pp. 525–716. DOI: 10.1016/j.nds.2010.03.001.

[57] Balraj Singh and Zhiqiang Hu. "Nuclear data sheets for A = 98". In: *Nuclear Data Sheets* 98.2 (2003), pp. 335–513. DOI: 10.1006/ndsh.2003.0003.

[58] Balraj Singh and Jun Chen. "Nuclear data sheets for A = 100". In: *Nuclear Data Sheets* 172 (2021), pp. 1–542. DOI: 10.1016/j.nds.2021.02.001.

[59] Jean Blachot. "Nuclear data sheets update for A = 101". In: *Nuclear Data Sheets* 63 (1991), pp. 305–371. DOI: 10.1016/s0090-3752(05)80006-7.

[60] D. De Frenne. "Nuclear data sheets for A = 102". In: *Nuclear Data Sheets* 110.8 (2009), pp. 1745–1915. DOI: 10.1016/j.nds.2009.06.002.

[61] Lixiong Wang et al. "Study on the method of preparation 97TC". In: *Journal of Radioanalytical and Nuclear Chemistry* 283.1 (2009), pp. 111–116. DOI: 10.1007/s10967-009-0129-0.

[62] E. Rutherford. "The Scattering of α and β Particles by Matter and the Structure of the Atom". In: *Philosophical Magazine*. 6th ser. 21 (1911), pp. 669–688.

[63] E. RUTHERFORD. "Conference on the theory of radiation". In: *Nature* 88.2194 (1911), 82â€"83. DOI: 10.1038/088082a0.

[64] M Thiel et al. "Neutron skins of atomic nuclei: Per Aspera ad astra". In: *Journal of Physics G: Nuclear and Particle Physics* 46.9 (2019), p. 093003. DOI: 10.1088/1361-6471/ab2c6d.

[65] W Vonoertzen, M Freer, and Y Kanadaenyo. "Nuclear clusters and nuclear molecules". In: *Physics Reports* 432.2 (2006), 43â€"113. DOI: 10.1016/j.physrep.2006.07.001.

[66] A. Einstein. "Equivalence of energy and inertial mass". In: *Nature* 135.3403 (1935), 111â€"111. DOI: 10.1038/135111b0.

[67] G Gamow. "Mass defect curve and nuclear constitution". In: *Proceedings of the Royal Society of London. Series A, Containing Papers of a Mathematical and Physical Character* 126.803 (1930), pp. 632–644. DOI: 10.1098/rspa.1930.0032.

[68] C. F. Weizs acker. "Zur Theorie der kernmassen". In: *Zeitschrift f ur Physik* 96.7-8 (1935), pp. 431–458. DOI: 10.1007/bf01337700.

[69] *Enhanced abundance of magic number nuclei*. URL: http://hyperphysics.phy-astr.gsu.edu/hbase/Nuclear/shell2.html.

[70] Roger D. Woods and David S. Saxon. "Diffuse surface optical model for nucleon-nuclei scattering". In: *Physical Review* 95.2 (1954), pp. 577–578. DOI: 10.1103/physrev.95.577.

[71] W. Pauli. "Über den Zusammenhang des abschlusses der elektronengruppen im atom mit der komplexstruktur der spektren". In: *Zeitschrift für Physik* 31.1 (1925), pp. 765–783. DOI: 10.1007/bf02980631.

[72] Ali Abdulwahab Ridha. "Chapter Two (Binding Energy amp; Nuclear Models)". In: *Nuclear Physics*, pp. 12–40.

[73] S. D. Drell. "Nuclear radius and nuclear forces". In: *Physical Review* 100.1 (1955), 97â€"112. DOI: 10.1103/physrev.100.97.

[74] Kenneth S. Krane. "Nuclear Reactions". In: *Introductory nuclear physics*. Wiley, 2016.

[75] H Bethe and J Ashkin. In: *Experimental Nuclear Physics* (1953), p. 253.

[76] D. M. Ziegler James F. Zeigler and P.J.Biersack. "SRIM - The stopping and range of ions in matter". In: *Publication: Nuclear Instruments and Methods in Physics Research* 268.11-12 (2010), pp. 1818–1832.

[77] David Parker and Carl Wheldon. "The Birmingham MC40 Cyclotron Facility". In: *Nuclear Physics News* 28.4 (2018), pp. 15–20. DOI: 10.1080/10619127.2018.1463021.

[78] Karolina Kolos et al. "Current nuclear data needs for applications". In: *Physical Review Research* 4.2 (2022). DOI: 10.1103/physrevresearch.4.021001.

[79] N. Otuka et al. "Towards a more complete and accurate experimental nuclear reaction data library (EXFOR): International collaboration between nuclear reaction data centres (NRDC)". In: *Nuclear Data Sheets* 120 (2014), pp. 272–276. DOI: 10.1016/j.nds.2014.07.065.

[80] *Experimental unevaluated nuclear data list (XUNDL)*. URL: https://www.nndc.bnl.gov/xundlarchivals/.

[81] Joel Kulesza et al. "MCNP Code Version 6.3.0 Theory & User Manual". In: (2022). DOI: 10.2172/1889957.

[82] Albert Comstock Kahler. "Using NJOY to create MCNP ACE files and visualize nuclear data". In: (2016). DOI: 10.2172/1250722.

[83] Jeremy Lloyd Conlin. "Development and maintenance of Njoy". In: (2019). DOI: 10.2172/1493523.

[84] A.J. Koning and D. Rochman. "Modern nuclear data evaluation with the TALYS Code System". In: *Nuclear Data Sheets* 113.12 (2012), pp. 2841–2934. DOI: 10.1016/j.nds.2012.11.002.

[85] A. Palumbo, M. Herman, and R. Capote. "Empire: A reaction model code for nuclear astrophysics". In: *Nuclear Data Sheets* 120 (2014), pp. 180–183. DOI: 10.1016/j.nds.2014.07.040.

[86] O. Iwamoto et al. "The CCONE code system and its application to nuclear data evaluation for fission and other reactions". In: *Nuclear Data Sheets* 131 (2016), pp. 259–288. DOI: 10.1016/j.nds.2015.12.004.

[87] Naohiko Otuka and Boris Pritychenko. "International Network of Nuclear Reaction Data Centres". In: (2021). DOI: 10.2172/1807954.

[88] A.B. Pashchenko, H. Wienke, and S. Ganesan. "FENDL: International Reference Nuclear Data Library for Fusion Applications". In: *Journal of Nuclear Materials* 233-237 (1996), pp. 1601–1606. DOI: 10.1016/s0022-3115(96)00153-5.

[89] M. Herman. "ENDF-6 formats manual data formats and procedures for the evaluated nuclear data file ENDF/B-VI and ENDF/B-VII". In: (2009). DOI: 10.2172/981813.

[90] C. M. Mattoon et al. *Generalized Nuclear Data: A new structure (with supporting infrastructure) for handling nuclear data*. 2012. URL: https://www.osti.gov/biblio/22131272-generalized-nuclear-data-new-structure-supporting-infrastructure-handling-nuclear-data.

[91] R. Capote et al. "RIPL - reference input parameter library for calculation of nuclear reactions and nuclear data evaluations". In: *Nuclear Data Sheets* 110.12 (2009), pp. 3107–3214. DOI: 10.1016/j.nds.2009.10.004.

[92] John Apostolakis and Dennis H. Wright. "An overview of the geant4 toolkit". In: *AIP Conference Proceedings* (2007). DOI: 10.1063/1.2720452.

[93] A. Ferrari et al. "Fluka: A multi-particle transport code". In: (2005). DOI: 10.2172/877507.

[94] Paul K. Romano and Benoit Forget. "The OpenMC Monte Carlo Particle Transport Code". In: *Annals of Nuclear Energy* 51 (2013), pp. 274–281. DOI: 10.1016/j.anucene.2012.06.040.

[95] R.F. Burstall. *Fispin - a computer code for Nuclide Inventory calculations*. 1979. URL: https://inis.iaea.org/search/search.aspx?orig_q=RN%3A11518686.

[96] J.-Ch. Sublet et al. "FISPACT-II: An advanced simulation system for activation, transmutation and material modelling". In: *Nuclear Data Sheets* 139 (2017), pp. 77–137. DOI: 10.1016/j.nds.2017.01.002.

[97] A.J. Koning et al. "Tendl: Complete Nuclear Data Library for Innovative Nuclear Science and Technology". In: *Nuclear Data Sheets* 155 (2019), pp. 1–55. DOI: 10.1016/j.nds.2019.01.002.

[98] Arjan Koning. Vol. 236. IAEA NDS Document Series IAEA(NDS). 2020.

[99] *Bluebear*. URL: https://intranet.birmingham.ac.uk/it/teams/infrastructure/research/bear/bluebear/index.aspx.

[100] A.J. Koning and J.P. Delaroche. "Local and global nucleon optical models from 1 keV to 200 MeV". In: *Nuclear Physics A* 713.3-4 (2003), pp. 231–310. DOI: 10.1016/s0375-9474(02)01321-0.

[101] H Feshbach. "The optical model and its justification". In: *Annual Review of Nuclear Science* 8.1 (1958), 49â€“104. DOI: 10.1146/annurev.ns.08.120158.000405.

[102] S. Hillaire. *TALYS: A tool to go from theoretical modeling of nuclear reactions to evaluations.*

[103] A.J. Koning and J.P. Delaroche. "Local and global nucleon optical models from 1 keV to 200 MeV". In: *Nuclear Physics A* 713.3-4 (2003), pp. 231–310. DOI: 10.1016/s0375-9474(02)01321-0.

[104] Thomas J. Bruno and Paris D. Svoronos. *Atomic Masses and abundances*. 2017. URL: https://www.nist.gov/publications/atomic-masses-and-abundances.

[105] *Project jupyter*. URL: https://jupyter.org/.

[106] *UK Atomic Energy Authority*. URL: https://www.gov.uk/government/organisations/uk-atomic-energy-authority.

[107] Christopher Ostrouchov, Yanwen Zhang, and William J. Weber. "Pysrim: Automation, analysis, and plotting of Srim calculations". In: *Journal of Open Source Software* 3.28 (2018), p. 829. DOI: 10.21105/joss.00829.

[108] Arjan Koning. Vol. 236. IAEA NDS Document Series IAEA(NDS). 2020.

[109] David R. Lide. In: *CRC Handbook of Chemistry and Physics: 1993-1994: A ready-reference book of Chemical and physical data*. CRC Press, 1993, p. 18.

[110] R. R. Trinder et al. "Theragnostics - alternative production of terbium isotopes at the University of Birmingham using an MC40 cyclotron". In: *Journal of Physics: Conference Series* 1643.1 (2020), p. 012209. DOI: 10.1088/1742-6596/1643/1/012209.

[111] F. Ditrói et al. "Investigation of the α-particle induced nuclear reactions on natural molybdenum". In: *Nuclear Instruments and Methods in Physics Research Section B: Beam Interactions with Materials and Atoms* 285 (2012), pp. 125–141. DOI: 10.1016/j.nimb.2012.05.030.

[112] F. Tárkányi et al. "Investigation of activation cross section data of alpha particle induced nuclear reaction on molybdenum up to 40 mev: Review of production routes of medically relevant 97,103 ru". In: *Nuclear Instruments and Methods in Physics Research Section B: Beam Interactions with Materials and Atoms* 399 (2017), pp. 83–100. DOI: 10.1016/j.nimb.2017.03.043.

[113] Mateusz Sitarz et al. "New cross-sections for natmo(α,x) reactions and medical 97ru production estimations with radionuclide yield calculator". In: *Instruments* 3.1 (2019), p. 7. DOI: 10.3390/instruments3010007.

[114] *W1*. URL: http://www.micronsemiconductor.co.uk/product/w1/.

[115] K A Mikkelson. "MIDAS: Multiple Instrument Data Acquisition Software user guide". In: (Aug. 1988). URL: https://www.osti.gov/biblio/6905641.

[116] Sae-Hoon Park, Sang-Hoon Lee, and Yu-Seok Kim. "Emittance measurement for beamline extension at the pet cyclotron". In: *Science and Technology of Nuclear Installations* 2016 (2016), iâ€“4. DOI: 10.1155/2016/4697247.

[117] D Radford. *Radware*. URL: https://radware.phy.ornl.gov/.

[118] Glenn F. Knoll. *Radiation Detection and Measurement*. John Wiley & Sons., 2020.

[119] D.C Radford. "ESCL8R and LEVIT8R: Software for interactive graphical analysis of hpge coincidence data sets". In: *Nuclear Instruments and Methods in Physics Research Section A: Accelerators, Spectrometers, Detectors and Associated Equipment* 361.1-2 (1995), pp. 297–305. DOI: 10.1016/0168-9002(95)00183-2.

[120] A. A. Sonzogni. "NuDat 2.0: Nuclear Structure and decay data on the internet". In: *AIP Conference Proceedings* (2005). DOI: 10.1063/1.1945075.

[121] D. De Frenne. "Nuclear data sheets for A = 103". In: *Nuclear Data Sheets* 110.9 (2009), pp. 2081–2256. DOI: 10.1016/j.nds.2009.08.002.

[122] L'Annunziata Michael F. *Handbook of radioactivity analysis*. Elsevier, 2012.

[123] Triskem International. 2021. URL: https://www.triskem-international.com/scripts/files/6167e9b2450050.28053696/PS_TK202-Resin_EN_210816.pdf.

[124] *Radioisotopes in Medicine*. URL: https://world-nuclear.org/information-library/non-power-nuclear-applications/radioisotopes-research/radioisotopes-in-medicine.aspx.

[125] P. Schaffer et al. "Cyclotron-based production of tc-99m and other metals". In: *Nuclear Medicine and Biology* 72-73 (2019). DOI: 10.1016/s0969-8051(19)30209-4.

[126] Peter Ivanov. Private Communication. National Nuclear Laboratory, 2022.

[127] *RadioGenix system*. 2022. URL: https://www.northstarnm.com/our-products/radiogenix/.

[128] *Home*. 2022. URL: https://www.shinefusion.com/.

[129] Norbert W. Golchert and Jacob. Sedlet. "Radiochemical determination of technetium-99 in environmental water samples". In: *Analytical Chemistry* 41.4 (1969), pp. 669–671. DOI: 10.1021/ac60273a021.

[130] Keliang Shi et al. "Determination of technetium-99 in environmental samples: A Review". In: *Analytica Chimica Acta* 709 (2012), pp. 1–20. DOI: 10.1016/j.aca.2011.10.020.

[131] Triskem International. 2015. URL: https://www.triskem-international.com/scripts/files/5f463452902878.84967331/PS_TEVA-Resin_EN_160927.pdf.

[132] Triskem International. 2021. URL: https://www.triskem-international.com/scripts/files/6167ea10645210.08957338/PS_TK-TcScint-Resin_EN_210902.pdf.

[133] Triskem International. 2017. URL: https://www.triskem-international.com/scripts/files/5f46345338d9b9.88790626/PS_TK200-Resin_EN_171016.pdf.

[134] Triskem International. 2022. URL: https://www.triskem-international.com/scripts/files/624a3ab0aba5d6.17415344/PS_TK201-Resin_EN_220330.pdf.

[135] Izabela Cieszykowska. *Separation of ^{99m}Tc from low specific activity ^{99}Mo using Tk202 resin*. 2020.

[136] R.V Parish. In: *The metallic elements*. Longman, 1977, p. 112.

[137] E. Anders. "The radiochemistry of technetium". In: *National Academy of Sciences National Research Council NUCLEAR SCIENCE SERIES* (1960). DOI: 10.2172/4073069.

[138] Izabela Cieszykowska et al. "Studies on electrochemical dissolution of sintered molybdenum discs as a potential method for targets dissolution in 99mtc production". In: *Journal of Radioanalytical and Nuclear Chemistry* 331.2 (2021), pp. 1029–1037. DOI: 10.1007/s10967-021-08155-3.

[139] I. Zanzi et al. "New cholescintigraphic agent: Ruthenium-97-DISIDA". In: (1986). DOI: 10.2172/5245276.

[140] M.R. Gilbert, L.W. Packer, and T. Stainer. "Experimental validation of inventory simulations on molybdenum and its isotopes for fusion applications". In: *Nuclear Fusion* 60.10 (2020), p. 106022. DOI: 10.1088/1741-4326/aba99c.

[141] Carl Wheldon. *Derivations for two-body kinematics (both relativistic and non-relativistic)*. 2019. URL: https://docslib.org/doc/9175494/derivations-for-two-body-kinematics-both-relativistic-and-non-relativistic.

[142] Libretexts. *Propagation of error*. 2022. URL: https://chem.libretexts.org/Bookshelves/Analytical_Chemistry/Supplemental_Modules_(Analytical_Chemistry)/Quantifying_Nature/Significant_Digits/Propagation_of_Error?bc=0.